



School of Engineering
Chemical, Process and Energy Engineering

Modelling of Multiphase Fluid flow in Heterogeneous Reservoirs

By:
Mohamed Ibrahim Hussein Balaha
ID: 3220737

Supervised by:

Dr. Elsa Aristodemou
Prof. Attia Attia

April 2022

Abstract

Computational modeling of multiphase fluid flow in highly heterogeneous problems with complicated geometries is a challenging problem for reservoir engineers, with a rich research in establishing best methods and approaches. The novelty in this work is centered around the implementation and comparison of simulation results from two software - the open source ICFESRT and the commercial software ECLIPSE - for a two-phase multiphase problem (oil-water) in both simple and complex geometries. The work involves: (a) implementation and comparison of simulation results from the two software on three different, hypothetical but typical geometries; (b) consideration of a real field case and the associated data analysis, rock characterization, and geostatistics of a real field representative of a highly heterogeneous reservoir; and (c) implementation of both software on the real field case for predictions of oil production at the site, and comparison of the simulation results from the two software.

The initial comparison of simulation results for was carried out using three hypothetical (but common) geometries, these being: (a) a quarter five spot with one geological layer; (b) the same geometry as in (a) but with a vertical heterogeneity i.e. 5 different geological layers; (c) and lastly a full 5 spot with 5 different geological layers was implemented. Three different mesh resolutions were applied in both software and comparisons were carried out for mesh-independency. The results showed that in all these three scenarios, good agreement was observed between IC-FERST (coarse mesh) and ECLIPSE (fine mesh) with an average percentage difference at the production well ranging between 2.5% and 10.5% for the oil production and 12% and 26% for the water production.

Both the ICFERST and ECLIPSE were subsequently implemented on a real, heterogeneous field – which consisted of 25 producing wells and 8 injections wells. Prior to the software implementation, a data analysis and rock characterization was carried out –Using data from the 33 wells. The logging and core data (a total of 30,000 log readings and 1150 core samples) were utilized and a novel rock characterization technique -Balaha Rock Characterization Code- was implemented to allow for the optimal clustering of rock types within the reservoir, The rock characterization resulted in identifying 7 rock types with their unique porosity-hydraulic permeability relationships. Subsequently, geostatistical methods were implemented – which

enabled populating the computational cells of the two software with the corresponding reservoir properties (porosity, hydraulic permeability). To achieve the property population into the unstructured computational domain of the ICFERST software, a newly-developed script was written in Matlab and Python. The rock properties data populated on IC-FERST consist of porosity, permeability, relative permeability, capillary pressure and connate water saturation.

A further comparison between the IC-FERST simulation results with the corresponding ECLIPSE simulations was carried out – were all simulations were carried out for a period of 40 years. The percentage differences between the two software simulations were estimated for : (i) ten individual production wells and (ii) the total of all production wells. The results showed that a good agreement exists between the IC-FERST and ECLIPSE simulations, with an average percentage difference for the total oil production of 10.5%, the total water production of 26% and the total water injection of 14%. The results for the ten individual wells showed an average percentage difference of 15.5% ranging from 3 to 29% for the oil production in the late time period. Slightly higher differences were observed when the overall period was considered, due to the large difference at the early time period of the simulation.

The results indicated that IC-FERST, when incorporating the necessary rock characterization information – which highlight the heterogeneity of the reservoir – can produce results that can compete with the industry standard ECLIPSE. Additional aspects need to be considered within the current real field IC-FERST simulation, the inclusion of possible fractures and faults, as these were incorporated in the computational domain of ECLIPSE. Additional capabilities also still need to be embedded into IC-FERST, such as the incorporation of the fluid density and viscosity variations with pressure and the consideration of the volume factors, in order to enhance its competitiveness with existing commercial reservoirs simulators such as ECLIPSE.

Table of Contents

Abstract.....	I
List of Figures.....	VII
List of Tables.....	XIII
Acknowledgement.....	XV
Nomenclature.....	XVI
Chapter 1 Introduction, Aims and Objectives.....	1
Chapter 2 Literature Review.....	5
2.1 Multiphase Fluid Flow.....	6
2.1.1 Numerical Schemes/Methods.....	8
2.1.2 Gridding/Meshing Approaches.....	13
2.2 Rock Typing.....	17
2.2.1 Permeability Prediction and Hydraulic Flow Unit(s) Identification Techniques ...	17
2.2.2 Techniques for Estimating the Flow Zone Indicator (FZI) from Well Log Data ...	24
2.2.3 Rock Typing Using Cluster Analysis.....	25
2.2.4 Effect of Packing on Permeability.....	26
2.2.5 Permeability Estimation from Well Logs.....	27
2.3 Geostatistics.....	29
2.3.1 Kriging.....	31
2.3.2 Variograms.....	31
2.3.3 Cokriging.....	32
2.3.4 Stochastic Simulation.....	33
2.3.5 Sequential Gaussian Simulation (SGS).....	34
2.3.6 Sequential Indicator Simulation (SIS).....	35
Chapter 3 Methodology.....	37

3.1	Theoretical Background	38
3.1.1	General Flow Equations – Single Phase Darcy’s Law	38
3.1.2	Two Phase Darcy’s Law	40
3.1.3	Multiphase Fluid Flow Equations within IC-FERST	42
3.1.4	Brief Introduction to Numerical Methods for Reservoir Simulation.....	43
3.1.5	Different Types of Gridding used in Reservoir Simulators	47
3.2	Implementation of the Commercial Reservoir Simulator ECLIPSE	51
3.2.1	PETREL (ECLIPSE Pre-Processor)	53
3.2.2	Rock Typing, Upscaling and Geostatistical Means within PETREL	54
3.2.3	ECLIPSE (Processor).....	56
3.2.4	ECLIPSE Post Processing.....	56
3.3	IC-FERST.....	58
3.3.1	Trelis (Pre-Processor)	60
3.3.2	Diamond (Processor)	61
3.3.3	Parallel Processing	64
3.3.4	Mesh Adaptivity.....	65
3.3.5	ParaView (Post Processor).....	67
3.3.6	Summary of IC-FERST versus ECLIPSE	68
3.4	Geostatistics	69
3.4.1	Semi (Variogram)	69
3.4.2	Geostatistical Software (SGems)	73
3.5	Reservoir Characterization (Rock-Typing).....	78
3.5.1	Amaeful Technique.....	80
3.5.2	Relative Permeability	81
3.5.3	New Rock Characterization MATLAB Technique Code (BRCC).....	82

3.5.4	S-Gems and MATLAB to Diamond.....	83
Chapter 4	Comparison Between IC-FERST and ECLIPSE Simulations for Standard/Benchmark Cases	86
4.1	Case 1: Quarter 5 Spot 1 Layer	86
4.1.1	Case 1 Computational Details.....	87
4.1.2	Case 1 Computational Results and Analysis	90
4.2	Case 2: Quarter 5 Spot 5 Layers.....	99
4.2.1	Case 2 Computational Details.....	99
4.2.2	Case 2 Computational Results and Analysis	103
4.3	Case 3: Full 5 Spot 5 Layers	107
4.3.1	Case 3 Computational Details.....	108
4.3.2	Case 3 Computational Results and Analysis	110
4.4	Conclusion.....	116
Chapter 5	Real Field Case: Reservoir Characterization and Geostatistics.....	117
5.1	General Field Description	117
5.2	Rock Characterization	119
5.2.1	Detecting Heterogeneity Level	119
5.2.2	Rock Characterization Using the Amaeful Technique	122
5.3	Geostatistics	124
5.3.1	Implementation of the S-GEMS Software – Scaling of the Domain.....	125
5.3.2	Porosity Population.....	126
5.3.3	Rock Typing Population	132
5.4	Relative Permeability and Capillary Pressure.....	139
5.5	Fluid Properties	140
Chapter 6	Computational Setup of the Real Field Case using IC-FERST and ECLIPSE simulators	143

6.1	IC-FERST.....	143
6.1.1	Pre-Processing Using Trelis (IC-FERST Pre-Processor) – Geometry Setup	143
6.1.2	Setting up the Computational Parameters Using the GUI Diamond IC-FERST simulator	148
6.2	ECLIPSE	152
6.2.1	Static Model Construction Using PETREL (ECLIPSE Pre-Processor)	152
6.2.2	Dynamic Model Construction Using PETREL (ECLIPSE Pre-Processor)	159
Chapter 7	Results and Analysis	160
7.1	Both Models Construction Summary	160
7.1.1	Boundary Conditions	160
7.1.2	Fluid Properties	161
7.1.3	Rock Properties	161
7.1.4	Grid and Computational Properties	162
7.2	Comparison Between the two Models	162
7.2.1	Total Field Results Comparison.....	162
7.2.2	Well by Well Comparison	165
7.2.3	Time Step Comparison	172
7.3	Conclusion.....	174
Chapter 8	Summary, Conclusion and Recommendations	175
8.1	Summary and Conclusion	175
8.2	Recommendations/Future Work	177
References	179

List of Figures

Figure (2.1): Variogram example (Remy et al., 2009)	32
Figure (2.2): Application of Kriging vs sequential stochastic simulation (Remy et al., 2009)	34
Figure (3.1): Typical relative permeability curves for an oil water system (Dake, 1978b).....	40
Figure (3.2): Interfacial tension between oil, water and solid(Dake, 1978a)	41
Figure (3.3): An example of a finite difference grid (Rokicki, 2014)	44
Figure (3.4): An example of a finite element grid (Morgan and Peraire, 1998).....	45
Figure (3.5): An example of a finite volume grid vs a finite element grid (Molina-Aiz et al., 2010)	46
Figure (3.6): An example of a control volume finite element grid (Xie et al., 2016).....	47
Figure (3.7): Local grid refinement representation(Mackay, 2013)	48
Figure (3.8): a) Block centered representation b) Point centered representation (Peaceman, 2000)	49
Figure (3.9): a) Hybrid grid representation b) Radial grid representation (Pedrosa and Aziz, 1986)	50
Figure (3.10): Common Voronoi elements used in reservoir simulators (Manchuk and Deutsch, 2008)	51
Figure (3.11): Example of an unstructured PEBI grid (Gholinezhad et al., 2017).....	51
Figure (3.12): ECLIPSE Flowchart	52
Figure (3.13): Contour map example.....	53
Figure (3.14): PETREL well logs visualization example	54
Figure (3.15): Upscaled wells example in PETREL.....	54
Figure (3.16): Populated grid example in PETREL.....	55
Figure (3.17): FloViz user interface using the EGRID output format.....	57
Figure (3.18): ECLIPSE Office user interface.....	58
Figure (3.19): IC-FERST Flowchart showing the main stages involved in the IC-FERST simulations	59
Figure (3.20): Trelis user interface	61

Figure (3.21): Diamond user interface a) Gravity and time step parameters b) Porosity and Permeability parameters c) Fluid properties and pressure initial and boundary conditions d) Fluid velocity and phase volume fractions initial and boundary conditions e) Multiphase parameters	63
Figure (3.22): Example of a decomposed domain subdivided into 6 subdomains showing how parallel processing is done	65
Figure (3.23): Diamond Interface showing adaptivity parameters	66
Figure (3.24) Mesh adaptivity example a) initial mesh before adaptivity b) final mesh after adaptivity.....	67
Figure (3.25): ParaView user interface visualizing in 3D the phase volume fraction of oil	68
Figure (3.26): 3D search ellipsoid 3 angles explanation (Journal and Deutsch, 1993)	70
Figure (3.27): Lag tolerance, azimuth tolerance and the bandwidth explanation (Journal and Deutsch, 1993)	71
Figure (3.28): Semi-variogram example (Nicolas Remy, 2009)	72
Figure (3.29): Different variogram models example (Remy et al., 2009)	73
Figure (3.30): Sample of S-Gems input data file.....	74
Figure (3.31): S-Gems Flowchart	75
Figure (3.32): S-Gems after data entry	76
Figure (3.33): Semi-variograms sample from S-GEMS	77
Figure (3.34): Sequential Gaussian Simulation output from S-GEMS.....	78
Figure (3.35): Lorenz plot example (Ahmed, 2001a).....	80
Figure (3.36): Balaha Rock Characterization Code (BRCC) flowchart	83
Figure (3.37): Python script written into Diamond to make Diamond read the CSV files of each property	85
Figure (4.1): Quarter 5 spot 1 layer case representation showing injector and producer well's locations	86
Figure (4.2): Quarter 5 spot 1 layer case a) Relative Permeability b) Capillary Pressure	88
Figure (4.3): Quarter 5 spot 1 layer case ECLIPSE meshes a) coarse (3,125 cells) b) medium (25,000 cells) c) fine (200,000 cells)	89
Figure (4.4): Quarter 5 spot 1 layer case IC-FERST meshes a) coarse (14840 elements) b) medium (25,946 elements) c) fine (345,048 elements)	89

Figure (4.5): IC-FERST adaptive mesh with water saturation at the top plane (Z=1) at different times a) 0 days, b) 10 days, c) 20 days, d) 30 days.....	90
Figure (4.6): Quarter 5 spot 1 layer case IC-FERST Adaptivity vs Non-adaptivity results a) water injection b) oil production.....	93
Figure (4.7): Quarter 5 spot 1 layer case IC-FERST Parallel vs Single processor simulation results a) water injection b) oil production rates.....	94
Figure (4.8): Quarter 5 spot 1 layer case IC-FERST Parallel vs ECLIPSE results a) water injection b) oil production c) water production	96
Figure (4.9): Quarter 5 spot 1 layer case oil saturation results for IC-FERST fine parallel vs ECLIPSE fine at 50 and 25 days.....	99
Figure (4.10): Quarter 5 spot 5 layers case representation showing injector and producer well's locations	99
Figure (4.11): Quarter 5 spot 5 layers case a) Relative Permeability b) Capillary Pressure	101
Figure (4.12):Quarter 5 spot 5 layers case ECLIPSE meshes a) coarse (3,125 cells) b) medium (25,000 cells) c) fine (200,000 cells)	102
Figure (4.13): Quarter 5 spot 5 layers case IC-FERST meshes a) coarse (99,221 elements) b) medium (434,013 elements) c) fine (1,107,286 elements)	103
Figure (4.14): Quarter 5 spot 5 layers case IC-FERST vs ECLIPSE results a) water injection b) oil production c) water production.....	105
Figure (4.15): Quarter 5 spot 5 layers case oil saturation results for IC-FERST fine parallel vs ECLIPSE fine at 75 and 25 days.....	107
Figure (4.16): 5 spot 5 layers case representation showing injector and producer well's locations	108
Figure (4.17): 5 spot 5 layers case ECLIPSE meshes a) coarse (13,005 cells) b) medium (102,010) c) fine (808,020).....	110
Figure (4.18): 5 spot 5 layers case IC-FERST meshes a) coarse (465,685) b) fine (1,120,720)	110
Figure (4.19): 5 spot 5 layers case IC-FERST vs ECLIPSE results a) water injection b) oil production c) water production.....	112
Figure (4.20): 5 spot 5 layers case oil saturation at 100 days in the 5 geological layers.....	115
Figure (5.1): Field boundary and well locations; 13 cored wells are marked in orange; all 33 wells have logging data.....	119

Figure (5.2): Porosity vs Permeability Semi-log plot	120
Figure (5.3): Dykstra Parsons Plot.....	121
Figure (5.4); Lorenz Coefficient a) normalized flow capacity vs normalized volume capacity, b) normalized flow capacity vs normalized thickness	122
Figure (5.5): First Flow Zone Indicator (FZI) plot using the Amaeful technique for rock characterization	122
Figure (5.6): Final FZI	123
Figure (5.7):Reservoir of interest enclosed in a computational box of dimensions (20,30,40) for S-Gems.....	125
Figure (5.8): Viewing of well locations in S-Gems after adding well locations a) unscaled b) scaled (factor of 100)	126
Figure (5.9): Log vs Core Porosity values: Porosity logs of Wells GI-1, HDZ-6, HDZS-2 & HTF-2 with corresponding core sample values Solid lines represent the log values, whilst the spherical dots represent the core values.....	127
Figure (5.10):Histogram based on the original porosity Log values from all wells, using all the 23,339 data points, showing a mean of 0.049 and a variance of 0.00075.	128
Figure (5.11): Transformation of the Log porosity histogram from all wells using the 23,339 data points and showing a mean of 0.039 and a variance of 0.86.	129
Figure (5.12): Porosity variograms	130
Figure (5.13): Porosity population a) scaled (factor of 100) b) unscaled	131
Figure (5.14): Porosity histogram after population on the grid showing 24,000 data points and a mean of 0.049, median of 0.0518 and a variance of 0.00068.....	132
Figure (5.15): Data preparation for Pytorch	133
Figure (5.16): Pytorch output.....	134
Figure (5.17): Rock types histogram after ANN on all the wells using 23,339 data points, showing a mean of 4.33 and a variance of 3.28.....	135
Figure (5.18): Rock type variogram sample	136
Figure (5.19): Rock type population a) scaled (factor of 100) b) unscaled	138
Figure (5.20): Rock type histogram after population on the grid showing 24,000 data points and a mean of 3.33 and a variance of 3.28	138
Figure (5.21): Rock type 1 2-phase relative permeability	140

Figure (5.22): Capillary Pressure from analogous field (Confidential).....	140
Figure (5.23): Field's fluid properties (Confidential).....	141
Figure (6.1): Model Vertices a) top view b) side view unscaled c) side view scaled in the Z-direction (factor of 100).....	144
Figure (6.2): Model surfaces a) top view (x-y plane) b) side view unscaled (y-z plane) (c) side view (y-z plane) scaled (factor of 100).....	145
Figure (6.3): Model with wells a) top view (x-y plane) (b) side view (y-z plane) unscaled (c) side view (y-z plane) scaled in the Z-direction (factor of 100).....	146
Figure (6.4): Model after subtracting wells a) scaled (factor of 100) b) unscaled.....	147
Figure (6.5): Final model after meshing a) scaled (factor of 100) b) unscaled	148
Figure (6.6): Distribution of Rock types as seen using Paraview.....	151
Figure (6.7): Porosity distribution within the computational domain as displayed by Paraview	152
Figure (6.8): Geological model construction within PETREL.....	153
Figure (6.9): Model after adding the well locations and data.....	153
Figure (6.10): Upscaled porosity on all wells as shown in PETREL	154
Figure (6.11): Geostatistics population options.....	155
Figure (6.12): PETREL Calculator option, showing the IF statement written for the first rock type equation.....	156
Figure (6.13): Populated rock types in PETREL.....	156
Figure (6.14): Populated porosity in PETREL	157
Figure (6.15): Populated porosity histogram within PETREL	158
Figure (6.16): populated rock type histogram within PETREL.....	158
Figure (7.1): Field boundary with Injection and Production well locations	160
Figure (7.2): Comparison between IC-FERST and ECLIPSE results a) Oil production b)Water production c) Water injection	163
Figure (7.3): Real field case water saturation after 40 years in a) ECLIPSE b) IC-FERST.....	165
Figure (7.4): 10 selected production wells with the 8 injection wells location	166
Figure (7.5): 10 selected production well locations in a) ECLIPSE b) IC-FERST	166
Figure (7.6): ECLIPSE total week vs month timestep a) Oil production b) Water production c) Water injection.....	172

Figure (7.7): IC-FERST total week vs month timestep a) Oil production b) Water production c)
Water injection..... 173

List of Tables

Table (2-1): Correlation Constants for equation (2-18).....	27
Table (2-2): Range of Applicability of equation (2-18).....	28
Table (3-1): Summary of IC-FERST versus ECLIPSE	68
Table (4-1): Quarter 5 spot 1 layer case IC-FERST and ECLIPSE inputs parameters	87
Table (4-2):Quarter 5 spot 1 layer case IC-FERST and ECLIPSE cases runtime and processors	92
Table (4-3): Quarter 5 spot 1 layer IC-FERST parallel and series percentage difference for each mesh with the coarse as a reference	95
Table (4-4): Quarter 5 spot 1 layer IC-FERST parallel vs ECLIPSE fine series percentage difference for each mesh.	98
Table (4-5): Quarter 5 spot 5 layers case, geological layers properties	100
Table (4-6): Quarter 5 spot 5 layers case IC-FERST and ECLIPSE inputs parameters.....	102
Table (4-7):Quarter 5 spot 5 layers case IC-FERST and ECLIPSE cases runtime and processors	104
Table (4-8): Quarter 5 spot 5 layer IC-FERST parallel vs ECLIPSE fine series percentage difference for each mesh.	104
Table (4-9): Quarter 5 spot 5 layers case IC-FERST and ECLIPSE inputs parameters.....	109
Table (4-10): 5 spot 5 layers case IC-FERST and ECLIPSE cases runtime and processors.....	111
Table (4-11): Full 5 spot 5 layer IC-FERST parallel vs ECLIPSE fine series percentage difference for each mesh.	111
Table (5-1): All well names in PETREL, Trelis & GSLIB, status, data available, well locations, well SSTVD, KB and MD	118
Table (5-2): Rock Types using the Amaeful technique: The FZI range, equations and R ² values	124
Table (5-3):S-Gems histogram before and after transformation mean, variance and median values	129
Table (5-4): Rock type percentages	137
Table (5-5): Lamda calculation.....	139
Table (7-1): Percentage difference between IC-FERST and ECLIPSE for the Oil and Water production and the Water injection.....	163

Table (7-2): Oil and Water production rates for the 10 selected well showing ECLIPSE (Orange line) vs IC-FERST (Blue line) water and oil production rates. 168

Table (7-3): Percentage difference between IC-FERST and ECLIPSE for the Oil and Water production 171

Acknowledgement

I am indebted to many people who have influenced and inspired me in my research but my thanks and indebtedness is directed first and always to God for all his graces, without the power he gave me, the accomplishment of this work would have been certainly impossible.

I would like to express my deep gratitude for the British University in Egypt and London Southbank University, for funding my research and giving me this opportunity. I also would like to express my appreciation and sincerest thanks to Dr Elsa and Prof. Attia, my thesis supervisors, for their outstanding supervision and unlimited support throughout my PhD.

I would like to extend my deep gratitude and appreciation to my family; for their love, help, understanding and continuous encouragement. This includes my wife Haidy, father Ibrahim, my mother Heba and my sister Farah.

Finally, I would like to express my gratitude to my friends and colleagues who helped me technically and mentally throughout my work period.

Nomenclature

AMCG	Applied Modelling and Computation Group
ANN	Artificial Neural Network
API	American Petroleum Institute
BRCC	Balaha Rock Characterization Code
CDF	Cumulative Distribution Function
CFD	Computational Fluid Dynamics
CN	Characterization Number
CV	Control Volume
CVFEM	Control Volume Finite Element Method
DFEFVM	Discontinuity Finite Element Finite Volume Method
DGFEM	Discontinuity Galerkin Finite Element Method
DOF	Degrees of Freedom
DRT	Discrete Rock Type
FDM	Finite Difference Method
FEFVM	Finite Element Finite Volume Method
FEM	Finite Element Method
FFI	Free Fluid Index
FQI	Flow Quality Indicator
FV	Finite Volume
FVM	Finite Volume Method
FZI	Flow Zone Indicator
FZI-SWPHI	Flow Zone Indicator - Irreducible Water Saturation and Porosity
GR	Gamma Ray
GSLIB	Geostatistical Software Library
GUI	Graphical User Interface
HFU	Hydraulic Flow Unit
IMPES	Implicit Pressure Explicit Saturation
KB	Kelly Bushing
LESA	Log Evaluation System Analysis
LGR	Local Grid Refinement
MD	Measured Depth
MFEM	Mixed Finite Element Method
MHFEM	Mixed Hybrid Finite Element Method
MPI	Message-Passing Interface
MRGC	Multi-Resolution-Graph-Based-Clustering Technique
NCRQI	Normalized Cumulative Reservoir Quality Index
NCVFEM	Node Control Volume Finite Element Method
NORMS	The Novel Reservoir Modelling and Simulation Group
NPFI	Neutron Porosity
NQI	Normalized Quality Index

PDE	Partial Differential Equation
PEBI	Perpendicular Bisector
PVT	Pressure Volume Temperature
R2	Coefficient of Determination
RES	Resistivity
RHOB	Bulk Density
RQI	Reservoir Quality Index
SCAL	Special Core Analysis
SGS	Sequential Gaussian Simulation
SIS	Sequential Indicator Simulation
SQRT	Square root
SSTVD	Sub-Surface true Vertical Depth
TPFA	Two-Point Flux Approximation

Chapter 1 Introduction, Aims and Objectives

The research is centered on the application of computational modelling of subsurface oil reservoirs. Accurate multiphase fluid flow modelling in porous media is of great importance in the oil field business and in many engineering and scientific fields, as assessment can be carried out at very low costs, and fast. A production oil field in real life, has very high production and maintenance costs over very long period of times; in contrast, assessment using numerical simulation models that represent production reservoirs can be generated with low costs and short period of times, to find out the optimum development and operational procedures.

A lot of research has been devoted to model, quantify and understand multiphase fluid flow in porous media, however, interpretation and understanding of the physics of the transport phenomena in porous media is still a challenge for research engineers. The development of mathematical modeling applications and methodology was one of the main reasons for the advancement in the multiphase fluid flow area. Due to the numerical technique simulation effectiveness in handling porous media transport problems, it has become the main tool used by engineers and scientists in studying fluid flow in porous media (Chen et al., 2006). Since the 1950's substantial development has been made in numerical reservoir simulation by authors like (Peaceman, 2000), (Aziz, 1979), and (Zheng and Bennett, 2002).

Advancement in reservoir simulation have also significantly benefited from the rapid advancing computer hardware, technology and computational algorithms. Reservoir simulators use different numerical approaches to model the subsurface fluids flow. Modeling approaches used in simulating multiphase transport and flow, involve solving fully coupled formulations using finite difference or finite element schemes using a volume averaging tactic (Brennen, 2005).

Calculations accuracy and the minimization of computational cost (time) are two contradictory goals of any numerical simulation. Reservoir simulation purpose is to create a computational model describing physical processes (such as fluid flow, interfacial tensions between various phases, gravity) in the reservoir to estimate the field performance, at the same time obtaining model accuracy for high formation heterogeneity on large scale simulations. The difficulties associated with development of simulators are often due to (I) heterogeneity (anisotropic permeabilities,

porosities), (II) irregular geometric features (faults/fractures), (III) large scale system, (IV) resolution, and (V) instability (Chen et al., 2006).

Aims

The main aim of this research is to assess the productivity/oil production of highly heterogeneous subsurface reservoirs using computational modelling. Two reservoir simulators are implemented, namely the new, open source, IC-FERST software developed by Imperial College London, and the commercial software ECLIPSE, developed by Schlumberger.

The aim is to assess how the newly developed IC-FERST software compares to the industry-standard ECLIPSE software, using both hypothetical and real reservoirs for two phase flow modelling – specifically oil and water - and identify weaknesses and strengths of the two software. Along with implementing and testing rock characterization and geostatistical methods. These comparisons, if favorable, would enhance the pool of reservoir simulators available to reservoir engineers for complex reservoir modelling.

The novelties of this work are:

1. Analyzing first time highly heterogeneous real field data and the implementation of a novel rock characterization technique to obtain the optimum number of rock types for the real field by using a new clustering code.
2. Implementation of an open source geostatistical package on the real field data to populate the rock properties along field and validating it against the benchmark PETREL geostatistical output.
3. Integrating both the novel rock characterization technique and the open source geostatistical package into the novel state of the art open source multiphase flow simulator IC-FERST, whilst overcoming the challenge of transferring structured hexahedral geostatistical data into the IC-FERST tetrahedral unstructured mesh.
4. Validation of IC-FERST against the petroleum benchmark ECLIPSE reservoir simulator using 3 benchmark scenarios.
5. Implementation of multiphase fluid flow modelling using IC-FERST for the first time on this highly heterogeneous field, and comparing the results with ECLIPSE.

Objectives

To achieve the above aims and sub-aims, the following objectives are addressed:

1. Implement the newly developed IC-FERST software that uses an unstructured adaptive mesh, for a number of computational scenarios (quarter-five spot, multiple layers, layers with fractures and horizontal well).
2. Implement for the same scenarios, using the industry-standard ECLIPSE software and compare/validate IC-FERST against ECLIPSE results.
3. Develop a new rock characterization and clustering technique using MATLAB. The code written was named Balaha Rock Characterization Code – BRCC, and it characterizes the reservoir into the optimum number of different rock types and outputs the permeability equations for each rock type.
4. Use of Artificial Neural Network (ANN) to populate all the uncored - well logged wells using the cored well data with rock types.
5. Use of S-GEMS geostatistical package to populate the porosity, permeability, relative permeability, capillary pressure and connate water saturation among the computational domain with respect to each rock type.
6. Write a Python code to integrate the structured hexahedral output from MATLAB and S-GEMS into the unstructured tetrahedral IC-FERST.
7. Implement IC-FERST and ECLIPSE on the highly heterogeneous real field size reservoir and compare/validate the results.

The work in this thesis is presented as follows:

- Chapter 1 outlines the overall objective of the work, and aims.
- Chapter 2 presents the literature review on both the computational modelling of reservoirs as well as reservoir characterization methodologies; the history and the latest multiphase fluid flow computational modelling advancements – identifying the weaknesses and advantages of the different approaches is firstly given; this is followed by a review of the different rock typing techniques, identifying the most appropriate reservoir; this review is accompanied by a review on the geostatistical means – also necessary for reservoir characterization.

- Chapter 3 presents a brief theoretical background of the fluid flow equations used; the different numerical schemes available, the different gridding techniques and geostatistics. Later the chapter discusses the methodology and the steps undertaken in the pre-processing, processing and post-processing stages for both IC-FERST and ECLIPSE.
- Chapter 4 presents the simulation work carried out using both the IC-FERST and ECLIPSE software, for three different standard geometries with different mesh sizes and different level of complexity and heterogeneity; the purpose of this work is the inter-comparison of the simulation results from the two software and the differences.
- Chapter 5 looks at the real field case study, and describes the rock characterization approach which involves, neural networks and geostatistical methods.
- Chapter 6 discusses the model construction of the real field case within both the IC-FERST and ECLIPSE software.
- Chapter 7 presents and discusses the intercomparison between the simulation results from IC-FERST and ECLIPSE.
- Chapter 8 summarizes the finding of this work and outlines the conclusion and future work.

Chapter 2 Literature Review

In this chapter a review is carried out of the research that has taken place over the years – starting from when Henry Darcy firstly started developing the theory of fluid flow through porous media in 1856, until the present time. Darcy's law established experimentally, the proportionality of pressure flux and gradient for water in saturated flow (Darcy, 1856b). Darcy's law has been extended by researchers such as (Hassanizadeh and Gray, 1979) to unsaturated multiphase flow, and also physical phenomena such as fracture flow by considering, varying fluid properties, surface tension, and gravity (Scheidegger, 1958).

(Buckley and Leverett, 1942) were one of the first scientists who contributed to understanding the fundamentals of displacement of Newtonian fluids and immiscible flow in porous media without gravity and capillarity. The effect of capillary pressure and gravity on water flooding have been included in subsequent studies by (Chen, 1988) and (Blunt, 1997).

Initially the governing equations have been solved using the Finite Difference Method (FDM) over structured meshes and Finite Volume Method (FVM) over unstructured meshes. Later, authors such as (Helmig and Huber, 1998) discusses using a *fully coupled upwind weighted finite element method* (FEM). The FEM allows for a more flexible representation of geological structures.

(Durlafsky, 1994) and other authors combined the Finite Element and Finite Volume Method (FEFVM). The FEFVM gives better results than the fully coupled upwind weighted FEM in terms of accuracy and runtime, while retaining the flexibility of the FEM method. (Schmid et al., 2013) used a Control Volumes (CV) together with finite elements also known as CVFEM. This method combines the advantages of the CV method to produce locally mass conservative stable solutions, with the flexibility of the FEM to capture complex geometries.

The chapter also gives a review on the research undertaken on the different rock characterization methods available starting from 1927 when (Kozeny, 1927) studied the relationship between rock properties to detect a correlation between both the permeability and the porosity which proved an important role of showing the rock fluid flow parameters and the factors governing it. Later, (Carman, 1939) considered the fluids flow through a certain path within a rock sample and proved that this path could be longer than the length of the rock sample itself. From this sense, the tortuosity factor was introduced into the Kozeny-Carman equation. In 1993, Amaefule and coworkers

developed the Hydraulic Flow Unit, which is a more practical technique that characterizes similar geometrical attributes (Amaefule et al., 1993). The Amaefule technique was applied worldwide for carbonate and clastic rocks and the results positively aided in improving the permeability prediction and permeability distributions from wireline well log data within both cored and uncored intervals/wells.

Lastly a review is done on the various geostatistical techniques required to populate the rock properties among a reservoir. Modelling spatio-temporal phenomena in Earth science deals with a huge number of variability in time and space. Geostatistics was firstly established in the 1950s by (Kriging, 1951) to estimate natural resources, his method depends on interpolating the variables from the sparsely available data using a linear least-square estimation technique. To calculate the statistical correlation between sampled values in space as their separation increases, a variogram is used. Stochastic simulations were introduced by (Matheron, 1973) and (Journel, 1974) to allow the reproduction of spatial variance predicted by the variogram model and correct the smoothing effect and other artifacts of Kriging.

2.1 Multiphase Fluid Flow

Accurate multiphase fluid flow modelling can be a very challenging task as properties such as fluid velocities, porosity and permeability may vary spatially over many orders of magnitude. Many reservoirs are highly heterogeneous and often contain complex 3D structures. The material properties across the domain – over many kilometers can therefore be highly discontinuous. Capturing these heterogeneities in the modelling process is a challenging problem. Because of these challenges, fluid flow in large scale models is often focused into much smaller scale structures such as fractures. In these cases, the interest of scale can go from a millimeter to a kilometer (Sampath et al., 2021).

The displacement and flow process of multiphase fluids in porous media happen to exist in a wide number of subsurface systems. It also has many applications in different fields such as subsurface waste disposal and resource storage; subsurface contamination investigations; development of geothermal energy; soil science; groundwater hydrology; and petroleum engineering. Tremendous development and research have taken place in the past century to understand the physics behind multiphase flow in fractured and porous media. As a result of this research and development,

scientific advances and significant progress have been made in the field of multiphase flow in porous and fractured media (Wu, 2015).

The development and study of multiphase flow has been enhanced over the past 50 years with concentrated efforts in field studies, theoretical analysis, mathematical modeling, and laboratory experiments. Many models and quantitative approaches have been applied and developed successfully to predict, understand and describe the multiphase flow (Regnier et al., 2022).

Apart from the scale challenge for multiphase fluid flows in subsurface reservoirs, another difficulty is the constitutive relations, i.e. the capillary pressure and the relative permeability functions. These functions are non-linear and to solve them numerically/computationally iterative schemes that are numerically costly are required (Gläser et al., 2022).

The theory of fluid flow through porous media was first developed by Henry Darcy in 1856 (Darcy, 1856b). Darcy's law established experimentally, the proportionality of pressure flux and gradient. When Darcy developed his law, it was for water in saturated flow. Since then, Darcy's law has been extended to unsaturated multiphase flow, and also physical phenomena such as fracture flow by considering varying fluid properties, surface tension, and gravity (Scheidegger, 1958); & (Hassanizadeh and Gray, 1979). This extension has been made possible using numerical computations that rely on advances in computational mathematics and powerful computational technology. The extension of Darcy's law has enabled its wide application within the petroleum engineering industry.

The most significant contribution towards understanding multiphase flow have been made in the 1940s due to the rapid expansion of the petroleum industry as well as other industries. Buckley and Leverett were one of the first scientists who contributed to the understanding of the fundamentals of displacement of Newtonian fluids and immiscible flow in porous media; this was done during their study of the fractional flow theory. Buckley and Leverett described an immiscible fluid displacement process in which a saturation profile is advancing in the flow direction with a sharp front. However, both the gravity and capillary pressures were ignored in their study (Buckley and Leverett, 1942).

The effect of capillary pressure and gravity on water flooding have been included in subsequent studies (Chen, 1988) (Blunt, 1997). Extensions to the Buckley Leveret theory have been carried

out to better understand the behavior of multiphase flow in porous media for Enhanced Oil Recovery. Modifications and developments have been carried out by DeZabala for the study of alkaline flooding (DeZabala et al., 1982); by Larson on the mechanism of chemical methods (Larson et al., 1982); Patton on polymer flooding (Patton et al., 1971), and Larson on surfactant flooding (Larson, 1978). The use of the coherence theory was also used by Helfferich in the extension to two and more immiscible phases (Helfferich, 1981).

Around the same time, problems involving two phase flow, unsaturated and transport in aquifers in subsurface soils were increasingly investigated and recognized in soil science and groundwater hydrology (Or and Tuller, 2000). In parallel, the problem of groundwater and soil contamination by Non-Aqueous Phase Liquids, was also receiving high attention. In the past 20 years, the concern of the increasing greenhouse gas emission and its solution of carbon capture and storage has been rising. All of these matters have raised interest in the research in the use of different numerical approaches for modeling flow in complicated reservoir systems (Chen et al., 2006). Different types of numerical schemes used for solving the complicated reservoir flow equations are discussed in section 2.1.1.

2.1.1 Numerical Schemes/Methods

Multiphase fluid flow models have been applied using different numerical methods', the governing equations have been solved initially using the Finite Difference Method (FDM) over structured meshes and Finite Volume Method (FVM) over unstructured meshes. Most of these methods use the Two-Point Flux Approximation (TPFA) to calculate the fluxes between the cells. This approximation is valid only for K-orthogonal meshes. K-orthogonal meshes have the disadvantage that they cannot discretize heterogeneous porous media (Aziz, 1979) (Peaceman, 2000).

Authors such as (Huyakorn and Pinder, 1978) (Dalen, 1979) (Forsyth, 1991) discussed a much more realistic representation of reservoirs using a *fully coupled upwind weighted finite element method* rather than the FDM. Another approach which is also suitable to model multiphase fluid flow and is similar to the fully coupled upwind weighted Finite Element Method (FEM) is the integrated FDM as discussed by (Pruess, 1991).

Later in 1998, Helming and Huber studied the difference between *Fully-Upwind Galerkin*, *Petrov-Galerkin* and *Standard Galerkin* methods for two-phase flow simulation in heterogeneous

reservoirs. They derived and analyzed a generalized formulation on the basis of the coupled pressure-saturation equations. Their results show that the Petrov-Galerkin method fails to capture correctly processes that take place at interfaces when it comes to heterogeneous media. On the other hand, the Fully-Upwind Galerkin method is able to give correct results for flow in both heterogeneous and homogeneous media. The Standard Galerkin method only works for diffusion-dominant processes (Helmig and Huber, 1998).

Narasimhan and Witherspoon (Narasimhan and Witherspoon, 1976) discussed the main difference between *the integrated finite difference method and the fully coupled upwind weighted FEM* in the calculation of the fluid pressure gradient. A finite difference approximation is used to compute the gradient in the integrated FDM; this approximation method requires that the interface between any two nodes to be perpendicular to the line connecting them. This is a disadvantage when trying to model complex geologies. Shewchuk discusses that the FEM calculates the gradient based on the element interpolation functions, so it does not suffer from the previously mentioned restriction. Therefore, the FEM allows for a more flexible representation of geological structures, especially when Delaunay triangulations are used (Shewchuk, 2002).

Huber & Helming stated that both the integrated FDMs and fully coupled upwind weighted FEMs, have difficulties with the application of fast matrix solvers. This is due to their disadvantage that the algebraic solution matrices are poorly conditioned and not diagonally dominant; this necessitates costly computational iterative schemes such as Newton method to solve for the nonlinearities (Huber and Helmig, 1999). Further advances in multiphase fluid flow modelling in complex reservoirs have considered flux continuous FDMs using hexahedral multi-block grids (Jenny et al., 2002).

Numerous authors such as Durlofsky, Eymard and Huber & Helming have tried the combination of Finite Element and Finite Volume Method (FEFVM) this combination is increasingly getting popular. In a FEFVM, the finite element grid is complemented by the construction of a Finite Volume (FV) subgrid. The FEFVM gives better results than the fully coupled upwind weighted FEM in terms of accuracy and runtime while retaining the flexibility of the FEM method, noting that the capillary pressure varies in continuous fashion (Durlofsky, 1993) (Helmig and Huber, 1998) (Eymard et al., 1989).

To simulate multiphase flow in reservoirs the FEFVM is usually embedded within IMPES. In the IMPES method, the pressure is fixed, and the mass balance of the fluid is calculated by the FVM by solving the transport equation using the fluid velocity yielded by solving implicitly through FEM the flow equation while fixing the saturation. Therefore the IMPES allows for the best features of the FV and FEMs to be implemented. Both the continuity and fluid pressure equations exhibit non-linearities that can be decoupled from each other. The inhomogeneous flow field over several orders of magnitude are resolved using the geometric flexibility of the FEM. This way it is not necessary to use a non-linear solution algorithm as mentioned earlier. The transport equation is solved efficiently by the FVM and the pressure equation by the FEM (Aziz, 1979).

An alternative to the FDMs and the FVMs is the use of Control Volumes (CV) together with finite elements also known as CVFEM. This method combines the advantages of the CV method to produce locally mass conservative stable solutions with the flexibility of the FEM to capture complex geometries (Schmid et al., 2013). Typically, the mass conservation properties (concentration & saturation) are represented by the CV, and the material properties (porosity & permeability), velocity and pressure are represented by the finite element. This method is also called Node Control Volume Finite Element Method (NCVFEM) (Abd and Abushaikha, 2020).

In the traditional CVFEM, the CVs span the boundaries. When there is a contrast in capillary entry pressure or permeability across the boundary the CV span creates a problem. A number of studies done by Helmig and Van Duijn considered the case of contrasting capillary entry pressure where appropriate conditions need to be implemented on the boundary to ensure the correct physical representation (van Duijn et al., 2016) (Van Duijn et al., 1995) (Helmig et al., 2007). Bazr-Afkan and Matthai, focused on the common geological situation where there are significant permeability contrasts across the boundary. They concluded that the CVs that span the boundary cause artificial leaks of mass from the high into low permeable domains and vice-versa. Therefore, component concentration and fluid saturation are smeared over neighboring elements. Moreover, capillary pressure and relative permeability are saturation based, so they are computed by the use of unphysical saturation values (Afkan and Matthai, 2011).

Around the same time Nick and Matthai, employed the average flux between elements at the interface after separating the CVs at the finite element interfaces. However, their approach did not guarantee local mass conservation between the discontinuous CVs, and it was tested on 2D

elements (Nick and Matthäi, 2011). Bazar and Matthai enforced mass conservation in a post processing step after using the boundary finite elements as CVs to calculate the fluxes between the CVs. Their method is computationally expensive and inconsistent as the number of unknowns, nodes, does not equal the number of elements, and it was tested on only 2D elements (Afkan and Matthäi, 2011).

Alternatively a Mixed Finite Element Method (MFEM) was used by many authors such as (Chavent and Jaffré, 1986), (Hoteit and Firoozabadi, 2006) and (Wang et al., 2022). In the MFEM, the velocity and pressure are simultaneously solved and the fluxes continue across the element interfaces. The use of a second grid is not needed as the CV is the element.

Durlofsky studied the accuracy of the flux, Darcy velocity, and stream functions computed from triangle-based, lowest-order, mixed finite element and CV approximations to the two-dimensional pressure equation. He showed that the CVFEM, similar to the interpolation of Galerkin finite element and analogous to integrated FDMs, yield over CVs a conservative velocity field and smooth streamlines. He compared the fluxes and streamlines computed with the MFEM, which approximates the pressure and velocity variables separately, against the CVFEM. The results show that the CVFEM is computationally more efficient for systems with only moderate degrees of heterogeneity. On the other hand, the MFEM is shown to approximate flow variables more realistically and accurately in the cases of more variables or discontinuous permeability fields (Durlofsky, 1994).

Geiger and coworkers in 2004 introduced an unstructured triangular grid with a complementary FV sub grid, a fully conservative node-centered FVM. The method was coupled with a Galerkin FEM and embedded within an IMPES formulation, to efficiently and accurately model multiphase flow in geologic media. They demonstrated the effectiveness of their approach by comparing it to multiphase flow simulations for heterogeneous permeability fields and traditional solution method (Geiger et al., 2004). Their method is similar to Durlofsky's method but different in three things. 1) Durlofsky uses MFEM, 2) Durlofsky's FVM is equal to the FV because the flux is continuous between two finite elements, 3) Durlofsky obtained a higher-order approximation of the flux between FVs by a pre-processing step (Durlofsky, 1994).

Huber and Helming studied the saturation profiles for both the node CVFEM and the MFEM in heterogeneous media. Their results showed that in the MFEM, sharper and less diffusive fronts are

produced and the stiffness matrix conductivity coefficients between neighboring elements are weighted by taking the harmonic mean. Meanwhile the NCVFEM are weighted arithmetically. This tends to *underestimate* the effective conductivity for the MFEM and *overestimate* them for the NCVFEM in heterogeneous models (Huber and Helmig, 1999).

Lachassagne and coworkers showed that for very large heterogeneous models the deviation from the theoretical solution for both the MFEM and the NCVFEM is similar (Lachassagne and Ledoux, 1990). Mose and coworkers along with Chavent, showed that the MFEM indefinite characteristics of the stiffness matrix can be avoided by the use of the Mixed Hybrid Finite Element Methods (MHFEM). The MHFE solves the system at the interfaces of the elements; this doubles the number of unknowns for a tetrahedral mesh leading to inconsistency, as the number of elements and CVs does not equal the number of unknowns (Mosé et al., 1994) (Chavent and Roberts, 1991).

Cumming and coworkers, showed that a CVFEM-based discretization can be used to solve the Darcy and coupled mass conservation equations in heterogeneous reservoirs with small computational cost, compared to traditional coupled velocity pressure-based formulations. However, in regions such as boundaries between different rock types or matrix-fracture interface where material properties vary abruptly, the CVFEM requires high resolution meshes. In regions where material properties are defined, CV boundaries span finite elements; therefore, across the CV interface average permeability values must be calculated. In highly heterogeneous media this leads to very high numerical dispersion (Cumming et al., 2011).

Nick and Matthai, developed a discretization/hybrid numerical method that uses discontinuities at the domain boundaries so that it does not average dependent-variable values at material interfaces while retaining the continuum approach elsewhere. They achieved this by extending the hybrid, finite-element, node-centered, finite-volume method. The hybrid element mesh is “exploded” along material interfaces, adding new nodes to support discontinuities in the result variables. They called this discretization the Discontinuous FEFVM (DFEFVM). They addressed both advective and diffusive transfer but restricted their study to single-phase flow through two-dimensional models of inhomogeneous porous media and passive solute transport. Their results showed that this method is conservative, and the concentration fronts remain sharp and free from oscillations; less refinement is needed to produce accurate results with the DFEFVM than with the FEFVM. Finally, the run time required to obtain similar accuracy with the DFEFVM is less than the

FEFVM; however, DFEFVM is computationally more expensive when the same mesh is used (Nick and Matthäi, 2011).

Originally, discontinuity capturing schemes were developed to resolve sharp changes in saturation and velocity, with the Discontinuous Galerkin FEM (DGFEM) being one of the most famous discontinuity capturing schemes. The DGFEM is designed to be high-order accurate, locally conservative, and stable, and allows sharp changes in the solution fields to be captured by explicitly enforcing the continuity of the solution. The solution handles discontinuities in material properties at internal boundaries because it is allowed to be discontinuous at the element faces. The method incorporates specially designed interface fluxes to deal with interface problems (Brooks and Hughes, 1982) (Tezduyar and Park, 1986). To use the different numerical schemes mentioned, different gridding approaches are used; these approaches are discussed in section 2.1.2.

2.1.2 Gridding/Meshing Approaches

The current gridding techniques used in commercial multiphase fluid flow packages are mainly Cartesian, approximately Cartesian, or Perpendicular-bisector/Voronoi grids. The spatial resolution is dictated by the early defined grid in the modelling process. Cells geometries are restricted by the requirement of K-orthogonality to be consistent with the TPFA invoked in the FV approach used to solve and discretize the governing equations (Heinemann et al., 1989) (Gunasekera et al., 1997).

Although these types of grids are so popular, it is known that they do not capture the key aspects of flow and the geologic heterogeneities, and they provide a poor representation of geologic heterogeneity. Geologic geometries such as pinch outs and faults require grids that deviate from K-orthogonality, moreover, these grids restrict the areal variation of cell sizes, not allowing for areas of complex geometry to be meshed at higher resolution (Jackson et al., 2015). The scaling up from a finer grid to a coarser grid results in a further loss of fidelity (Renard and De Marsily, 1997).

Authors such as (Denver and Phillips, 1990) (Hamilton and Jones, 1992) (MacDonald et al., 1998) and (Regnier et al., 2022) discussed surface-based geologic modeling. Very few studies considered dynamic reservoir behavior, with most of the studies only considered static models. The ones that considered dynamic reservoirs used FV schemes with conventional gridding to discretize space

depending on the TPFA to simulate flow. Therefore, the capturing of the reservoir complexity was limited by using K-orthogonal grids (Sech et al., 2009).

Authors such as (Huyakorn and Pinder, 1978) (Dalen, 1979) (Forsyth, 1991) (Durlafsky, 1993) (Verma and Aziz, 1997) (Helmig and Huber, 1998) and (Xie et al., 2022) discussed various methods to solve governing multiphase equations based on the extension of the FVM or the FEM using unstructured meshes to discretize space. However, conventional modeling grid-based models do not give the appropriate representation of heterogeneity to be used in such simulation and meshing methods. There is a limited scope to improve the representation of complex geometries by the use of unstructured meshes, if petrophysical properties are initially discretized on the K-orthogonal grid that is required by the available modeling algorithms.

Studies done by (Fung et al., 1994) (Hoteit and Firoozabadi, 2006) (Forsyth, 1991) on finite element based schemes consider only simple one dimensional and two dimensional geological heterogeneous cases or homogeneous cases. Although they presented numerical methods that better capture flow aspects, they did not address the representation of complex heterogeneity. (Bastian and Helmig, 1999) (Geiger et al., 2004) (Matthäi et al., 2007) and (Zhan et al., 2022) have included heterogeneity in three dimensional models using a surface-based approach to represent fractures.

Prakash was the first to pioneer the CVFEM in solving the Navier-Stokes equation where local mass conservation and flexible meshing are achieved on heat transfer problems (Prakash, 1987a). Dalen was the first to apply the same discretization for oil reservoir simulation (Dalen, 1979).

Schmidt and Jacobs stated that conventional reservoir simulation packages use the same coarse grid throughout the reservoir. However, higher mesh resolution/finer grids is often required in regions where gradients of a property of interest such as saturation or pressure is large, and low resolution meshes is accepted elsewhere. For instance, during a water flooding simulation, higher resolution is needed close to the water front; however, behind the front the saturation changes gradually and high mesh resolution is no longer needed. Computational time can better be used to adapt the mesh in time and space to coarsen and refine where it is necessary (Schmidt and Jacobs, 1988).

Several authors used several methods used to refine and coarsen the discretization. 1) h-adaptivity: here the existing elements are split and the connectivity of the nodes is changed (Budd et al., 2009). 2) r-adaptivity: here the vertices of elements are moved while retaining the same connectivity to make new elements (Budd et al., 2009). 3) p-adaptivity: here the polynomial order of approximation is varied (Babuška and Suri, 1994).

The h-adaptivity method together with the FV discretization is mostly used for porous media applications. (Schmidt and Jacobs, 1988) was among the few of the first authors that introduced the idea of dynamic mesh refinement. To better capture the saturation fronts he suggested the use of h-adaptivity on a cartesian grid. Similar approaches were later developed by authors such as (Dahle et al., 1990) (Edwards and Christie, 1993) (Trangenstein, 2002) (Sammon, 2003). The significant disadvantage of previous dynamic mesh applications lies in the ability of the approach to preserve and capture geologic heterogeneity. Dahle and Schmidt neglected heterogeneity entirely. Sammon started with a fine scale conventional Cartesian mesh, and used simple averaging technique to the cell's values to adaptively coarsen simulation grid. (Renard and De Marsily, 1997) stated that the problem in Sammon's technique is that averaging only yields representative values of permeability for a small subset of fine-scale permeability distribution.

Trangenstein and Edwards, both also started with a fine scale conventional Cartesian mesh, but instead of using simple averaging techniques to scale up the permeability, they used homogenization methods. The scaled-up permeability is assigned before the simulation preselected range of coarse grid-cell sizes. During the simulation the precalculated values are assigned to the adaptively sized cells. Their approach lacks h-adaptivity flexibility due to the requirement of a preselected range of cell sizes (Trangenstein, 2002) (Edwards and Christie, 1993).

Wol and coworkers simulated two-phase flow in porous media by combining an adaptive grid method and local upscaling method based on multipoint flux approximation including capillary pressure effects. They showed that their method is proven to work for varying heterogeneous parameter fields and different flow regimes. The only drawback in their method is that their adaptivity was limited to the use of h-adaptivity (Wolff et al., 2013).

After the improvement of hydraulic fracturing and horizontal drilling technologies in the petroleum industry, a lot of unconventional petroleum reserves from tight shale have been recovered. The United States oil production has increased from five million barrels of oil per day

in the year 2004 to eight million barrels of oil per day in 2014 due to the advancement in these areas (EIA, 2014).

The technology and the understanding needed for the development of unconventional reservoirs are still not mature enough, and the recovery rates from these unconventional reservoirs remain very low. The formation of an unconventional reservoir is characterized by very small pore sizes and very low permeability. The fluid flow in very low permeabilities is subjected to more coupled physical processes, non-linear, non-Darcy flow, and coexisting with very complex geometries, multiscaled heterogeneity and rock deformation within nanofractures and micropores. Therefore, the process of quantifying flow in unconventional reservoirs is a significant challenge that motivated a lot of efforts in understanding and developing, mathematical models, quantitative methods, and modeling tools (Chen, 2007).

A lot of models were established for flow in fractures. Vauclin, Munoz and Rengifo proposed a 2 dimensional numerical model in 1997, their model was founded on the finite difference discretization of the Darcy law (Munoz et al., 1997). In 2012 a FV approach was applied by Cross, McBride and Gebhardt trying to model a gold oxide heap and they were successful (McBride et al., 2012). Sepulveda, Cariaga and Sepulveda established in 2005 a MHFEM in a two dimensional pilot scale heap that solves for air and liquid flow (Cariaga et al., 2005). Galvez, Mellado and Cisternas established an analytical method in 2009 that was based on Bernoulli flow to model the recovery in heap leaching (Mellado et al., 2009).

In 1992 Fung proposed a CVFEM for thermal simulation in porous media. The numerical approximation of the continuity equation in his method was converted to a form of algebraic approximation employed in a FDM. As a result to this, the run time and grid orientation error were reduced (Fung et al., 1992). CVFEM was applied by (Jackson et al., 2015) and (Al Kubaisy et al.) to simulate multiphase flow in using an IMPES formulation to decouple both pressure and saturation equations.

Geiger suggested a CVFEM in 2004 in which the pressure equation was discretized using a FVM and a Galarkin FEM to solve the saturation at each node (Geiger et al., 2004). In 2009 Sech proposed that the geologic design complexity cannot be captured by these methods (Sech et al., 2009).

Marcondes and Sepehrnoori developed in 2010 a similar method called the element-based based FVM. Their method partitioned elements into sub elements but the mass conservation principle was still integrated into sub volumes. Results were limited to 2D, later a 3D domain was created on a gas flooding case (Marcondes and Sepehrnoori, 2010).

(Hamzehloo et al., 2022) applied an unstructured mesh technique that included both the CVFEM and mesh adaptively techniques along with parallel processing to integrate a workflow that provides the ability to maximize the advantages of each method.

The employment of IMPES and *hr*-adaptivity approach together was suggested by Mostaghimi. This method with unstructured mesh allowed for conventional discretization of porous media flow (Mostaghimi et al., 2014). Though many techniques are available for discretization, the FV discretization merged with the *hr*-adaptivity method are frequently used in porous media.

2.2 Rock Typing

Rock typing is a technique used in highly heterogeneous reservoirs where simple facies will not be enough to characterize the reservoir. There have been a lot of research in this area to develop new methods to better characterize heterogeneous reservoirs using the available data. Rock typing techniques divide the reservoir into different flow zones/ rock types and equates the permeability in wells where cores are not present. This subsection will sum the literature of the following:

- Permeability Prediction and HFU(s) Identification Techniques
- Techniques for estimating the Flow Zone Indicator (FZI) from Well Log Data
- Rock Typing Using Cluster Analysis
- Effect of Packing on Permeability
- Permeability Estimation From Well Logs

2.2.1 Permeability Prediction and Hydraulic Flow Unit(s) Identification Techniques

Kozeny studied the relationship between rock properties including permeability and porosity. The study aimed to detect a correlation between the two significant rock properties which proved an important role in showing the rock fluid flow parameters and the factors governing it (Kozeny, 1927). The study expressed the permeability as a function of porosity and added a breakthrough for considering the specific surface area. The Kozeny permeability correlation was expressed as:

$$k = \left(\frac{1}{2 * Sv_{gr}^2} \right) * \frac{\varphi^3}{(1 - \varphi)^2} \quad (2-1)$$

Where S_{vgr} specific surface area of grains, and φ is the porosity (fraction).

In conclusion the, correlation found aimed at estimating permeability with the knowledge of porosity and considering the rock grains specific surface area. The correlation became one of the fundamental relations which acted as an introduction to more studies and researches to find better estimates of the reservoir rock permeability.

Carman studied the rock parameters that related the rock permeability to the porosity. The analysis was developed on the basis of studies including the Kozeny permeability-porosity correlation which took in consideration the grain specific surface area but was not extended to consider that the fluids flow through a certain path within a rock sample. This actual path was proved to be longer than the length of the rock sample (Carman, 1939). The tortuosity factor was introduced to define this measurement as a ratio of the actual length of the fluid flow (L_a) to the rock sample's measured length (L). The tortuosity coefficient ratio was defined as follow:

$$\tau = \left(\frac{L_a}{L} \right)^2 \quad (2-2)$$

Eventually, relating the tortuosity factor to Kozeny correlation and taking in consideration the rock grains shape as the shape factor (K_{ps}) a new developed correlation was established for most porous materials as follow which was known as the Kozeny-Carmen permeability porosity correlation:

$$k = \left(\frac{1}{K_{ps} * \tau * Sv_{gr}^2} \right) * \frac{\varphi_e^3}{(1 - \varphi_e)^2} \quad (2-3)$$

Where, K is in μm^2

The K-C correlation helped to calculate the rock permeability with better estimates compared with Kozeny correlation. Other developments on that correlation specified the product K_{ps} by tortuosity factor as a parameter called the effective zoning factor K_T which could be estimated from capillary pressure lithology index.

An additional parameter was considered in the evaluation of petroleum reservoirs as presented in the work of (Timur, 1968). He defined the commonly used parameters in the evaluation of any petroleum reservoirs as the porosity (φ), permeability (K) and relative hydrocarbon saturation (S_h).

The paper ascribed that both porosity and relative hydrocarbon saturation were accurately determinable through developed logging techniques but the permeability determination was still in need for coring and other tests as drill-stem testing. They present in their paper the following relationship between permeability, porosity and hydrocarbon saturation:

$$K = A \frac{\varphi^B}{S_{wr}^C} \quad (2-4)$$

Where: K: Permeability, φ : Porosity, S_{wr} : Irreducible water saturation and A, B and C are constants that were dependent on the rock types. For sandstones, the constants were 0.136, 4.4 and 2 respectively.

Hence, for the field by entering the measured values of porosity and residual water saturation into this Chart, the permeabilities of sandstones could be estimated within the stated limitations and was found to be the best estimator of permeability.

Coates and Dumanoir studied the permeability prediction methods that were presented in studies and stated that none of them were applicable globally from field to field, or even zone to zone without making adjustments to constants or exponents (Coates and Dumanoir, 1973). Hence, a more generalized and practical correlation was needed. The paper discussed that correlations such as Chart K-2 (Schlumberger, 1972) and Timur (Timur, 1968) were established for clean sandstone formations with medium value of porosity (15 to 25 percent).

(Amaefule et al., 1993) studied the permeability prediction techniques to enhance reservoir rock classification and developed a more practical technique which characterized and identified units with similar geometrical attributes or as named, the HFUs. The paper introduced another parameter which was named the Reservoir Quality Index (RQI) which is defined as:

$$RQI (\mu m) = 0.0314 \sqrt{\frac{k}{\varphi_e}} \quad (2-5)$$

Hence, the FZI parameter, that combined the geological characteristics and mineralogy (hydraulic units), could be obtained from the log-log plot of RQI vs Normalized Porosity φ_z , as the unit slope as:

$$FZI = \frac{RQI}{NPI} = \frac{0.0314 \sqrt{\frac{k}{\phi_e}}}{\frac{\phi_z}{1 - \phi_z}} \quad (2-6)$$

Where NQI: Normalized Quality Index. Hence, by algebraic rearrangement of equation (2-6), the permeability could be calculated as:

$$k = 1014 (FZI^2) \phi_R \quad (2-7)$$

In conclusion, the technique was applied worldwide for carbonate and clastic rocks and the results positively aided in improving the permeability prediction and permeability distributions from wireline well log data within both cored and un-cored intervals/wells. The paper also provided the unique parameter, known as the FZI, which was used to delineate the number of layers HFUs presented and enhance the petrophysical evaluation by numerical simulators.

Shedid and Almehaideb studied three different techniques that were used to enhanced description of heterogeneous carbonate reservoir and developed the Characterization Number (CN) Technique. The paper discussed three important techniques as follow, the Porosity-Permeability Correlation Technique, the J-function Technique and the Amaefule et al (1993) concept of RQI Technique to identify the HFUs (Shedid and Almehaideb, 2003). However, these techniques did not consider other parameters that should yield more detailed results. From this point of view a technique was developed to consider

- Properties of rock such as pore diameter, permeability and porosity
- Properties of fluid such as oil and water viscosities and oil density
- Fluid-rock properties such as wettability and interfacial tension (σ)
- The dynamic conditions (water and oil flow velocities)

These properties were reduced to a dimensionless combining parameter named the CN and was driven by:

$$CN = 1.0067 \times \left(\frac{\rho_o \sigma_{o-w}}{\mu_o^2 \cos\theta} \right) \times \left(\frac{k_{ro}}{k_{rw}} \right) \times \sqrt{\frac{k}{\phi}} \quad (2-8)$$

Where, ρ_o is the oil density (kg/m^3), μ_o is the oil viscosity (centipoise), σ_{o-w} is the Interfacial Tension (N/cm) and K_{rw} and K_{ro} are the water and oil relative permeabilities (Darcy) respectively.

Then, the CN was plotted vs the $(\text{SQRT } K/\phi)$ to identify HFUs in a more accurate manner. In conclusion, a comparison between the application of RQI and CN techniques in a certain field showed that the application of the developed concept (CN) was able to identify 4 flow units as opposed to only two flow units with the RQI method. Thus, enhanced reservoir characterization is achieved with the CN approach. Hence, the CN technique achieved more accurate results as it took in consideration many parameters that were not included in the RQI technique.

Siddiqui and coworkers presented a slightly different approach to aid in selecting the representative samples for the Special Core Analysis (SCAL) tests. The method required an accurate interval identification with similar porosity-permeability relationships and with combining wireline logs, with gamma-ray (GM) scans and other tools such as CT-scanning tool, a calculation of appropriate depth-shifted RQI and FZI data was obtained. This calculation enhanced the selection criteria of representative plugs from each reservoir section. The paper showed that by plotting the Normalized Cumulative Reservoir Quality Index (NCRQI) against the depth, then a predictable plot results which could enhance in zoning or dividing the reservoir to several zones (Siddiqui et al., 2006).

Desouky acknowledged the concept FZI, primarily defined by (Amaefule et al., 1993) from the log-log plot of RQI vs the Normalized porosity ϕ_z as the intercept of the plotted straight line(s) (each represents a HFU) with the line of $\phi_z = 1$ and taking in consideration that this value is the mean FZI for each HFU. The paper described that for a certain field data a permeability-porosity correlation technique was applied. However, the correlation coefficient was found equal to 0.276. due to heterogeneity and data scattering. Hence, a more efficient method was developed to identify the optimal number of HFUs by applying the Iterative Multi-linear Regression Clustering Technique (Desouky, 2005).

The results obtained from a cross-plot that compared the predicted permeability with the measured ones have shown an average relative error 6.05% which proved that the HFUs concept enhanced the permeability prediction and reservoir description from well log data in un-cored wells.

Al-Dhafeeri and Nasr-El-Din, studied the concept of FZI technique and allowed for definitive zonation of reservoirs. The FZI method was used to classify the reservoir rock quality in carbonate reservoirs, which made it the perfect choice for the identification of high permeable zones in the field under study named the Ghawar field (Al-Dhafeeri and Nasr-El-Din, 2007). The paper initially

indicated a relation between the FZI, Tortuosity factor and specific surface area which could be algebraically identified from the similarity of permeability equations by Amaefule and Carmen-Kozeny as follow:

$$\left(\frac{FZI}{0.0314} \right)^2 = \frac{1}{2 \tau a^2} \quad (2-9)$$

Where FZI: Flow zone indicator (μm). a: Specific surface area per unit volume, (μm^{-1}). And τ : Tortuosity (dimensionless).

The paper discussed that with the aid of certain logs such as calliper logs, production logs, and core data analyses, the prediction of highly permeable zones could be achieved. Eventually, the results indicated that the application of the FZI method aided in identification of high permeable zones (super-K) in the three wells under study in the Ghawar field. Also, the results of the research obtained the main objectives as, early water breakthrough was avoided, the well life for oil production increased and the cost of maintenance and oil wells lifting processes was reduced.

Akam and coworkers studied the concept of flow units and proposed an innovation for permeability prediction. The paper discussed an indication representing the fluid Flow Quality (FQI). The concept assumed in a certain reservoir, three parameters were available for determination of the FQI which are the volume of impermeable member (V_{imp}), porosity and the remaining grain volume that holds the permeable member (V_{pm}). The paper concluded that, the FQI concept achieved many advantages as quick estimation of permeability in the continuous manner for several flow units. However, logging recordings must account for pore size and V_{imp} ; nevertheless, the accuracy of the predicted permeability value will be low (Akam et al., 2010).

Nooruddin and coworkers informed that studies approved the good theoretical bases of the Kozeny model which expressed the permeability as function of porosity, specific surface area and tortuosity. A correlation was driven when the porous medium was considered as a bundle of tortuous capillary tubes with the same radius. The paper presented a modification to the K–C model which was developed by treating the tortuosity term in a more proved approach. The tortuosity could be accurately approximated from the electrical property measurements and the effective porosity (Nooruddin et al., 2011). The modification was initially verified experimentally through linear regression steps and then was developed theoretically on the basic concept of the Tortuosity factor as the squared ratio of the assumed path traveled by a fluid particle throughout the porous

medium (L_a), to the actual length of the porous medium (L). Then, combining the tortuosity defined equation with the formation resistivity factor (F_R), derived by Archie, and the cementation exponent (m) a tortuosity-porosity relationship was developed:

$$\tau = \left(\frac{a}{\varphi^{m-1}}\right)^2 \quad (2-10)$$

Where (m) is the cementation exponent and (a) is the lithology factor. The resulting expression for the RQI is as follows:

$$RQI = FZI_m * \varphi_z * \varphi^{m-1} \quad (2-11)$$

Hence, the determination of HFUs was accomplished through the modified K-C model and the results comparing the application of the conventional model with the modified model indicated more accurate identification of similar HFUs and improved the permeability calculations.

Fazel acknowledged that the application of the FZI method, in un-cored intervals/wells, faced a superior challenge of determining HFUs from logs or geological information (Alavi, 2014). Their paper highlighted the methods of estimating HFUs in un-cored wells and how the HFUs, among many approaches, were correlated with log features in cored wells and subsequently implemented these to un-cored wells. Yet, a consistent relationship between log attributes and FZIs did not exist in most lithofacies, and this led to inaccurate permeability prediction. Hence, the paper researched a theoretical and more practical technique called the Flow Zone Indicator - Irreducible Water Saturation and Porosity (FZI-SWPHI) method. The method related FZI from core data with the water saturation and porosity from log data leading to the expression:

$$K = 1014 \left[\frac{a}{S_{wir} \varphi_e} + b \right]^2 \frac{\varphi_e^3}{(1 - \varphi_e)^2} \quad (2-12)$$

The paper concluded that this method aided in more accurate permeability prediction through directly relating permeability to the reciprocal of ($S_{wir} * PHI_e$) and therefore, dissecting the reservoir rocks. The method was applied to three different wells, two of which were at a middle cretaceous carbonate reservoir and the third was a mississippian formation. Eventually, a good correlation coefficient was obtained of ($R^2 = 0.86$) when correlating the FZI to the reciprocal of ($S_{wir} * PHI_e$). Moreover, this method was directly applied in un-cored wells and the results encompassed those obtained from applied ANN and regression methods.

Tiab and Donaldson, when dealing with a heterogenous reservoir, implemented the flow unit concept to divide heterogenous zones into homogenous subzones which led to more accurate estimates of permeability throughout these zones, and subsequently throughout the whole reservoir. The four factors in identifying the flow unit are (I) RQI, (II) FZI, (III) the Tiab flow unit characterization factor (HT) (IV) and the Free Fluid Index (FFI). The HT incorporated many petrophysical parameters such as the size and sorting of grains, pores sizes, rock consolidation degree, cementation and interconnections within porous media; a relationship was subsequently developed between the HT and the FZI (Tiab and Donaldson, 2015).

$$H_T = \frac{1}{FZI^2} \quad (2-13)$$

2.2.2 Techniques for Estimating the Flow Zone Indicator (FZI) from Well Log Data

Chandra studied the concept of HFUs approach which had been used for rock types classification and the prediction of various flow properties. The paper emphasized that the HFUs approach was critical to predict permeability in un-cored intervals/wells and divided these approaches according to their methodology into logarithmic regressions that evaluated the rock permeability from defined log-porosity. The paper presented another method to obtain FZI for un-cored intervals/wells from the several parameters identified from log data. Some of these parameters were GR, ϕ_n (neutron porosity)(NPHI), ρ_b (density) and R_t (true resistivity). FZI was calculated for certain intervals using a technique based on the transformation of each log of the discussed parameters (Chandra, 2008).

The method indicated that at the field under study, the selected zones were classified and at certain depth a sand layer (gas-bearing layer) with the highest FZI value was calculated which indicated an important breakthrough of sand layers. From this sense, another breakthrough could be stated that shaly layers may exhibit low FZI values. Eventually, the log transform technique gave an approach for calculating the FZI and hence; permeability prediction was achieved in the un-cored intervals under study in this paper. However, permeability predicted values were not compared with core measured ones which did not give an indication if the results were accurate or not.

Adnan, studied the concept of HFUs initially proposed by (Amaefule et al., 1993), and acknowledged its importance for reservoirs in general and in carbonate reservoirs for their heterogeneity. The study was developed upon the basis of ascertaining the different flow units and

FZIs to subdivide the reservoir into distinct petrophysical classes, with each having a unique FZI value (Abed, 2014).

The FZI values were obtained through a set of correlation expressions based on the well log data , using all logs available. Subsequently, the FZI expression was implemented to the un-cored wells and hence, permeability was estimated for each HFU (using mean FZI values) using the following equation which was based on Amaefule technique to find 5 HFUs:

$$K = 1.014(FZI)^2 * \frac{\varphi_e}{(1 - \varphi_e)^2} \quad (2-14)$$

In conclusion, the used method proved its efficiency. With a correlation coefficient ($R^2 = 0.86$) between calculated permeability and core permeability and the objective of predicting permeability in the un-cored carbonate well was accomplished. The paper concluded also that other methods used could be put in order from lowest to highest errors as follows, Least Squares Regression, Normal Probability Analysis, Histogram Analysis (which objected difficulty in applying and erroneous results) respectively.

Sokhal and coworkers, studied the various methods for the reservoir rock permeability and acknowledged the importance of estimating the permeability at un-cored intervals. The paper highlighted the fact that permeability estimates by a traditional method was based on simple logarithmic regressions, using only the rock porosity, without considering the features of geology – thus treating an entire reservoir as a single flow unit with homogeneous petrophysical properties. The paper discussed the idea of indicating a correlation of the FZI from log data with the FZI values obtained from the histogram method. The paper concluded that the FZI method has proved to be an accurate method in the permeability estimation with good comparison between the core permeability and permeability calculated by the FZI method. The results effectively allowed to achieve a better static model and dynamic reservoir modeling. And when the results were compared with the core description or Masterlog, better assumptions of every rock type were achieved (Abdallah et al., 2016).

2.2.3 Rock Typing Using Cluster Analysis

D'Windt, acknowledged that many techniques were applied successfully to assign data into its respective cluster and to identify the number of clusters present in core data. From these approaches, one suggested a non-linear optimization technique. However, it was not applied to

determine the number of HFUs presented in core data. While others suggested probability logs for facies identification, when combining well log data with a petrologic description via Bayes Theorem. The paper discussed a combined approach to determine HFUs, to perform data clustering, by applying non-linear optimization coupled with the Bayes rule. Obviously, this technique helped to infer HFUs in un-cored wells but via a bayesian hybrid approach. The method was applied at two different locations as to emphasize the application of Venezuelan sandstone reservoir and a sandstone reservoir in the Middle East. The paper concluded that the novel technique presented was successfully applied for clustering core data. Also, coupling non-linear optimization with Bayes Theorem for grouping core data, allowed the determination of reliable (not estimates) mean and standard deviation of each HFU. Hence, accurate prediction of permeability was achieved by applying Kozeny-Carman equations and the results were reliable when compared to other techniques (D'Windt, 2007).

Aguilar and coworker studied the concept of HFUs to classify rock types and predict permeability and other texture properties. The paper informed that most approaches required prior information to achieve the objective while others stated non-linear relationship between log and lithology data which complicated the sediment description. Hence, this paper presented the Multi-Resolution-Graph-Based-Clustering technique (MRGC). It was powerful nonparametric algorithm which allows to define the optimal number of HFUs of five HFUs. The method included two steps, First based on behavior of underlying multivariable probabilistic density function the algorithm is able to recognize important structures which suggest a different class. Then the user had the possibility to merge different clusters based on geological meaning and histograms analysis, cross-plots and the integration of all the geological information available, core descriptions, image log, lithofacies, XRD, thin sections and SEM information. The major advantage of MRGC is that it does not need any prior knowledge to perform the clusters analysis and offers reliability in processing very complex data configurations such as varied shapes, different densities/volumes, small sizes and not well-separated clusters (Aguilar et al., 2014).

2.2.4 Effect of Packing on Permeability

Slichter was the first to demonstrate mathematically the influence of packing and grain size on permeability (Slichter, 1899). The semi-empirical equation is:

$$k = 10.2 * \frac{d_{gr}}{a_p} \quad (2-15)$$

where k is the permeability in Darcy, d_{gr} is the diameter of spherical grains in mm, and a_p is the packing constant which may be estimated from:

$$a_p = 0.97 * \varphi^{-3.3} \quad (2-16)$$

Substituting with equation (2-17) gives:

$$k = 10.5 * d_{gr} * \varphi^{3.3} \quad (2-18)$$

This correlation is valid primarily for sandstone formations.

2.2.5 Permeability Estimation from Well Logs

Shokir studied the Fuzzy Logic Theory in order to provide an approach for rock permeability prediction (Shokir, 2006). The approach was based on developing a correlation that relates the core and well log data to create an estimation of permeability in un-cored intervals. The study, for a heterogenous sandstone formation, related the effective porosity and GR log values as follow:

$$\log(k) = C_{G1} * \varphi + C_{G2} * GR + C_{G3} \quad (2-19)$$

Where k: permeability, mD. GR: gamma ray, API units, 20 (clean sands)<GR<140 (very shaly formation). φ : effective porosity, %

And C_G are the correlation constants which were identified by the TSK Fuzzy logic model and their values were recorded as shown in Table (2-1).

Table (2-1): Correlation Constants for equation (2-19)

	C_{G1}	C_{G2}	C_{G3}
High GR and low porosity	0.1769	-0.0165	-1.3986
Above medium GR and medium porosity	0.1486	-0.016	-0.9148
Medium GR and above medium porosity	0.1299	-0.0196	-0.2487
Low GR and high porosity	0.099	-0.0221	0.7877

In conclusion the approach results showed very good agreement between the measured core permeability and the new calculated permeability with correlation coefficients ($R^2=0.98$) in the two wells under study. However, the approach selected only two wells for the following reasons.

Firstly, these two wells had an optimum geological location as they covered the whole area under study. Secondly, due to limitations of the fuzzy logic model as it could only derive realistic values within minimum and maximum ranges of GR from log data, which are shown in Table (2-2).

Table (2-2): Range of Applicability of equation (2-19)

	Minimum	Maximum	Average
GR, API units	7.64	83.56	29.5
Core Porosity	5.1	36.9	26.84
Core Permeability	0.1	9358	287.6

In another approach, Mohaghegh and coworkers developed a robust model aiming to predict the permeability when only well log data are available (Mohaghegh et al., 1997). The study helped to use virtual measurements and apply for GR log, in API units, bulk density log (g/cc) (RHOB), and deep induction log (I_D), Ohm-m, data from a highly heterogeneous formation in West Virginia. The study presented the following equation:

$$\log(k) = C_1 * GR^{C_2} * \rho_B^{C_3} * I_D^{C_4} \quad (2-20)$$

Where k (mD), C1=38.254, C2= -0.5874, C3= -0.409438 and C4: 0.4066.

In conclusion, the equation presented helped with good agreement to predict the permeability when compared with the core measured one. Moreover, the approach was then applied in other heterogeneous sandstone locations to prove its validity and the results gave a near match of the permeability values with core permeability values.

Bagci and Akbas, studied the evaluation of formation permeability for a carbonate reservoir from well logs and core data throughout the concept of HFUs (Bagci and Akbas, 2007). The study was targeting carbonate reservoirs due to their tendency to be tight and heterogeneous due to diagenetic and depositional processes which generally show a challenge to deal with these type of rocks. The application of well log data was initiated with Log Evaluation System Analysis (LESA) software to generate lithology crossplots needed for porosity determination. The porosity-permeability plot showed good correlation coefficient. Then the reservoir quality was determined using Winland equation of pore throat radius (R35) as follow:

$$\log R_{35} = 0.732 + 0.88 \log(k_{air}) - 0.864 \log(\varphi) \quad (2-21)$$

Where R_{35} is in microns (μ), k_{air} is the air permeability in milli-Darcy (md) and φ is the porosity in percentage.

The reservoir was divided into several flow units depending upon pore throat radius according to (Blunt, 1997) as follow:

PETRO PHYSICAL UNITS	R35 RANGE (MICRONS)
Megaport	Greater than 10 micron
Macroport	From 2 to 10 microns
Mesoport	From 0.5 to 2 microns
Microport	From 0.1 to 0.5 microns
Nanoport	Lower than 0.1 microns

In conclusion, the multi-regression model was run three times as, first run with 8 variables, second run with 6 variables and third run with 7 variables. The models gave a correlation coefficient of 14.22%, 85.76% and 84.55% respectively. Therefore, the third run was chosen in order to neither overestimate nor underestimate the results. Permeability was hence related to well log data such as GR, Sonic Porosity, NPHI, Density-Neutron Porosity, Water Saturation, RHOB and Formation Resistivity as shown in the equation below:

$$\log(k) = 116.65 - 0.06 * GR + 40.39 * \varphi_s + 1.17 * \varphi_N - 0.87 * \varphi_{DN} - 0.17 * S_w + 40.69 * \rho_b - 0.0009 * R_T \quad (2-22)$$

2.3 Geostatistics

In all Earth sciences, prediction of system behavior is needed to make decisions based on information at hand. The important feature that exists in all Earth sciences in the representation of spatial uncertainty. In early years, managers where expecting from engineers to get one and only one oil recovery estimate using deterministic approaches, and the presence of any uncertainty showed a sign of unskillfulness. Nowadays uncertainty in modelling geological subsurface has become an acceptable practice. Geostatistics aids in producing many stochastic realizations that can help capture spatial uncertainty (Goovaerts, 1997).

Modelling spatio-temporal phenomena in Earth science deals with a huge number of variability in time and space. This variability is quantified by the tools provided by geostatistics. The term ‘geostatitics’ designates the statistical study of natural phenomena. Geostatistics allows practitioners to make informative decisions and predict the behavior of the system under the constrain of time, limited knowledge and resources. We can think of geostatistics as a number of statistical and mathematical techniques of a philosophical approach to spatial data in the presence of natural variability that is used to model and analyse data with spatial locations (Azevedo and Soares, 2017).

Geostatistics initially was used by geological surveyors and geologists who wanted to map geological phenomena across landscapes. Today geostatistics is being used across a range of disciplines such as geoscience, oceanography, hydrogeology, remote sensing, agriculture, environmental sciences, petroleum geology, and for a vast range of data types. Geostatistics deal with spatial data and their distribution and essentially is a subfield of statistics. Spatial data are data that includes, spatial coordinates such as latitude and longitude (Chiles and Delfiner, 2009).

Geostatistics was firstly established in the 1950s and the 1960s in the mining industry; it is used to estimate natural resources such as petroleum deposits and minerals. Geostatistics is also used to predict property values in unsampled locations such as lithology, mineral grade and porosity. A very important advantage of geostatistics is that it allows the quantification of uncertainty in the predicted values. Geostatistical spatio-temporal models provide a probabilistic framework for data analysis and predictions that build on temporal dependence and the joint spatial between observations (Kyriakidis and Journel, 1999).

Geostatistics relies mainly on interpolation techniques, but it goes much more than simple interpolation. It relies on the theory of random function statistical models to model and simulate the uncertainty associated with spatial estimation (Chiles and Delfiner, 2009).

Fluid flow equations are required for the prediction of oil and gas production properties such as permeability and porosity. Unfortunately, in oil and gas reservoirs it is not possible to model the system with complete certainty due to the limited amount of data available because permeability and porosity are only available at sparse drilled well locations. However, simulating fluid flow governing physics equations need these properties at every spatial location. Due to high cost it is

not possible to obtain all the properties needed to accurately model the subsurface (Goovaerts, 1997).

The notation of regionalized variable $Z(\mathbf{u})$ has been introduced by Matheron, as the value at location \mathbf{u} of the characteristics Z of the geological phenomenon (Matheron, 1971). Matheron indicates that the variable exhibits a certain spatial structure and is spread in space. The regionalized notation cannot be ignored, because if it is, the variable will be positioned randomly on the area, hence, not exhibiting any spatial continuity. However, this is not the case when dealing with physical processes. Therefore, the main principle that makes geostatistics different from pure statistics is the regionalized aspect of the variables. The different geostatistical methods depend mainly on their models of spatial uncertainty and continuity, and how they integrate indirect data such as seismic, or direct data such as cores, to create stochastic realizations of the subsurface (Isaaks and Srivastava, 1989). The different geostatistical techniques used are discussed in the following subsections.

2.3.1 Kriging

DG. Krige was one of the first to create an estimation method for the unknown variables at the unsampled locations; his method was then named Kriging. Kriging was first developed to be applied on mineral deposits for mining efforts by assuming a continuous mineralization between grades. His method depends on interpolating the variables from the sparsely available data using a linear least-square estimation technique. Kriging is close to linear regression analyses, it uses data from sampled locations and estimates values between them using different techniques in minimizing the expected error (Krige, 1951).

To obtain the unsampled location values Kriging uses a combination of linearly measured data one at a time, without assuming their statistical distribution type. To minimize the variance of estimation in the least-square sense, Kriging determines the weight used for these linear combinations (Journel and Huijbregts, 1978).

2.3.2 Variograms

A Variogram is the structural function used to characterize the geology physics or the variables spatial variability in linear geostatistics. The variogram provides the statistical correlation between sampled values in space as their separation increases. In other words, it simply is the linear

correlation between any two points in space. Variograms are the easiest technique to relate an unsampled variable location from its nearest observations (Journel and Huijbregts, 1978).

A variogram is a quantitative measure of the standardized smoothness of a data set. It measures the potential change in correlation between data based on the geographical proximity of the spatial points at which the data are measured. A variogram is defined as the variance of the difference between field values at two locations (Ver Hoef et al., 1993). Variograms are used to calculate the weighting schemes in Kriging.

Each variogram is distinct for an exact spatial direction through the vector \mathbf{h} of lag distances. How unrelated or related an unsampled variable at a location is to the measured variable in its proximity, is defined by the spatial model of continuity. For example, due to the physics behind the geological phenomena, spatially close together locations tend to have values in similar range. This is proven by Tobler's first law of geography that states that '*Everything is related to everything else, but near things are more related than distant things*' (Tobler, 1970).

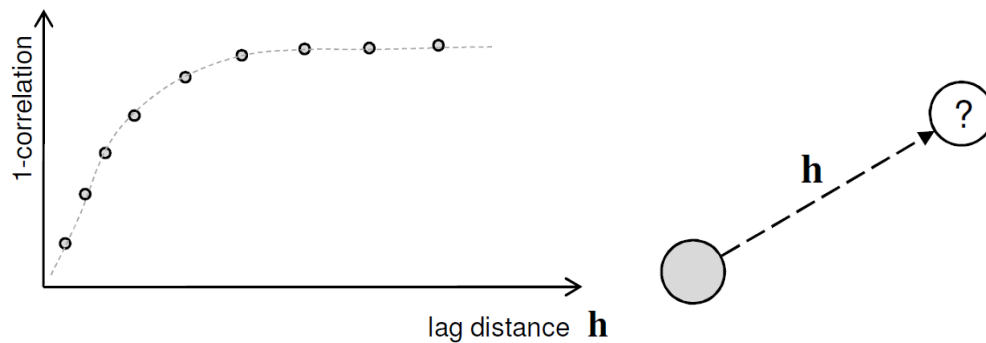


Figure (2.1): Variogram example (Remy et al., 2009)

2.3.3 Cokriging

Moreover multivariate geostatistics was introduced as the extension of linear geostatistics to several variables. For example, Cokriging is the method of linearly estimating one variable from several other variables. For example, porosity values can be estimated from a linear combination of nearby porosity measurements and corresponding acoustic impedance values. The most widely used multivariate technique of collocated Cokriging estimates the primary variable of interest from the nearby measurements of primary variables and the collocated secondary variable at the unsampled location (Doyen, 1988).

2.3.4 Stochastic Simulation

All Kriging approaches derive the 'best unbiased linear estimator' according to the specified variogram model. Therefore, they provide only one smooth representation of the modeled Earth. In reality, due to uncertainty, generation of one deterministic model is not enough. Consequently, alternative approaches for stochastic modeling of the reservoir facies that can result in a different set of property distribution models were required (Ma and Zhang, 2019).

Stochastic simulation was introduced by (Matheron, 1973) and (Journel, 1974) to correct for the smoothing effect and other artifacts of Kriging, which also allows the reproduction of spatial variance predicted by the variogram model. It is the process of generating several alternative models of the spatial distribution of variables under study. According to (Journel and Deutsch, 1993) there are two major differences between Kriging and sequential simulation:

1. Kriging provides the 'best' linear estimator of a variable regardless of the spatial statistics of the estimates taken together. In other words, Kriging provides locally accurate representations of the variable. Simulation, on the other hand, provides global representations of the variable, and instead of local accuracy it focuses on the reproduction of patterns of spatial continuity such as a variogram model.
2. Kriging provides only local measures of accuracy, while simulation provides both the local measures of accuracy and the joint accuracy involving several locations.

Sequential simulations are particularly important for numerical modeling of spatial systems. For example, the global spatial permeability field in an oil reservoir predominantly controls the dynamic flow behavior, and as such, simulation algorithms that honor the global structures specified by the variogram are preferred over the locally accurate methods of Kriging for construction of relevant reservoir models. The smoothing effect of Kriging can lead to significant biases when non-linear physical processes are involved. Sequential simulations, besides providing alternative realizations, generate realistic pictures of spatial variability of the geological phenomena. Each realization can lead to different conclusion regarding the connectivity or fluid flow of the reservoir, especially in extreme situations (Deutsch, 2002). Therefore, if we are interested in some complex non-linear response functions of the subsurface, we can compute the result for each simulation, and obtain a probabilistic description for the variable of interest.

An example application of Kriging vs sequential stochastic simulation is provided in Figure (2.2). In both approaches, the models are conditioned to the 200 available hard data. One can observe that Kriging can only produce one unique Earth model representing the best local estimate of the variable. On the other hand, three different realizations, obtained through sequential simulation, are shown. These realizations provide a more realistic depiction of the fluctuations in geological processes.

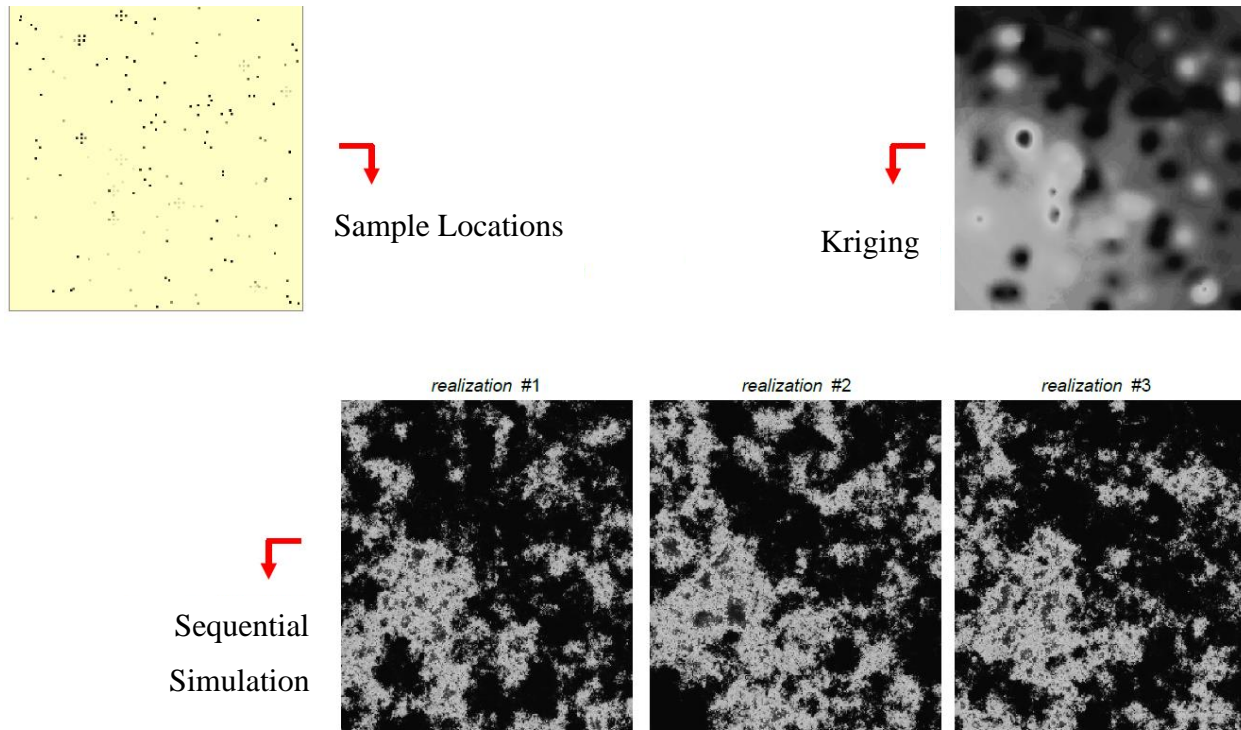


Figure (2.2): Application of Kriging vs sequential stochastic simulation (Remy et al., 2009)

The mathematical principle behind stochastic simulations is simple. It relies on the conditional probabilities of the variable $Z(\mathbf{u})$ given all previously simulated values in the neighborhood of \mathbf{u} .

2.3.5 Sequential Gaussian Simulation (SGS)

Sequential Gaussian Simulation (SGS) is the first sequential algorithm; it is the most straightforward algorithm that produces multi-gaussian field realizations. The Gaussian assumption makes the SGS very flexible and simple, and this is the reason behind its popularity. The idea of the SGS is that each variable is simulated according to its normal conditional Cumulative Distribution Function (CDF) obtained from a simple Kriging method. The estimate

for the unsampled location in the SGS is randomly sampled from its corresponding Gaussian distribution, taking into account both the variance and the mean, unlike Kriging where only the mean is considered (Ma and Zhang, 2019).

The conditioning of continuous variables $Z(\mathbf{u})$ in SGS proceeds as follow:

1. Choose a stationary domain, and obtain the univariate CDF $F_Z(z)$ representative of the domain under study
2. Transform the data Z into a normal distribution
3. Define a random path visiting each node \mathbf{u} of the grid
 - a. Search for nearby data and all previously simulated values
 - b. Use simple Kriging approach to obtain the mean and the variance of the conditional distribution
 - c. Draw a single value from the conditional distribution
 - d. Assign the simulated value to grid node \mathbf{u}
 - e. Proceed to next node until all nodes of the grid are simulated
4. Back transform from normal distribution to their original univariate CDF $F_Z(z)$

In the above SGS approach, each random path will lead to a different realization. Several realizations that all honor the given spatial continuity model can thus be used for uncertainty quantification.

2.3.6 Sequential Indicator Simulation (SIS)

Kriging is appropriate to well behaved variables where smooth realizations are able to predict geological features. Unfortunately, simple variograms become useless when it comes to long-tailed distributions in highly variant variables. Therefore Kriging has limited capability when it comes to modeling non-linear variables. Kriging will over-estimate low values and under-estimate high values. Indicator Kriging (Journel, 1983) is the first geostatistical method to model non-linear geological systems.

One of the problems in SGS is that it is unable to respect significant spatial correlations between extreme values (Journel and Alabert, 1989). A single covariance model is used by SGS to characterize the spatial geological phenomenon. The spatial variability in some cases is different for each range of values. For instance, shale barriers that have a permeability less than a specific

threshold, have reasonably good spatial continuity, but in SGS approach will underestimate the desired continuity. In other words, values at the long tails of the distribution are spatially uncorrelated (Journel and Deutsch, 1993). In cases like these a non-parametric and a non-linear technique of SIS is used.

SIS uses the specific variograms of the given data threshold and draws a categorical local probability distribution by building a categorical image using an algorithm that is pixel-based (Journel and Alabert, 1989). SIS accommodates different indicator variograms for different facies easily (Journel and Deutsch, 1993).

The simulation process is similar to SGS approach where the nodes are visited in a random manner, constructing the conditional distribution and sampling a value from the local conditional CDF for that node, and proceeding to next location with the addition of previously simulated value to data conditioning. The process continues until all nodes of the simulation grid have been visited (Ma and Zhang, 2019).

Chapter 3 Methodology

As we have seen in the literature review (Chapter 2), there is a continuous effort towards improving both: (a) the representation of subsurface reservoirs more accurately, using advanced reservoir characterization techniques and geostatistics models and (b) accurate modelling/predictions of the complex 3D multiphase flow equations in porous media. Until this date no one software has all the advances integrated into it. In the oil industry, ECLIPSE is referred to as the petroleum reference simulator; however, it has several drawbacks: (I) it lacks mesh adaptivity options; (II) it is not an open source package which means it is expensive to use; (III) it is used as a black box; the user cannot adjust any option in it; (IV) lastly it does not have flexibility in reservoir characterization and geostatistics settings.

As alternatives to ECLIPSE, several advanced, open source software have been developed by researchers, within mainly academic institutions; these open source software implement new numerical techniques and methodologies on unstructured meshes, and also consider mesh adaptivity. One such open source software is the IC-FERST software, developed within the AMCG of Imperial College London (NORMS, 2015). It uses the CVFEM with a tetrahedral unstructured mesh, and thus be able to capture the geological heterogeneity more accurately. It also has a mesh adaptivity option to help increase mesh resolution where and when needed. However it lacks the advantage of geostatistics and rock characterization.

In this project both ECLIPSE and IC-FESRT are implemented, with the aim of comparing the output from the two software. Initially, ECLIPSE is used to validate the new novel state of the art IC-FERST software (Chapter 4) using standard benchmark case studies from literature, whilst in Chapter 5, Chapter 6 and Chapter 7, a comparison between the output from both software is carried out on a real case study. As rock characterization is of prime importance in both ECLIPSE and IC-FERST, Chapter 5 is devoted to reservoir characterization and geostatistics for determining the properties of the real field; a new rock characterization MATLAB technique code has been written as part of Chapter 3 - called (Balaha Rock Characterization Code - BRCC), and it is implemented together with an open source geostatitics software (SGems) (Remy, 2005) and on open source neural network python code to produce the reservoir properties (porosity and permeability) of the

real case scenario. These properties were determined for every cell of the computational domain of both software.

In this chapter, a brief theoretical background of the two main software is firstly presented together, with a description of the validation process and followed by the geostatistics and rock characterization approaches which are necessary for the real case scenario.

3.1 Theoretical Background

3.1.1 General Flow Equations – Single Phase Darcy’s Law

Absolute permeability is a property of a medium indicating the ease with which a fluid can flow through it. Permeability is the proportionality constant relating the pressure difference and flowrate across a porous media section. In 1856 a French scientist known as Darcy performed a number of flow tests through sand packs to experimentally model an aquifer for ground water supply. He derived an empirical relationship known as Darcy’s Law(Darcy, 1856a) – as shown in equation (3-1), relating the volumetric flow rate Q , through the medium, with the pressure gradient $\frac{\Delta P}{L}$. This law today provides the basis for the study of fluid flow through porous media.

$$Q = \frac{K\Delta PA}{\mu L} \quad (3-1)$$

Where:

Q : Volumetric flow rate (cm³/sec)

K : Absolute Permeability (Darcy)

ΔP : Pressure difference (atm)

A : Cross section area (cm²)

μ : Viscosity (centipoise)

L : Length (cm)

Darcy’s law states that the flowrate through a given media is directly proportional to the product of the pressure difference across the bed with the surface area of the media, and inversely proportional to the length of the media and the viscosity of the fluid. The unit of Darcy is defined as the permeability which will allow a fluid with a viscosity of one centipoise and under a pressure

gradient of one atmosphere per centimeter to flow with a velocity of one centimeter per second (Todd, 2013).

Introducing the Darcy velocity (u), a more useful way to write Darcy's law is shown in equation (3-2). The negative sign designates that the fluid flow direction is from high to low pressure down the pressure gradient, in other words it is opposite to the positive pressure gradient (Todd, 2013).

$$u = \frac{Q}{A} = -\frac{k}{\mu} \cdot \frac{\Delta P}{L} = -\frac{K}{\mu} \cdot \left(\frac{\partial P}{\partial x} \right) \quad (3-2)$$

Darcy's law in the presence of gravity [g] in one dimension [1D] e.g. the x-direction in a Cartesian coordinate system, and for an inclined system with an angle θ results in the following:

$$u_x = -\frac{1}{\mu} k_x \left(\frac{\partial P}{\partial x} - \rho g \sin \theta \right) \quad (3-3)$$

3.1.1.1 Effective and Relative Permeability

The absolute permeability (K) is the permeability for single fluid flows in the pore space (Dake, 1978b). It reflects 100% saturation of rock by a single fluid. However, when more than one fluid is present, the permeability changes resulting in the effective permeability (K_{eff}) with the corresponding change in Darcy's law as it will be shown further below.

It is important to note that the effective permeability is a tensor – meaning possible different values in different planes and direction; this is very important when heterogeneity is addressed.

Relative permeability (K_x) reflects the ability of fluid to flow in a porous media in the presence of more than one fluid. For a given medium the effective permeability is the ability of this phase to flow at a specific saturation. The effective permeability of each fluid is less than the absolute permeability, also the sum of the effective permeabilities of all the fluids present is lower than the absolute permeability (Dake, 1978b).

Relative permeability for a given fluid is a dimensionless factor usually written in the form of percentage of fractions. It is calculated by the expression $K_r = \frac{K_{eff}}{K}$.

Figure (3.1) is an example of typical relative permeability curves for an oil-water system, where k_{rw} is the relative permeability of water – as a function of water saturation – and k_{ro} is the relative permeability of oil (also as a function of water saturation).

It is noted that the introduction of the second phase decreases the relative permeability of the first phase. Also when the relative permeability of a fluid reaches zero, it can be seen that there is still some of this fluid present.

The value of the water saturation S_w at $k_{rw}=0$ is known as the irreducible water saturation and the value of the oil saturation S_o at $k_{ro}=0$ is the residual oil saturation.

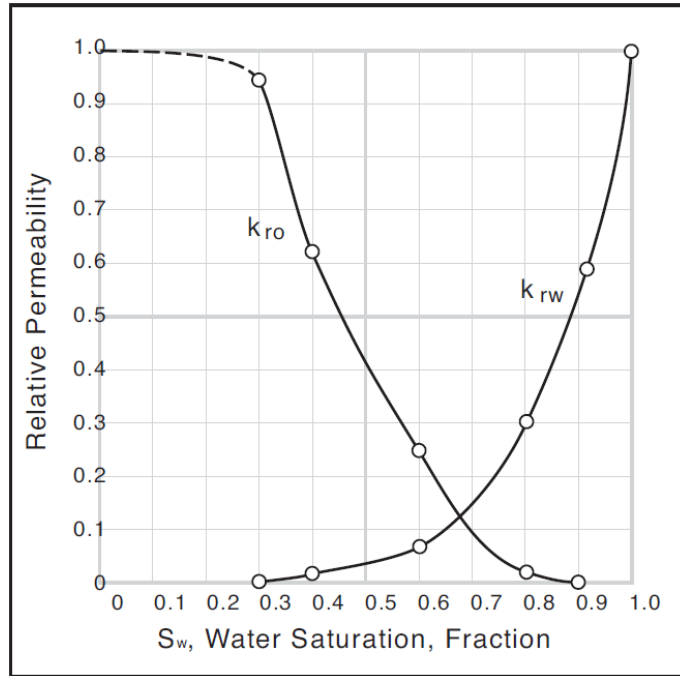


Figure (3.1): Typical relative permeability curves for an oil water system (Dake, 1978b)

3.1.2 Two Phase Darcy's Law

Darcy's Law was first applied to single phase flow, but it has been extended to describe the flow of multiple phases in the reservoir engineering field. This is done by including the term of relative permeability, which as described above denotes the decreasing ability of fluid to flow in the presence of another fluid (Todd, 2013).

Darcy's Law in the presence of two fluids is modified as follows:

$$Q_w = \frac{K \cdot k_{rw} \cdot A}{\mu_w} \cdot \left(\frac{P_w}{L} \right) \quad Q_o = \frac{K \cdot k_{ro} \cdot A}{\mu_o} \cdot \left(\frac{P_o}{L} \right) \quad (3-4)$$

Where:

Q_w : Water flow rate

Q_o : Oil flow rate

μ_w : Water viscosity

μ_o : Oil viscosity

K: Absolute permeability
 K_{rw} : Water relative permeability
 K_{ro} : Oil relative permeability
 P_w : Water phase pressure
 P_o : Oil phase pressure

The two phase Darcy's Law with gravity in its differential form is as follows:

$$u_w = -\frac{K.K_{rw}}{\mu_w} \cdot \left(\frac{\partial P_w}{\partial x} - \rho_w g \frac{\partial z}{\partial x} \right) \quad u_o = -\frac{K.K_{ro}}{\mu_o} \cdot \left(\frac{\partial P_o}{\partial x} - \rho_o g \frac{\partial z}{\partial x} \right) \quad (3-5)$$

The phase pressures P_w and P_o at a given saturation are not equal, but they are related to each other by the capillary pressure such that:

$$P_c(S_w) = P_o - P_w \quad (3-6)$$

3.1.2.1 Capillary Pressure and Interfacial Tension

Capillary pressure always exists when there are two immiscible phases present; it is defined as the pressure drop across the curved liquid interface. At the interface between two fluids the equilibrium forces between the phase molecules gets disrupted, due to the difference in the distance between the molecules and the different masses of the molecules of the different phases (Dake, 1978b).

Droplets are produced due to the interfacial tension distorting the outer surface of immiscible fluids. Figure (3.2) shows two liquids on a surface, the interfacial tension distorts the fluids to produce a contact angle. The wetting phase here is the one which spreads over the surface and wets it, the contact angle for this phase will always be less than 90° and tends to approach zero. The non-wetting phase here will have little or no attraction to the surface and the

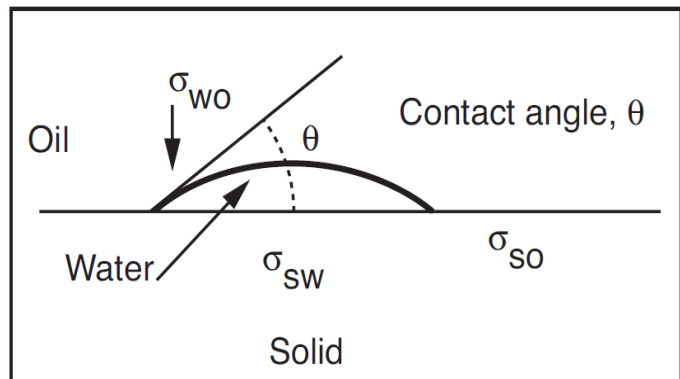


Figure (3.2): Interfacial tension between oil, water and solid(Dake, 1978a)

contact angle will always be bigger than 90° (Dake, 1978a).

Where:

σ_{wo} : Interfacial tension between the water and oil

σ_{sw} : Interfacial tension between the solid and water

σ_{so} : Interfacial tension between the solid and oil

Capillary pressure is a very important parameter for multiphase flow calculations; it is defined as the non-wetting phase pressure minus the wetting phase pressure; and it is a main term in the pressure and saturation equations. The capillary pressure is also used to identify the rock wettability.

3.1.3 Multiphase Fluid Flow Equations within IC-FERST

Darcy's law along with conservation of mass form the basis of multiphase flow in porous media in IC-FERST. Darcy's law for the l th fluid phase is given by (Mostaghimi et al., 2015a):

$$u_l = -\frac{Kk_{rl}}{\mu_l} (\nabla p_l - \rho_l \underline{g}) \quad (3-7)$$

Where:

K : absolute permeability

\underline{g} : gravitational acceleration vector

u_l : Darcy velocity of the l th phase

p_l : Pressure of the l th phase

k_{rl} : Relative permeability of the l th phase

μ_l : Isotropic viscosity of the l th phase

ρ_l : Density of the l th phase

Mass conservation for each phase, assuming no mass sources or sinks, can be written as:

$$\frac{\partial(\phi \rho_l S_l)}{\partial t} + \nabla \cdot (\rho_l \underline{u}_l) = 0 \quad (3-8)$$

Where:

ϕ : Porosity

S_l : Saturation of the l th phase such that the sum of saturation of all phases is given by: $\sum_l S_l = 1$

Assuming incompressible fluids and substituting for u_l from equations (3-7) and (3-8), the mass conservation equation of phase l is obtained as:

$$\frac{\partial(\phi S_l)}{\partial t} - \nabla \cdot \left[\frac{Kk_{rl}}{\mu_l} \nabla p_l - \frac{Kk_{rl}\rho_l}{\mu_l} \underline{g} \right] = 0 \quad (3-9)$$

A global continuity equation is then formed by summing equation (3-9) for all the phases and using the constraint from equation (3-8)

$$\nabla \cdot \left[\sum_l \left(\frac{Kk_{rl}}{\mu_l} \nabla p_l - \frac{Kk_{rl}\rho_l}{\mu_l} \underline{g} \right) \right] = 0 \quad (3-10)$$

The phase conservation equation is a non-linear hyperbolic equation while the global continuity equation is parabolic. Therefore, the governing equations for flow in porous media are classified as mixed hyperbolic-parabolic type. Equations (3-11) and (3-12) are also known as the saturation and pressure equations, respectively.

3.1.4 Brief Introduction to Numerical Methods for Reservoir Simulation

As shown in the previous sections, the multi-phase flow equations are very complex and it is not possible to solve them analytically – hence, they need to be solved numerically. The numerical techniques provide approximate solution to the nonlinear partial differential equations that cannot be solved using analytical techniques. To solve a Partial Differential Equation (PDE) numerically, firstly the equations must be converted to a numerical equation, and then solved on a discretization grid. This conversion is known as spatial discretization and the standard numerical methods in reservoir simulators are the FDM, FEM and the FVM (Gholinezhad et al., 2017) as found in the literature review.

(a) Finite Difference Method (FDM)

The FDM is a differential scheme - it is the oldest of all numerical methods and it is the most direct approach in discretizing PDE. A point in space is considered where the continuum representation of the equation is taken and is replaced with a set of discrete equations, called finite difference equations (Gholinezhad et al., 2017). The FDM is typically defined on a regular/structured grid - that's why it is a very efficient solution method and a very fast one compared to other methods. As

the FDM grid is defined dimension per dimension, it is very easy to increase the number of elements in each direction/dimension to increase the spatial resolution and hence solution accuracy. The use of structured grids is very useful in large scale simulations. For unsteady, time-dependent problems, the time derivatives are approximated using either the explicit or implicit approaches, one of the drawbacks of the FDM is the fact that it can only be used on structured grids, and therefore it is very hard to handle curved boundaries. It is not able to capture accurately curved boundaries. The second limitation is the inability to lend itself to adaptive mesh refinement (Gholinezhad et al., 2017). The ECLIPSE software implemented in this work solves the reservoir equations on a structured, finite difference grid, using the IMPES method.

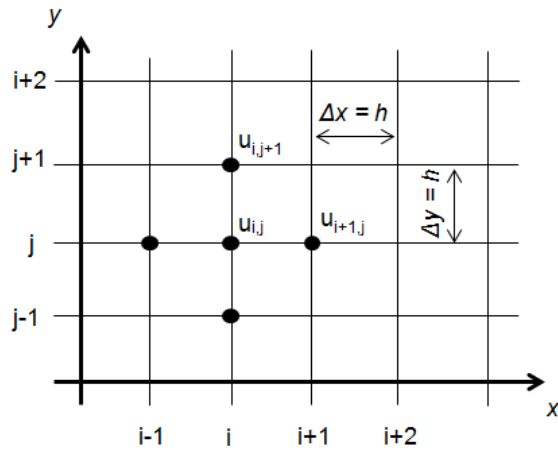


Figure (3.3): An example of a finite difference grid (Rokicki, 2014)

(b) Finite Element Method (FEM)

The FEM is an integral approach, it subdivides the computational space into finite, very small elements of simple geometrical shapes e.g. tetrahedral, hexagonal, or polygonal. All of these elements create the so-called finite element mesh. The analytical, PDE equations are subsequently converted into numerical equations – solved within each element; this is done by the approximation of the fields of each element into a simple function, with a finite number of Degrees of Freedom (DOF). This gives a local description of the properties by a set of simple equations. When this is implemented for all of the elements, a large sparse matrix equation system is assembled. This can then be solved by any sparse matrix solver (Manchuk and Deutsch, 2008).

The great advantage of the FEM is that it allows for the use of unstructured meshes so capturing irregular and curved geometries with great accuracy. What makes the FEM so successful is that it allows: (I) enhanced accuracy of the approximations -using higher order elements; (II) adaptive mesh refinement, (III) combination of different functions within each element – hence enhancing the accuracy, this is referred to as mixed formulation (Gholinezhad et al., 2017).

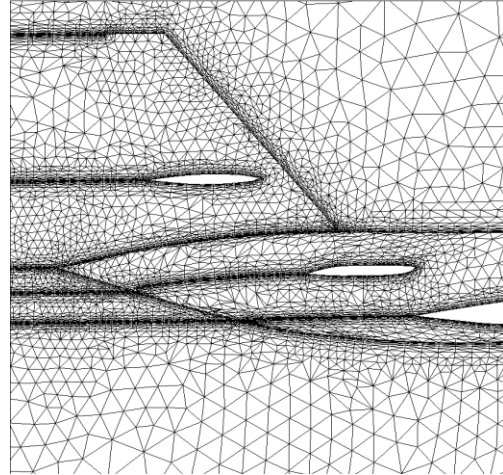


Figure (3.4): An example of a finite element grid (Morgan and Peraire, 1998)

The biggest disadvantage of the FEM is the complex mathematical numerical expressions. They are more advanced and complicated compared to FDM and FVM. It is also computationally more expensive, and tends to be unstable for complex problems (Gholinezhad et al., 2017).

(c) Finite Volume Method (FVM)

The FVM is also an integral scheme - it is fairly recent in the field of reservoir simulation. It is similar to FEM in that it subdivides the computational domain into finite very small elements of simple geometrical shapes. The FVM is based on conservation laws, so we end up with formulations that consist of flux conservation equations that are averaged over the cells. Since the PDE we are trying to solve is originally a conservation equation, this makes the FVM a natural choice for Computational Fluid Dynamics (CFD) in general. FVM is easier and faster to implement compared to FEM, while at the same time it provides more accurate solutions and works with unstructured meshes when compared to FDM. FVM has an advantage of speed and memory use for very large problems when compared to FEM. FVM can, like FEM, refine the mesh in desired locations, but unlike FEM it cannot easily increase the order of elements (higher degrees) (Manchuk and Deutsch, 2008).

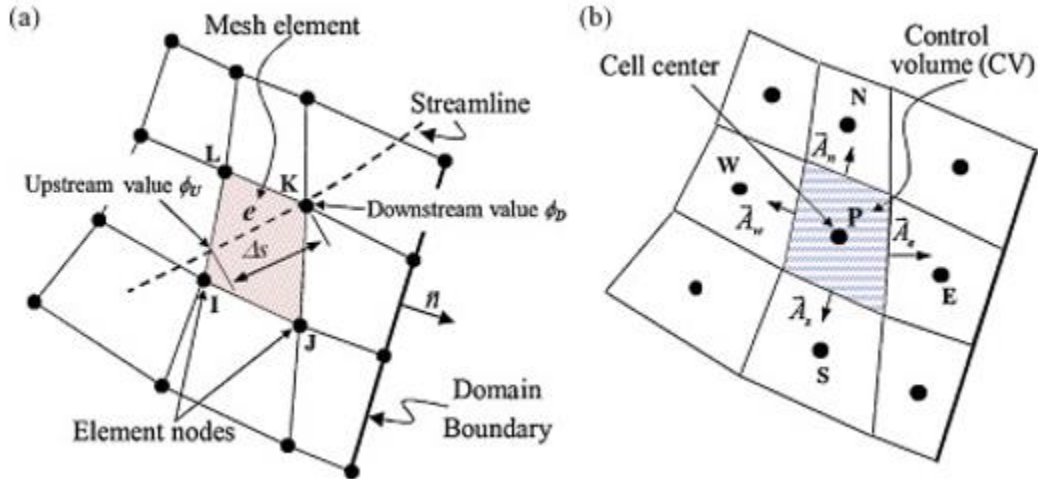


Figure (3.5): An example of a finite volume grid vs a finite element grid (Molina-Aiz et al., 2010)

(d) Control Volume Finite Element Method (CVFEM)

FEM is attractive for numerical methods because it uses unstructured meshes that are capable of meshing complex geometries and allows for the use of adaptive meshing techniques. FVM is attractive for formulating discrete equations in transport processes because it is based on the idea of flux balance over a CV. Combining the two, a new approach, called the CVFEM has been developed, which can maintain the flexibility of the FEM while yielding mass conservation principles (Prakash, 1987b).

The CVFEM elements are constructed in the same way as in FEM. Several forms of the PDE is merged over non-overlapping CVs, which is the same as creating balance conservation for these CVs. Moreover, FEM gives its maximum accuracy on coarse grids, which makes it an attractive method for free surface and diffusion dominated problems. But unfortunately in large scale problems it is slow and is not suitable for turbulent flow. But the FVM does not limit mass, energy conservation and momentum making the CVFEM an efficient iterative solver (Matthäi et al., 2005).

As mentioned above, to solve numerical equations, discretization grids are needed. Typical discretization/computational grids used in the computational methods described above are described below.

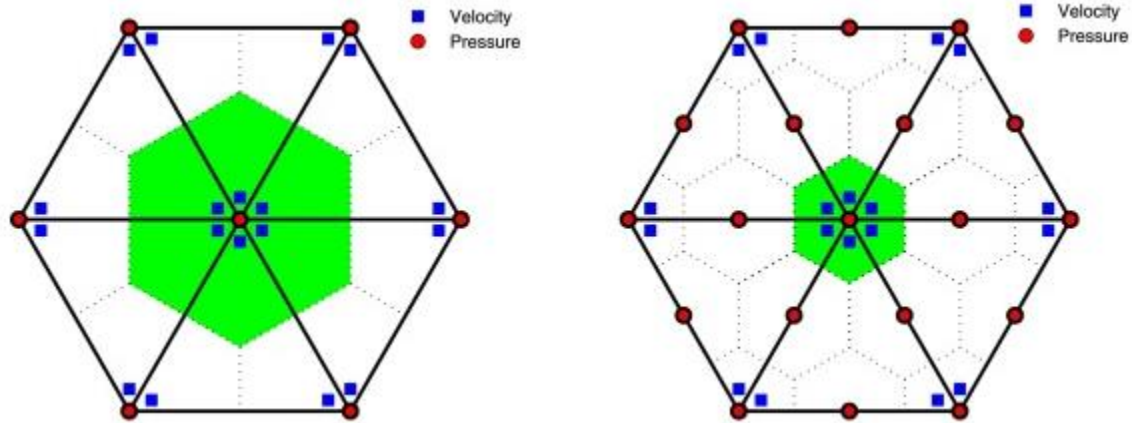


Figure (3.6): An example of a control volume finite element grid (Xie et al., 2016)

3.1.5 Different Types of Gridding used in Reservoir Simulators

Gridding is simply the process of dividing the reservoir domain into a large number of smaller spatial blocks - this process is known as spatial discretization. The process of splitting up time into discrete steps is known as temporal discretization. A spatial grid is required in reservoir simulators so that the nonlinear flow equation can be solved to predict the reservoirs performance. The type of the grid used is selected based on many factors, such as: the desired numerical accuracy; available computational power; acceptable run times; and mainly the geometry that is modeled (Yaghi, 1999).

There are several gridding techniques used these days in reservoir simulators, but these different techniques can be divided into two main categories which are, structured and unstructured grids.

3.1.5.1 Structured Grids

Structured grids are sometimes also called regular grids, structured grids are almost always cartesian, meaning that all cell faces meet at right angles. The best numerical results are obtained on a regular Cartesian grid, they are also the best when it comes to efficiency and computational time (Yaghi, 1999). Structured grids are the ones used in this work in the ECLIPSE simulations.

(a) Block Centered Grids

In a block centered grid, element sizes are chosen and then the nodes are determined to be at the center of these elements, there are no nodes at the boundaries of the elements. The block centered grid is advantageous for calculating accumulation terms (Aziz, 1993). Figure (3.8) (a) shows an

example of a block centered grid. The block centered structured grids are the grids used in this work ECLIPSE simulations.

(b) Point Centered Grids

The point centered grid is also referred to as corner point grid and point distributed grid. Then nodes in this type of system are located at the boundaries (corners) of the elements. The point centered grid is advantageous for calculating the flow between blocks. The use of the point centered grid is not as common as the block centered not because of its accuracy or computational time, but because most of the engineers prefer dividing the reservoir into blocks, rather than choosing points that generate blocks as in the point centered grid (Aziz, 1993). Figure (3.8) (b) shows an example of a point centered grid.

(c) Local Grid Refinement (LGR)

In petroleum reservoirs, the change in saturations and pressure tend to be different in different parts of the reservoir. To be able to represent these rapid changes in these parts of the reservoir, a finer grid will be required in this area. The refinement of this area only is referred to as Local Grid Refinement (LGR). Using LGR achieves the desired accuracy of a fine mesh but with less elements, resulting in less computational time (Peaceman, 2000). Figure (3.7) shows an example of a local grid refined. LGR was not used in the ECLIPSE simulations in this work because, it needs to be applied in a specific location of interest, and in our simulations we didn't concentrate on one specific location.

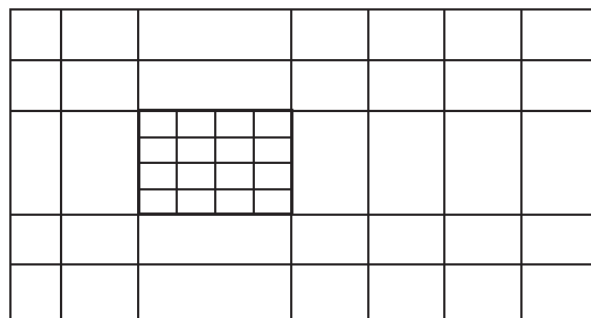


Figure (3.7): Local grid refinement representation(Mackay, 2013)

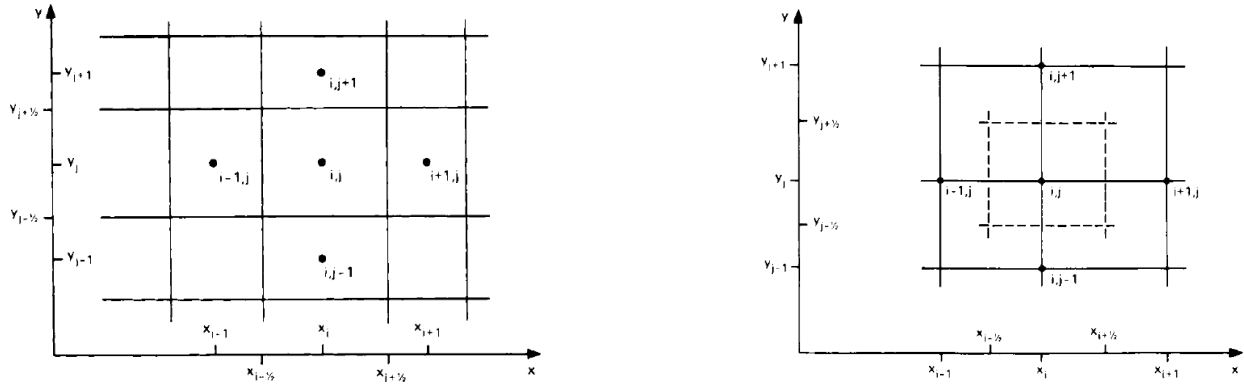


Figure (3.8): a) Block centered representation b) Point centered representation (Peaceman, 2000)

3.1.5.2 Unstructured Grids

When it comes to modelling more complex areas of a reservoir, for example, near wellbore and through or around faults, structured grids are inflexible and cannot represent these areas accurately. So the use of unstructured grids also called irregular grids, in these areas is very much needed. The number of elements are not necessarily increased, but the element shape is much more flexible. Unstructured grids have no constraints on the geometry of their elements or their configuration; they allow for elements with any number of faces and geometry to be modelled, the only rule is that they cannot intersect each other (Manchuk and Deutsch, 2008). Unstructured grids are the type of grids that are being used by IC-FERST.

(a) Radial Grids

Near the well bore, the flow is more radial, so a cylindrical mesh system is preferred in this area. This type of grids are also sometimes called r/z geometry, because it applies Darcy's law in its radial form using the radius (r) and the thickness (z), instead of the normal $x y z$ coordinates (Yaghi, 1999). An example of a radial geometry is shown in Figure (3.9) (b).

(b) Hybrid Grid

Hybrid grid is when a grid uses a mixture of geometry combinations which are used to improve the modelling of flow in different areas of the reservoir. The most common use of hybrid grids are combining Cartesian grids with LGR where needed and Radial grids representing the near wellbore area (Pedrosa and Aziz, 1986). An example of a hybrid grid is shown in Figure (3.9) (a).

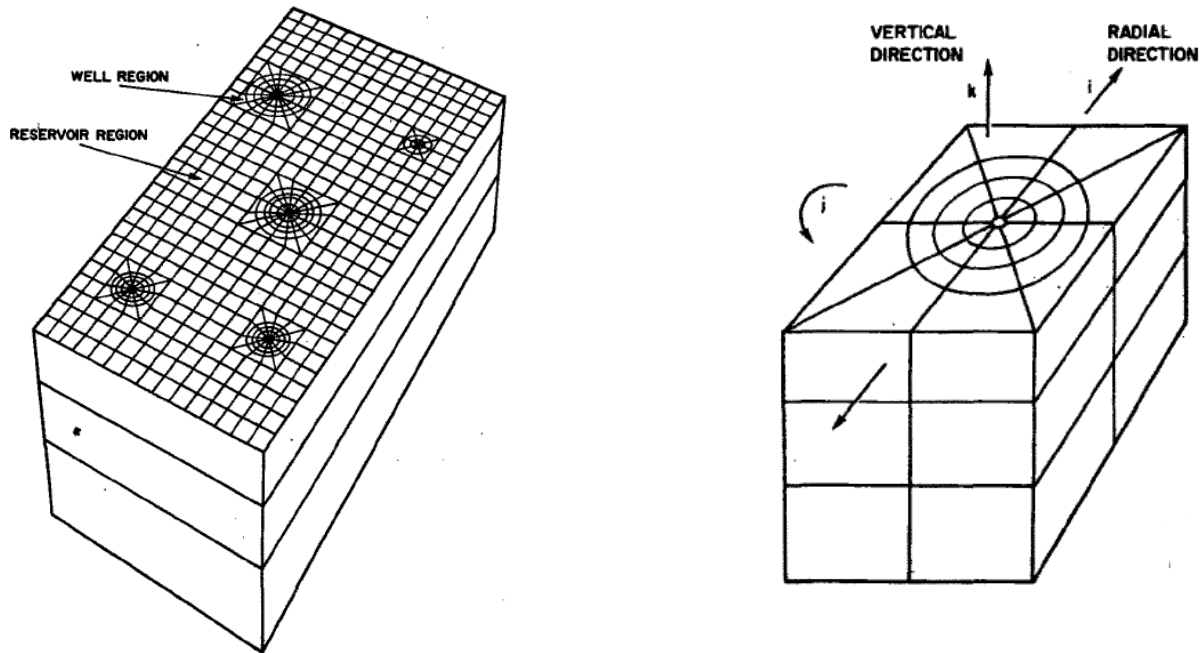


Figure (3.9): a) Hybrid grid representation b) Radial grid representation (Pedrosa and Aziz, 1986)

(c) Perpendicular Bisector (PEBI) Grids

PEBI grids are also referred to as locally orthogonal grids and Voronoi grid. These types of grids are defined by the PEBI of the lines joining neighboring centers. The PEBI grid can be thought of as a generalization of the point centered grid system, with points being distributed anywhere in the domain. A Voronoi element is then built around each point by considering a line that is orthogonal to, and centered along a line connecting two adjacent points (Consonni et al., 1993). The Voronoi elements should always have straight boundaries.

Khalid Aziz also defined a Voronoi element as “the region in space closer to its grid point than to any other grid point. Consequently a line that joins grid points of any two connected grid blocks is perpendicular to the grid block boundary between these two grid points and is bisected into two equal parts by the boundary” (Aziz, 1993). The Tetrahedral unstructured PEBI grid is the type of grid generated by Trelis and used within IC-FERST.

Figure (3.10) shows the common Voronoi elements used in reservoir simulators, and Figure (3.11) shows an example of an unstructured PEBI grid.

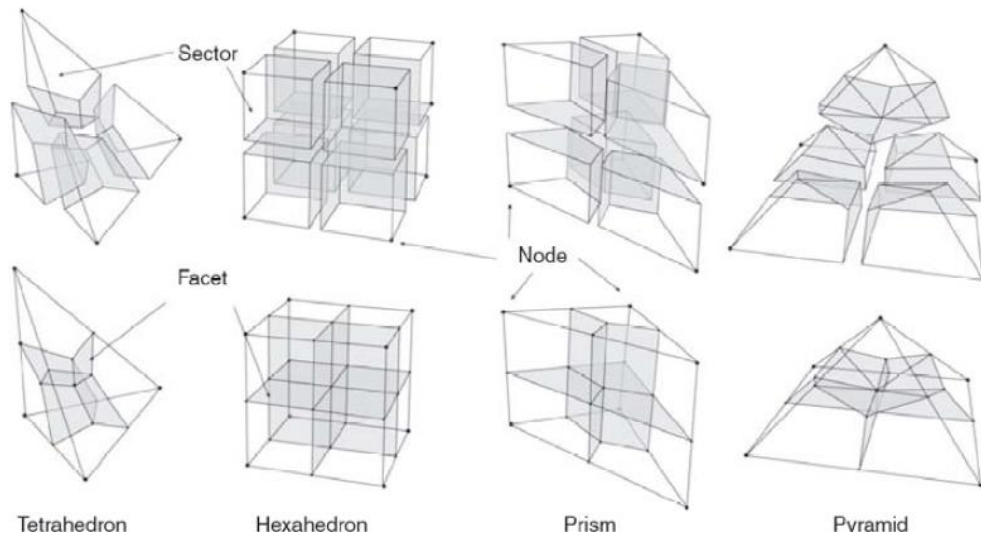


Figure (3.10): Common Voronoi elements used in reservoir simulators (Manchuk and Deutsch, 2008)

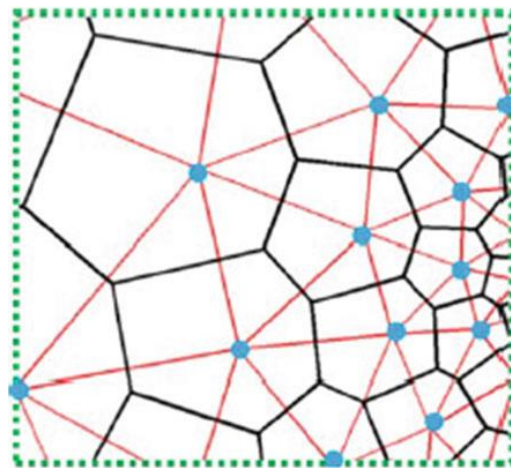


Figure (3.11): Example of an unstructured PEBI grid (Gholinezhad et al., 2017)

3.2 Implementation of the Commercial Reservoir Simulator ECLIPSE

For the simulations within this project, two reservoir simulators are used. The first one is the commercial ECLIPSE simulator, developed by Schlumberger and it is considered as the petroleum industry standard simulator, due to its robustness and reliability. The second software is the open source IC-FERST software, developed by Imperial College London, which will be discussed in the next section.

In this section we describe the main steps involved in implementing the ECLIPSE simulator. ECLIPSE offers the industry’s most complete set of numerical solutions for accurate and fast predictions for all types of reservoirs. It has been the industrial commercial benchmark reservoir simulator for more than 25 years, and it has been used over 800 sites in 70 countries around the world (Schlumberger, 2018).

ECLIPSE has a number of features, including different numerical schemes such as the FDM, FEM and FVM approaches presented briefly earlier, for solving the multiphase fluid flow equations, depending on the mesh used and the problem under investigation. ECLIPSE, allows for structured and unstructured meshes as well (Schlumberger, 2009). In this thesis, the structured grid option is being utilized and hence the numerical scheme implemented in the FDM for solving the flow equations.

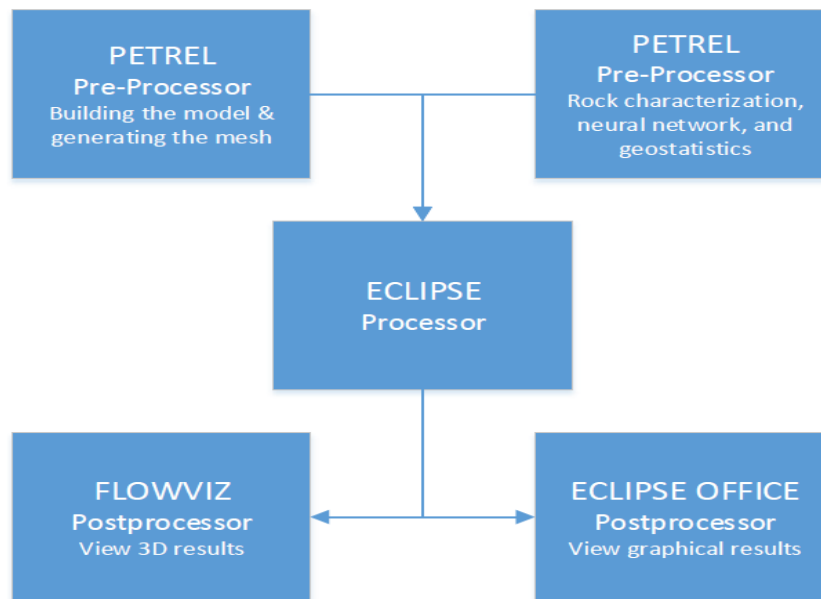


Figure (3.12): ECLIPSE Flowchart

Figure (3.12) summarizes - the steps taken in setting up the simulations in ECLIPSE, as well as viewing the results within this simulator. These involve: (I) implementing the preprocessor PETREL, which enables the creation of the geometry and mesh, as well as inputting all the reservoir properties (rock characterization) and fluid properties (single or multiphase) – following the implementation of geostatistical techniques which enable determination of reservoir properties (porosity and hydraulic permeability) using well log and core data. This is followed by the second

step i.e. (II) processing step – where the calculations are carried out; (III) finally, the post-processing step, where the results can be displayed/visualized in different forms. The following section discusses in more detail how PETREL is implemented.

3.2.1 PETREL (ECLIPSE Pre-Processor)

PETREL is ECLIPSE's Pre-Processor, and its development began in the 1990s as a tool to analyze seismic data and introduce seismic information into simulations. Its development began in 1996 in an attempt to tackle the growing trend of specialized geoscientists working in isolation, and it was commercially available in 1998. PETREL was developed specifically for PCs and the Windows OS. In 2002 Schlumberger acquired the PETREL software, and the result was an integrated workflow tool for exploration and productions companies (Schlumberger, 2010).

PETREL has since incorporated ECLIPSE in its framework for carrying out the complex physico-chemical equations. Thus, PETREL can be thought of as ECLIPSE's pre-processor. Creating the model and mesh for ECLIPSE becomes very challenging and sometimes impossible when simulating a very complex geometry. For

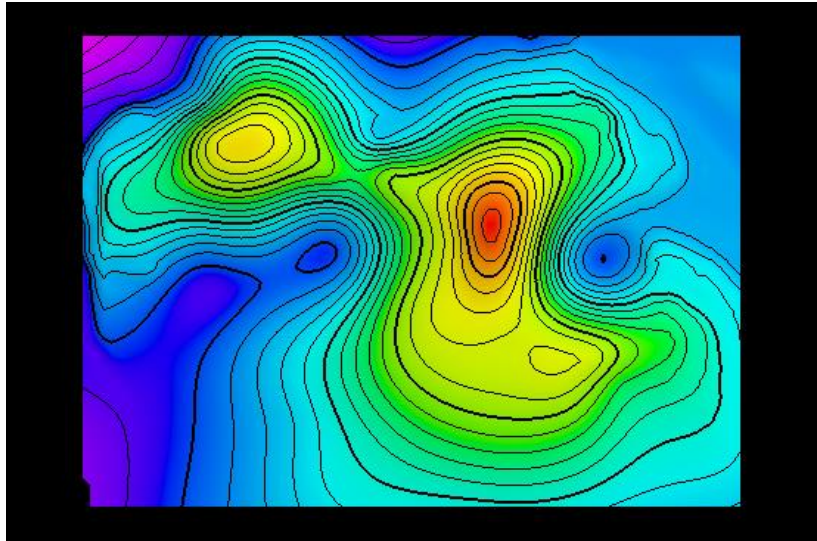


Figure (3.13): Contour map example

such cases, PETREL becomes very beneficial as it allows the user to build the ECLIPSE data file using a very friendly Graphical User Interface (GUI) – as provided by PETREL. As its name implies PETREL builds static models or the geometry from seismic data or from interpreted seismic data such as contour maps as shown in Figure (3.13). The user gets the choice of refining the model mesh in locations of interest and how many layers in the vertical (Z) direction (Cartesian coordinate system) are needed.

PETREL can also read well log files in a LAS format or from a CSV file to populate the static model with rock properties such as porosity and permeability and to get the fluid contacts; in addition, properties from core data can also be imported. It subsequently displays them in a very

user-friendly way so that geological interpretation can be carried out. Wells could also be completed/perforated in the productive zone or the zone of interest only, identified from the well logs. Figure (3.14) gives an example of PETREL’s user interface and a sample of 2 well logs.

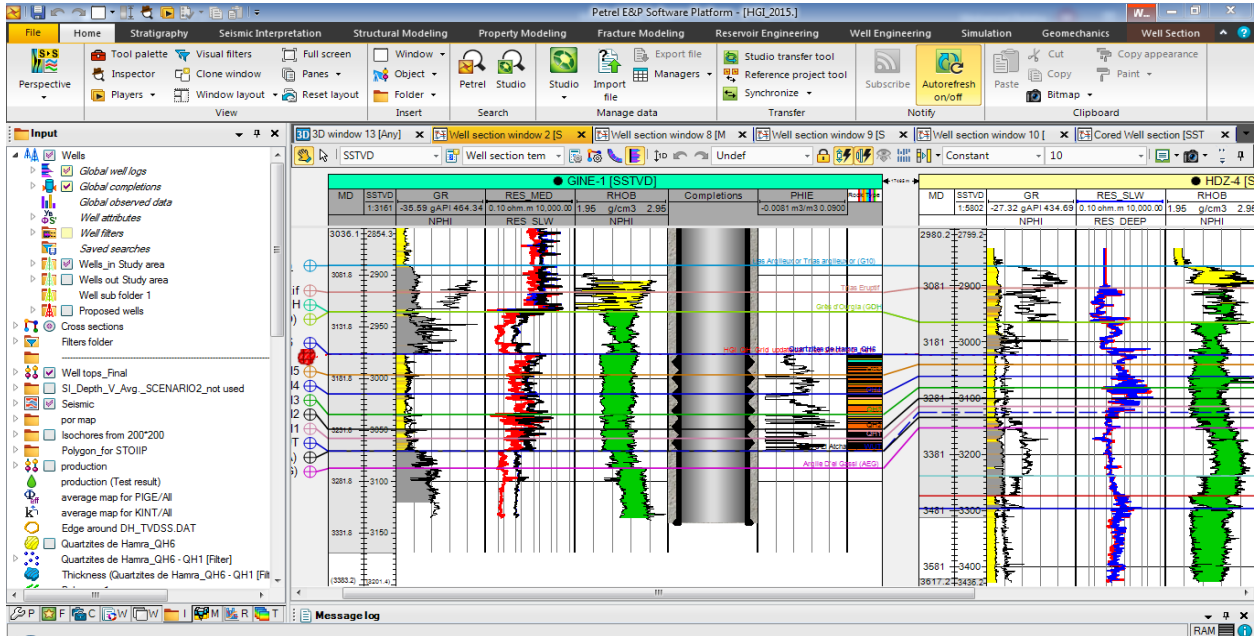


Figure (3.14): PETREL well logs visualization example

3.2.2 Rock Typing, Upscaling and Geostatistical Means within PETREL

Most petroleum companies do not carry out core analysis on all drilled wells due to its high cost, but they do carry out well logging in all wells. Porosity can be calculated from the density porosity logs with high accuracy but unfortunately permeability calculated logs do not share the same accuracy. To obtain accurate values of permeability, the core samples are used along with the technique of rock typing.

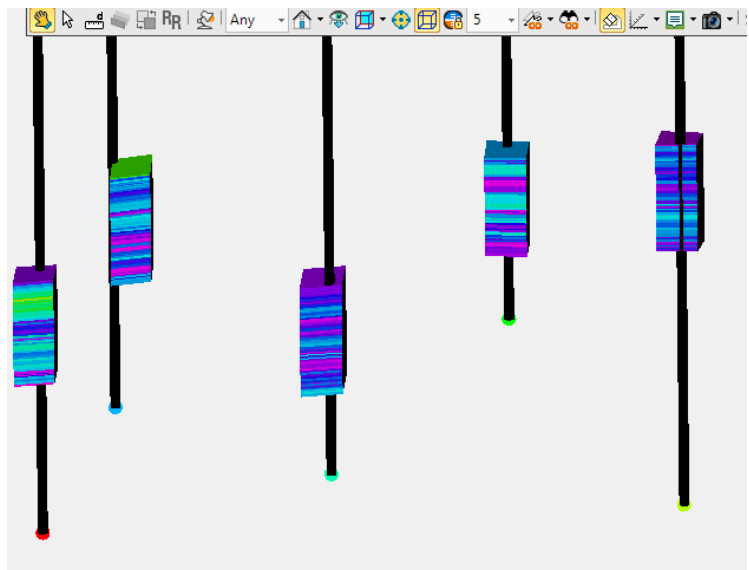


Figure (3.15): Upscaled wells example in PETREL

PETREL has a built-in Neural Network module that is trained from the available core samples and core data to categorize the reservoir into different rock types and predicts the permeability in the un-cored wells. After having permeability and porosity along with rock types in all the wells PETREL utilizes a Well Log upscaling function that populates these properties on the grid in the well location. This function is necessary because

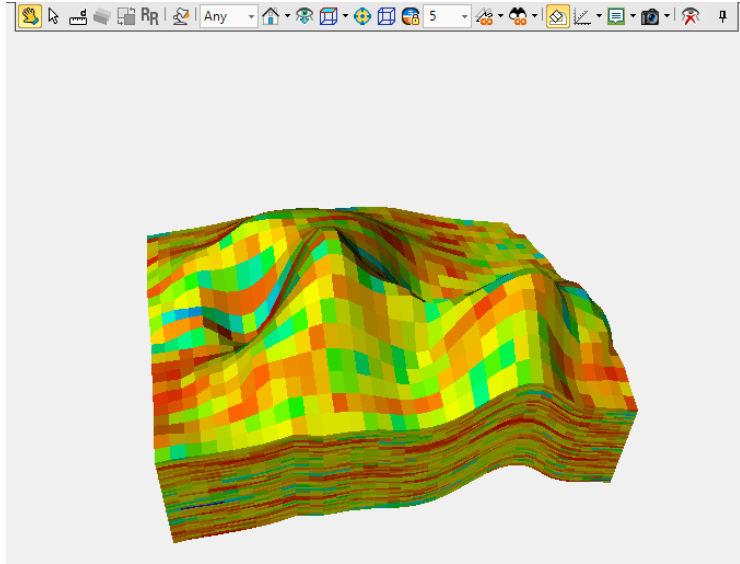


Figure (3.16): Populated grid example in PETREL

usually well logs take readings at very small spatial intervals such as 4 readings per meter. As we cannot consider a large number of Z layers in the model due to computational power constraints, an averaging technique must be used to assign only one value that represent all of these readings in each Z layer/cell. Figure (3.15) shows samples of porosity logs upscaled to match the Z layers mesh.

Now that all the properties are on the grid in the well locations as shown in Figure (3.15), a *geostatistical mean* is needed to populate the properties within all the cells of the computational domain. PETREL has various geostatistical means used for population. Geostatistical methods will be discussed in more detail further below, but a reference is made here as these values are requested as input to PETREL. The most popular approaches are: (I) the SGS used for continuous properties such as porosity and permeability and (II) the SIS used for categorical properties such as rock types and facies. These geostatistical approaches allow us to assign reservoir properties (porosity and hydraulic permeability values) in all cells of the computational domain – properties that are needed for the simulations. Lastly after assigning all the properties in the grid cells, new wells and constraints can be established if necessary, the ECLIPSE input data file can be created within PETREL. The last step is to solve the equations using ECLIPSE, within PETREL. Details for the ECLIPSE processor is given further below.

Figure (3.16) shows a sample of a computational domain/model with the porosity values in each cell – which was created using a contour map, and the well logs, followed by the upscaling process and subsequently assigning the corresponding properties in each cell of the domain.

3.2.3 ECLIPSE (Processor)

To run a simulation using ECLIPSE, first an input data file must be created. This is generated in any word processor such as notepad or word with an extension format of `.data`. This data file contains all of the data required to run the simulation, starting from the `unit system`, `field`, `lab`, or `metric`, the dimensions of the model specifying the number and dimensions of grid blocks, rock properties such as porosity, permeability, relative permeability and capillary pressures. Relative permeability and capillary pressure data is entered as a table giving the values corresponding to different saturations. Next the fluid properties are specified, such as the Pressure Volume Temperature (PVT) data, density and viscosities; subsequently, the initial conditions such as pressures and saturations; lastly the wells locations and dimensions are specified and their controls (boundary conditions) and the time step. As mentioned earlier PETREL now has ECLIPSE integrated into it and this data file can be created internally within PETREL.

ECLIPSE is available only in Windows, and hence for this thesis, the Windows 7 desktop was used, with an Intel i7 which goes up to 2.0 GHz and has 8 cores with 8GB of RAM memory. All simulations were run in series meaning that only one core/processor was used. The units used are field units meaning that the permeability is in mdarcy, pressure in psi, distance is in feet, flow rates in barrels per day etc. The simulation in ECLIPSE as mentioned earlier was done using a structured grid and a FDM.

3.2.4 ECLIPSE Post Processing

Output from ECLIPSE is in two formats – the first – is known as the EGRID output, which is opened by a package that is integrated in ECLIPSE called FloViz. FloViz displays the initial conditions, fluid and rock properties can be viewed for the whole computational domain, together with calculated parameters such as pressure and phase saturations. The mesh can also be displayed and vertical or horizontal slices/planes can be made at any location for visualizing the results.

Figure (3.17) is a screenshot showing the FloViz user interface for the 5 spot 5 layers scenario geometry mesh that will be used later in the validation section Chapter 4.

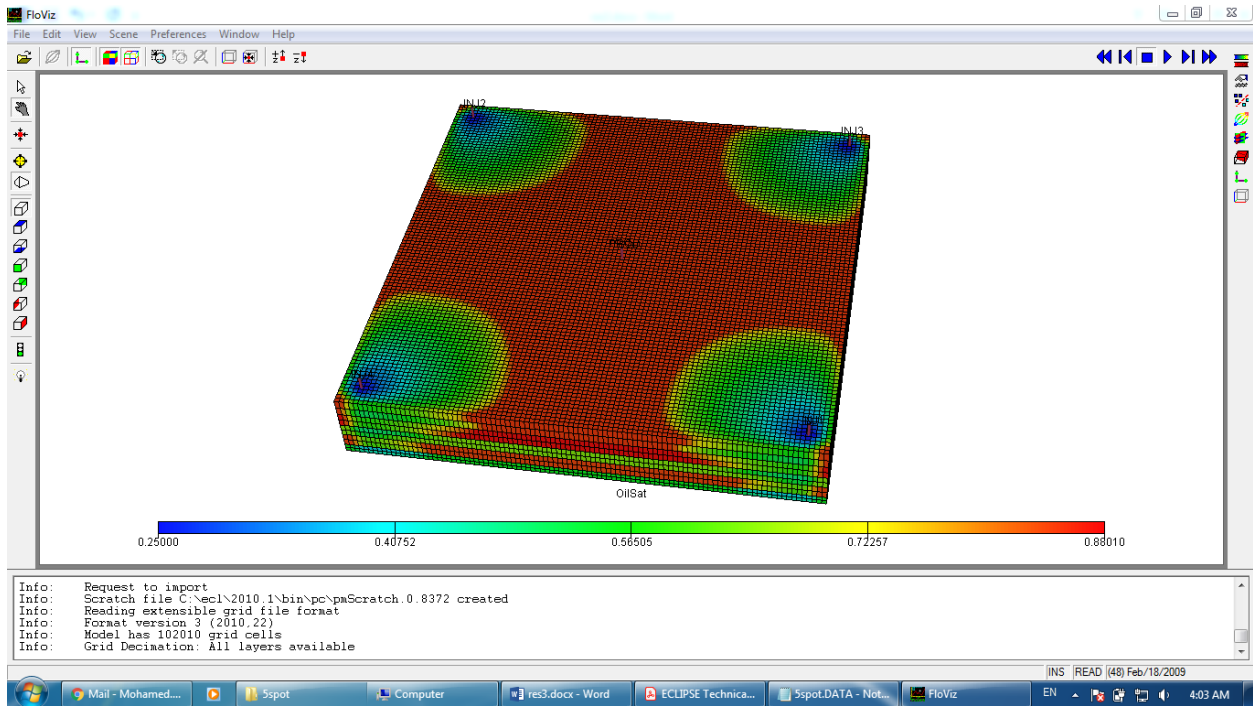


Figure (3.17): FloViz user interface using the EGRID output format

The second output format that ECLIPSE outputs is known as the SMSPEC format, which is also opened by a package that is integrated in ECLIPSE called ECLIPSE Office. This tool is mainly for the display of plots/graphs. The office displays all the graphs outputted from ECLIPSE; data from these graphs can be exported to a CSV file, which can again be opened by any spreadsheet package. For this thesis, the Microsoft Excel spreadsheet tool was used to compare both outputs from ECLIPSE and IC-FERST. Figure (3.18) is a screenshot of the ECLIPSE Office user interface along with an example graph.

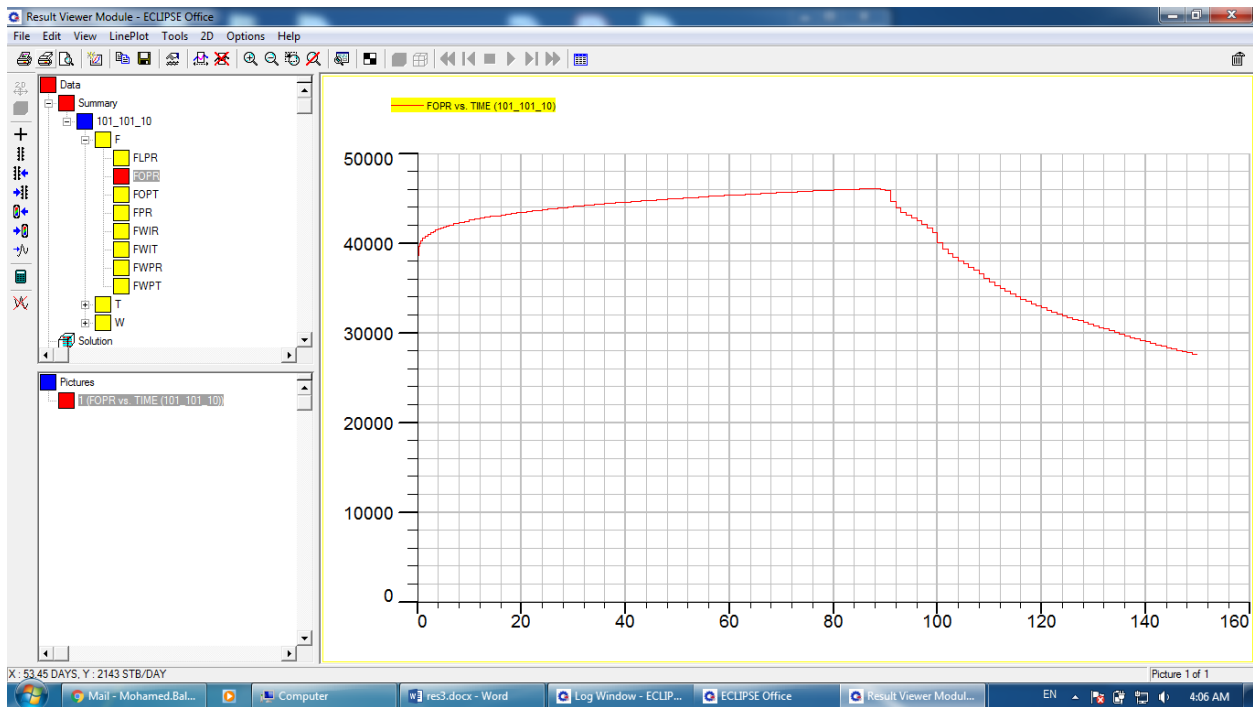


Figure (3.18): ECLIPSE Office user interface

3.3 IC-FERST

IC-FERST stands for The Imperial College Finite Element Reservoir Simulator and, it aims to be the next generation multiphase fluid flow simulator due to its many novel computational features – primarily its unstructured mesh and mesh adaptivity capability. It uses CVFEM (see earlier in section 3.1.4) which allows arbitrary mesh movement and flexibility with time dependent problems. IC-FERST uses a dynamic unstructured tetrahedral mesh optimization option and has been parallelized using Message-Passing Interface (MPI), which is a communication protocol for parallel computing i.e. the computational domain is divided into several sub-domains, and each processor solves for each sub-domain, with exchange of information between the sub-domains. IC-FERST also has the additional capability of mesh-adaptivity i.e. it allows the user to choose adaptivity options so that the mesh can be adapted so that higher resolution can be achieved in regions of interest in response to the user guidance and the physical demands. The governing equations in IC-FERST are like in many multiphase flow simulators the Darcy Law and the mass conservation equations described above in section 3.1.1 (NORMS, 2015). The numerical simulation used in IC-FERST is carried out using an unstructured mesh and CVFEM.

Figure (3.19) summarizes the steps taken in setting up the IC-FERST simulations as well as viewing the results in IC-FERST.

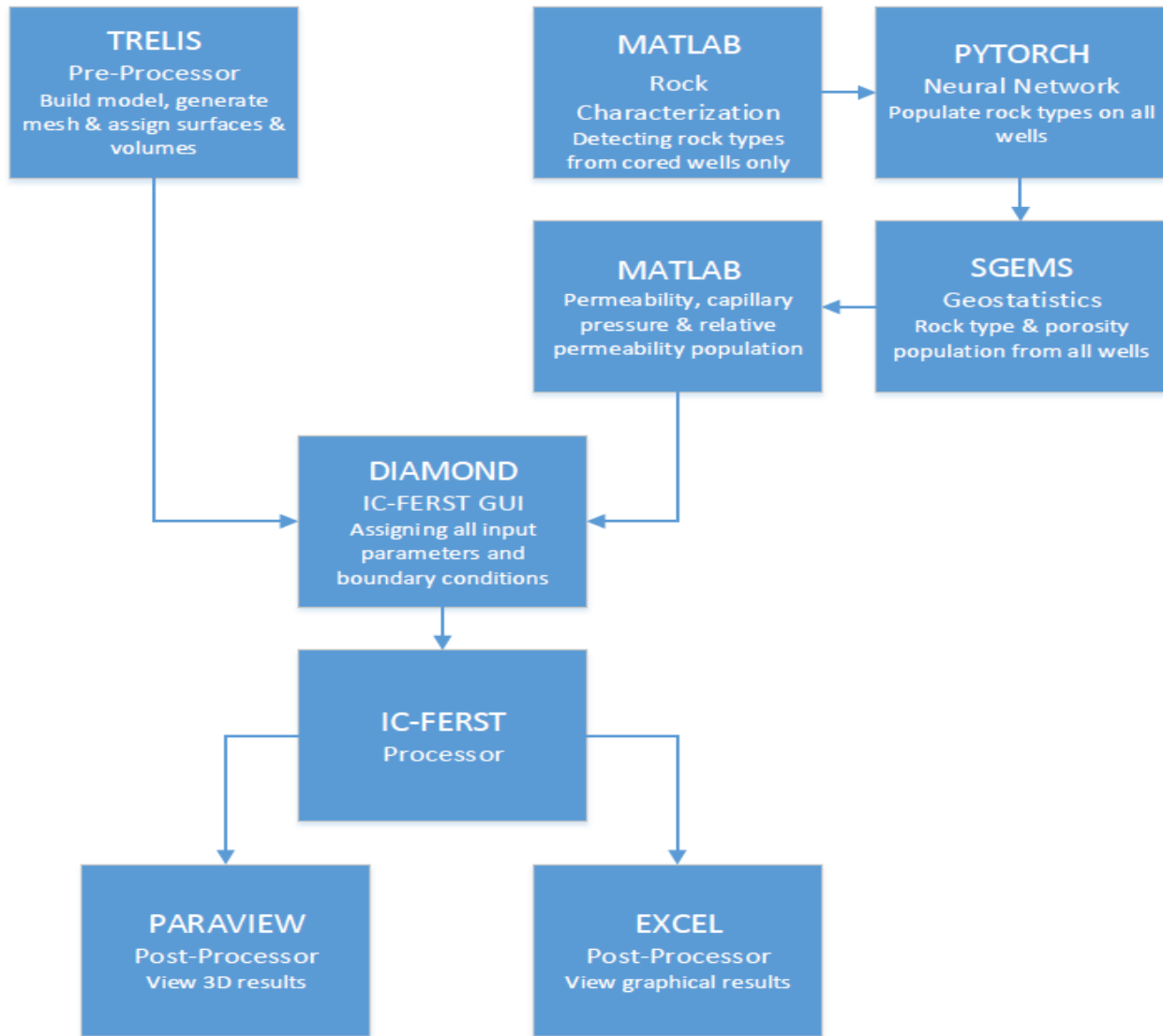


Figure (3.19): IC-FERST Flowchart showing the main stages involved in the IC-FERST simulations

There are typically three stages, depending on the problem, but for this thesis five stages are identified – to include preprocessing required for real case scenarios. The main stages are: (I) Pre-processing involving the mesh generation i.e. the generation of the computational domain; (II) for real case scenarios, where data analysis is involved, we have the rock characterization stage – which involves analyzing data from well bores as well as core data, for establishing the properties of the reservoir and translating them into the computational grid; (III) the 3rd stage involves the

setup of the input file – with the properties of the fluids; the initial and boundary conditions; the properties of the reservoir; the computational solvers to be used; the adaptivity options, and essentially anything that is required for the simulation to run effectively; (IV) the fourth stage/step is to run the simulator; and (V) final step is to post process the results using post processing software, such as Paraview (section 3.3.5).

3.3.1 Trelis (Pre-Processor)

Prior to implementing IC-FERST, the geometry needs to be defined and the mesh generated. For this, a pre-processor is needed. One such pre-processor is Trelis software, which is a high-end, commercial pre-processor/mesh generator for CFD simulations that is developed by Csimsoft. Trelis can generate high-quality tetrahedral, hexahedral or even a mixture of different element types; IC-FERST utilizes only tetrahedral elements. A smart meshing tool is available in Trelis that meshes the geometry with the best quality mesh allowed by the geometry. The mesh quality is then checked and smoothed using various smoothing algorithms (Csimsoft, 2017).

The smart meshing tool within Trelis was used to generate the meshes in this thesis (Chapter 4 and 6). The vertices or points that bound the geometry need to be first defined; these points have then to be connected with lines such as straight lines or curves; next, a set of lines that make up a surface need to be defined and finally a set of surfaces that build up a volume are specified. After the geometry is built, the volume IDs and surface IDs are defined - which are essential later in setting up the simulation using IC-FERST. Trelis can be run on Windows, Mac, or even Linux operating systems; for this work Trelis Windows version 16.3 was used. Figure (3.20) is a screenshot showing the Trelis user interface along a 5 spot 5 layers scenario geometry mesh that will be used later on (Chapter 4).

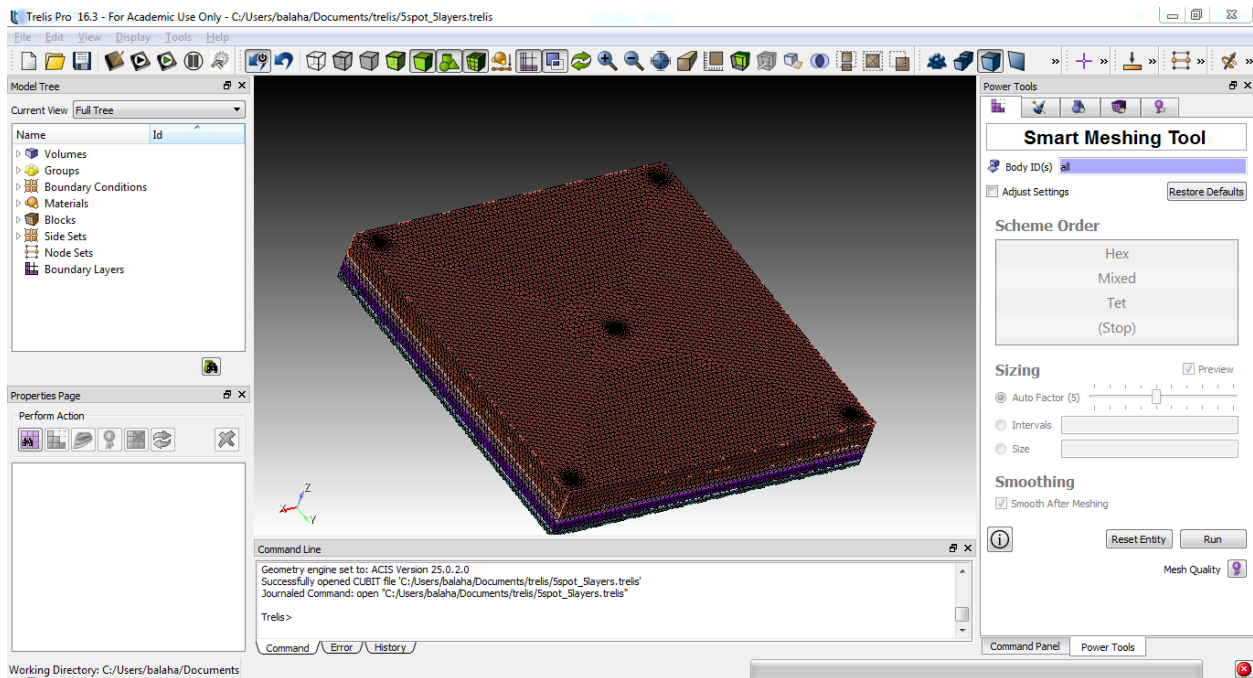


Figure (3.20): Trelis user interface

3.3.2 Diamond (Processor)

Diamond is the GUI of IC-FERST which is specifically designed in a tree format that helps in configuring the simulations without the user having to go into the code itself. It also has the capability of allowing the user to add in python scripts to describe any property in a way that is not already pre-defined (NORMS, 2015).

Diamond and IC-FERST currently runs only on the Linux-operating system. For this work IC-FERST was run using the Ubuntu 16.04 LTS operating system, on a machine with 16GB of RAM memory and an Intel core i7 processor that goes up to 3.4 GHz and has 8 cores. Some of the simulations were run in series meaning only one core/processor was used, whilst others were run in parallel meaning more than one core/processor was used.

To run a simulation using IC-FERST a mesh file describing the geometry with IDs specifying the volume and surfaces numbers is required. This file is created from Trelis in an Exodus format, which is then converted into a .msh format, as IC-FERST can only currently read geometry files in the GMSH (.msh) format. A python script is, thus first used to convert the Exodus to GMSH format.

The Diamond GUI, creates an MPML input file that is used for the simulations. This MPML file includes all the simulation parameters required for the simulation – specifically: (I) time step, (II) the physical parameters of the phases present such as, density and viscosity; (III) initial conditions such as phase saturations and initial pressures; (IV) boundary conditions for the inlets and outlets, which can be specified either as velocity or pressure boundaries; (V) the porosity and permeability properties of the reservoir; (VI) capillary pressures and relative permeabilities, using the corresponding volume IDs or by using location with the help of importing a python script; (VII) adaptivity options – when adaptivity is implemented; (VIII) the solvers that are chosen for solving the equations. Figure (3.21) outlines the various components within the Diamond user interface for setting up the simulations.

One of the most crucial parameters to be specified within IC-FERST for reservoir modelling are the relative permeability and capillary pressure functions, and how they vary with water saturation. These are defined using Corey’s correlations that are shown in equations (3-13) and (3-14) respectively (Brooks and Corey, 1966). These values should be defined for each grid block, and to do that geostatistics, rock characterization and neural network will be used later on.

$$K_{rw} = K_{rwm\max} \left(\frac{S_w - S_{wr}}{1 - S_w - S_{or}} \right)^2 \quad K_{ro} = K_{rom\max} \left(\frac{S_w - S_{or}}{1 - S_w - S_{or}} \right)^2 \quad (3-13)$$

$$P_c = P_b \left(\frac{S_w - S_{wr}}{1 - S_{wr}} \right)^{-\frac{1}{\lambda}} \quad (3-14)$$

Where:

$K_{rwm\max}$: is the maximum water relative permeability

$K_{rom\max}$: is the maximum oil relative permeability

S_{wr} : is the irreducible water saturation

S_{or} : is the irreducible oil saturation

P_b : is the entry pressure

λ : is Corey’s coefficient that changes with different formations

IC-FERST uses SI units, so permeability is in m^2 , pressure is in Pascals and velocity is in meters per second, distance in meters etc. IC-FERST outputs results in two formats, the first is VTU format, which is opened with ParaView that is discussed in section 3.3.3. It contains all the outputs such as phase volume fractions, fluxes, and pressures for each time step distributed on the 3D or 2D grid. The second is a CSV format file, which can then be opened by any spreadsheet package,

and in this thesis MS Excel 2016 was used. The CSV file contains outputs such as volume rates and fluxes from the inlets and outlets of the model at each time step.

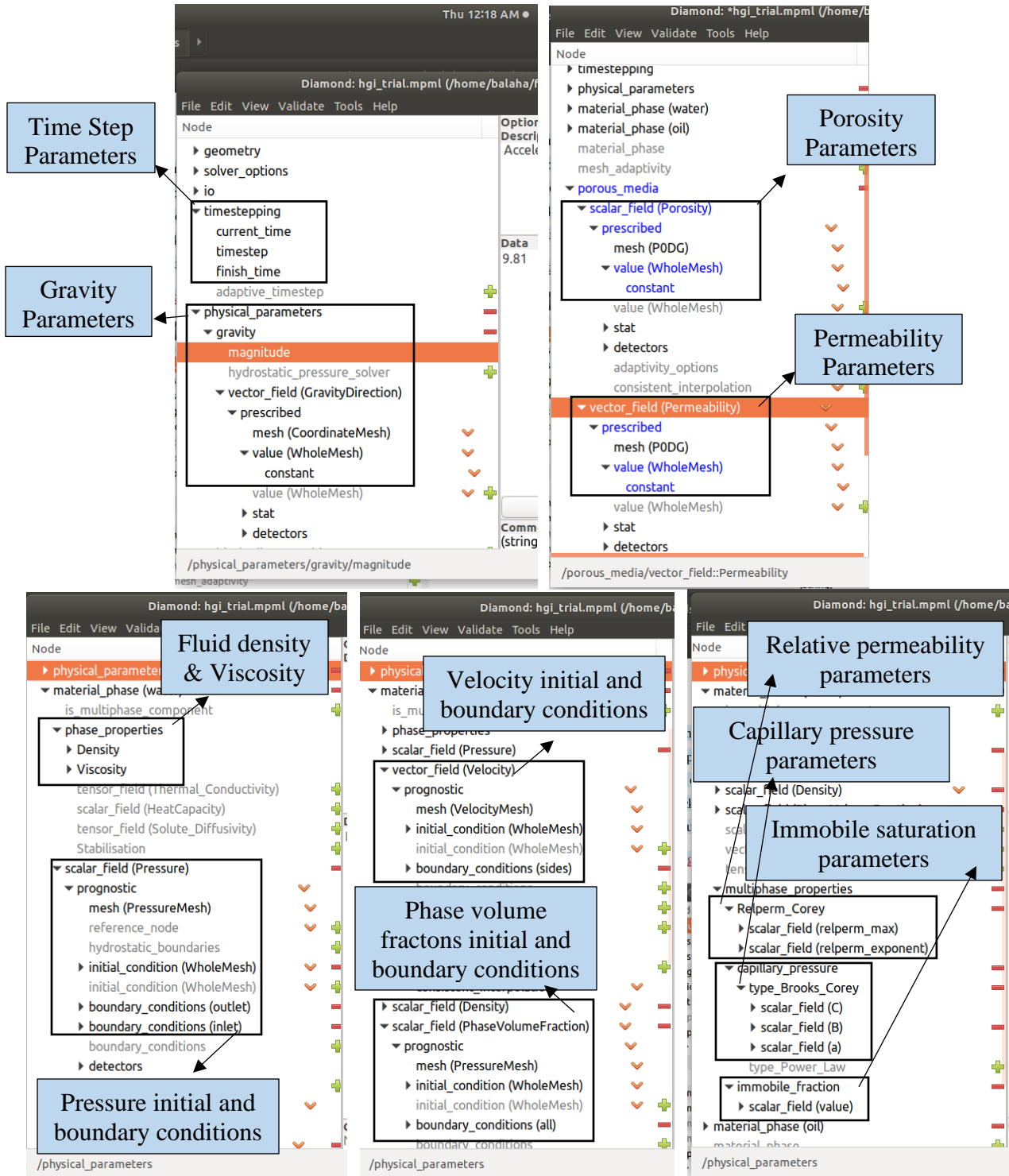


Figure (3.21): Diamond user interface a) Gravity and time step parameters b) Porosity and Permeability parameters c) Fluid properties and pressure initial and boundary conditions d) Fluid velocity and phase volume fractions initial and boundary conditions e) Multiphase parameters

3.3.3 Parallel Processing

IC-FERST as already stated is parallelized using MPI; MPI is a standardized and portable message-passing standard designed by a group of researchers from academia and industry to function on a wide variety of parallel computing architectures. The standard defines the syntax and semantics of a core of library routines useful to a wide range of users writing portable message-passing programs in C, C++, and Fortran.

To be able to do so IC-FERST has a built-in module called FLDECOMP that decomposes or splits the computational domain into the number of processors desired to be used in the simulation process. Before using the FLDECOMP module the mesh needs to be converted into binary format; this is done using an option in Diamond. Calculations are then carried out in each one of these subdomains. At the boundaries of each subdomain a halo file is created, which is used to connect all the decomposed subdomains together. The commands to decompose the initial computational domain to several subdomains are as follows:

- `fldecomp -n 2 ./NAME_OF_MESH_FILE`
- `mpirun -n 2 EXECUTABLE INPUT_FILE_NAME.MPML`

Where: 2 is the number of processors desired.

Figure (3.22) shows a 5 spot mesh example that is being simulated using six processors and how it is decomposed into six different sub-domains and finally combined together to make the final output; this example is used in Chapter 4. In this thesis some simulations were carried out using up to 16 processors. Details parameters are given in the later chapters.

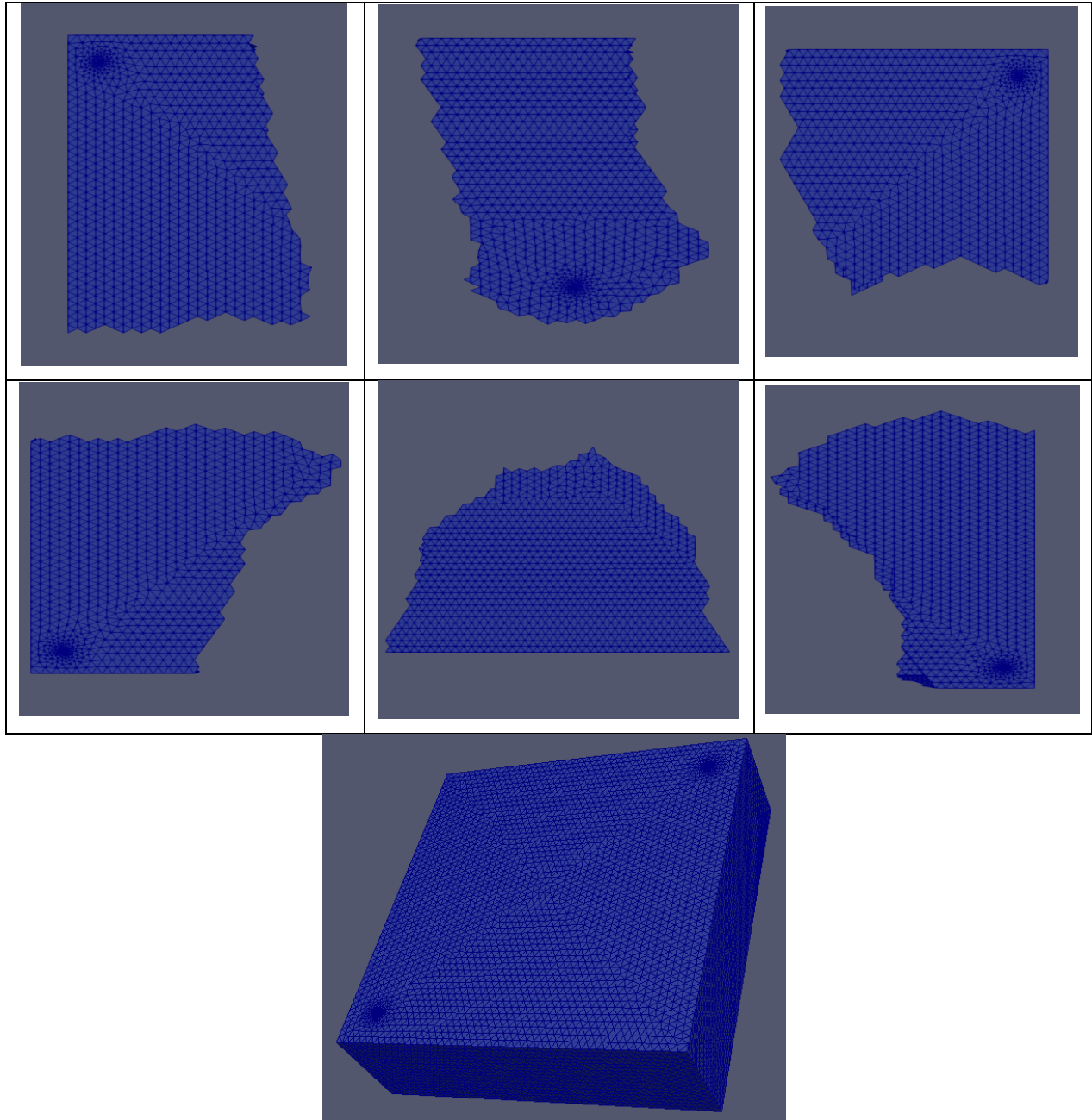


Figure (3.22): Example of a decomposed domain subdivided into 6 subdomains showing how parallel processing is done

3.3.4 Mesh Adaptivity

Mesh adaptivity as described earlier, optimizes the mesh to enable different mesh resolutions in response to an error. It allows remeshing of the domain based on a posteriori error estimates, whilst achieving certain targets for error.

IC-FERST hr-adaptivity algorithm attempts to refine the mesh resolution by (I) splitting up existing elements and reproducing elements that share the refined mesh and embracing more DOF alongside an existing edge (Berger and Colella, 1989); (II) elimination of an existing DOF by decreasing the length of current edge to 0 - this results in replacing 2 vertices by 1, causing the mesh to become coarsened (Mostaghimi et al., 2015b); (III) node movement wherein a highest node is moved by the element that shares it within the convex hull distance (Budd et al., 2009); (IV) rearrangement of the way existing element groups are connected (Mostaghimi et al., 2015b). Figure (3.23) shows the adaptivity options in Diamond interface.

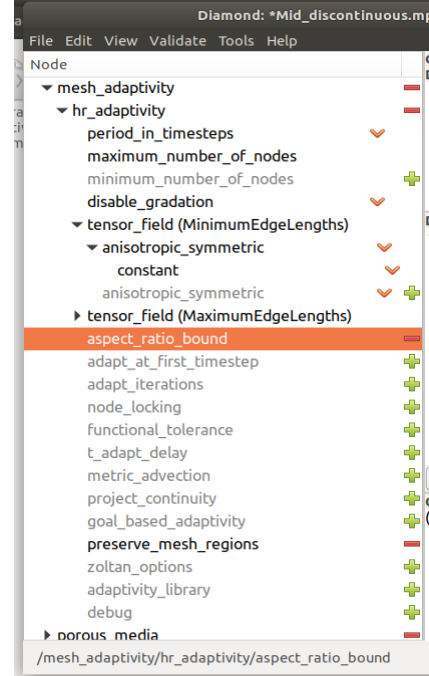


Figure (3.23): Diamond Interface showing adaptivity parameters

As mentioned earlier, adaptivity enables the automatic determination of the element sizes, based on certain criteria (e.g. velocity, phase saturation etc.). To reduce the measured error the mesh continues to refine itself. The main aim of adaptivity is to reduce the computational time and minimize errors by ensuring that the right mesh is used in the right place (Quirk, 1991).

Figure (3.24) shows a quarter five spot example with a refined/adaptive mesh that will later be used in this thesis in Chapter 4. The mesh here has been set to adapt to the water saturation. Figure (3.24) shows: (a) is the initial mesh before any adaptivity; (b) the final mesh after adapting to the water front from the water injection well on the top right corner. As can be seen in Figure (3.24), the mesh is refined all around the water front and is coarsened everywhere else to save computational time.

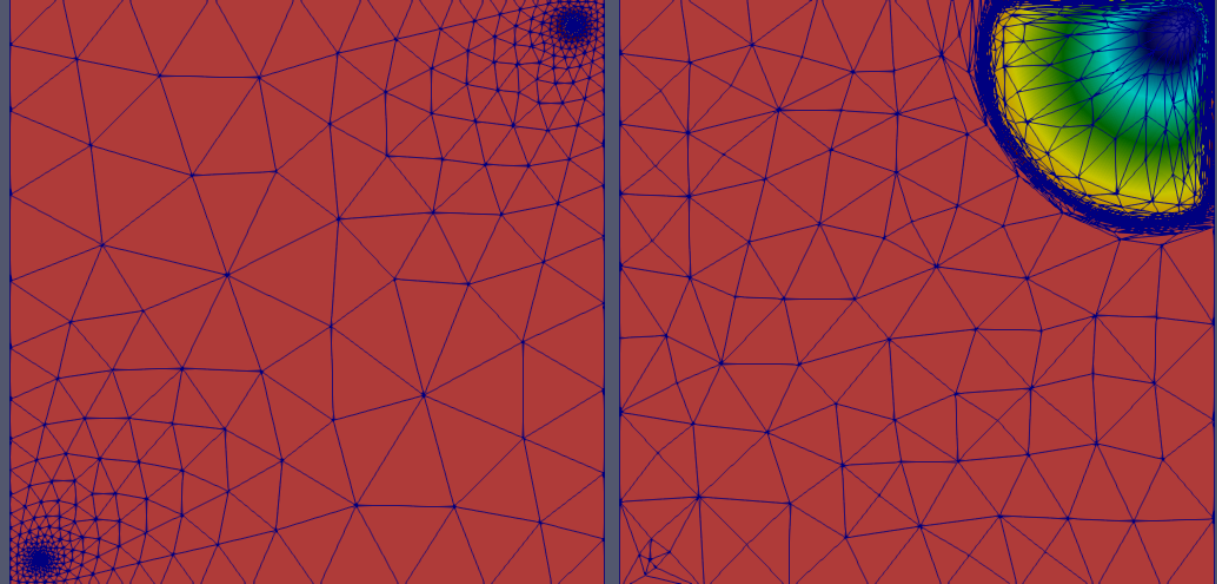


Figure (3.24) Mesh adaptivity example a) initial mesh before adaptivity b) final mesh after adaptivity

3.3.5 ParaView (Post Processor)

ParaView is an open source post processor that is used as a multi-platform data analysis and visualization application. ParaView allows for quick build visualization to analyze data using quantitative and qualitative techniques. Data can be explored in both 2D (vertical or horizontal planes) and 3D dimensions (surface/volumes; isosurfaces; streamlines etc.). It can also export data into Excel files for further analysis and manipulation. The software is developed by KITWARE and is available for Windows, Mac and Linux (KITWARE, 2017). In this thesis ParaView version 5.0.1 was run on an Ubuntu 16.04 LTS system.

ParaView uses the VTU output files as generated by IC-FERST. All information linked with the simulations can be observed – from the initial conditions, fluid and rock properties to the calculated parameters such as phase pressures, saturations, and velocities. The mesh can also be seen step by step, so mesh adaptivity can also be viewed; vertical or horizontal slices/planes can be generated within any part of the domain and display any property of interest. Lastly any point or line can be specified within the domain at which simulation results can be extracted and exported to spreadsheets and analyzed further. Figure (3.25) shows a screenshot of the ParaView user interface along with a 5 spot 5 layers scenario geometry mesh that will be used later on in Chapter 4.

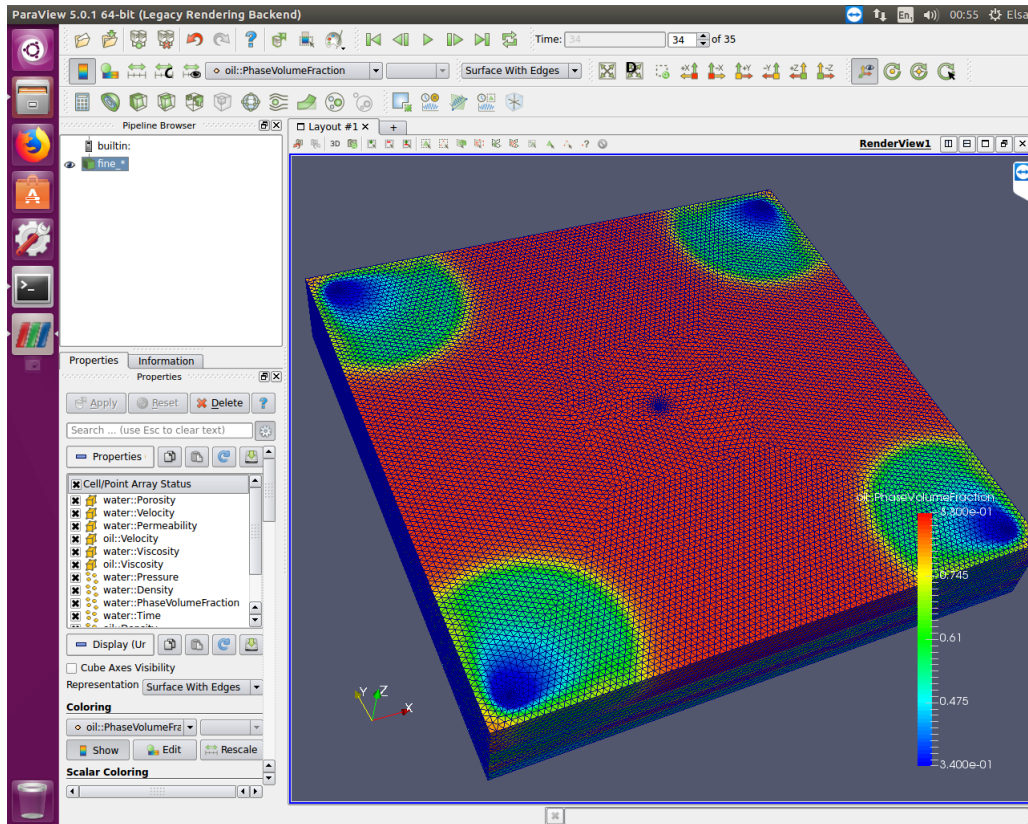


Figure (3.25): ParaView user interface visualizing in 3D the phase volume fraction of oil

3.3.6 Summary of IC-FERST versus ECLIPSE

Table (3-1) summarizes the main features difference between IC-FERST and ECLIPSE.

Table (3-1): Summary of IC-FERST versus ECLIPSE

	IC-FERST	ECLIPSE
Mesh Type	Unstructured Tetrahedral	Structured Hexahedral
Numerical Method	CVFEM	FDM
License	Opensource	Prepaid License
Units	SI units	Field units
Pre-processor	Separate package	Built-in package
Post-processor	Separate package	Built-in package
Geostatistics	Separate package	Built-in package

Runtime	Slow	Fast
Formation Volume Factor and Dissolved Gas Oil Ratio	Does not consider both	Considers both
User friendly	Hard to learn/use and does not have a full user manual	Easy to learn/use
Density and viscosity a function of pressure	No	Yes
Mesh Adaptivity	Yes	No
Ability to edit and add features	Yes	No

3.4 Geostatistics

Geostatistics has been defined as the study of phenomena that vary in space and/or time (Deutsch, 2002). It is also regarded as a collection of numerical techniques that deal with the characterization of spatial attributes, employing primarily random models in a manner similar to the way in which time series analysis characterizes temporal data (Olea, 2012). To some researchers Geostatistics also offers a way of describing the spatial continuity of natural phenomena and provides adaptations of classical regression techniques to take advantage of this continuity (Isaaks and Srivastava, 1989).

3.4.1 Semi (Variogram)

The Semi-Variogram characterizes the spatial continuity or roughness of a data set. Analysis of a variogram consists of two parts, the experimental variogram and the variogram model. The experimental variogram is defined as half of the average squared difference between two attribute z-values approximately separated by vector h specifying a separation distance and direction. The variogram model is fitted to the data using a set of mathematical functions that describe the spatial relationship. The best model is chosen by matching the shape of the experimental variogram curve to the shape of the mathematical function (Remy, 2005).

The mathematical definition of the variogram is:

$$\gamma(\Delta x, \Delta y) = \frac{1}{2} \varepsilon \{ [Z(x + \Delta x, y + \Delta y) - Z(x, y)]^2 \}$$

Where:

$Z(x, y)$ is the value of the variable of interest at location (x, y)

$\varepsilon[\]$ is the statistical expectation operator

$\gamma(\)$ is a function of the separation between points $(\Delta x, \Delta y)$

The vector h specifying the separation distance and direction is specified in 3D by defining a 3D search ellipsoid. To specify the 3D search ellipsoid 3 angles, have to be specified and 3 ranges. These angles and ranges are better described by Figure (3.26).

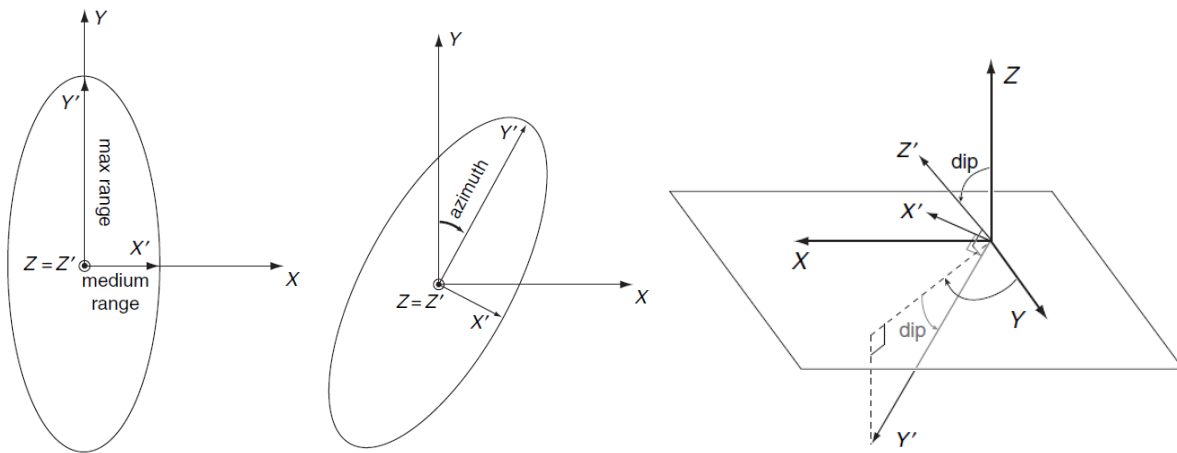


Figure (3.26): 3D search ellipsoid 3 angles explanation (Journal and Deutsch, 1993)

The first angle is traditionally called the *azimuth* and it rotates the Y axis in the horizontal plane and is measured in clockwise degrees. The second angle is called the *dip* angle and it rotates the principle direction from the horizontal and is measured from the horizontal in negative degrees. The third angle is called the *plunge* or *rake angle* and it leaves the principle direction unchanged, it rotates the two directions orthogonal to the principle direction in a clockwise direction. The anisotropy factors are the ranges in the minor directions (Journal and Deutsch, 1993).

Other factors that needs to be defined to define a Semi-Variogram are the Lag distance, Lag tolerance, azimuth tolerance and the bandwidth. Figure (3.27) explains these parameters.

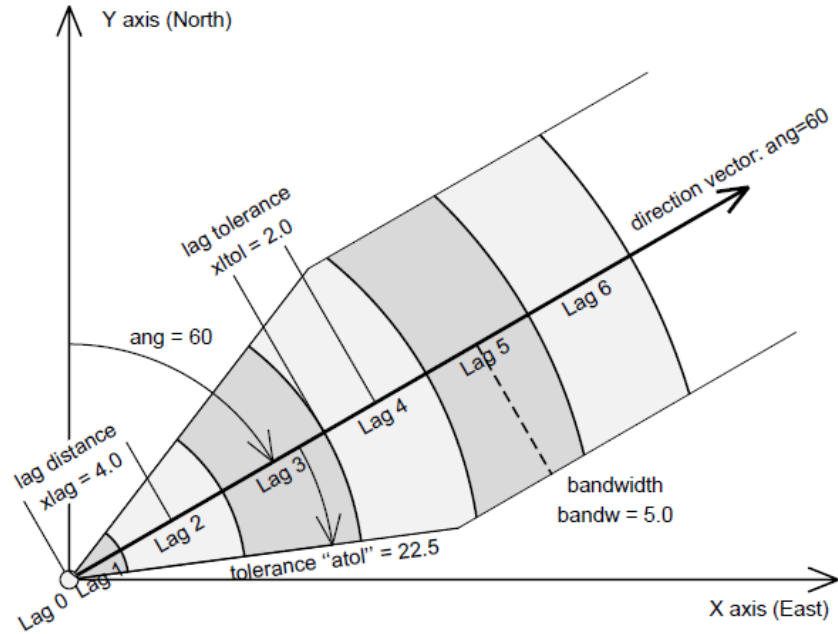


Figure (3.27): Lag tolerance, azimuth tolerance and the bandwidth explanation (Journel and Deutsch, 1993)

To specify the separation vector h it is required to define a lag distance, the lag is defined as the separation distance between to Z variables. Because most of the Z variables used in geostatistics are irregularly distributed, it is not expected to find many pairs of Z data values separated by exactly the lag distance specified. So, a lag tolerance must be introduced to account for any data point within this range. For the same reason lag tolerance was introduced, also the azimuth angle tolerance was introduced, and to avoid the azimuth angle tolerance tending to 360^0 the bandwidth parameter is introduced. The azimuth angle is measured clockwise from North; the angle tolerance (half window) is restricted once the deviation from the direction vector exceeds the bandwidth (Journel and Deutsch, 1993).

3.4.1.1 Characteristics of a Semi-Variogram

Every Semi-Variogram is characterized by 3 main parameters; these are the Sill, Range, and Nugget. These parameters are better described by Figure (3.28).

The Sill is the Semi-Variogram/Semi-Variance value at which the variogram values off to 1. The sill is sometimes used to refer to the amplitude of a certain component of the Semi-Variogram. In Figure (3.28) the sill could refer to the difference (0.8) between the nugget (0.2) and the overall sill (1) or referred to as the overall sill (1).

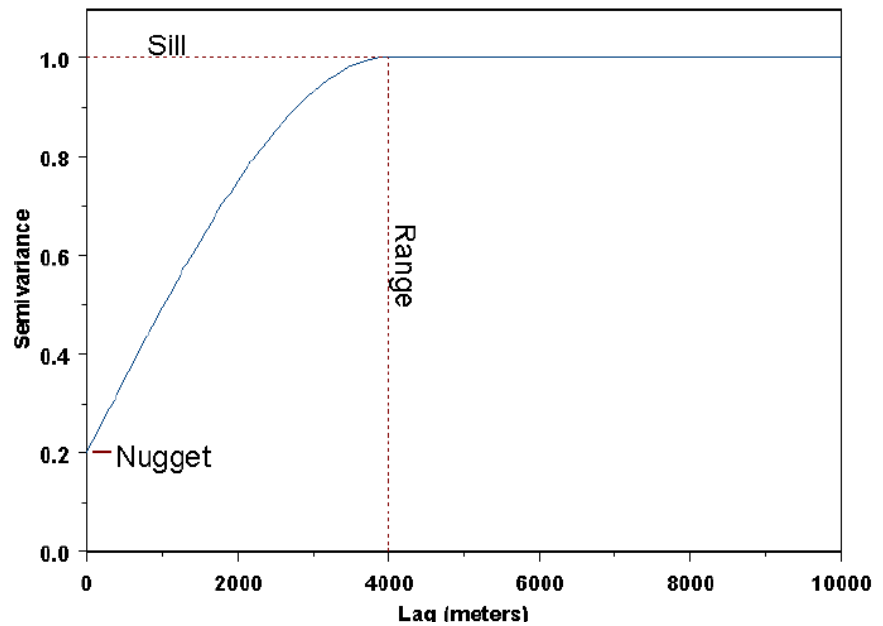


Figure (3.28): Semi-variogram example (Nicolas Remy, 2009)

The range is defined as the lag distance at which the Semi-Variogram reaches the sill value, beyond this value there is no more correlation between the Z values.

In theory the Semi-Variogram value at the origin should be zero, if this value is not zero then this value is referred to as the nugget. The nugget represents variability at distances smaller than the typical sample spacing, including measurement error.

3.4.1.2 Semi-Variograms Models

When variogram models are combined with a nugget effect, there are many possible variogram models;. the most common models that are most of the time adequate are the linear, exponential, and the spherical models and are shown in Figure (3.29).

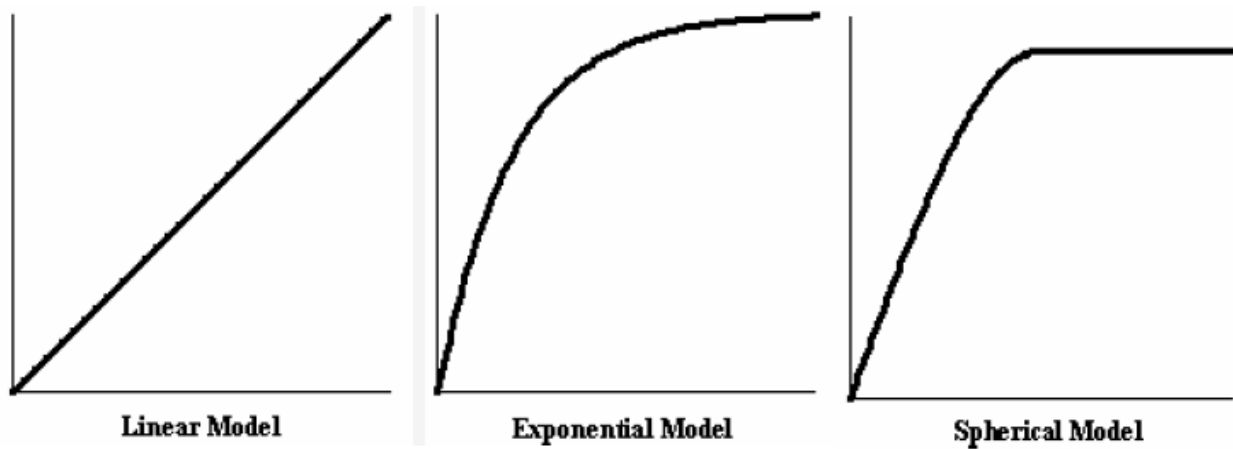


Figure (3.29): Different variogram models example (Remy et al., 2009)

The linear model is used when the variogram never levels out, the exponential model is used when the variogram is curvy and levels out, lastly the spherical model is used when the variogram starts out straight, then bends over sharply and levels out (Remy et al., 2009).

3.4.2 Geostatistical Software (SGems)

Almost all petroleum reservoirs are heterogeneous, that is they do not have constant rock properties such as porosity and permeability along all the reservoir, or along a complete geological layer. IC-FERST does not have any population means to distribute rock properties along the reservoir, it only allows allocation using volume IDs or based on X,Y,Z locations. To be able to model any heterogeneous formation it is crucial to capture these heterogeneities, for this reason it is important to use a geostatistical software, to allow definition of properties (porosity and permeability) in each cell on the computational domain of IC-FERST.

The Geostatistical Software Library GSLIB (Deutsch and Journel, 1998) is the most widely used and one of the first geostatistical libraries. GSLIB was first a collection of geostatistical programs developed by students at Stanford University. GSLIB was inspired by Clayton Deutsch and Andre Journel during 1990-1992. GSLIB original codes were rewritten and new programs were added in the second edition in march 1997 (Deutsch and Journel, 1998).

GSLIB originally was only run on FORTRAN, WinGslib is an open source toolbox written for windows that provides a front-end to all the GSLIB programs. WinGslib does not provide a user friendly interface, so a new cross-platform software for geostatistics that retains most of the

libraries and advantages of GSLIB called the Stanford Geostatistical Modelling Software (S-Gems) was developed by researchers in Stanford University and its sources was made available to everyone (Remy et al., 2009). S-Gems provides classical geostatistics algorithms such as:

- Kriging
- Indicator Kriging
- Cokriging
- SGS
- SIS

The other main reason it is crucial to use a Geostatistical software such as S-Gems is to help with the limited property information from specific wells either from cores of well logs, to be “upscaled” in the whole domain.

S-Gems takes its input as a notepad file or any word processor file that has an extension of .dat. in this file first you specify the headers of each column, and the number of columns, then the values in the columns. Wells names are entered along with the X Y coordinates of the well and the depth of the corresponding input data. The data entered could be continuous data such as porosity or permeability, or categorical such as rock types or facies. Figure (3.30) shows a sample of the S-Gems input data file and Figure (3.31) shows a flow chart showing the steps used to setup a SGS for continuous variables and a SIS for categorical variables.

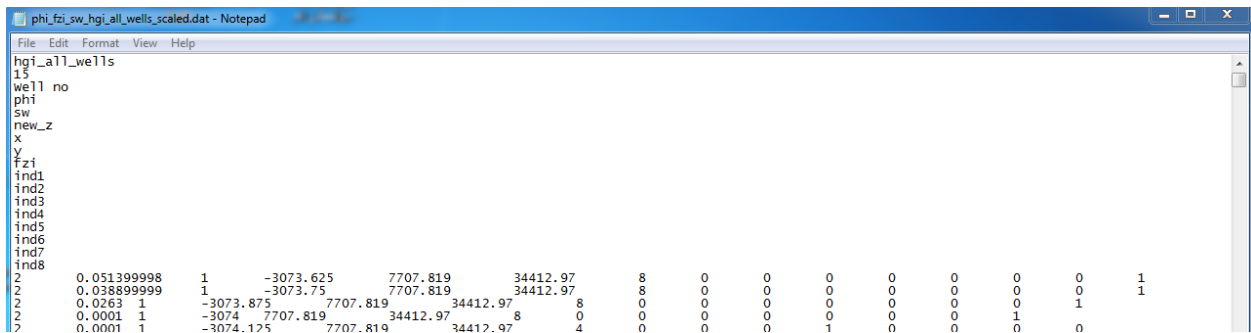


Figure (3.30): Sample of S-Gems input data file

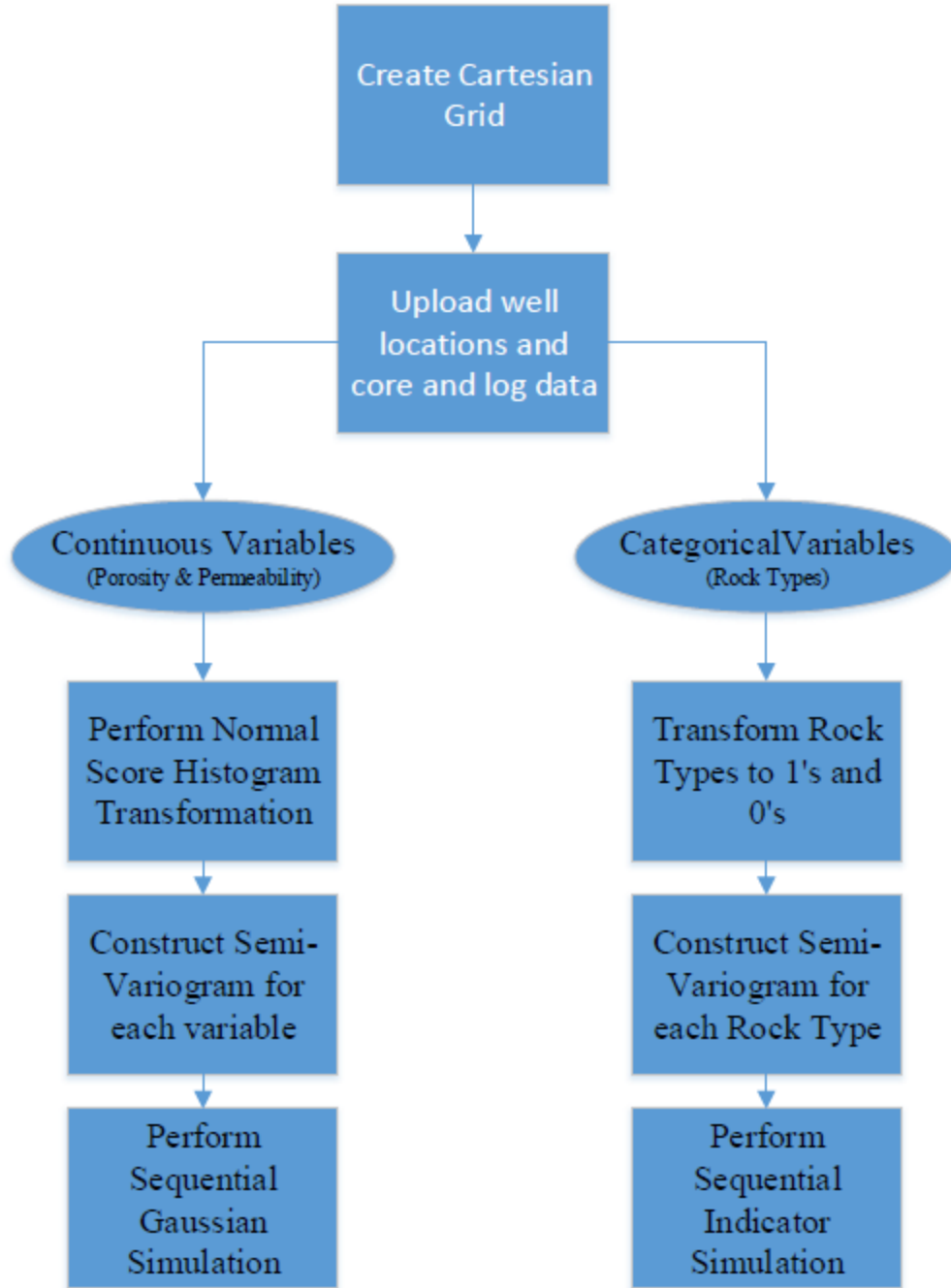


Figure (3.31): S-Gems Flowchart

The first step is to setup a grid in the (X,Y,Z) coordinate system and allocate the given data in the cells of the grid. Unfortunately S-Gems only works with structured grids, so a conversion is later needed to transfer the output to the IC-FERST unstructured mesh, as seen later in section 3.5.4. The number of X,Y and Z cells is entered along with the size of each cell, depending on the level

of accuracy wanted. Figure (3.32) shows S-Gems user interface and a sample of a cartesian grid with porosity values entered from cores in various wells.

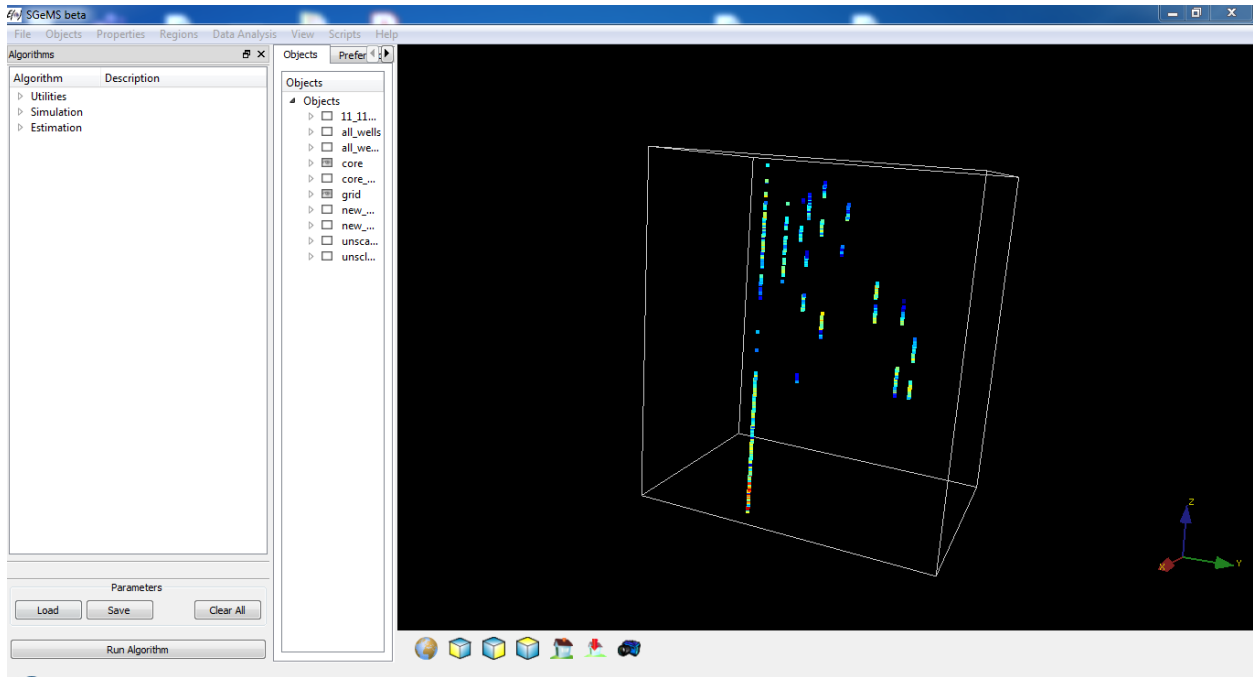


Figure (3.32): S-Gems after data entry

3.4.2.1 Histograms

S-Gems provides some basic data analysis displays such as Histograms, QQ/PP-plot, Scatter-plot and Variograms. First the continuous data should be previewed on a histogram to make sure that it is normally distributed to perform SGS, because the SGS algorithm assumes that the variable is Gaussian. Unfortunately, most Earth sciences data do not present symmetric Gaussian histograms, hence Normal Score Histogram Transformation is needed. S-Gems comes with an algorithm called TRANS that allows the user to transform any histogram of a continuous attribute into a Gaussian histogram (Remy et al., 2009).

3.4.2.2 Sequential Gaussian Simulation (SGS)

To perform SGS a semi-variogram of the simulated variable is required. The semi-variogram measures the average dissimilarity between two variables at two different locations. To create a semi-variogram in S-Gems first you have to specify the property, then the number of lags, lag separation, lag tolerance, number of directions, azimuth angle, dip angle, tolerance in angle, and

lastly the bandwidth. S-Gems creates all the semi-variograms in the number of directions specified. Three directions are usually used, these directions are horizontal semi-variograms with an azimuth angle of 45 and dip angle of 0, an omni directional horizontal semi-variogram that has a tolerance of 180 and big bandwidth to capture all the data, and lastly a vertical semi-variogram with a dip angle of 90. Figure (3.33) shows a sample of these 3 standard semi-variograms outputted from S-Gems.

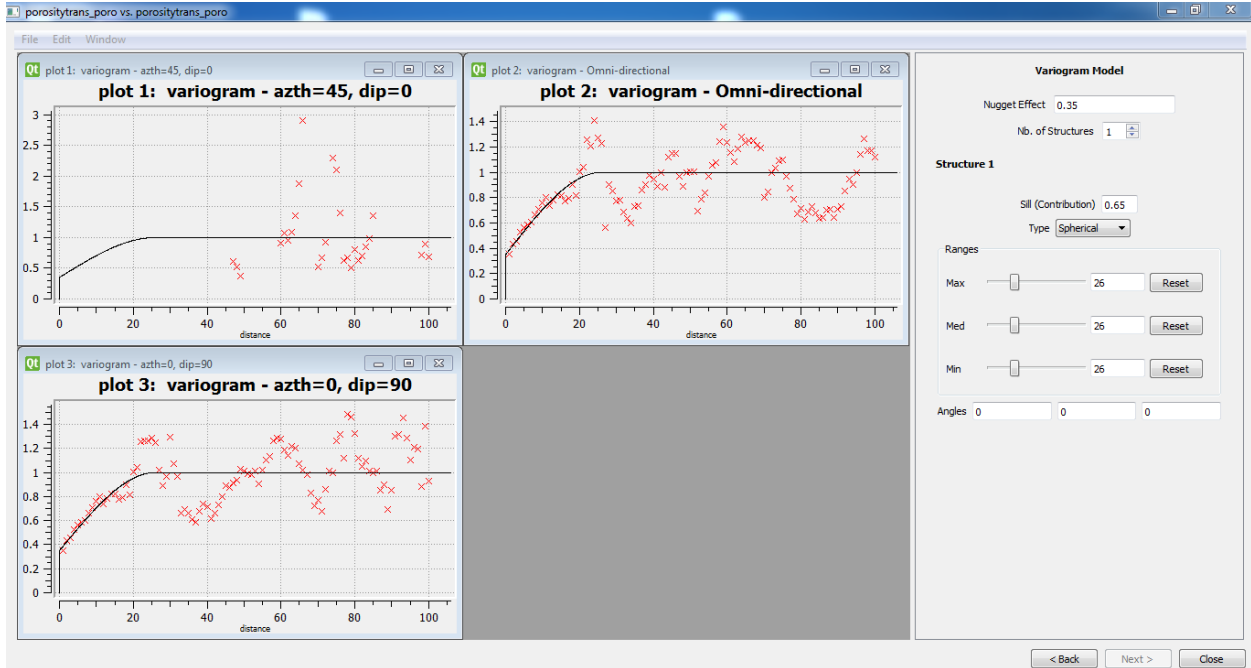


Figure (3.33): Semi-variograms sample from S-GEMS

Now the SGS algorithm can finally be run by first selecting the simulation grid then the variable that will be simulated is selected along with its histogram, then the search ellipsoid ranges and angles is set, finally the saved semi-variogram model is selected. S-Gems automatically does the upscaling for the values entered from the wells to be allocated to the simulation grid. After the algorithm is done all the cells in the grid have now assigned values.

3.4.2.3 Sequential Indicator Simulation (SIS)

Doing a SIS for a categorical parameter such as rock types is very similar to running a SGS except that a small change in the input is required. The categorical variable should be transformed to 1 and 0, meaning that if this cell has this rock type, then it should display 1 and if not, it should be 0

as shown in Figure (3.30). This process is done to every rock type. Unfortunately S-Gems does not have a built-in function that does that, so a MATLAB categorical code was written to do that automatically. In this case a separate semi-variogram is required for each rock type. Then all the steps are the same. Figure (3.34) shows a sample of a porosity data after being populated all over the grid in S-Gems.

S-Gems output the populated variables in a CSV file that contains a value for each grid block in the sequence from X,Y then Z respectively. The output does not have the X,Y and Z coordinates assigned to each value, instead the values are ordered starting from X then Y then Z. Each output variable gets a separate output CSV file, the MATLAB population code is then used to assign the X,Y and Z coordinates as mentioned later in section 3.5.4.

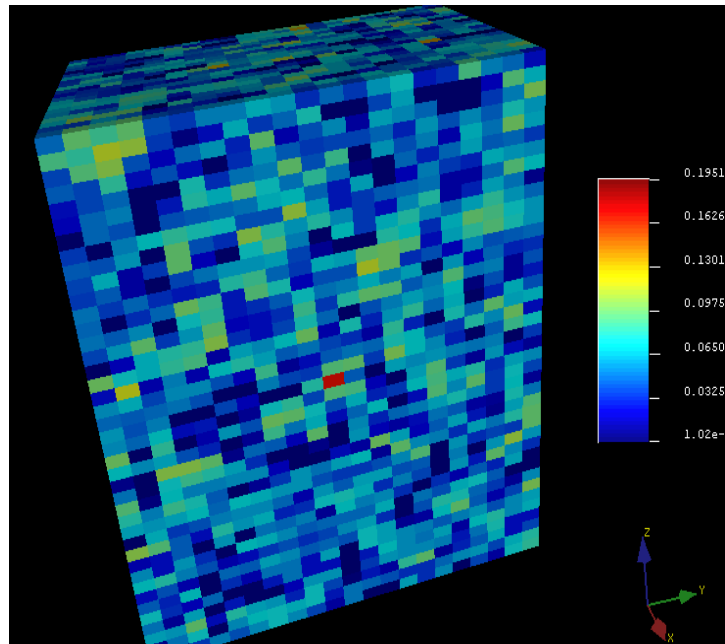


Figure (3.34): Sequential Gaussian Simulation output from S-GEMS

3.5 Reservoir Characterization (Rock-Typing)

Reservoir characterization is the process of building a petrophysical and geological model for a reservoir. Rock typing is a method of reservoir characterization that models the reservoir geologically and hydraulically, it subdivides the pay zone into layers for reservoir simulation. Rock typing can be defined as the unit of rocks deposited under the same conditions resulting in similar porosity-permeability relationship. The ultimate goal of rock typing is to predict the permeability in the un-cored wells in heterogeneous reservoirs (Izadi and Ghalambor, 2013).

If a reservoir is mostly homogeneous the process of rock typing is not needed; a simple porosity-permeability plot with a simple fitting application will do the trick. To check the degree of heterogeneity of a reservoir 3 techniques can be used, these techniques are:

- Simple R²
- Dykstra-Parson
- Lorenz Coefficient

(a) Simple R²

The first is simply plotting a semi-log permeability porosity plot and getting the best fit R². R-squared is defined as the coefficient of determination and is a statistical measure of how close the data is to the fitted regression line. if the R² is greater than 90% then this correlation can be used in the un-cored wells.

(b) Dykstra-Parson

The second technique used to detect reservoir heterogeneity is the Dykstra-Parsons method (Dykstra and Parsons, 1950), Dykstra and Parson introduced the concept of permeability variation coefficient V. To get the V coefficient all core samples are arranged in decreasing permeability order, the percentage of thickness is calculated for each sample. Permeability vs percentage of thickness is plotted on a log-probability graph paper and a best fit straight line is drawn through the points. The V coefficient is calculated using equation (3-15):

$$V = \frac{K_{50} - K_{84.1}}{K_{50}} \quad (3-15)$$

These Ks are the permeability to the corresponding percentage. As the V coefficient increases toward one this indicates that the reservoir is being more heterogeneous.

(c) Lorenz Coefficient

The third technique used to detect reservoir heterogeneity is the Lorenz coefficient method (Schmalz and Rahme, 1950), Schmalz and Rahme introduced a single parameter called Lorenz coefficient L to describe the degree of heterogeneity. This coefficient varies between zero and one, zero is for a homogeneous reservoir and one is for a completely heterogenous reservoir. To get the Lorenz coefficient just like the Dykstra-Parson technique all permeability values are arranged in descending order, then the cumulative volume and permeability capacities are calculated and

normalized. A plot of the normalized cumulative permeability capacity vs the normalized cumulative volume capacity on a cartesian scale is drawn. A unit slope straight line from the origin is also drawn, and the area above this line and below this line is calculated. Figure (3.35) shows a sample of a Lorenz plot. L is finally calculated using the equation (3-16) :

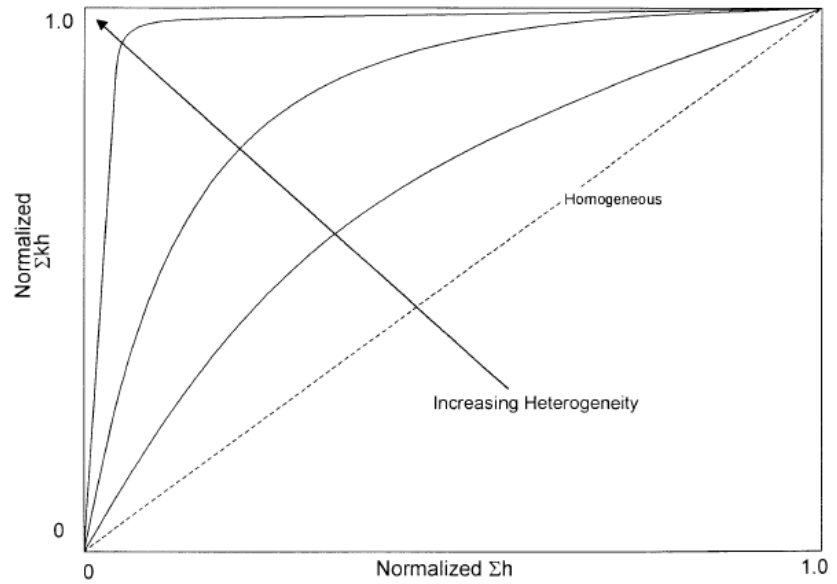


Figure (3.35): Lorenz plot example (Ahmed, 2001a)

$$L = \frac{\text{Area above the straight line}}{\text{Area below the straight line}} \quad (3-16)$$

3.5.1 Amaeful Technique

The most widely acceptable rock typing methodology in the oil and gas industry is the Amaefule technique (Amaefule et al., 1993). Amaefule modified the Kozeny-Carmen correlation and introduced the concept of RQI and FZI to enhance its capability to capture the various reservoir flow behaviors. To get the FZI equations (3-17), (3-18), and (3-19) are used.

$$RQI = 0.0314 \sqrt{\frac{k}{\phi}} \quad (3-17)$$

$$\phi_z = \frac{\phi}{1 - \phi} \quad (3-18)$$

$$FZI = \frac{RQI}{\phi_z} \quad (3-19)$$

RQI is plotted on a log-log scale vs ϕ_z , values with similar FZI will lie on a straight line with a unit slope, the FZI value can be determined from the intercept of the unit slope straight line at

$\phi_z=1$. Another more reliable and easy clustering technique called the Discrete Rock Type (DRT) can be used using equation (3-20) :

$$DRT = \text{round}(2 \times \ln(FZI) + 10.6) \quad (3-20)$$

3.5.2 Relative Permeability

In the absence of SCAL, two phase relative permeability can be calculated from resistivity data in porous media from logs using the model reported by (Li, 2008). This model correlates K_{rw} with S_w and resistivity index I as follows:

$$K_{rw} = S_w^* \frac{1}{I_r} \quad (3-21)$$

$$S_w^* = \frac{S_w - S_{wr}}{1 - S_{wr}} \quad (3-22)$$

$$I_r = \frac{R_t}{R_o} \quad (3-23)$$

Where:

- K_{rw} is the relative permeability of water
- S_w is the water saturation
- S_{wr} is the irreducible water saturation
- R_o is the formation resistivity when saturated 100% by water
- R_t is the formation resistivity

According to (Purcell, 1949) K_{rw} can also be expressed as:

$$K_{rw} = (S_w^*)^{\frac{2+\lambda}{\lambda}} \quad (3-24)$$

λ is the pore size distribution index and it can be derived from equation (3-21) and (3-24). After deriving the λ and the K_{rw} , Brook-Corey model (Brooks and Corey, 1966) can be used to obtain the K_{ro} using equation (3-25) :

$$K_{ro} = (1 - S_w^*)^2 \left(1 - (S_w^*)^{\frac{2+\lambda}{\lambda}} \right) \quad (3-25)$$

This process is repeated for each rock type to get the two-phase relative permeability for each rock type. This process is shown later in section 5.4.

3.5.3 New Rock Characterization MATLAB Technique Code (BRCC)

To make the process of rock characterization easier specially in the clustering stage the MATLAB BRCC was written to do all the above mentioned steps immediately by just taking a spreadsheet file containing the porosity and permeability values from cores. Figure (3.36) shows a flowchart showing the BRCC algorithm.

The BRCC first plots a porosity vs permeability plot on a semi log plot and gets the R^2 , then it does all the steps needed to get the Dykstra K coefficient and the Lorenz L coefficient and plots both graphs and indicated whether the reservoir is a homogeneous or a heterogeneous one.

The code then calculates the RQI, ϕ_z , FZI, and DRT and gets the best fit of each rock type with its R^2 , the beauty of this code is that it re-clusters rock types according to the R^2 , to ensure the best fitting regression. If a certain rock type has few core values compared to the total core number taken from the reservoir and its R^2 is high it combines this rock type with the previous rock type to try and minimize the rock typing numbers in the reservoir to minimize the computational power needed later in the simulation. On the other hand if a rock type has a low R^2 and has many core values compared to the total core number taken from the reservoir it splits this rock type into two rock types; it keeps doing this process until it gets the highest R^2 for all the rock types with the minimum number of rock types.

At the end the BRCC will output an equation that is a function of porosity and calculates the permeability for each rock type. Outputs from the BRCC will later be shown in the Data Preparation section.

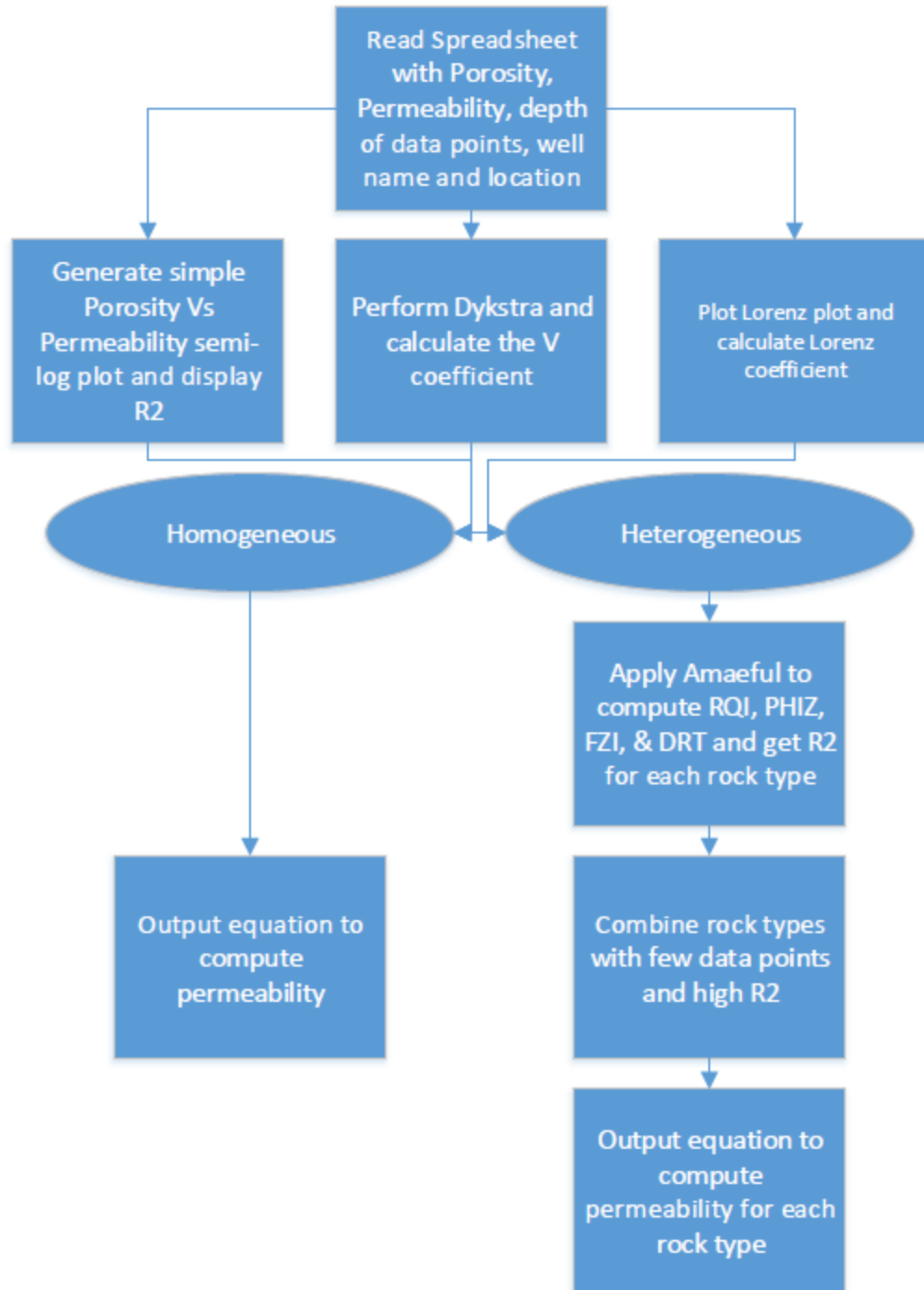


Figure (3.36): Balaha Rock Characterization Code (BRCC) flowchart

3.5.4 S-Gems and MATLAB to Diamond

As mentioned earlier S-Gems outputs a CSV file containing the porosity and the rock type for each grid block ordered firstly by X, then Y, then Z, but does not write the corresponding coordinates

next to each value. Also, BRCC gives out a number of equations to calculate the permeability as a function of porosity for each rock type. Diamond does not take properties using coordinates, it only uses location or predefined volumes. Thus, to integrate S-Gems output with BRCC output and make them suitable for Diamond another MATLAB population code was written.

The MATLAB population code takes the S-Gems output and the rock type equations from the BRCC as inputs. First the MATLAB population code computes the permeability in each grid by checking the rock type number in the corresponding grid block and apply its equation using the porosity of this grid block. Then by using X,Y and Z increments used in S-Gems to build the cartesian grid, it allocates X,Y, and Z to each grid block by location in meters. Last the MATLAB population code outputs a separate CSV file for the porosity, permeability and rock type using the X,Y and Z locations.

The two-phase relative permeability could also be entered to the MATLAB population code and the code will assign for each rock type its relative permeability variables, these variables are the variables used by the Brooks and Corey function as mentioned in Section 3.3.2.

Finally to make Diamond read the outputted files from MATLAB population code a python script was written into Diamond to make Diamond read the CSV file of each property. The script loops through the CSV file and checks if the X,Y and Z values corresponding to the location from S-Gems are between the X,Y, and Z values of the unstructured grid block that Diamond is now assigning properties in, the value is assigned to the block, if not it keeps looping through the CSV file until it finds the value. Figure (3.37) shows the python script in Diamond.

This process is done for every grid block in the mesh generated by Trelis, so if for example we have a mesh that contains 100,000 elements, and the S-Gems model was created with another 100,000 grids, so the Python script will make Diamond loop 100,000 times (Trelis mesh) each time it searches for the value in the 100,000 (S-Gems grid) values from the CSV file, this means it runs 10 billion readings to completely populate one property only.

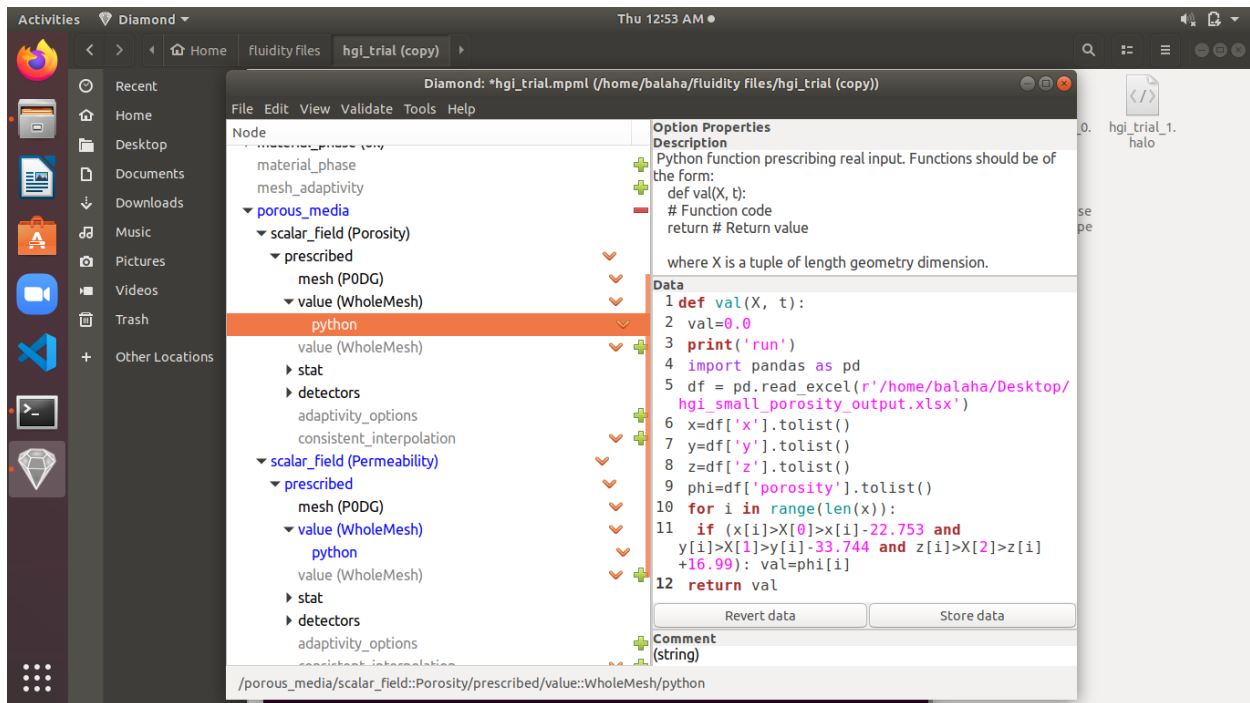


Figure (3.37): Python script written into Diamond to make Diamond read the CSV files of each property

Chapter 4 Comparison Between IC-FERST and ECLIPSE Simulations for Standard/Benchmark Cases

Brief Summary: This chapter presents and discusses the comparison of IC-FERST against ECLIPSE simulations using three benchmark scenarios. The simulations are carried out using classic production/injection well configurations in the oil industry, and a comparison is subsequently made between the outputs from both software. The outputs considered are the flow rates of water and oil at both injection and production wells, and the phase volume fractions at these points. The run time of each case in each package is also compared. The three cases investigated are: (I) a quarter 5 spot case with one geological layer (homogeneous case); (II) the quarter 5 spot case with five geological layers (heterogeneous case); and (III) lastly a full 5 spot model with also five geological layers. The full description of each case is given and the results and discussion/conclusion are given at the end of each case section. The simulations results from all three cases show the difference between the two software to be ranging between: (I) 2% to 8% for oil production; (II) 14% to 30 % for water production and (III) 1% to/11% for water injection. If it is assumed that ECLIPSE is the more reliable software - due to its longevity and wide commercial implementation, IC-FERST seems to be producing results within acceptable ranges of the ECLIPSE results.

4.1 Case 1: Quarter 5 Spot 1 Layer

A 5 spot water flood scenario is a very well known secondary recovery scenario used in the petroleum industry; it comprises a production well in the middle of the domain, which is surrounded by 4 water injection wells at equal distances from the producer. In a quarter 5 spot scenario, only one quarter of the full 5 spot scenario is considered-with the producer being at one end of the domain and the injector at the other end. Figure (4.1) shows a representation of the quarter 5 spot case.

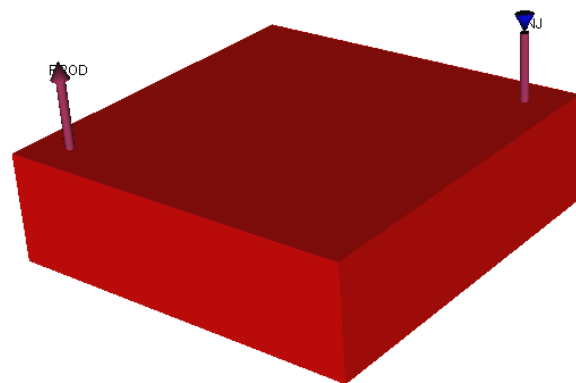


Figure (4.1): Quarter 5 spot 1 layer case representation showing injector and producer well's locations

4.1.1 Case 1 Computational Details

Model dimensions and fluid properties: The model shown in Figure (4.1) is a 250m x 250m x 75m computational domain, initially saturated with 85% oil and 15% water which is the irreducible water saturation. The formation has a connate oil saturation of 25% - this being the amount of oil that cannot be displaced by water; a porosity of 20%, and a permeability of 1000md that is the same in the X,Y and Z direction i.e. the formation is considered homogeneous and isotropic. The relative permeability curves and the capillary pressure curves used are shown in Figure (4.2) (a) and (b) respectively. The wells have a radius of 0.25 m; they are located at 101.25m from the origin (center of the domain) in both the X and Y directions, and they are perforated to a depth of 66.6m. Oil has a density of 784.9 kg.m³ and water a density of 1009.1 kg/m³; oil viscosity is 8.9cp and water viscosity is 0.89cp.

Initial and boundary conditions: Initial pressure in the middle of the reservoir is 4500 psi; the producer is controlled with an outlet pressure of 4000 psi and the injector is controlled with an inlet pressure of 6500 psi. All the sides of the reservoir are considered no flow boundaries with the wells being inlet or outlet points.

Simulation details: The time step chosen for all simulations, in both software, is one day and the simulations are run for 100 days. All these input parameters are summarized in Table (4-1) – with the values used in each software – based on the conversions between the industry standard units (ECLIPSE units) and the international units used in IC-FERST.

Table (4-1): Quarter 5 spot 1 layer case IC-FERST and ECLIPSE inputs parameters

	IC-FERST	ECLIPSE
Model dimensions	250 m x 250 m x 75 m	820.21 ft x 820.21 ft x 246 ft
Mesh quality	Coarse: 14,840 elements Medium: 25,946 elements Fine: 345,048 elements	25_25_5 (3,125 cells) 50_50_10 (25,000 cells) 100_100_20 (200,000 cells)
Well locations (X,Y)	Producer: -101.25 m,-101.25 m Injector:101.25 m,101.25 m	Producer: cell 10,91 Injector: cell 91,10
Well perforation	0-66.6 m	0≈66.6 m
Well radius	0.25 m	0.82 ft

Fluid density	Oil: 784.905 kg/m ³ water: 1009.16 kg/m ³	Oil: 49 lb/ft ³ water: 63 lb/ft ³
Fluid Viscosity	Oil: 8.9E-3 Pa.s Water: 8.9E-4 Pa.s	Oil: 8.9 cp Water: 0.89 cp
Initial reservoir pressure	3.1026E+7 Pa.	4500 psi
Flowing pressures	Inlet: 4.4816E+7 Pa. Outlet: 2.7579E+7 Pa.	Inlet:6500 psi Outlet:4000 psi
Time step	86400 sec	1 day
Porosity	0.2	0.2
Permeability	X=9.869233E-13 m ² Y=9.869233E-13 m ² Z=9.869233E-13 m ²	X=1000 md Y=1000 md Z=1000 md

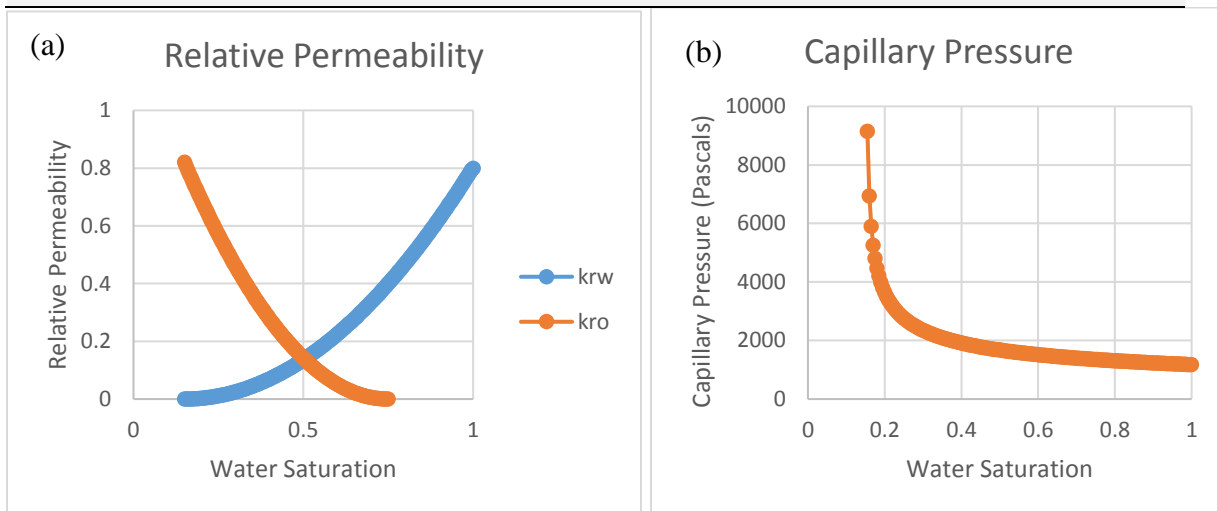


Figure (4.2): Quarter 5 spot 1 layer case a) Relative Permeability b) Capillary Pressure

Different meshes were also tried out in both software to see the effect of refining and coarsening the mesh; it is noted that ECLIPSE uses a structured mesh, whilst IC-FERST is based on unstructured meshes. The number of elements generated by each mesh in each case is also shown in Table (4-1).

Figure (4.3) and Figure (4.4) show screenshots from the different mesh sizes used in ECLIPSE and IC-FERST respectively.

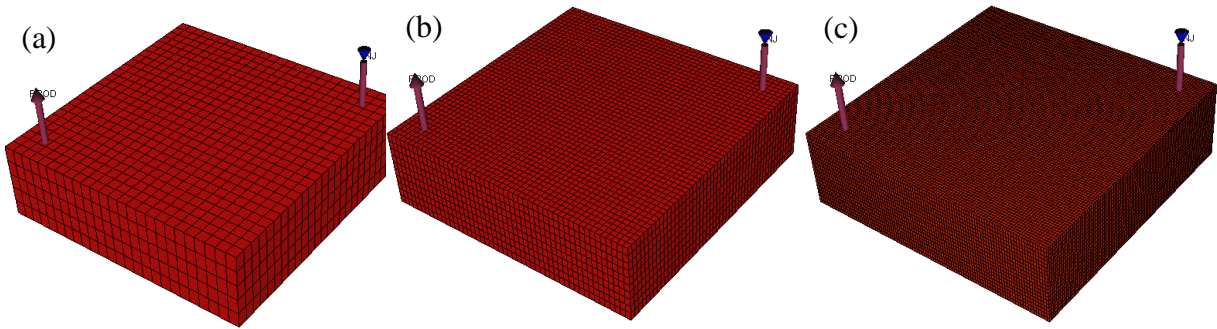


Figure (4.3): Quarter 5 spot 1 layer case ECLIPSE meshes a) coarse (3,125 cells) b) medium (25,000 cells) c) fine (200,000 cells)

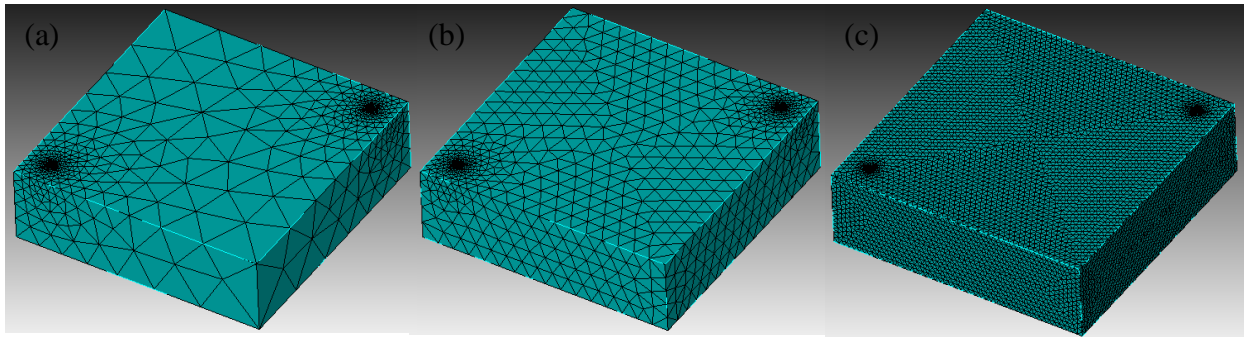


Figure (4.4): Quarter 5 spot 1 layer case IC-FERST meshes a) coarse (14840 elements) b) medium (25,946 elements) c) fine (345,048 elements)

Adaptivity options were set to adapt every time step based on the water saturation, so the mesh will refine itself based on the water saturation front to capture the highest resolution there.

Figure (4.5) shows the mesh at 4 different time steps; (a) at the start of the simulation; (b) after 10 days; (c) after 20 days; and (d) after 30 days; from the images, it can be clearly seen how the mesh gets finer around the water front and coarser elsewhere.

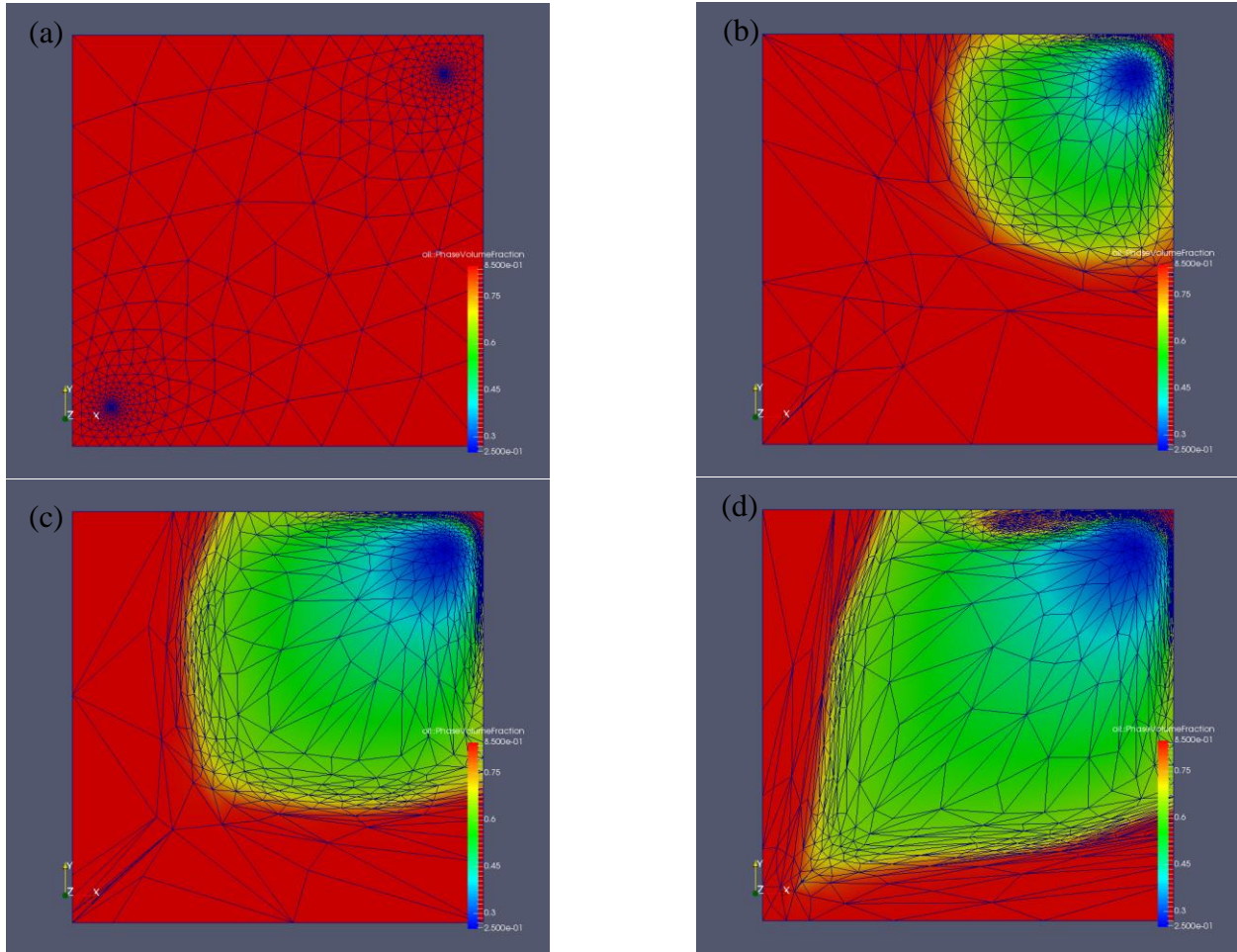


Figure (4.5): IC-FERST adaptive mesh with water saturation at the top plane ($Z=1$) at different times a) 0 days, b) 10 days, c) 20 days, d) 30 days

Case 1 Computational Results and Analysis Table (4-2) shows the different cases that were run with different meshes and options, along with how many processors were used and the time the run took to complete. More simulations were carried out with the ICFESRT software to allow for implementation of the adaptivity options, as well as the parallel processing. ECLIPSE does not allow for mesh adaptivity.

As expected the coarse meshes in both simulators took the least time to complete; the medium meshes took a bit more time whilst the fine meshes took the longest to complete. However, there was a distinct difference between the simulation times between ECLIPSE and IC-FERST. A number of observations are made:

- (a) *ECLIPSE vs IC-FERST simulation run times*: ECLIPSE simulation times are much shorter than the ICFERST ones. This seems to be for all three type of meshes (coarse, medium and fine). For example, a medium mesh ECLIPSE simulation takes only 33 seconds to complete, on a single processor, whilst the corresponding simulation with ICFERST takes ~ 1.30 hours.
- (b) *Parallel processing*: When comparing the simulation times for the ICFERST simulations, it is interesting to see that the simulations with more than one processor result in simulation run times slightly shorter than for a single processor; time taken for the parallel simulations is as expected also much less than the single processor simulations. The results showed that by adding more number of processors, the computational time is decreased by at least 50%. However, this may not always be the case; increasing the number of processors does not always mean a decrease in the computational time, because when the mesh is decomposed into several subdomains, a computational time is also requires to exchange information between the boundaries of the subdomain; thus the optimum number of processors must be figured out by a trial and error method. Using the wrong number of processors will result in a poor decomposition resulting in poor results and slower computational time. This can be seen between the coarse and the coarse parallel case;, by adding 1 processor the time is decreased by 270%. In the medium and the medium parallel case, by adding 2 processors the time is decreased by 246%. Lastly in the fine and fine parallel case, by adding 5 processors the time is only decreased by 60%.
- (c) *Adaptivity within the coarse mesh*: When the adaptivity option is enabled within the IC-FERST simulator, it is interesting to see that the simulation run times for the coarse mesh increase nine-fold; without adaptivity, the coarse mesh simulation run time is approximately one hour, whilst when adaptivity is enabled, the simulation run time is approximately 9 hours. This is due to the fact that the adaptivity option refines the mesh in areas of interest; hence taking more computational time to complete the run.
- (d) *Adaptivity enabled – fine mesh*: When the adaptivity option is enabled in the fine mesh, the simulation run time hardly changes. The simulation run time for a fine mesh is approximately 12 hours, and it remains roughly the same when the adaptivity option is enabled; this implies that the fine mesh was already in an “optimal” resolution.

Table (4-2): Quarter 5 spot 1 layer case IC-FERST and ECLIPSE cases runtime and processors

Software	Case	No. of processors	Number of elements	Run time (H:M:S)
IC-FERST	Coarse	1	14,840	00:54:13
	Coarse parallel	2	14,840	00:14:41
	Coarse with adaptivity	1	N/A	09:00:01
	Medium	1	25,946	01:35:31
	Medium parallel	3	25,946	00:27:41
	Fine	1	345,048	12:03:59
	Fine parallel	6	345,048	07:31:19
	Fine with adaptivity	1	N/A	12:00:06
	ECLIPSE	Coarse	1	3,125
Medium		1	25,000	00:00:33
Fine		1	200,000	00:47:28

A more detailed investigation of the graphical results within IC-FERST simulations are shown in Figure (4.6). Figure (4.6) (a) shows the water injection rates, as predicted by IC-FERST, using the single processor simulations for the three type of meshes (coarse, medium and fine – cases) together with the results when the adaptivity option was enabled for the coarse and fine meshes. Figure (4.6) (b) shows the oil production rates for the same cases as in Figure (4.6) (a). In both graphs it is noticed that when the adaptivity is enabled, the simulations show some oscillations, which happens every time the mesh is adapted. This is very noticeable at the initial stages of the simulations e.g. the first 30 days of a 100 day simulation. To try and solve this problem various adaptivity options have been tried – for example: (I) reduce the frequency of adaptation e.g. allow the mesh to adapt every 5 time steps instead of every time step; (II) adjust the aspect ratio and the minimum and maximum edge of the elements; (III) increase the absolute and relative error values; however, these adjustments did not eliminate the oscillation problem. Considering this oscillation issue, and the fact that the computational time of the adaptivity runs were high, all subsequent simulations with IC-FERST were carried out without adaptivity option.

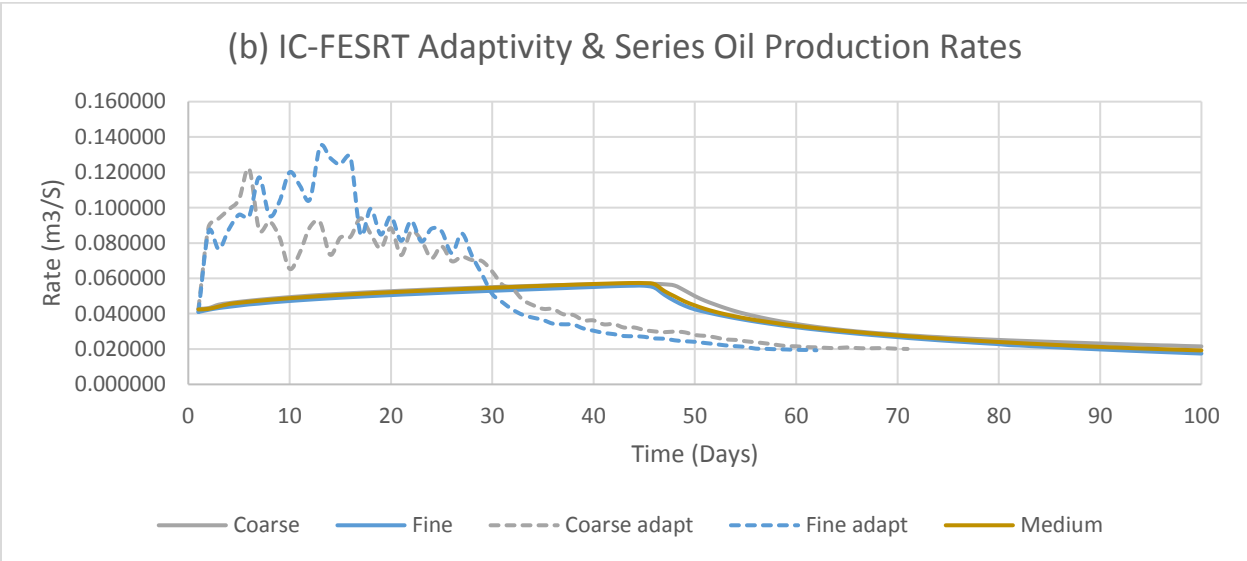
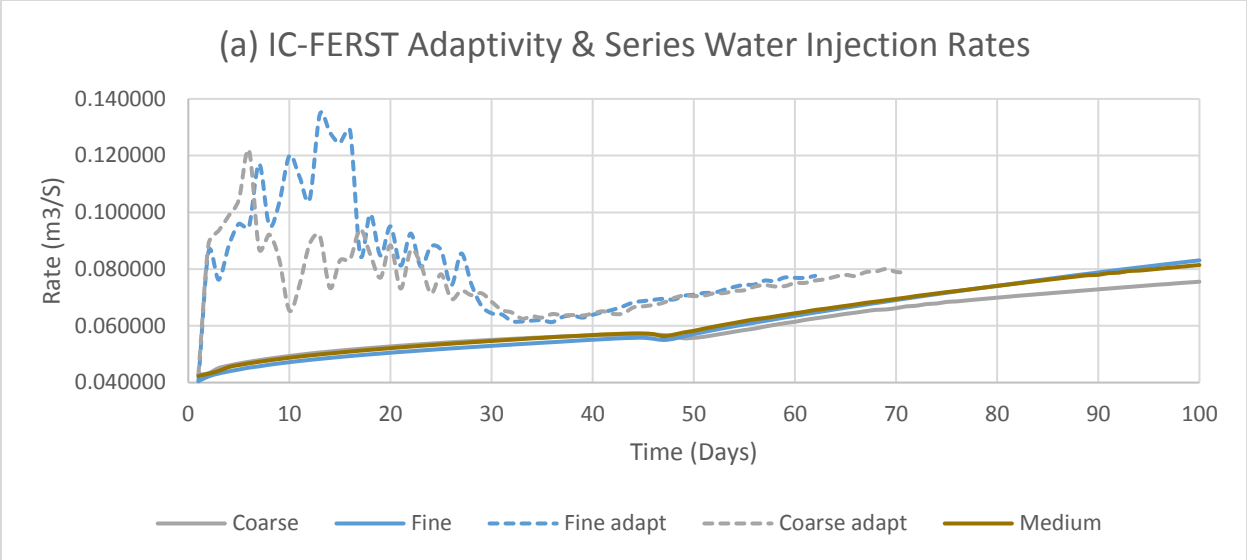


Figure (4.6): Quarter 5 spot 1 layer case IC-FERST Adaptivity vs Non-adaptivity results a) water injection b) oil production

The parallel options already showed a decrease in the computational time. Figure (4.7) shows a comparison of the IC-FERST simulations for the three meshes (coarse medium and fine) with single processor and parallel processors (coarse and fine). Figure (4.7) (a) shows the water injection rates at the injection wells whilst Figure (4.7) (b) shows the oil production rates at the production wells. Looking on both the graphs we can easily tell that the parallel processing option seems to work fine with no oscillations and with results close to the one processor results, along with the fact that it reduces the computational time with a very good factor.

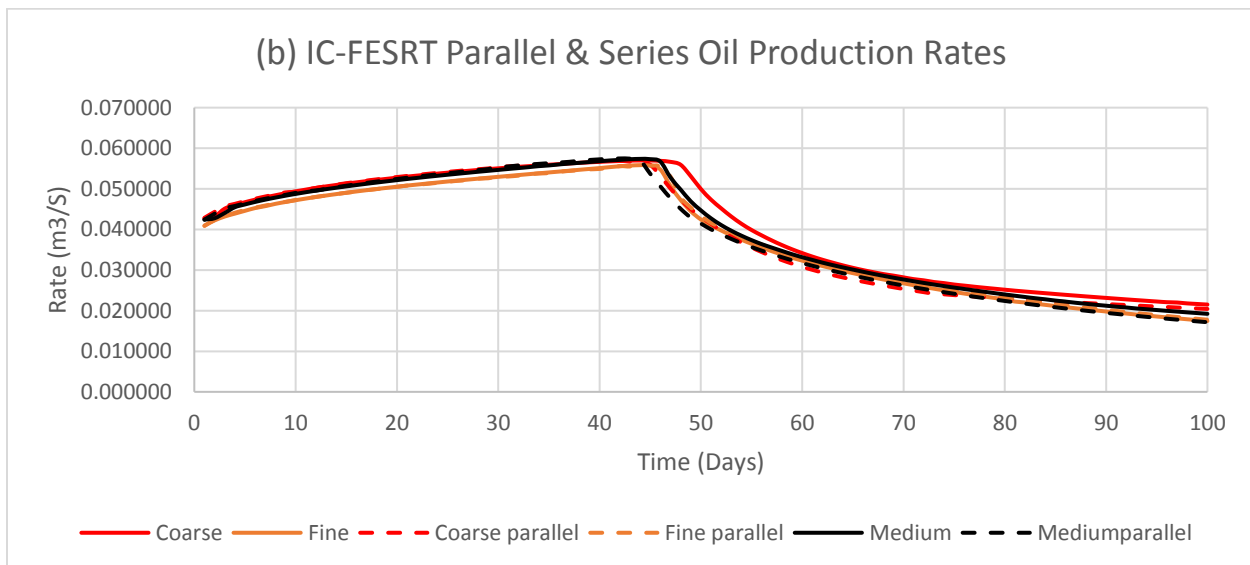
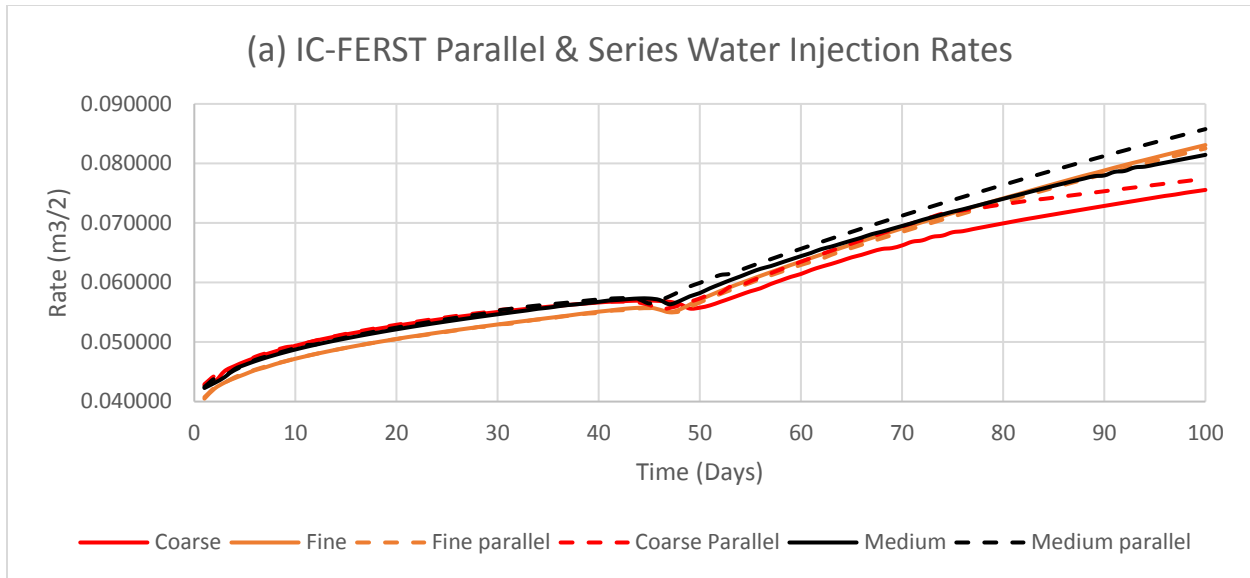


Figure (4.7): Quarter 5 spot 1 layer case IC-FERST Parallel vs Single processor simulation results a) water injection b) oil production rates

Table (4-3) shows a more quantitative comparison between the results shown in Figure (4.7), it shows the percentage difference between the coarse IC-FERST series results and all the other different meshes in series and parallel. It can be seen that the biggest difference between any mesh and its parallel result is 4%; and that is between the coarse and the coarse parallel; all the other meshes showed a very close percentage difference with the maximum difference being 3.5 %

between the medium and medium parallel. The least difference was between the fine and fine parallel with a maximum difference of 1%

Table (4-3): Quarter 5 spot 1 layer IC-FERST parallel and series percentage difference for each mesh with the coarse as a reference

Well	Mesh	Percentage Difference
Water Injection	Coarse parallel	2
	Medium	12
	Medium parallel	8.5
	Fine	4.5
	Fine parallel	4
Oil Production	Coarse parallel	4
	Medium	5.5
	Medium parallel	4.5
	Fine	8
	Fine parallel	7

The final comparison dealt with the results from the two simulators. Figure (4.8) (a) shows the water injection rates from the three parallel processors simulation for the three meshes (coarse, fine and medium) using IC-FERST simulator vs the results from the single processor simulations of ECLIPSE for the three meshes (coarse, fine and medium). Figure (4.8) (b) shows the oil production rates for the same cases, for both software, whilst Figure (4.8) (c) shows the water production rates, again for the same cases. Taking the ECLIPSE fine series run results as a reference, the percentage difference between the IC-FERST runs with different meshes is computed and shown in Table (4-4).

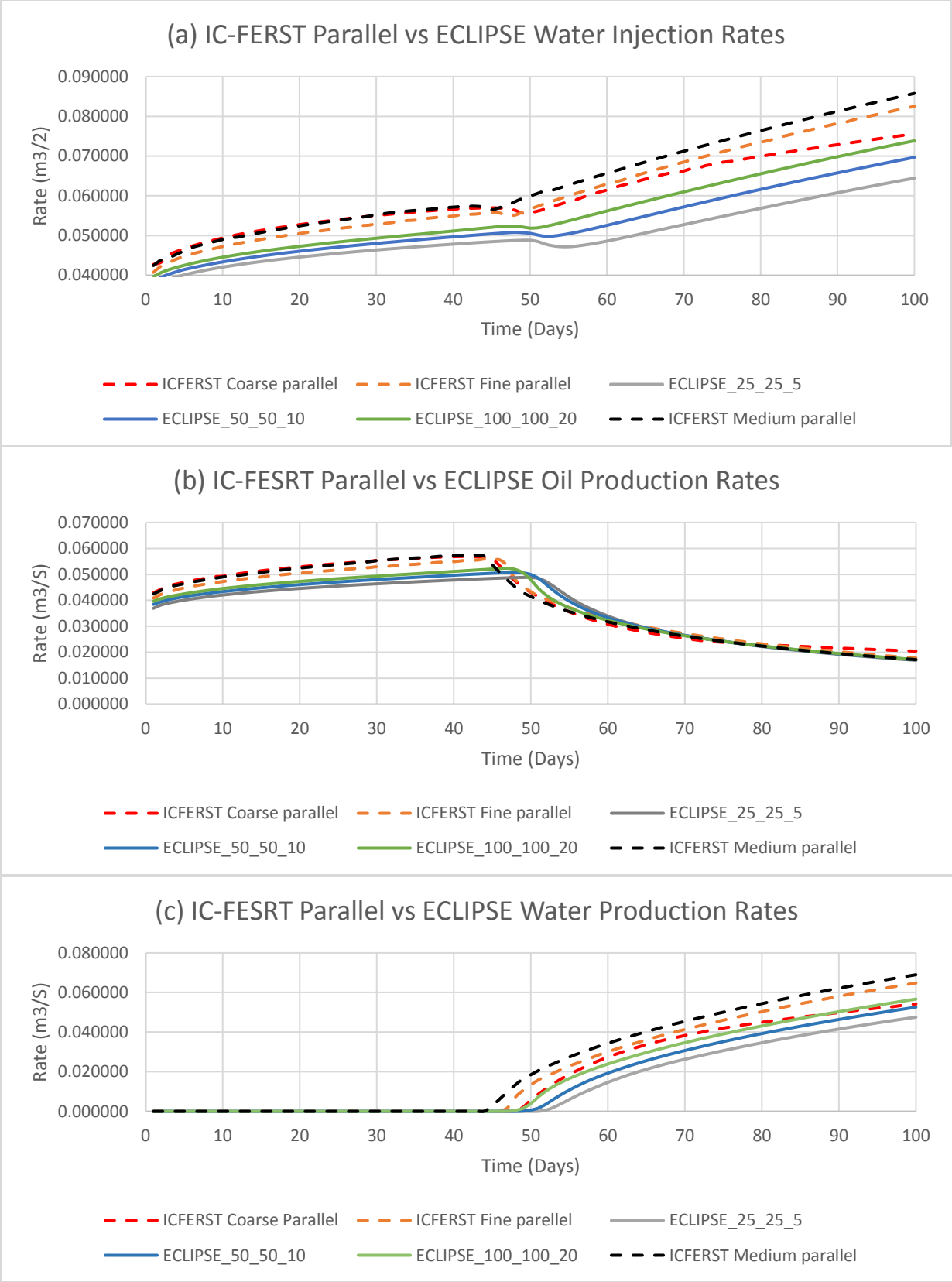


Figure (4.8): Quarter 5 spot 1 layer case IC-FERST Parallel vs ECLIPSE results a) water injection b) oil production c) water production

Looking at Figure (4.8) (a),(b) and (c) and Table (4-4), comparing the IC-FERST and the ECLIPSE results; a number of observations are made:

- (a) Looking at Figure (4.8) (a) and (c) we can tell that the IC-FERST fine run is the closest to ECLIPSE run at the beginning of the simulation (until 45 days), this is when the water breaks through the production well; and the flow rate becomes a two phase flow. After the water breakthrough (after 45 days), it is clear that the IC-FERST coarse run is now the one closest to the ECLIPSE run results.
- (b) Looking at the percentage difference in Table (4-4), where a comparison between IC-FERST run results using different meshes and ECLIPSE fine run results as a reference of comparison; we can firstly see that both the water injection and oil production percentages showed a relatively low percentage of difference (up to 11% for the water injection when medium mesh is considered and 8% for oil production when coarse mesh is considered); the water production gave a higher percentage difference ~30% for medium mesh. Comparing the differences between the meshes, we can see that both the coarse and the fine mesh gave similar percentages for the water production and injection – with the coarse giving a lower percentage; whilst the coarse gave the highest percentage in the oil production case (8%).
- (c) The computational run time of the ECLIPSE simulation and the coarse IC-FERST (single processor in both cases) are very similar (47 minutes vs 54 minutes - Table (4-2)).
- (d) It is interesting to note also that the ICFERST simulation for the coarse mesh, when carried out with only 2 parallel processors (case (II), Table 4.2) leads to a reduced computational time of nearly 223% (computational times reduces to 14 minutes from 54 minutes).

Table (4-4): Quarter 5 spot 1 layer IC-FERST parallel vs ECLIPSE fine series percentage difference for each mesh.

Case	Mesh	Percentage Difference
Water Injection	Coarse	8.5
	Medium	12
	Fine	10
Water Production	Coarse	23
	Medium	30.5
	Fine	23.5
Oil Production	Coarse	8
	Medium	5.5
	Fine	4.5

The above results appear very encouraging regarding the ICFERST simulator. Two more complex cases will be investigated before any conclusion is drawn. However, prior to these, some visualization comparisons are carried out showing the oil volume fractions.

To assess visually how similar (or different) the results from the two simulators are, an initial visualization comparison of the oil phase volume fraction over the whole domain surfaces is carried out. The two cases considered in this comparison are: (I) the fine parallel case of IC-FERST and (II) the fine single processor simulation case using ECLIPSE – as these two cases showed the least difference when looking at the oil production rates earlier; given that we are mostly interested in oil. The comparison is carried out at two different time steps: (I) 50 days and (II) 25 days. The left section of Figure (4.9) shows the oil phase volume fraction at a time step of 50 and 25 days from the IC-FERST simulation, whilst the right section of Figure (4.9) shows the oil phase volume fraction at a time step of 50 and 25 days from the ECLIPSE simulation. The color legend implies a red color for a high oil saturation and a blue color for a low oil saturation, hence, a high water saturation. Looking at Figure (4.9) we can say that the two packages give very close oil phase volume fractions across the domain, although, IC-FERST shows a wider spread of water specially toward the boundaries of the model.

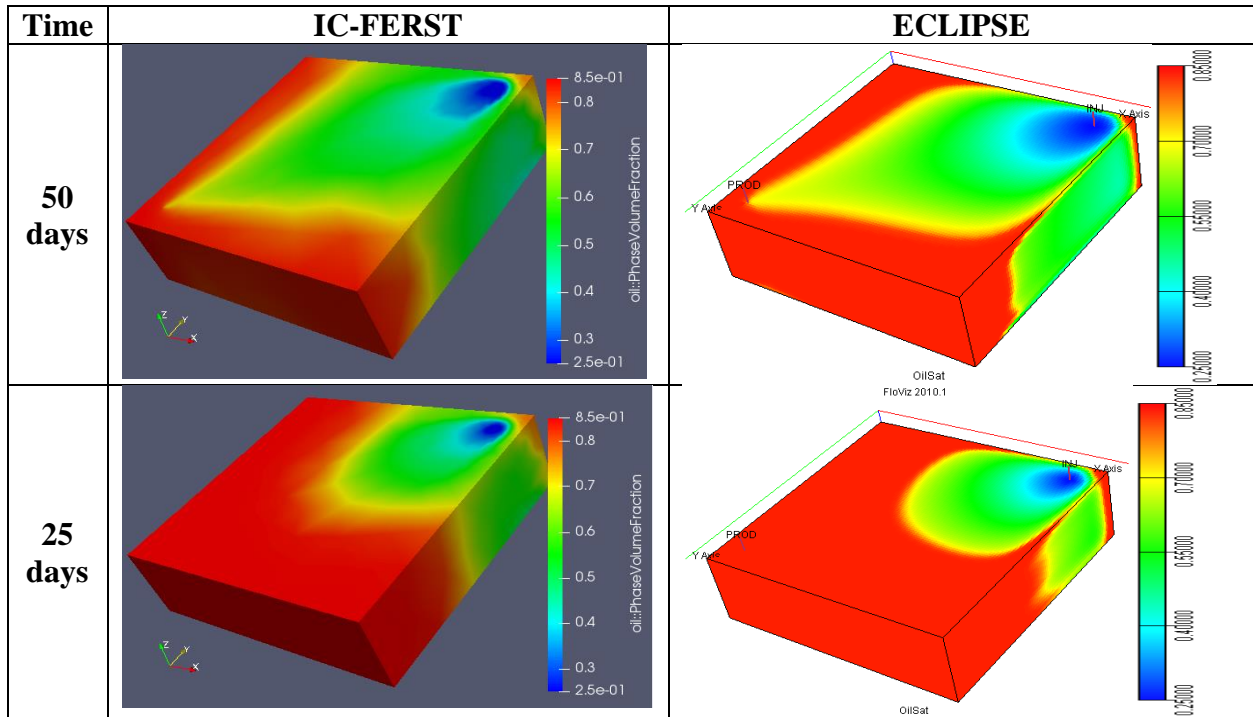


Figure (4.9): Quarter 5 spot 1 layer case oil saturation results for IC-FERST fine parallel vs ECLIPSE fine at 50 and 25 days

4.2 Case 2: Quarter 5 Spot 5 Layers

In this section a similar case is investigated – however some heterogeneity is introduced – with the model consisting of five different geological layers instead of one geological layer. Each layer has different properties based on a real field in the North Sea. Figure (4.10) shows a representation of the case showing the different geological layers.

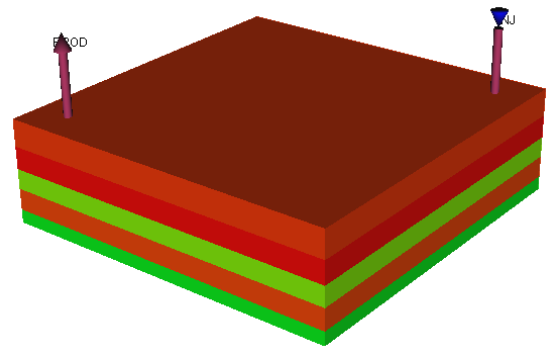


Figure (4.10): Quarter 5 spot 5 layers case representation showing injector and producer well's locations

4.2.1 Case 2 Computational Details

Model dimensions: The geometrical dimensions of this model are exactly the same as the one described in section (4.1) with the exception that now five layers of different thicknesses and properties make up the reservoir. The computational domain in Figure (4.10) has the dimensions of 250mx250mx75m in the (X,Y,Z) cartesian coordinate system. Both the wells are also located

at 101.25m from the center of the domain; both wells, are perforated to a depth of 75m and have a radius of 0.25m.

Fluid properties: Oil has a density of 784.9 kg.m³ and water a density of 1009.1 kg/m³; oil viscosity is 8.9cp and water viscosity is 0.89cp.

Boundary conditions: Initial pressure in the middle of the reservoir is 4500 psi, whilst the producer is controlled at an outlet pressure of 4000 psi and the injector is controlled at an inlet pressure of 6500 psi. All the sides of the reservoir are no flow boundaries; any inlet or outlet flow occurs at the wells. The time step chosen for the simulation is one day and the model is run for 100 days.

Rock properties: The relative permeability curves and the capillary pressure curve of the five geological layers are shown in Figure (4.11) (a) and (b) respectively. Table (4-5) shows the geological properties of the 5 layers and their thickness. The properties are shown in both SI units and field units. In this case the permeabilities in the three directions (X,Y and Z) vary; the variation is denoted by the Kv/Kh ratio which gives the ratio of vertical to horizontal permeabilities. It is noted that the permeabilities vary only vertically. In each layer, the horizontal permeabilities Kx and Ky are the same i.e Kx=Ky. Looking on Table (4-5) and Figure (4.11) it can be seen that layers 1,2 and 4 are good production layers with high permeabilities and porosities, initial oil in place and low entry capillary pressure compared to layers 3 and 5.

Table (4-5): Quarter 5 spot 5 layers case, geological layers properties

Layer No.	1	2	3	4	5
avg Kh (md)	1633	1101	319	925.2	518
avg Kh (m ²)	1.612e-12	1.087e-12	3.148e-13	9.131e-13	5.112e-13
Kv/Kh ratio	0.9	0.9	0.9	0.9	0.9
Porosity (%)	0.264	0.271	0.204	0.261	0.23
Thickness	64 ft/19.5 m	53 ft/16.2 m	47 ft/14.3 m	50 ft/15.24 m	32 ft/9.75 m
Swr	15%	12%	35%	16%	45%
Sor	25%	31%	33%	33%	34%

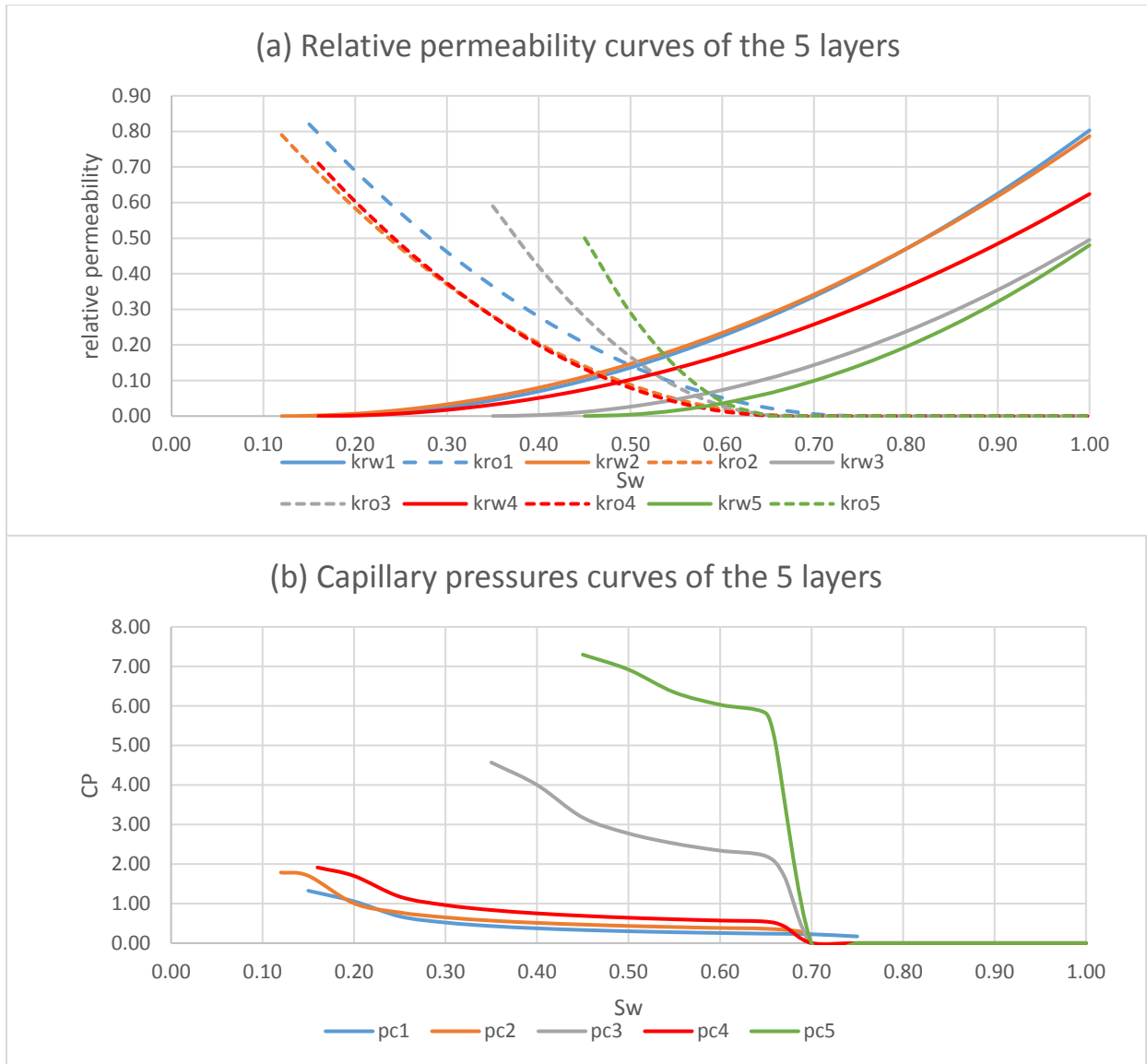


Figure (4.11): Quarter 5 spot 5 layers case a) Relative Permeability b) Capillary Pressure

Again the same model parameters were considered in both ECLIPSE and IC-FERST simulators. Given the two simulators use different units, Table (4-6) shows all the inputs with the different units for each simulator. As in Case 1, different meshes were also tried out to see the effect of refining and coarsening the mesh, the number of elements generated by each mesh in each case is also shown in Table (4-6); these are highlighted in italic, showing the difference in value to the ones used for Case 1 in Table (4-1).

Figure (4.12) and Figure (4.13) show the different meshes used in both ECLIPSE and IC-FERST respectively. There were no adaptivity simulations with the IC-FERST simulator for this case.

Table (4-6): Quarter 5 spot 5 layers case IC-FERST and ECLIPSE inputs parameters

	IC-FERST	ECLIPSE
Model dimensions	250 m x 250 m x 75 m	820.21 ft x 820.21 ft x 246 ft
Mesh quality	<i>Coarse: 99,221 elements</i>	25_25_5 (3,125 cells)
	<i>Medium: 434,013 elements</i>	50_50_10 (25,000 cells)
	<i>Fine: 1,107,286 elements</i>	100_100_20 (200,000 cells)
Well locations(X,Y)	Producer: -101.25 m,-101.25 m	Producer: cell (10,91)
	Injector:101.25 m,101.25 m	Injector: cell (91,10)
Well perforation	0-75 m	0≈ 75 m
Well radius	0.25 m	0.82 ft
Fluid density	Oil: 784.905 kg/m ³	Oil: 49 lb/ft ³
	water: 1009.16 kg/m ³	water: 63 lb/ft ³
Fluid Viscosity	Oil: 8.9E-3 Pa.s	Oil: 8.9 cp
	Water: 8.9E-4 Pa.s	Water: 0.89 cp
Initial reservoir pressure	3.1026E+7 Pa.	4500 psi
Flowing pressures	Inlet: 4.4816E+7 Pa.	Inlet:6500 psi
	Outlet: 2.7579E+7 Pa.	Outlet:4000 psi
Time step	86400 sec	1 day

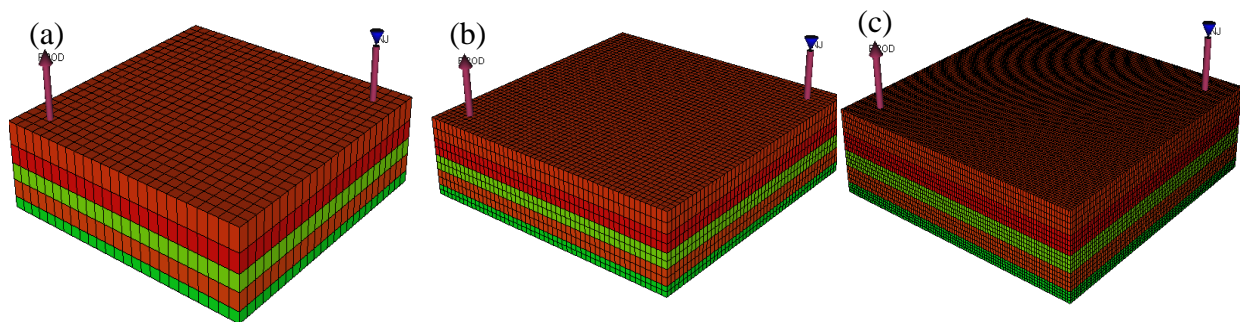


Figure (4.12):Quarter 5 spot 5 layers case ECLIPSE meshes a) coarse (3,125 cells) b) medium (25,000 cells) c) fine (200,000 cells)

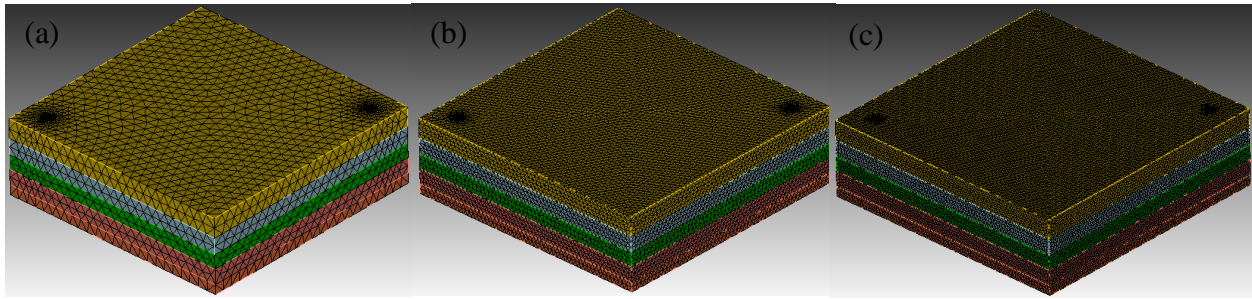


Figure (4.13): Quarter 5 spot 5 layers case IC-FERST meshes a) coarse (99,221 elements) b) medium (434,013 elements) c) fine (1,107,286 elements)

4.2.2 Case 2 Computational Results and Analysis

Table (4-7) shows the different cases that were run with different meshes and options, along with a number of processors used and the time the run took to complete. It is interesting to note a number of things:

- (a) The simulation run times for this more complex case are much higher than for the simpler Case 1 (Table (4-2) vs Table (4-7)). For example the IC-FERST coarse scenario, with 6 processors takes nearly 3 and half hours to complete, as opposed to 14 minutes with 2 processors for the homogeneous case (Table (4-2)). This is due to the increased number of cells – as seen in Table (4-7) – required to capture the geological heterogeneity in the vertical direction.
- (b) The IC-FERST simulation run times increase with increased spatial resolution i.e. for the fine mesh, the simulation run time is much higher than for the other two types of meshes (12 hours vs 5 hours for the medium mesh, and nearly 3 and half hours for the coarse mesh).
- (c) The single processor ECLIPSE simulations for all 3 meshes (E1, E2, and E3) are faster than the IC-FERST parallel simulations.

Table (4-7): Quarter 5 spot 5 layers case IC-FERST and ECLIPSE cases runtime and processors

Software	Case	No. of processors	No. of elements	Run time
IC-FERST	Coarse parallel	6	99,221	03:35:14
	Medium parallel	6	434,013	05:18:08
	Fine parallel	6	1,107,286	11:57:06
ECLIPSE	Coarse	1	3,125	00:00:02
	Medium	1	25,000	00:01:09
	Fine	1	200,000	01:28:04

The simulation results for the water and oil injection and production rates, from the two simulators are shown in Figure (4.14). Figure (4.14) (a) shows the water injection rates from the 3 parallel processor simulators for the three meshes (coarse, fine and medium) using IC-FERST simulator vs the results from the single processor simulations of ECLIPSE. Figure (4.14) (b) shows the oil production rates for the same cases, for both software, whilst Figure (4.14) (c) shows the water production rates, again for the same scenario. Taking the ECLIPSE fine series run results as a reference, the percentage difference between the IC-FERST runs with different meshes is computed and shown in Table (4-8).

Table (4-8): Quarter 5 spot 5 layer IC-FERST parallel vs ECLIPSE fine series percentage difference for each mesh.

Case	Mesh	Percentage Difference
Water Injection	Coarse	1
	Medium	1
	Fine	25
Water Production	Coarse	12
	Medium	12
	Fine	14.5
Oil Production	Coarse	4
	Medium	4
	Fine	2.5

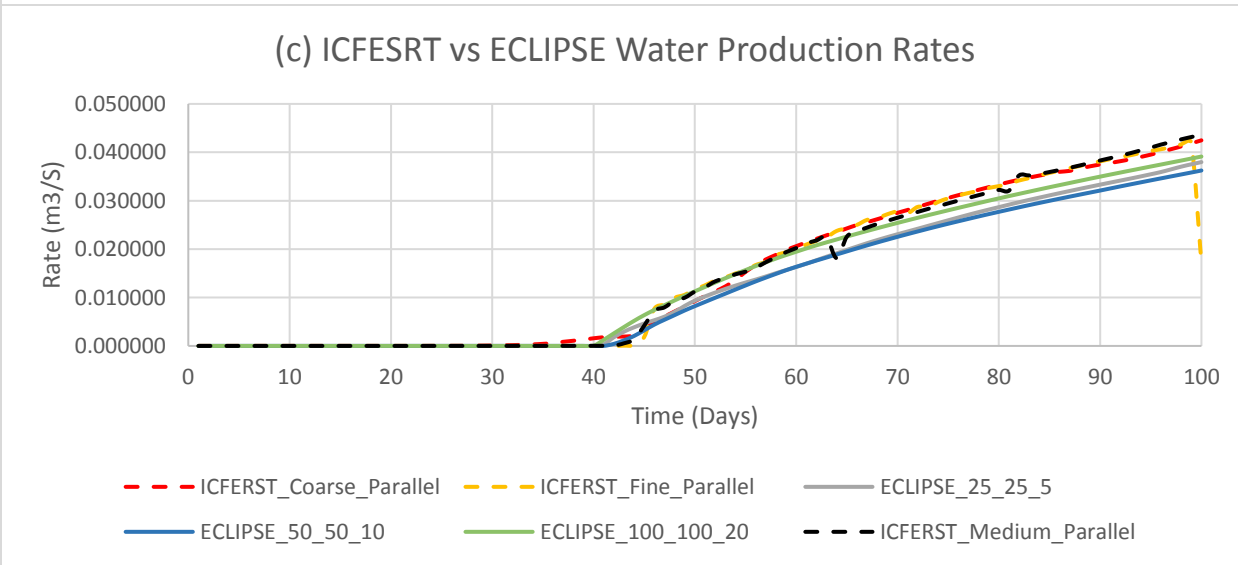
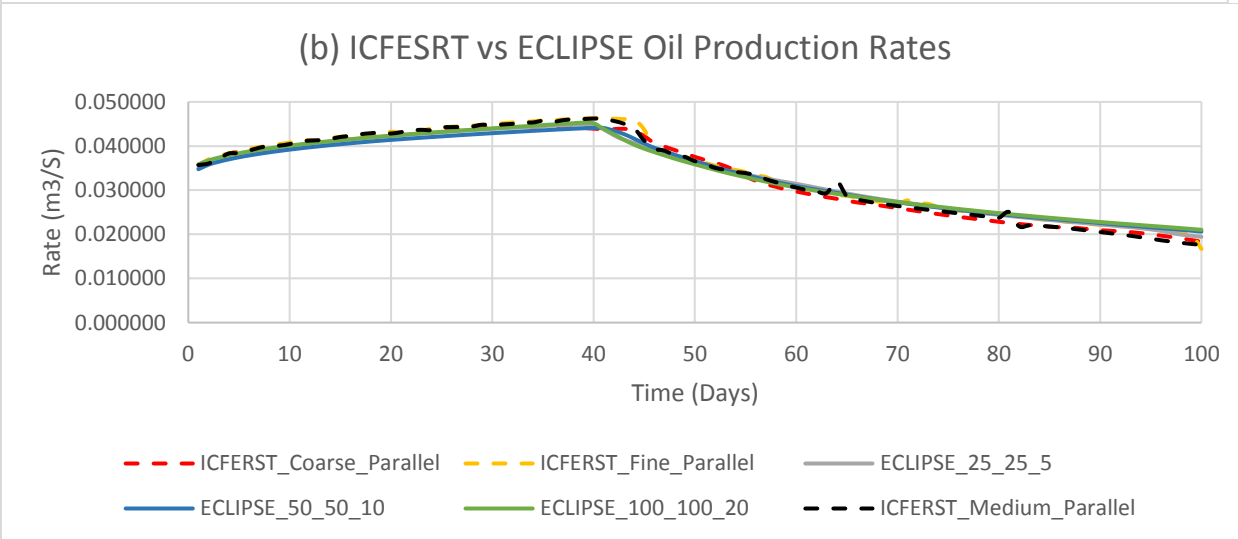
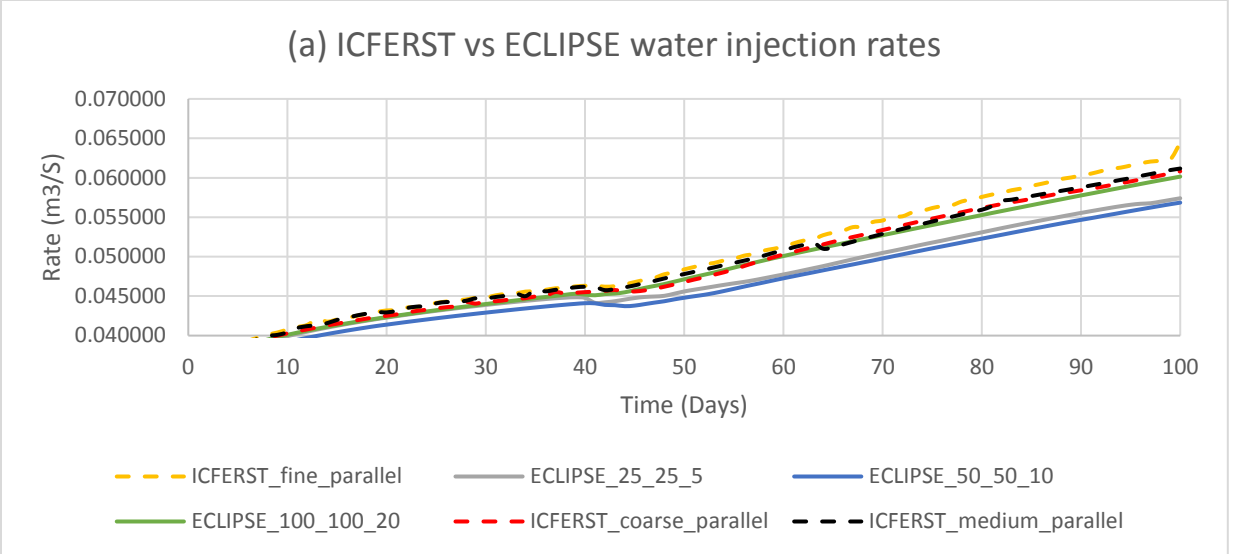


Figure (4.14): Quarter 5 spot 5 layers case IC-FERST vs ECLIPSE results a) water injection b) oil production c) water production

Looking at Figure (4.14) (a), (b) and (c) and Table (4-8) a number of observations can be made:

- (a) Looking at the water injection rates in Figure (4.14) (a), it can clearly be seen that the ECLIPSE fine again is the closest to all the IC-FERST meshes results, with the coarse IC-FERST being the closest to it. Looking at the oil production rates in Figure (4.14) (b), it can be clearly seen that all the graphs are very close to each other. Lastly looking at the water production rates at Figure (4.14) (c), we can again see that the fine ECLIPSE result is the closest to the IC-FERST results, both the fine and coarse IC-FERST results are very close to the fine ECLIPSE results; noting that the medium mesh shows some sort of irregularity and the fine mesh towards the end of the simulation shows a significant drop in the rate.
- (b) Looking at the percentage difference between ECLIPSE fine and IC-FERST run results showed in Table (4-8), we can see that again the highest difference is shown in the water production rates (12 to 15%) just like in case 1 (Table (4-4)). In the oil production the fine mesh gave the lowest percentage difference (2.5%); whilst in the water injection the coarse mesh gave the lowest difference (1%).

Once again just like in the Case 1 in section (4.1), these results appear very encouraging regarding the IC-FERST simulator.

A visualization comparison of the oil phase volume fraction over the whole domain surfaces is also carried out. The two cases considered are: (I) the fine parallel case of IC-FERST and (II) the single processor fine ECLIPSE simulation – as these two cases showed the least difference by comparison with the earlier oil production rates, given that we are interested mainly in the oil rates. The comparison is carried out at two different time steps: (I) 75 days and (II) 25 days. The left section of Figure (4.15) shows the oil phase volume fraction at a time step of 75 and 25 days from the IC-FERST simulation, whilst the right section of Figure (4.15) shows the oil phase volume fraction at a time step of 75 and 25 days from the ECLIPSE simulation. The red color indicates for a high oil saturation and the blue color for a low oil saturation, hence, a high water saturation.

Looking at Figure (4.15) we can see that both the simulators in both the time steps gave close oil phase volume fractions results, although looking at the side view of layer 1 and 4 at the boundaries we can see that water in the ECLIPSE simulations has traveled further distance than in the IC-

FERST; whilst looking at the top view of the first layer we can see that the water in the IC-FERST simulation near the injection well shows a wider spread.

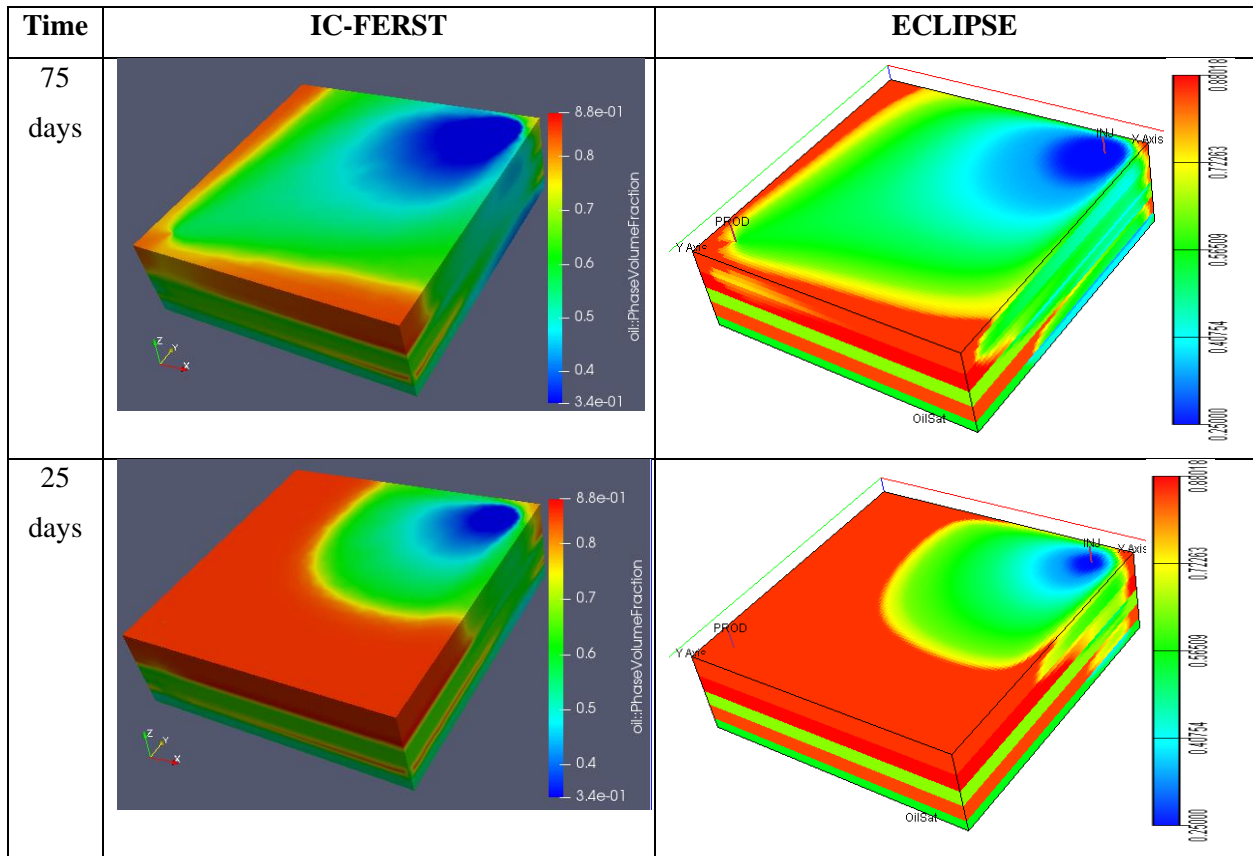


Figure (4.15): Quarter 5 spot 5 layers case oil saturation results for IC-FERST fine parallel vs ECLIPSE fine at 75 and 25 days

4.3 Case 3: Full 5 Spot 5 Layers

A 5-spot water flood scenario is a very well-known secondary recovery scenario used in the petroleum industry. It comprises, a production well in the middle of the domain, which is surrounded by 4 water injection wells at equal distance from the producer. In a quarter 5 spot scenario (Case 1 & 2), only one quarter of the full 5 spot scenario is considered – with the producer at one end of the domain, and the injector diagonally opposite of the domain. The case investigated in this section is the full 5-spot scenario, with a vertical heterogeneity - 5 layers with different properties, as in Case 2.

The fluid and rock properties, the boundary conditions and the time step are the same as in Case 2 (Table (4-6)), but the geometry is now larger – the domain is now four times the one in Cases 1 and 2. Figure (4.16) shows a representation of the complete 5 spot 5 layers model. This scenario will test IC-FERST capabilities with a larger scale model and with more wells.

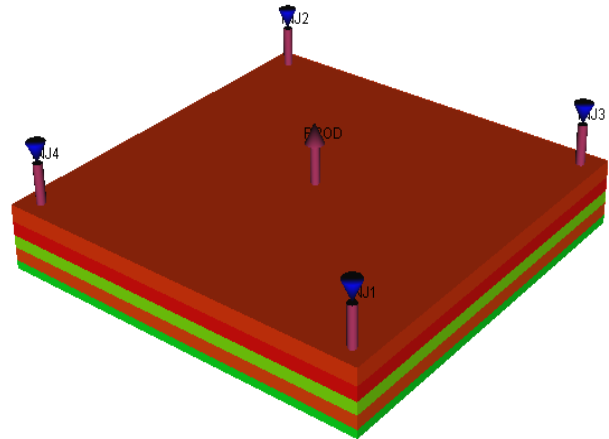


Figure (4.16): 5 spot 5 layers case representation showing injector and producer well's locations

4.3.1 Case 3 Computational Details

Model dimensions: As already stated, the

computational domain in Figure (4.16) is now four times larger than in Cases 1 and 2, with the dimensions in the (x, y and z) coordinate system being: 500m x500m x75m. The injection wells are located at 226.4m from the center of the domain in the x and y directions and the producer is in the center of the domain (origin x=0; y=0; z=0). The wells are perforated to a depth of 75m and have a radius of 0.25m.

Fluid properties: Oil has a density of 784.9 kg.m³ and water a density of 1009.1 kg/m³, oil viscosity is 8.9cp and water viscosity is 0.89cp.

Boundary conditions: Initial pressure in the middle of the reservoir is 4500 psi, the producer is controlled at an outlet pressure of 4000 psi and the injector is controlled at an inlet pressure of 6500 psi. All the sides of the reservoir are no flow boundaries, any flow that happens is from the wells. The time step chosen is one day and the model is run for 100 days.

Rock properties: The relative permeability curves and the capillary pressure curve of the five geological layers are the same as in section (4.2) and are as shown in Figure (4.11) (a) and (b) respectively. Table (4-5) shows the geological properties of the 5 layers and their thickness, the properties are shown in both SI units and field units. In this case the K_x, K_y and K_z permeabilities are not the same; this is reflected in the K_v/K_h ratio which gives the ratio of vertical to horizontal permeability. Looking at Table (4-5) and Figure (4.11) it can be seen that layers 1,2 and 4 are

highly permeable layers – with high permeabilities, porosities, and initial oil in place values and low entry capillary pressure compared to layers 3 and 5.

As in Cases 1 and 2 above, the model parameters were the same in the two simulators. Table (4-9) shows all the inputs with the different units used in both software. Also different meshes were tried out to see the effect of refining and coarsening the mesh; the number of elements generated by each mesh in each case is also shown in Table (4-9), the italic font represents the values that have changed compared with Cases 1 and 2. Figure (4.17) and Figure (4.18) show screenshots from the different mesh sizes used in ECLIPSE and IC-FERST respectively. Again there was no adaptivity runs in this case.

Table (4-9): Quarter 5 spot 5 layers case IC-FERST and ECLIPSE inputs parameters

	IC-FERST	ECLIPSE
Model dimensions	<i>500 m x 500 m x 75 m</i>	<i>1640.42 ft x 1640.42 ft x 246 ft</i>
Mesh quality	<i>Coarse: 465,685 elements</i> <i>Fine: 1,120,720 elements</i>	<i>51_51_5 (13,005 cells)</i> <i>101_101_10 (102,010 cells)</i> <i>201_201_20 (808,020 cells)</i>
Well locations (X,Y)	<i>Producer: 0 m,0 m</i> <i>Injector:226.4 m,226.4 m</i> <i>Injector:- 226.4 m,- 226. 4m</i> <i>Injector: 226.4 m,- 226.4 m</i> <i>Injector:- 226.4 m, 226.4 m</i>	<i>Producer: cell 100,100</i> <i>Injector: cell 191,191</i> <i>Injector: cell 10,10</i> <i>Injector: cell 191,10</i> <i>Injector: cell 10,191</i>
Well perforation	0-75 m	0≈ 75 m
Well radius	0.25 m	0.82 ft
Fluid density	Oil: 784.905 kg/m ³ water: 1009.16 kg/m ³	Oil: 49 lb/ft ³ water: 63 lb/ft ³
Fluid Viscosity	Oil: 8.9E-3 Pa.s Water: 8.9E-4 Pa.s	Oil: 8.9 cp Water: 0.89 cp
Initial reservoir pressure	3.1026E+7 Pa.	4500 psi
Flowing pressures	Inlet: 4.4816E+7 Pa. Outlets: 2.7579E+7 Pa.	Inlet:6500 psi Outlets:4000 psi
Time step	86400 sec	1 day

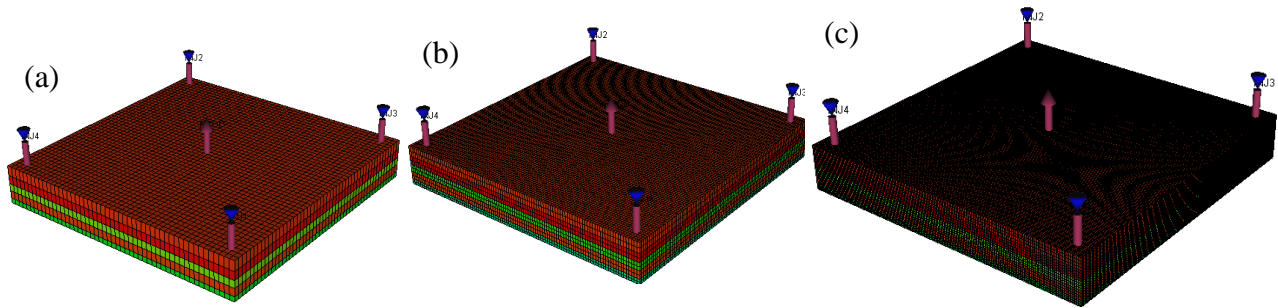


Figure (4.17): 5 spot 5 layers case ECLIPSE meshes a) coarse (13,005 cells) b) medium (102,010) c) fine (808,020)

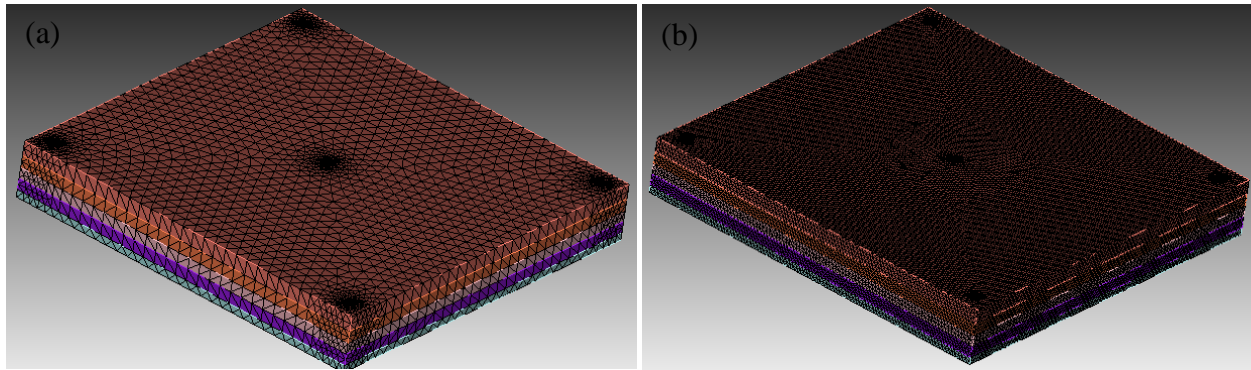


Figure (4.18): 5 spot 5 layers case IC-FERST meshes a) coarse (465,685) b) fine (1,120,720)

4.3.2 Case 3 Computational Results and Analysis

Table (4-10) shows the different cases that were run with different meshes, along with the number of processors used and the time the run took to complete. The ICFERST simulations were carried out using 6 processors, while the ECLIPSE ones were carried out on single processors.

As in Cases 1 and 2, the following are observed with regard to the simulation times:

- (a) Simulation run times have increased compared with Case 2 run times; this is again due to the increased spatial resolution. This is seen in both simulators. The coarse mesh simulations in both software were carried out with the fastest simulation run times, followed by the medium mesh simulations and lastly the fine mesh.
- (b) The ECLIPSE simulations were much faster than the ICFERST ones – independent of mesh.

No IC-FERST simulations were carried out with the adaptivity option due to the oscillation issue – as already discussed in the Case 1 section.

Table (4-10): 5 spot 5 layers case IC-FERST and ECLIPSE cases runtime and processors

Software	Case	No. of processors	No. of elements	Run time
IC-FERST	Coarse parallel	6	465,685	10:03:23
	Fine parallel	6	1,129,720	1.5 days
ECLIPSE	Coarse	1	13,005	00:00:20
	Medium	1	102,010	00:09:02
	Fine	1	808,020	08:18:27

The simulation results for the water and oil injection and production rates, from the two simulators are shown in Figure (4.19). Figure (4.19) (a) shows the water injection rates from the parallel processors simulators for the two meshes (coarse and fine) using the IC-FERST simulator vs the results from the single processor simulations of ECLIPSE. Figure (4.19) (b) shows the oil production rates for the same cases, for both software, whilst Figure (4.19) (c) shows the water production rates, again for the same cases. Using the ECLIPSE fine mesh case again as the base, the percentage differences between the different simulation results from IC-FERST is shown in Table (4-11).

Table (4-11): Full 5 spot 5 layer IC-FERST parallel vs ECLIPSE fine series percentage difference for each mesh.

Case	Mesh	Percentage Difference
Water Injection	Coarse	2
	Fine	3
Water Production	Coarse	24
	Fine	23.5
Oil Production	Coarse	4
	Fine	4

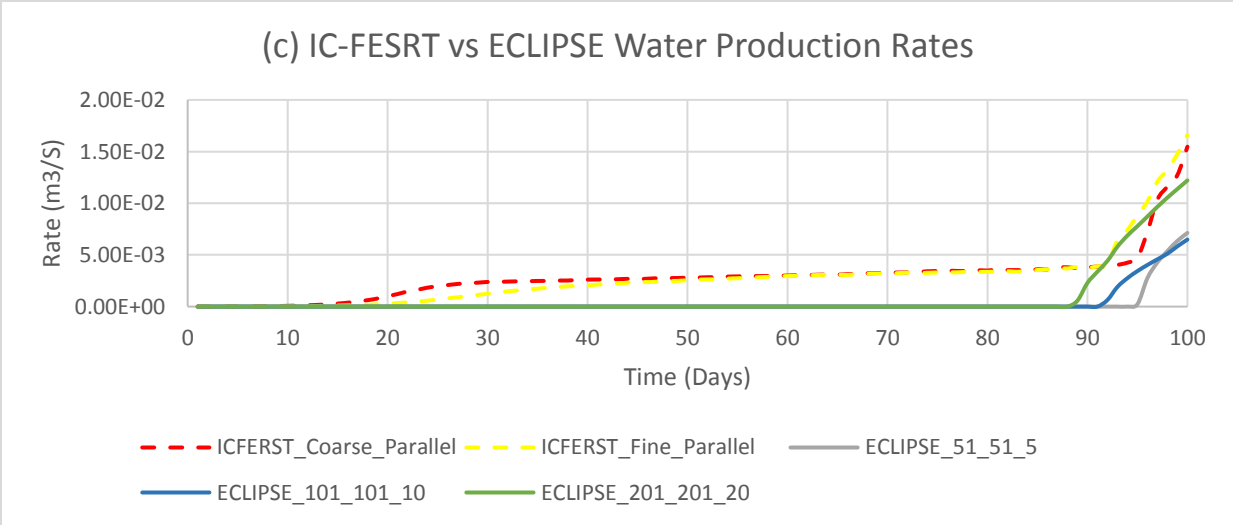
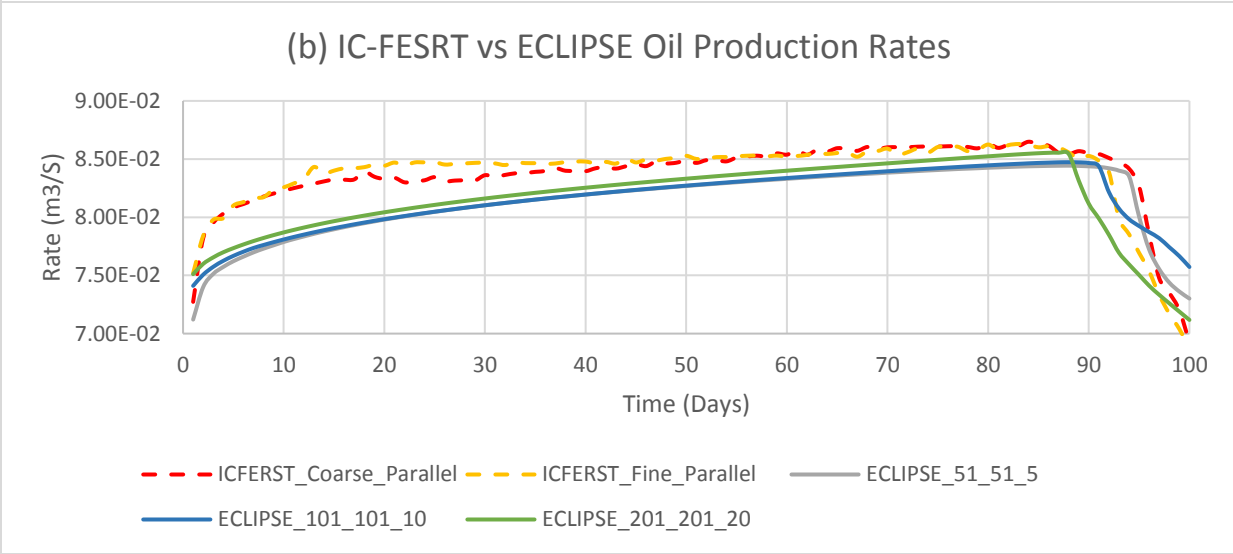
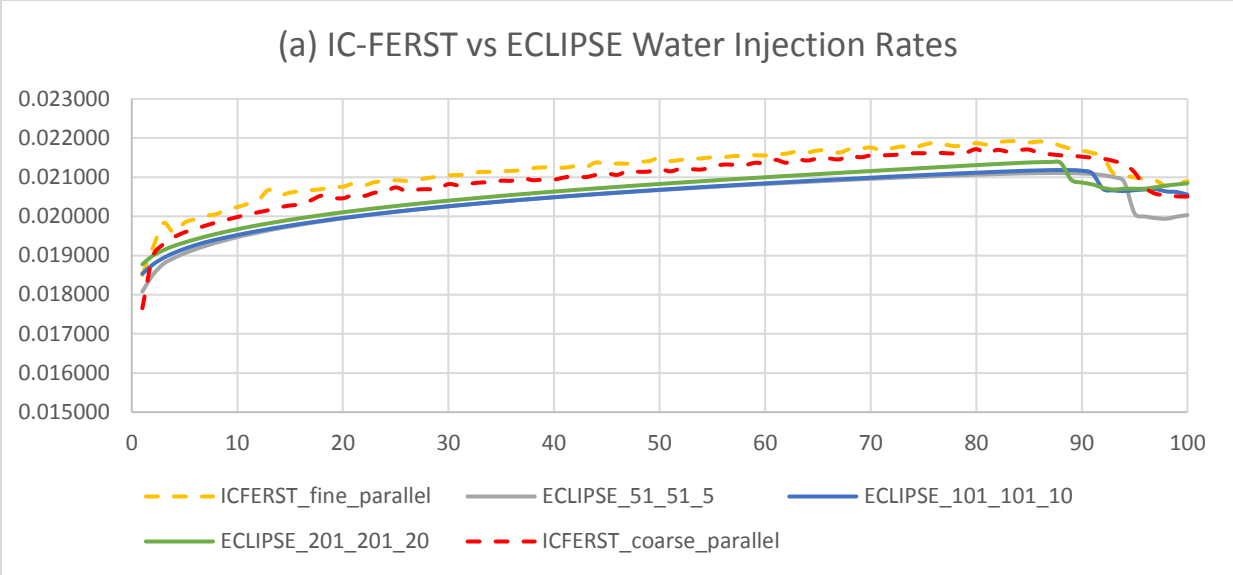


Figure (4.19): 5 spot 5 layers case IC-FERST vs ECLIPSE results a) water injection b) oil production c) water production

Looking at Figure (4.19) (a), (b) and (c) and Table (4-11), comparing the IC-FERST and the ECLIPSE results; a number of observations are made:

- (a) Looking at Figure (4.19) (a) and (b) we can see the water injection and oil production rates respectively, it can clearly be seen that before the water breakthrough (90 days); the IC-FERST fine and coarse runs results are very close to each other – indicating mesh independence – and also with the ECLIPSE fine mesh. After the water breakthrough, it is hard to tell from the graphs which mesh is closest to which; hence, we will compare through the percentage difference from Table (4-11).
- (b) Looking at Figure (4.19) (c), which shows the water production rates, we can see that both the IC-FERST meshes results are very close, and also show a very early water production but with low rates. However, with the ECLIPSE simulations, the water breakthrough occurs at around 90 days. Again, the fine mesh results from ECLIPSE is the closest to the IC-FERST results – for both coarse and fine meshes of IC-FERST.
- (c) Looking at the results presented in Table (4-11), showing the percentage difference between the IC-FERST runs and the ECLIPSE fine run results; it can easily be seen that as from the graphs in Figure (4.19) that the water production rates gave the highest difference, just as in Cases 1 and 2 earlier. Looking at all three cases we can see that the difference between the coarse and fine meshes results compared to the ECLIPSE fine results is small; with the oil production percentage differences being ~4% and water injection percentage difference being 2 to 3%; lastly the water production showed a percentage difference of ~23%. This is encouraging – as it indicates mesh independence has been reached with the IC-FERST simulations.

Once again as in Cases 1 and 2, these results are encouraging regarding the IC-FERST simulator, as very small differences seem to exist between the coarse and fine meshes – hence encouraging in terms of mesh – independence i.e. that with the fine mesh results, a mesh independence has been reached; and in addition the percentage differences with the ECLIPSE fine-mesh results are also small (4%) – except for the water production rates, which are around 23% (Table (4-11)).

Visualization comparison of the *oil phase volume fraction* over the five different geological layers is carried out at 100 days in Figure (4.20). The two cases considered are: (I) the coarse parallel case of IC-FERST and (II) the single processor fine ECLIPSE simulation – as these two cases

showed less difference when looking at Table (4-11) earlier. The left section of Figure (4.20) shows the oil phase volume fraction at a time step of 100 from the IC-FERST simulation, whilst the right section of Figure (4.20) shows the oil phase volume fraction at a time step of 100 from the ECLIPSE simulation. The red color represents a high oil saturation and the blue color for a low oil saturation, hence, a high water saturation.

Looking at Figure (4.20) we can say that both the simulators in all the different geological layers once again give similar if not identical oil phase volume fraction distribution across the computational domain. It can also be seen as anticipated that water reached further in layers 1, 2 and 4, but in layers 3 and 5 the water movement was slow. This is explained by the good flowing properties of layers 1,2 and 4 and the poor flowing properties of layers 3 and 5 as shown and stated in Table (4-5) and Figure (4.11). Lastly looking at the IC-FERST results from layer 4, we can see some strange phase volume fractions in the middle of the domain; these can be explained as numerical errors within the IC-FERST simulator.

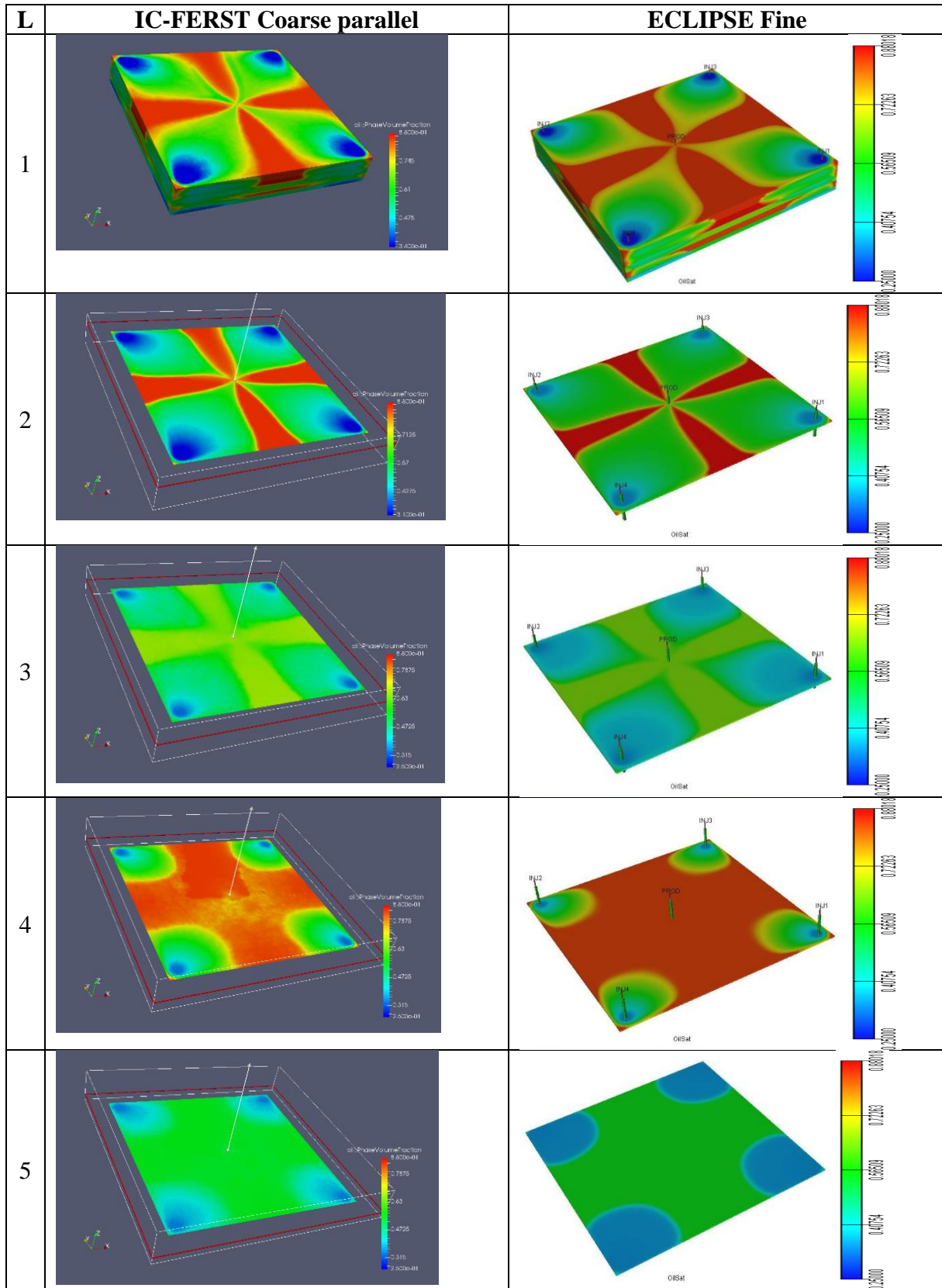


Figure (4.20): 5 spot 5 layers case oil saturation at 100 days in the 5 geological layers

4.4 Conclusion

After running both IC-FERST and ECLIPSE on 3 different cases, starting with a very simple case and increasing the level of complexity and heterogeneity gradually. What can be concluded from the results is that:

- IC-FERST using a fine and coarse mesh and parallel processing gives a very good match with the results outputted from ECLIPSE using a fine mesh..
- IC-FERST coarse mesh gives very close results to the fine mesh; this is due to the fact that it uses a CVFEM, whilst ECLIPSE gives more accurate results only using a finer mesh because of the fact that it uses a FDM.
- ECLIPSE runs much faster in simple cases, while IC-FERST using a coarse mesh and 6 processors takes a close enough run time compared to ECLIPSE in complicated cases.
- With the big run time difference between the IC-FERST fine and coarse meshes, and the very small percentage difference between the two meshes compared to ECLIPSE fine mesh it is concluded that it is best to run IC-FERST in a coarse mesh for simple geometries to get the best results with the lowest computational time.
- The adaptivity option in IC-FERST is not yet able to output stable results; although, different options were tried.

Chapter 5 Real Field Case: Reservoir Characterization and Geostatistics

After comparing the IC-FERST simulations with ECLIPSE for the 5 spot, quarter 5 spot single and multilayer models in Chapter 4, in the following chapters the IC-FERST simulator will be implemented to simulate a real scale field. The results will also be tested again against ECLIPSE. In this chapter we will incorporate results from the reservoir characterization and the geostatistics techniques (Section 3.4 and 3.5) as a real field is being used in this work. This information is confidential – thus only information needed for this study is given, as identification of the field is not allowed.

5.1 General Field Description

An important aspect of this PhD is the implementation of the newly developed ICFERST software to a real site, and the comparison of the results with ECLIPSE simulations. A site has been chosen where a full 3D land seismic processing has already been carried with the survey area covering approximately 863.6 km². The seismic processing work was done nearly twenty years ago, in 2002-2003. The field's dimensions in the (X, Y and Z) directions are 22.75 km, 33.75 km, and 350 m respectively. Unfortunately, production data was not given for the field, but all the initialization data such as core data, log data, PVT and pressure data has been made available for this study.

The field has a total of 33 wells; due to high cost of core analysis, only 13 wells had porosity and permeability core analysis done on them. All 33 wells had well logging, specifically the triple combo of NPHI, RHOB, Resistivity (RES), together with the GR logs. Figure (5.1) shows the boundaries of the field with the location of all the cored and logged wells.

The core and log data are necessary to establish the reservoir properties for the simulations. Before analyzing the available log or core data, all the data depths should be converted from Measured Depth (MD) to Sub-Surface True Vertical Depth (SSTVD) to ensure all the depths are taken from the same datum. To achieve this the Kelly Bushing (KB) height for each well is subtracted from the MD to get the SSTVD. Table (5-1) shows the original names of all wells as shown in PETREL, Trelis and GSLIB; the status of the wells (injector or production); the availability of core and log data; the well locations (X, Y, and Z coordinates) together with their SSTVDs, MDs and KBs are also shown.

Table (5-1): All well names in PETREL, Trelis & GSLIB, status, data available, well locations, well SSTVD, KB and MD

Well Name (PETREL)	trelis name	gslib name	Status	Cores	logged	x location (m)	y location (m)	KB (m)	ztop MD (m)	ztop SSTVD (m)
GINE-1	3	1	Injection	no	yes	773255.5	3439766	182	-3158	-2976
GI-1	4	2	producer	yes	yes	770781.9	3441297	179	-3245	-3066
GI-3	5	3	producer	yes	yes	778010.5	3447896	183	-3256	-3073
HDZ-1	6	4	producer	yes	yes	784307.9	3454772	173	-3217	-3044
HDZ-2	7	5	producer	yes	yes	779390.2	3456337	185	-3249	-3064
HDZ-3	8	6	producer	yes	yes	780396.6	3451904	173	-3291	-3118
HDZ-4	9	7	producer	no	yes	783930.7	3453588	181	-3203	-3022
HDZ-5	10	8	injector	no	yes	785968	3458559	163	-3285	-3122
HDZ-6	11	9	producer	yes	yes	777607.6	3460153	172	-3307	-3135
HDZ-7	12	10	producer	yes	yes	777865.3	3455413	164	-3270	-3106
HDZ-8	13	11	producer	no	yes	779735	3455212	179	-3301	-3122
HDZ-9	14	12	producer	no	yes	778253.9	3455782	165	-3246	-3081
HDZ-10	15	13	producer	no	yes	785394.9	3457525	174	-3205	-3031
HDZ-11	16	14	producer	no	yes	784766.3	3456127	176	-3217	-3041
HDZ-12	17	15	producer	no	yes	778186	3454193	170	-3257	-3087
HDZ-13	18	16	producer	no	yes	778864	3454879	178	-3153	-2975
HDZ-14	19	17	producer	no	yes	783430.8	3452770	180	-3217	-3037
HDZ-15	20	18	producer	no	yes	782686	3453116	179	-3238	-3059
HDZ-17	21	19	injector	no	yes	782868.2	3451453	178	-3209	-3031
HDZS-1	22	20	producer	yes	yes	773736	3450927	179	-3219	-3040
HDZS-2	23	21	injector	yes	yes	772790.4	3451549	178	-3331	-3153
HDZW-1	24	22	injector	yes	yes	778911.8	3465818	171	-3379	-3208
HGI-2	25	24	producer	no	yes	779295.7	3446986	183	-3271	-3088
HOD-1	26	26	injector	yes	yes	769799.3	3446395	180	-3248	-3068
HTF-2	27	27	producer	yes	yes	788355.8	3466451	171	-3328	-3157
HTF-9	28	28	producer	no	yes	789394.8	3467555	166	-3303	-3137
HTF-11	29	29	producer	no	yes	788832.1	3468716	160	-3214	-3054
HTF-15	30	30	injector	no	yes	789150	3469498	168	-3228	-3060
HTF-7	31	31	producer	yes	yes	784268.2	3462242	179	-3392	-3213
HTF-16	32	32	producer	no	yes	787581	3467144	168	-3285	-3117
HBM-1	33	33	producer	no	yes	774083.3	3448084	190	-3251	-3061
HBM-2	34	34	producer	no	yes	772697.4	3446686	171	-3255	-3084
RHM-1	35	35	injector	no	yes	770638.6	3459104	177	-3325	-3148

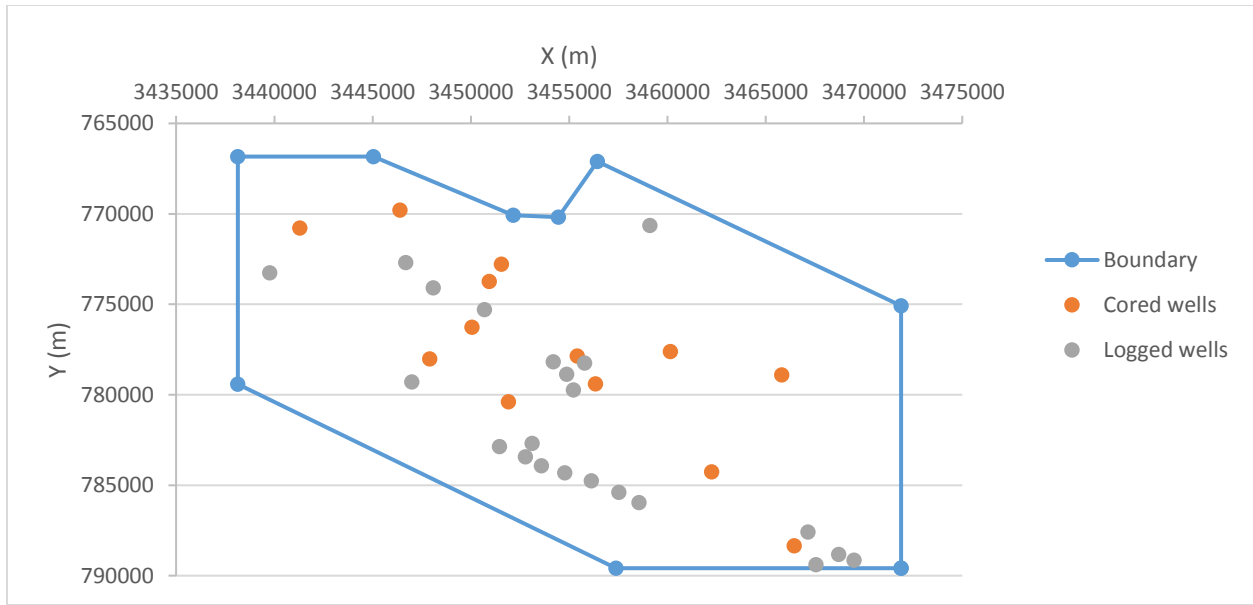


Figure (5.1): Field boundary and well locations; 13 cored wells are marked in orange; all 33 wells have logging data

5.2 Rock Characterization

5.2.1 Detecting Heterogeneity Level

A total of 1150 core samples is available from the 13 cored wells. As mentioned in section 3.5 the first step before performing reservoir characterization is to check the degree of heterogeneity of the data available i.e. the degree of the change of both the porosity and the permeability. As mentioned in Chapter 3 the BRCC MATLAB code was written to do the full reservoir characterization calculations. A number of techniques are implemented to determine the heterogeneity of the real case reservoir. These, as explained in Chapter 3, are:

- a) The simple porosity vs permeability plot
- b) The Dykstra-Parsons method
- c) The Lorenz coefficient method

(a) Porosity vs Permeability plot: First the simple porosity vs permeability plot was plotted for all the 1150 core samples on a semi-log plot as shown in Figure (5.2). As can be seen the R^2 (correlation coefficient) is 0.0107, which is a low value indicating the reservoir is a highly heterogeneous reservoir.

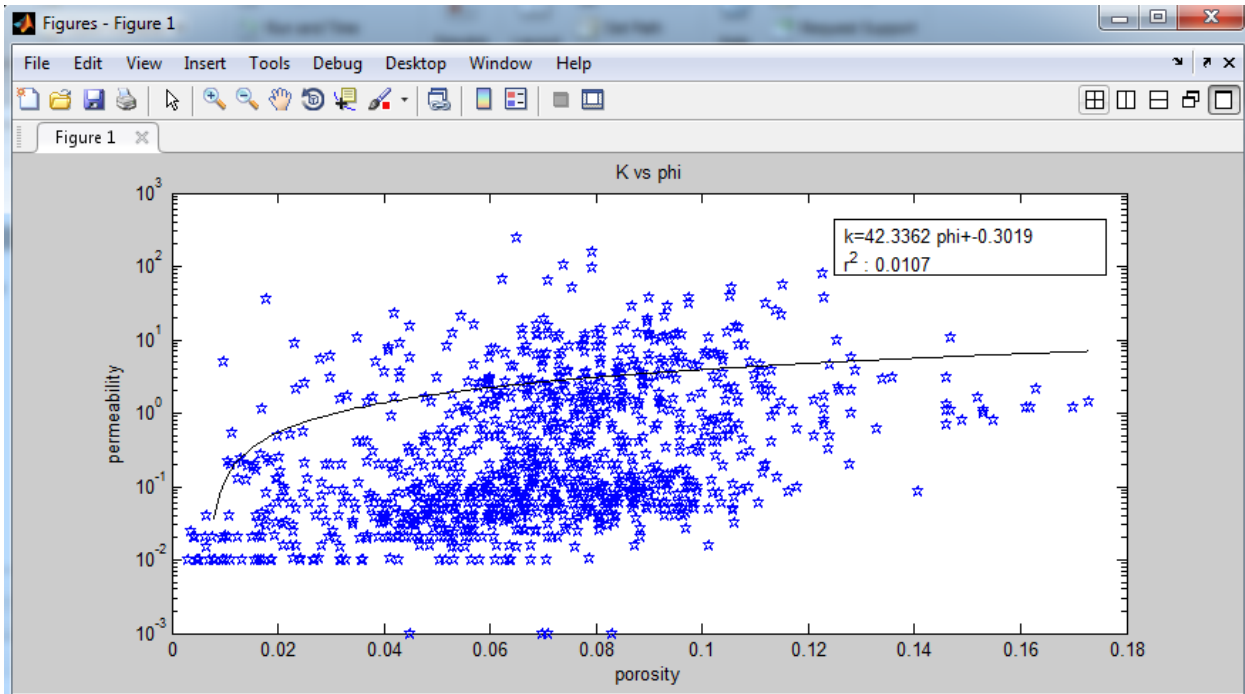


Figure (5.2): Porosity vs Permeability Semi-log plot

(b) The Dykstra-Parsons method: As mentioned in section 3.5) the second technique used to detect reservoir heterogeneity is the Dykstra-Parsons method (Dykstra and Parsons, 1950). The BRCC rearranges all the core samples in decreasing permeability order, and the percentage of thickness is calculated for each sample. Permeability vs percentage of thickness is plotted on a log-probability plot and a best fit line is drawn. This plot is shown in Figure (5.3), The V coefficient (a measure of heterogeneity) is calculated automatically using equation (3-15) by getting the K corresponding to the 50% as 0.2355 and the 84.1% as 0.01999. The V value calculated was 0.9155 - this value is close to one, which again means that the reservoir is highly heterogeneous.

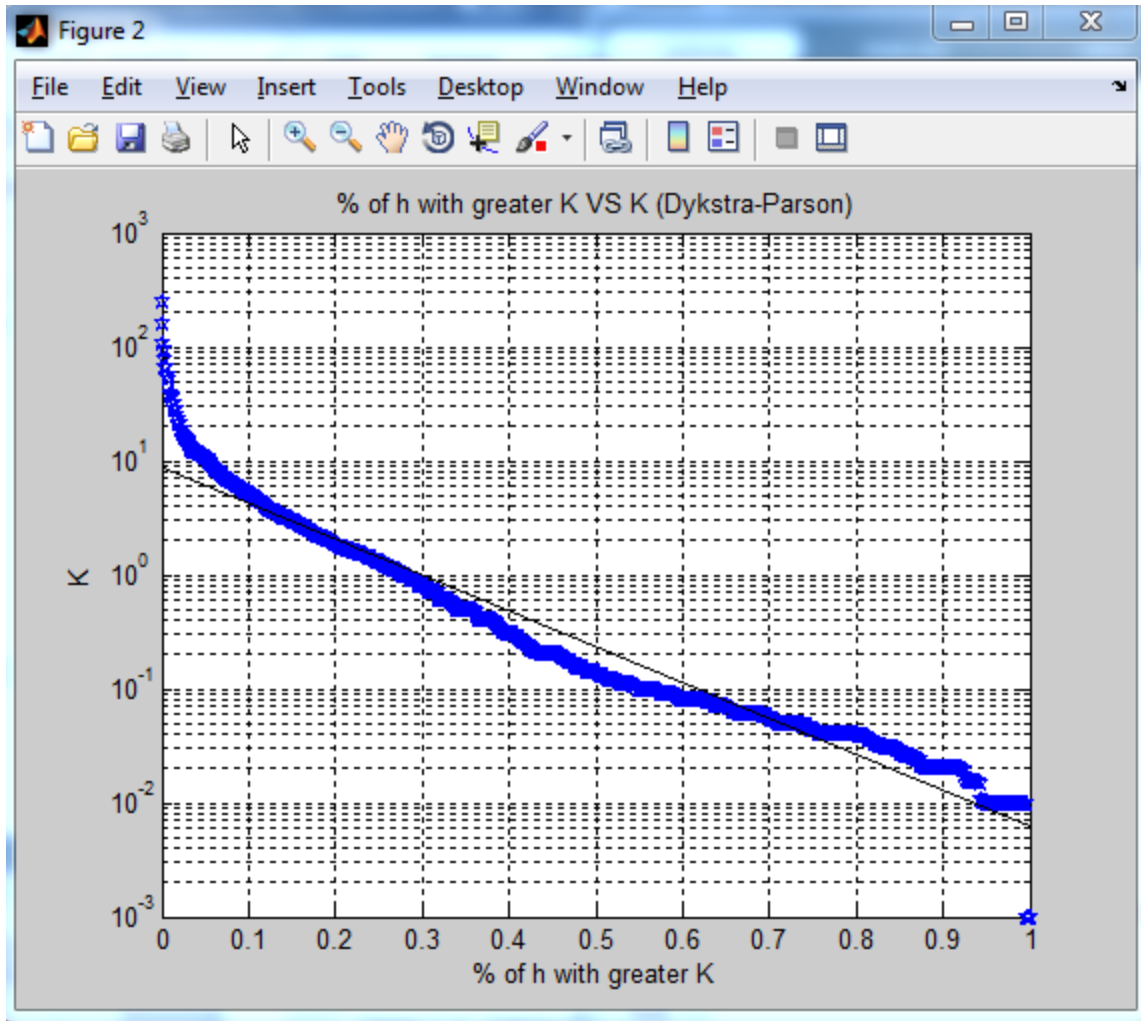


Figure (5.3): Dykstra Parsons Plot

- (c) The Lorenz coefficient (L) method: In this method the core samples are ordered in descending permeability order; subsequently the cumulative volume and permeability capacities are calculated and normalized. Two plots are generated by BRCC. Figure (5.4) (a) shows normalized cumulative permeability/flow capacity vs the normalized cumulative volume capacity on a cartesian scale and (b) shows normalized cumulative permeability/flow capacity vs the normalized cumulative thickness on a cartesian scale. The Lorenz coefficient (L) is calculated automatically by computing the area above and under the straight line, using equation (3-16); the value of L was 0.8436. Looking at the graph deviations from the straight lines and the value of the L coefficient we can tell that the reservoir is highly heterogeneous.

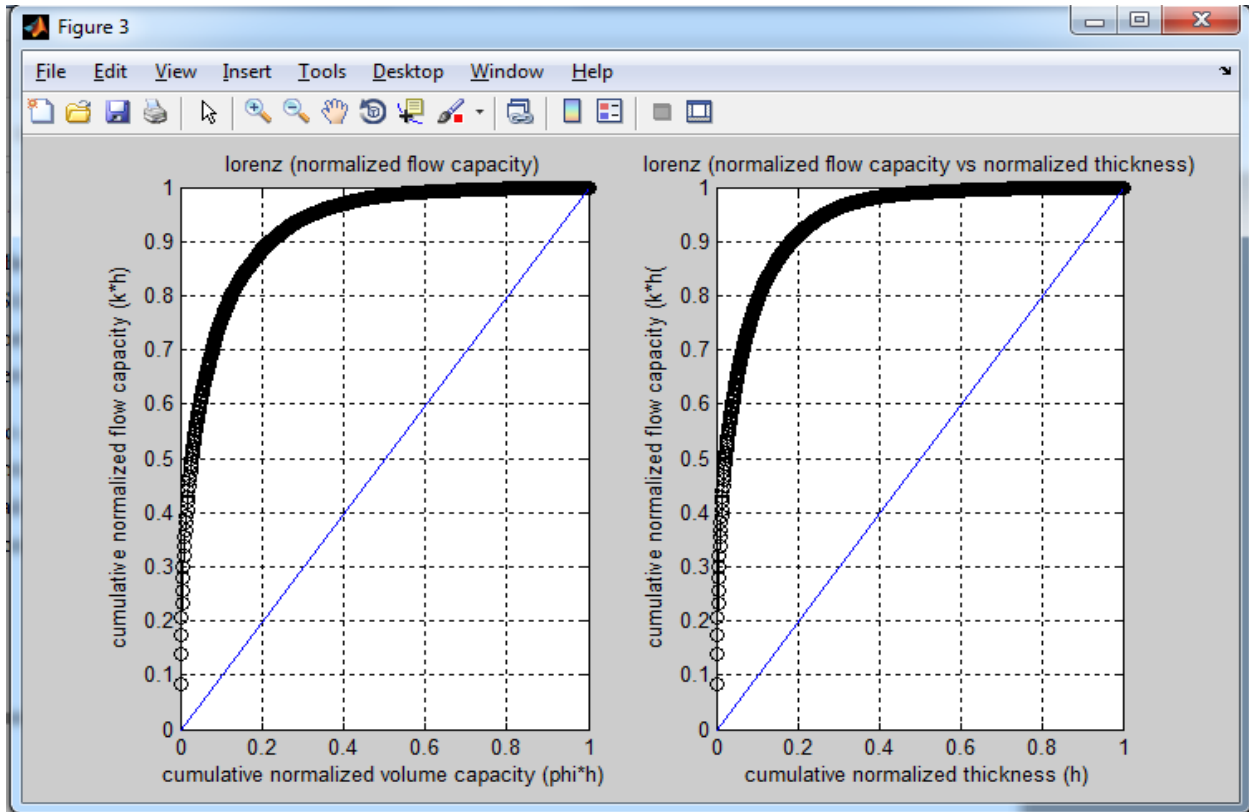


Figure (5.4); Lorenz Coefficient a) normalized flow capacity vs normalized volume capacity, b) normalized flow capacity vs normalized thickness

5.2.2 Rock Characterization Using the Amaeful Technique

Having identified the reservoir as highly heterogeneous, it is necessary now to implement a rock characterization procedure. The BRCC starts the rock characterization of the reservoir using the Amaeful technique (Amaefule et al., 1993) by applying equations (3-17), (3-18), (3-19), and (3-20) on all the 1150 core samples and plotting a porosity vs permeability log-log plot with a best fit line in each clustered rock type, as shown in Figure (5.5).

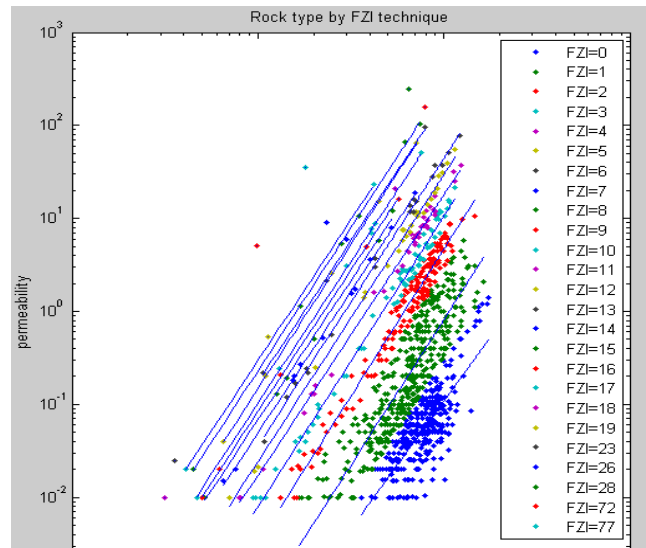


Figure (5.5): First Flow Zone Indicator (FZI) plot using the Amaeful technique for rock characterization

As shown in Figure (5.5) there are 25 rock types in this reservoir, a rather high number of rock types, which will become computationally expensive when carrying out simulations. Hence within the BRCC as mentioned in section 3.5.3, there is a procedure to reduce these number of rock types by re-clustering them according to the R^2 value - thus ensuring the best fitting regression. At the end of this process the code returns only 8 rock types. The information for these rock types are exported into EXCEL and plotted as in Figure (5.6), showing the R^2 value as well as the associated FZI equations.

The legend in Figure (5.6) on the right shows the FZI range of values for each DRT; for example the first rock type is for FZI values ranging from 0 to 0.24 and so on. The dotted lines are the best fit lines of each rock type that show the correlation between porosity and permeability for this rock type and the corresponding R^2 . Table (5-2) shows the equations, FZI range and R^2 for each rock type.

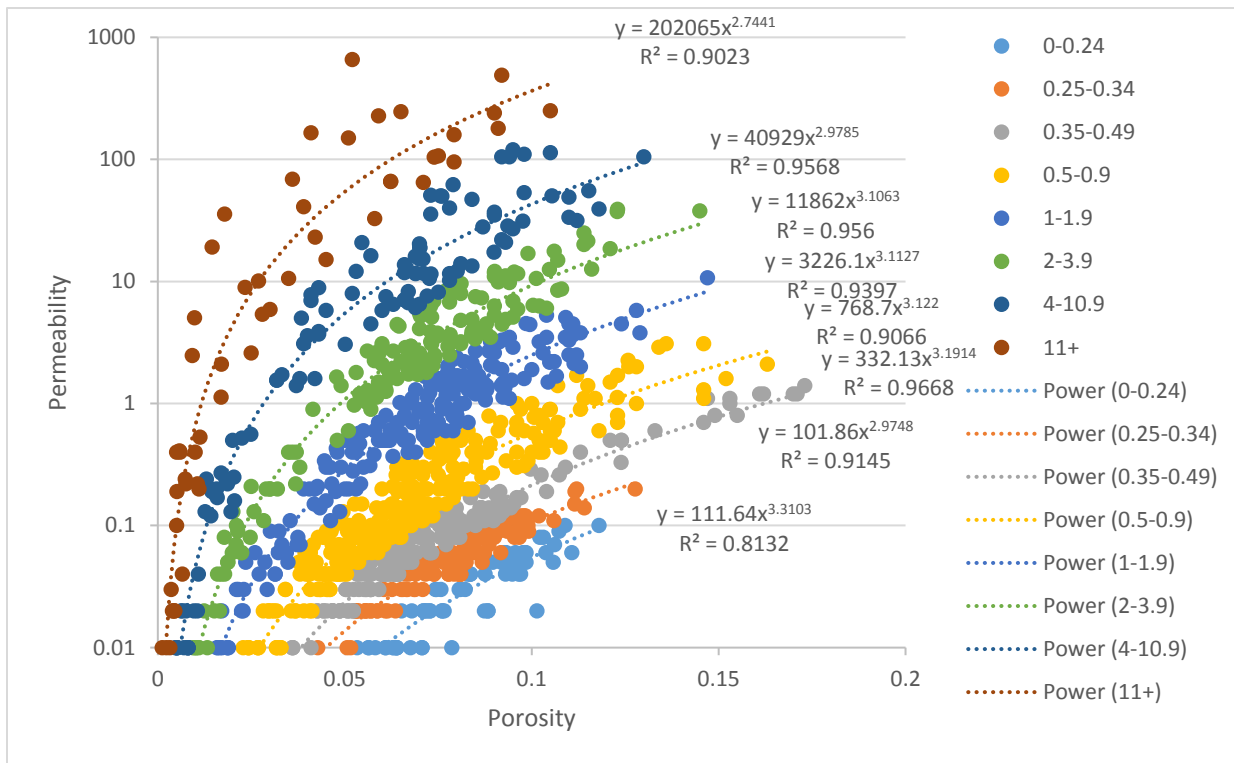


Figure (5.6): Final FZI

Table (5-2): Rock Types using the Amaeful technique: The FZI range, equations and R² values

Rock Type	FZI Range	Equation	R ²
1	0-0.24	$k = 111.64\phi^{3.3103}$	0.8132
2	0.25-0.34	$k = 101.86\phi^{2.9748}$	0.9145
3	0.35-0.49	$k = 332.13\phi^{3.1914}$	0.9668
4	0.5-0.9	$k = 768.7\phi^{3.122}$	0.9066
5	1-1.9	$k = 3226.1\phi^{3.1127}$	0.9397
6	2-3.9	$k = 11862\phi^{3.1053}$	0.956
7	4-10.9	$k = 40929\phi^{2.9785}$	0.9568
8	11+	$k = 202065\phi^{2.7441}$	0.9023

The main aim of the reservoir characterization was to find a correlation for the permeability in terms of the porosity for each rock type. Looking at Figure (5.6), we can tell that we have successfully subdivided the reservoir into 8 rock types, each with a unique porosity – permeability correlation. Now that these correlations have been established, they can be applied anywhere within the reservoir, using geostatistics to determine the permeability in regions where core data is not available. This is absolutely necessary for the computational modelling.

5.3 Geostatistics

Geostatistics is a class of statistics used to analyze and predict the values associated with spatial phenomena; it is used to populate each and every computational cell within the computational domain with the properties of interest, dependent on each rock type, these being: porosity, permeability, relative permeability, capillary pressure and connate water saturation. Hence, a geostatistical software is required – with specific techniques to achieve this. The software package used is called S-GEMS, and it was introduced earlier in section 3.4.2. The techniques implemented for populating the computational domain are: (I) SGS and (II) SIS. The following sections describe the process, as implemented for the real field.

5.3.1 Implementation of the S-GEMS Software – Scaling of the Domain

As mentioned in section 3.4, S-Gems is used in the geostatistics process to populate the cells of the computational domain with the reservoir properties, as evaluated for each rock type. S-Gems does not accept unstructured grids or grid files; hence - some modifications and adjustments had to be made e.g. a box grid that surrounds the full reservoir's boundary was created with 20 grid blocks in the X direction, 30 grid blocks in the Y direction and 40 grid blocks in the Z direction, making the total number of grid blocks 24,000. Figure (5.7) shows an example of the box surrounding the model; the individual grid blocks will be shown after running the simulation.

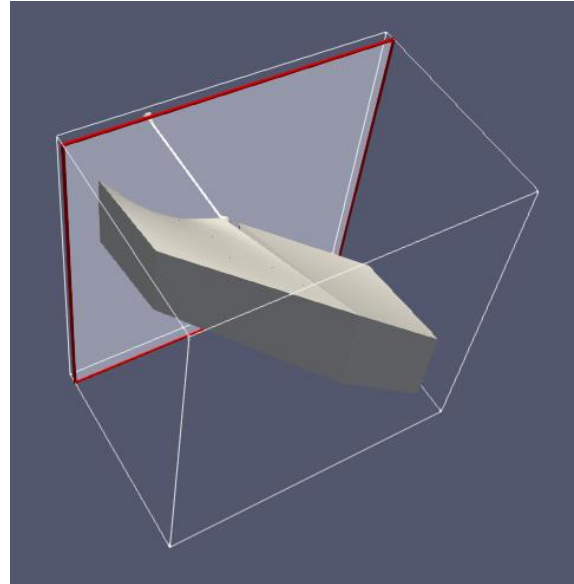


Figure (5.7): Reservoir of interest enclosed in a computational box of dimensions (20,30,40) for S-Gems

Before adding the wells into S-Gems the log data must be filtered to save computational time, because most of the well logs were taking readings in areas outside of the reservoir area, which leaves a huge number of data points that are not used in the reservoir area.

Due to the fact that the field's horizontal area span is much greater than its vertical area span – recall: dimensions in the (X, Y) directions are: 22.75 Km, and 333.75 Km, respectively, whilst in the Z-direction the depth is only 0.35 Km. Some visual scaling was carried out. Figure (5.8), (a) shows the unscaled version of the computational domain – highlighting the difference in the vertical and horizontal dimensions, where the reservoir model can be seen as a very thin sheet. Figure (5.8) (b) shows a scaled version in which the Z dimension was enlarged by a factor of 100 to view the wells better. This is carried out for purely visualization purposes.

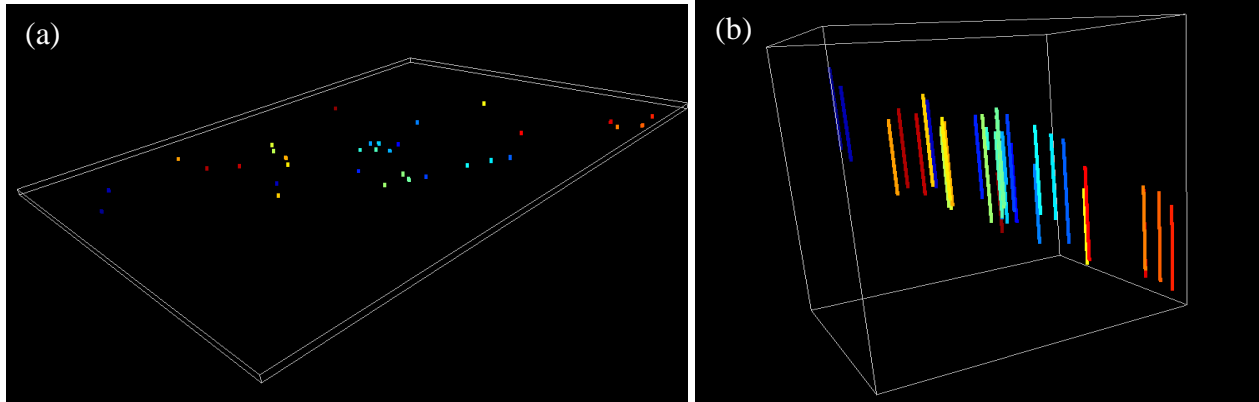


Figure (5.8): Viewing of well locations in S-Gems after adding well locations a) unscaled b) scaled (factor of 100)

5.3.2 Porosity Population

Porosity values are obtained from: (a) core samples, and (b) well logs. The porosity values to be used for populating the whole reservoir domain – obtained from the core samples – are limited in number; there are only 1150 porosity readings from core samples from the 13 wells. However, there are 30,000 porosity readings from the well logs of all 33 wells. Hence, the well log porosity values are used for “populating” the computational domain with the required porosity values at different depths, whilst the 1150 core readings will be used to test the accuracy of the well log’s porosity readings.

Prior to comparing core sample porosity values with well log values, at the same depth, both the core and log data must be all aligned i.e. have the same reference point. Figure (5.9) shows an example of 4 wells.

To make it easier to view the readings, only depth intervals of the log where core samples were taken are shown (denoted by spherical dots). As can be seen from Figure (5.9) the core porosity readings show a good match with the log porosity readings in these 4 wells. As log porosity readings match very well with core values, log porosity readings are now used to populate the computational domain of the whole reservoir.

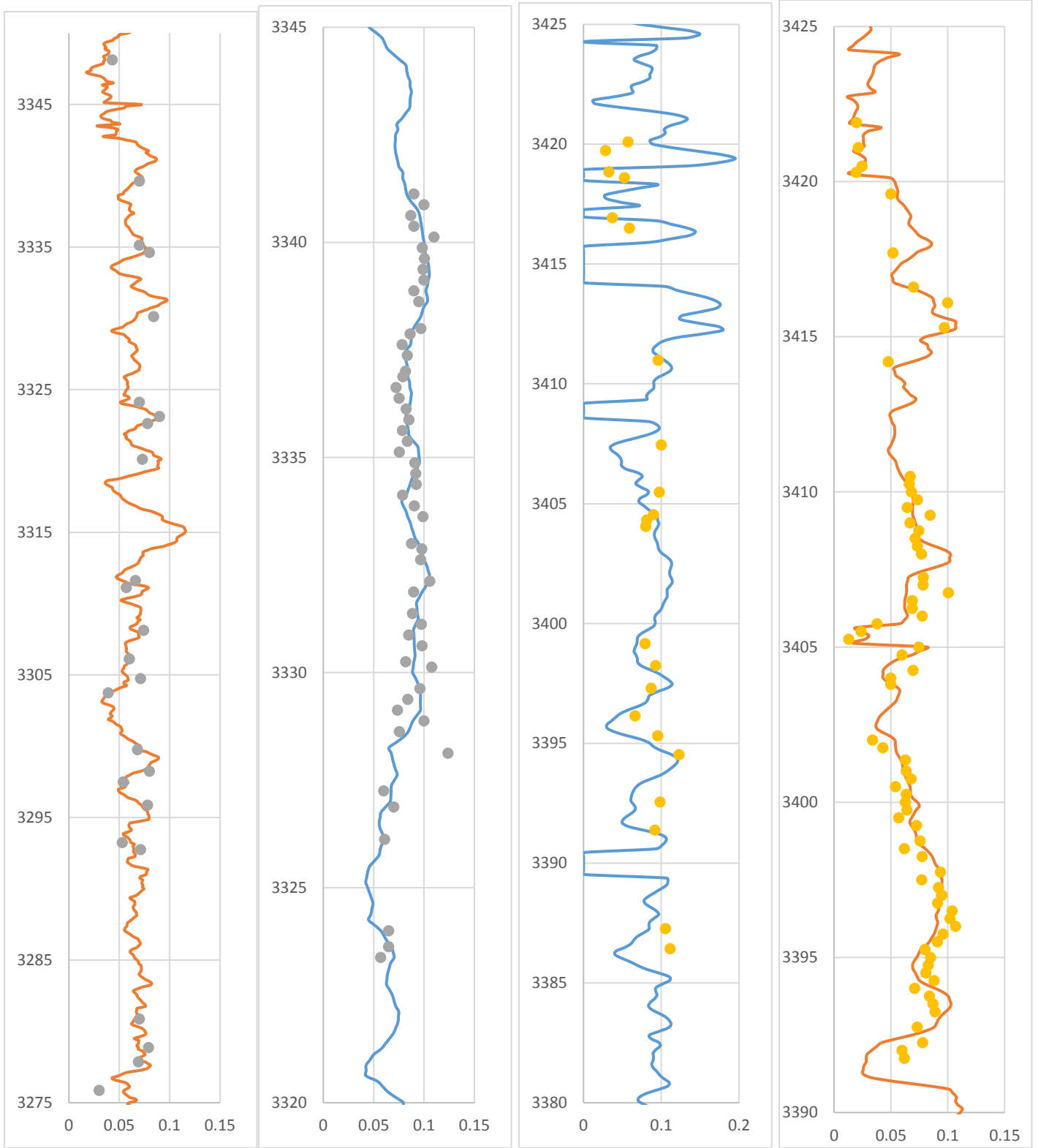


Figure (5.9): Log vs Core Porosity values: Porosity logs of Wells GI-1, HDZ-6, HDZS-2 & HTF-2 with corresponding core sample values Solid lines represent the log values, whilst the spherical dots represent the core values.

One of the first steps taken before populating the computational domain with the necessary properties, is to carry out an SGS. Prior to this however, it is important to produce a set of variograms, based on a normal/Gaussian distribution of porosity values. As mentioned in section 3.4, and as shown in the S-Gems flow chart in Figure (3.31), the porosity data is first previewed on a histogram to make sure that it is normally distributed. Figure (5.10) shows the histogram of all the log porosity data (from the 33 wells) points in the reservoir. Looking at the histogram in Figure (5.10) we can tell that the data is not perfectly normally distributed – as in most Earth sciences data do not present symmetric Gaussian histograms. A Normal Score Histogram Transformation is needed. The S-Gems TRANS algorithm is first used to transform the porosity data, so as to follow, as close as possible, a Normal Distribution prior to producing the necessary variograms.

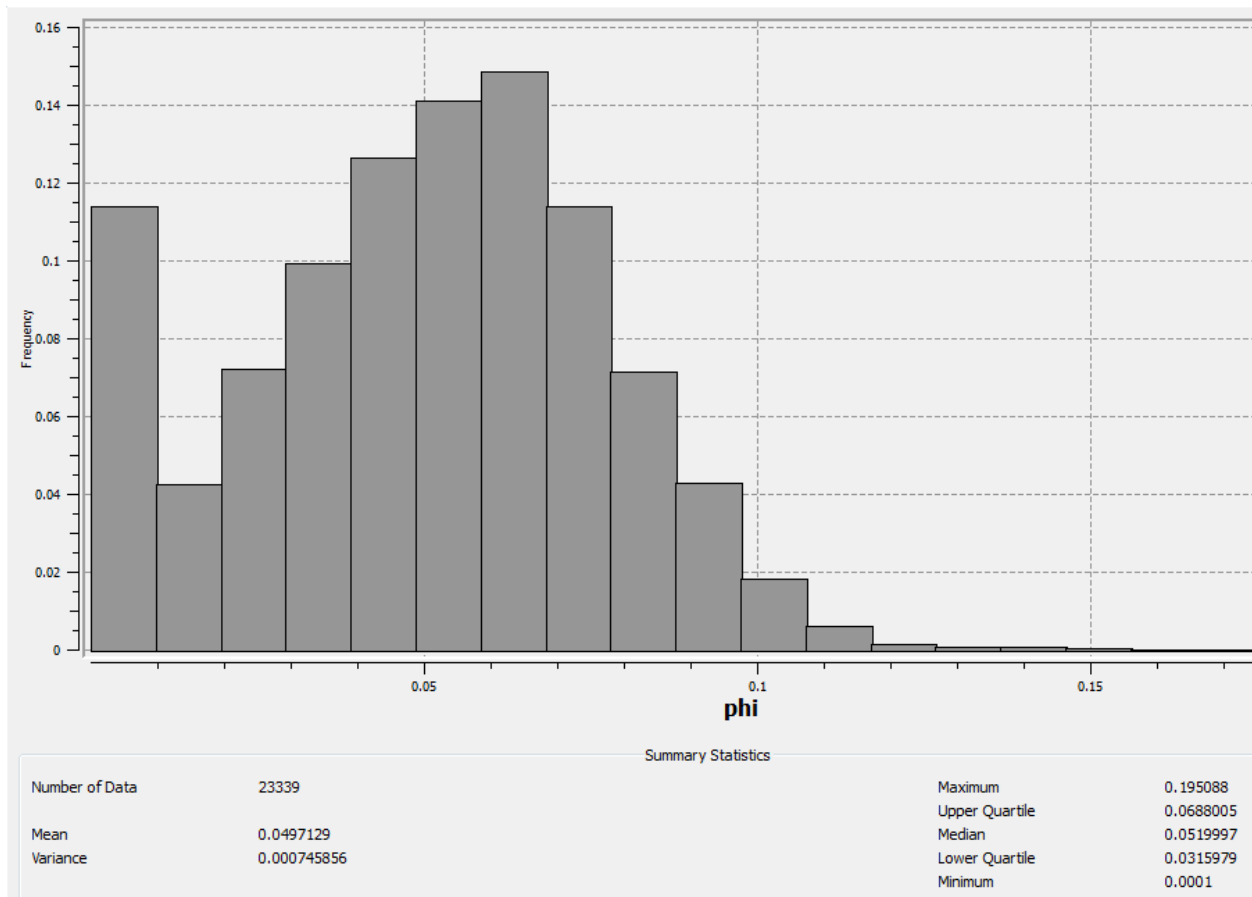


Figure (5.10): Histogram based on the original porosity Log values from all wells, using all the 23,339 data points, showing a mean of 0.049 and a variance of 0.00075.

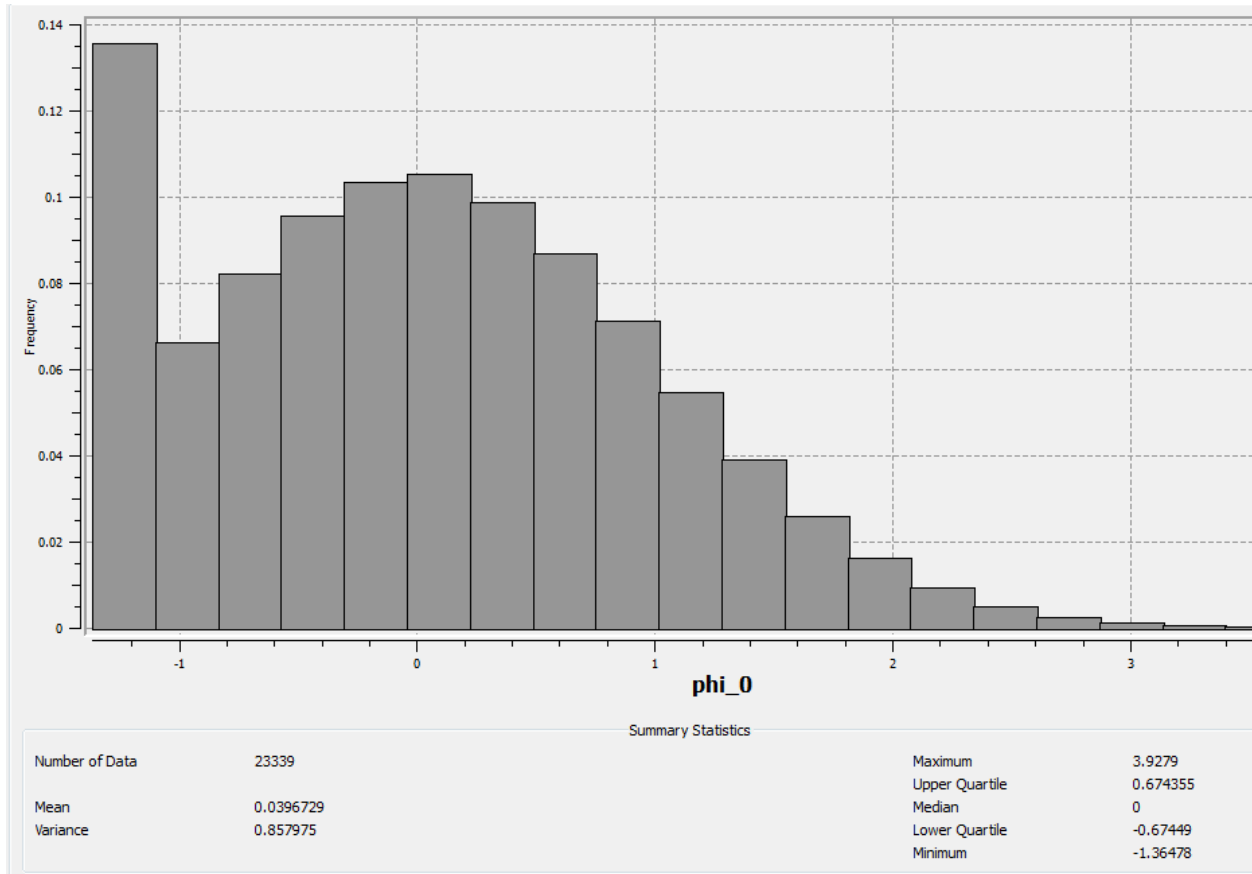


Figure (5.11): Transformation of the Log porosity histogram from all wells using the 23,339 data points and showing a mean of 0.039 and a variance of 0.86.

Figure (5.11) shows the porosity histogram after the normal score transformation. It can be seen that the histogram looks now more normally distributed and that the values are no longer fractions of 1 as it was before. The values now are normally distributed with the median being exactly zero. Table (5-3) shows the mean, variance and median values from both the histograms.

Table (5-3): S-Gems histogram before and after transformation mean, variance and median values

Histogram	Mean	Variance	Median
Original	0.049	0.00075	0.052
Transformed	0.39	0.86	0

Now that the porosity data is transformed, the next step is to produce the three variograms as mentioned in section 3.4. All the variograms had a lag number of 100, a lag distance of 10 meters and a lag tolerance of 5 meters. The three types of variograms produced are:

- i. Horizontal semi-variogram with an azimuth angle of 45 degrees, a dip angle of 0 degrees, a tolerance of 25 degrees, and bandwidth of 100 meters.
- ii. Omni directional horizontal semi-variogram with an azimuth angle of 0 degrees, dip angle of 0 degrees, a tolerance of 180 degrees, and a bandwidth of 1000 meters to capture all the data.
- iii. Vertical semi-variogram with an azimuth angle of 0 degrees, dip angle of 90 degrees, tolerance of 1 degree, and a bandwidth of 1 meter.

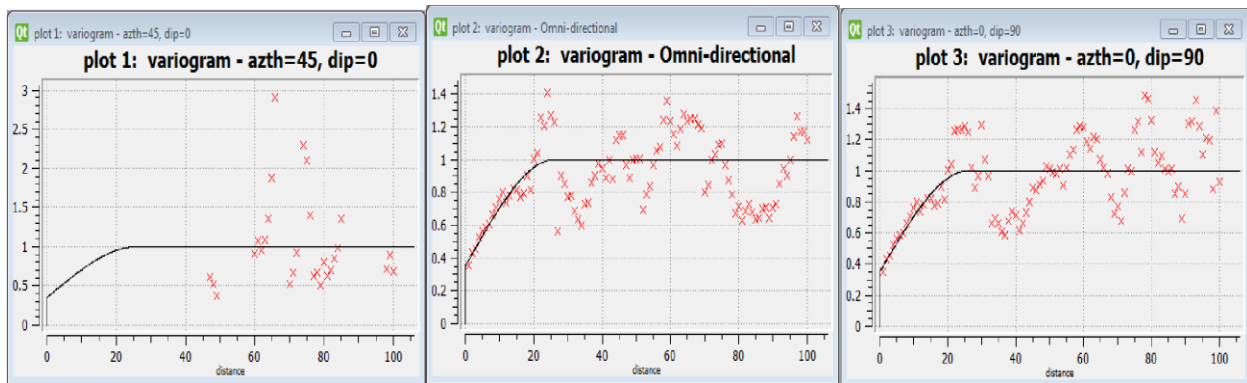


Figure (5.12): Porosity variograms

Figure (5.12) shows the 3 porosity variograms; in theory, they should all give the same values of range, nugget and sill. As can be seen in Figure (5.12) plot 2 of the omni directional variogram and plot 3 of the vertical variogram show the same trends, but plot 1 with an azimuth of 45 degrees does not show any reliable results. This is expected because the wells in the field are not all aligned in one direction – thus, the variogram could not be implemented successfully. In this case the values will be taken from plot 2 and 3 only. The sill as can be seen from plot 2 and 3 is 1 exactly; this was expected as the data were transformed (Gaussian distribution) before computing the variograms. The variograms also showed a range of around 25 meters and a nugget effect of around 0.35. Lastly all the variograms showed a spherical behavior.

The output from the variograms is used to start the SGS algorithm in S-Gems. This process populates the computational domain cells with the porosity values. After the implementation of this algorithm all the 24,000 grid blocks now have been allocated porosity values.

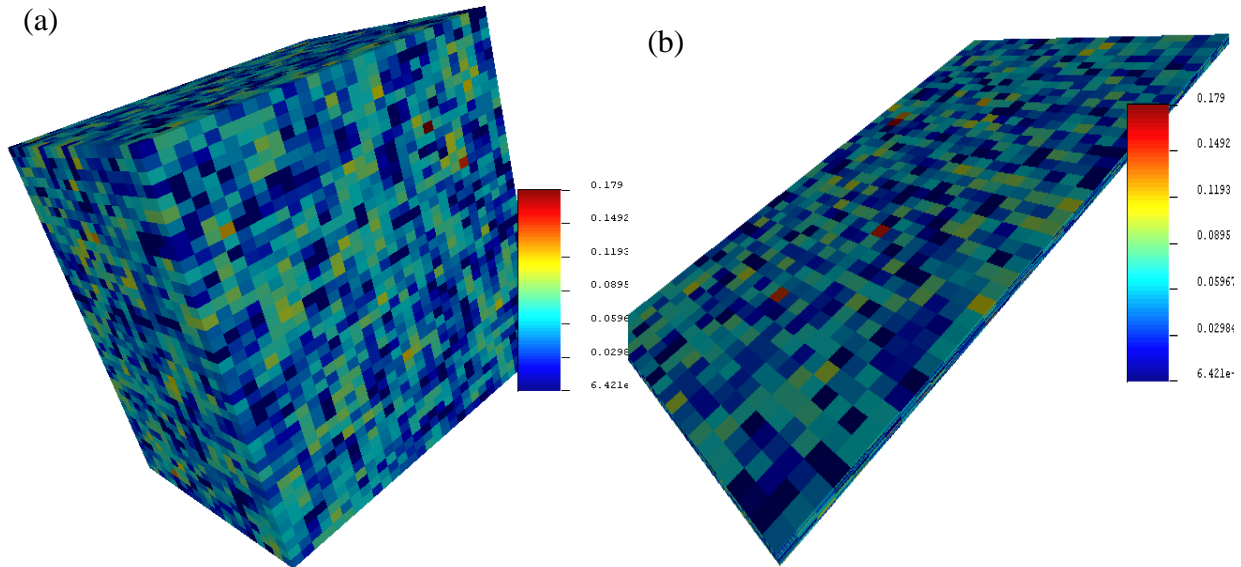


Figure (5.13): Porosity population a) scaled (factor of 100) b) unscaled

Figure (5.13) like Figure (5.8) due to the fact that the field's horizontal dimensions are much greater than the vertical length/dimension two figures were produced, to be able to see clearly the variation of the porosities in the domain. Figure (5.13), (a) is an unscaled version where the model can be seen as a very thin sheet, and (b) the Z - dimension was enlarged to view the distribution better. It can be seen that most of the grid blocks have a blue color, indicating that most of the reservoir has porosity value of around 5%. This is in agreement with the median value of 5.18% obtained from Figure (5.14).

To ensure the population process is carried out correctly, it is important to compare the porosity statistical values after population, as shown in Figure (5.14) with the porosity statistical values before population as shown in Figure (5.10). Comparing the mean, variance, median, upper and lower quartile we see that the values are very similar, which means that the distribution from the well logs is the same as the distribution after the population.

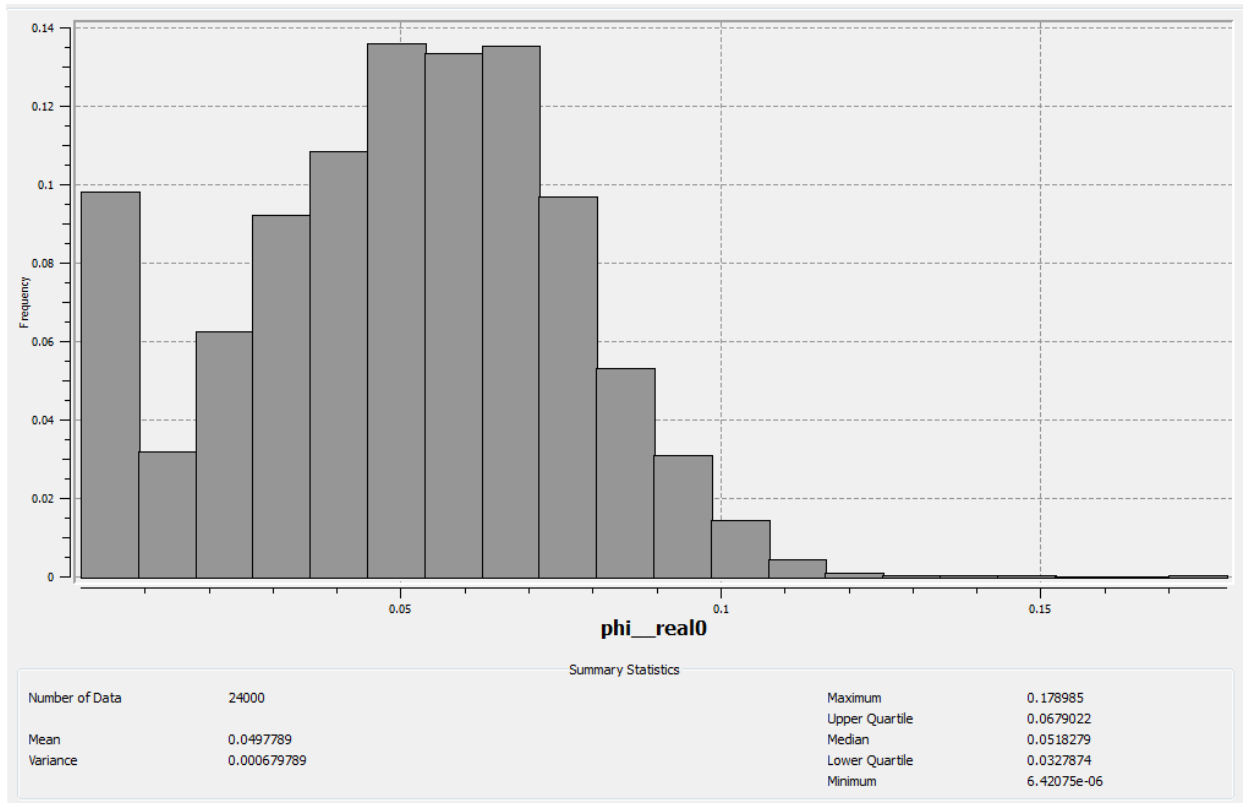


Figure (5.14): Porosity histogram after population on the grid showing 24,000 data points and a mean of 0.049, median of 0.0518 and a variance of 0.00068

5.3.3 Rock Typing Population

In section 5.2 rock characterization procedures were implemented, which led to the identification of 8 different rock types. These rock types need to be distributed within the computational domain, so that the permeability values can be obtained within each grid cell. As with the porosity population, the log data from the 33 wells is used, whilst using the core permeability values for comparison/validation with the log data. Unfortunately, we can not use the rock characterization techniques on the permeability log data because the permeability calculated from the log data is not reliable as the porosity from the log data or as the core data.

5.3.3.1 Implementation of the Artificial Neural Network (ANN)

To effectively make use of the porosity log data, an ANN technique is used. The 1150 core samples available from the 13 wells, are used to train an ANN to predict the rock type. The logs, as stated

earlier, are available from all 33 wells. The ANN predicts the rock type in all the areas where porosity log data is present i.e. in all 33 wells – whether cored or uncored.

The **Pytorch** (Paszke et al., 2019) open source machine learning library is used in this process. The ANN used was 2 layers deep with 120 nodes in each layer. The input data for the ANN that is used to predict the rock type are the NPHI, RHOB, RES, and the GR logs.

The input data was prepared such that each core sample’s rock type that was calculated in the rock characterization process, has the 4 log readings at the same depth as the core sample. This process was done on all the 1150 rock samples, to find the log reading corresponding to the same depth of the core in the same well.

The Pytorch library works with categorical/indicator variables – hence the input data are transformed into 1 and 0; just like it was mentioned in section 5.2.7 for the S-Gems when dealing with categorical variables. When the rock type values are transformed to 1 and 0, we will end up having 8 indicators; indicating a 1 if this rock type is present and a 0 if it is not. This process is done to all the 1150 data sets and on all the 8 rock types. The BRCC created to do this for S-Gems was used to do the same for Pytorch. Figure (5.15) shows a sample of the data prepared for Pytorch.

	A	B	C	D	E	F	G	H	I	J	K	L	M	N
1	core no.	Gamma	Neutron	RHOB	R(D)	fzi	i1	i2	i3	i4	i5	i6	i7	i8
2	1	41.32	0.06	2.52	6.09	8	0	0	0	0	0	0	0	1
3	2	14.62	0.03	2.52	12.26	8	0	0	0	0	0	0	0	1
4	3	14.25	0.03	2.5	16.15	5	0	0	0	0	1	0	0	0
5	4	35.78	0.05	2.52	13.47	5	0	0	0	0	1	0	0	0
6	5	26.87	0.02	2.54	18.57	5	0	0	0	0	1	0	0	0
7	6	20.41	0.04	2.53	11.47	7	0	0	0	0	0	0	1	0
8	7	14.89	0.03	2.52	15.28	3	0	0	1	0	0	0	0	0
9	8	16.73	0.03	2.51	22.77	6	0	0	0	0	0	1	0	0
10	9	11.97	0.02	2.5	25.28	4	0	0	0	1	0	0	0	0
11	10	11.39	0.02	2.52	38.46	7	0	0	0	0	0	0	1	0
12	11	25.61	0.03	2.5	12.24	3	0	0	1	0	0	0	0	0
13	12	15.04	0.02	2.51	57.37	1	1	0	0	0	0	0	0	0
14	13	28.49	0.03	2.49	12.62	4	0	0	0	1	0	0	0	0
15	14	22.18	0.03	2.55	12.41	4	0	0	0	1	0	0	0	0
16	15	11.4	0	2.55	63.85	6	0	0	0	0	0	1	0	0
17	16	15.31	0.02	2.53	23.04	6	0	0	0	0	0	1	0	0
18	17	12.52	0.02	2.51	19.95	5	0	0	0	0	1	0	0	0
19	18	13.86	0.03	2.52	10.55	2	0	1	0	0	0	0	0	0
20	19	14.34	0.03	2.49	9.51	6	0	0	0	0	0	1	0	0
21	20	11.44	0.02	2.53	49.78	6	0	0	0	0	0	1	0	0

Figure (5.15): Data preparation for Pytorch

	A	B	C	D	E	F	G	H	I
1	sample no.	i1	i2	i3	i4	i5	i6	i7	i8
2	1	0.002337	0.068463	0.217132	0.239527	0.131334	0.173058	0.140304	0.027845
3	2	0.000593	0.036123	0.218684	0.269395	0.118305	0.200896	0.091006	0.064998
4	3	0.000582	0.037245	0.23347	0.26807	0.114194	0.221014	0.079894	0.045531
5	4	0.000265	0.023411	0.19912	0.296734	0.123738	0.207077	0.094576	0.055078
6	5	0.000112	0.013141	0.153826	0.327682	0.131193	0.153938	0.111708	0.108401
7	6	9.27E-05	0.011717	0.1477	0.335309	0.133041	0.149459	0.114623	0.108058
8	7	0.000103	0.012653	0.153045	0.330915	0.132521	0.15793	0.113286	0.099547
9	8	0.000767	0.041457	0.229972	0.260005	0.112073	0.192783	0.080387	0.082557
10	9	5.97E-05	0.00754	0.104402	0.333205	0.117167	0.061702	0.105584	0.27034
11	10	2.23E-05	0.004712	0.082376	0.315516	0.103022	0.051722	0.103533	0.339097
12	11	0.000177	0.014464	0.136318	0.314779	0.123184	0.086372	0.10895	0.215756
13	12	9.27E-05	0.010408	0.124773	0.339612	0.136051	0.103369	0.132001	0.153693
14	13	0.000554	0.031	0.190088	0.272425	0.114767	0.133369	0.091025	0.166772
15	14	0.000624	0.035258	0.208168	0.267221	0.114917	0.165557	0.088331	0.119924
16	15	0.001637	0.062557	0.262157	0.235809	0.101532	0.186298	0.064995	0.085015
17	16	0.00567	0.112624	0.28642	0.195575	0.088099	0.139934	0.054294	0.117384
18	17	0.000136	0.014517	0.15349	0.325143	0.136674	0.157213	0.125723	0.087104
19	18	0.001101	0.051448	0.248209	0.245896	0.106845	0.199562	0.072756	0.074183
20	19	0.003365	0.084999	0.247323	0.222919	0.113654	0.167586	0.098124	0.06203

Figure (5.16): Pytorch output

Figure (5.16) shows the output from the Pytorch, which is the percentage probability for each indicator to occur in this data set with these log input parameters. The sum of the probabilities of all the indicator classes is always 1; for example, the sum of all probabilities for core sample 1 in all the rock types is 1. The indicator of the highest probability was chosen to be the indicator at this corresponding data point.

To check the accuracy of the ANN, after the network was trained using the core samples, the trained ANN was run again without the core data rock types. The ANN predicted the rock type of all 30,000 log readings, at the exact location of each core sample. The predicted rock type from the ANN was compared with the actual rock type from the core samples. To calculate the accuracy an IF statement was written on EXCEL; if the actual value minus the predicted value gives a zero, then the cell shows 1; if the result is anything other than zero the cell shows 0. At the end the sum of all the 1150 cells was taken to see how many correct predictions were made by the ANN. The

total number of correct predictions was 984 data point, hence the percentage of correct values is $(984/1150)*100 = 85.6\%$.

This percentage of accuracy is accepted in the petroleum industry, especially as our only other option would be to use the 1150 samples from the 13 wells to populate the whole reservoir and neglect the information from the 33 wells.

5.3.3.2 Implementation of the Sequential Indicator Simulation (SISIM) approach

After identifying the rock type in all the wells, it is necessary to populate the rock types within the whole computational domain representing the reservoir, following a similar process as was done with populating the porosity values section 5.3.2. As explained in section 3.4, unlike porosity; rock type is a categorical property. Thus, a slightly different method is used – known as the SIS instead of SGS. To perform SIS the data must first be transformed into 0 and 1 just like when dealing with the ANN. Also unlike porosity the data here does not have to be normally distributed because the data is already in the categorical 0 and 1 format. Figure (5.17) shows the histogram of the rock types from all the 33 wells after using them as input into the S-Gems software and before population.

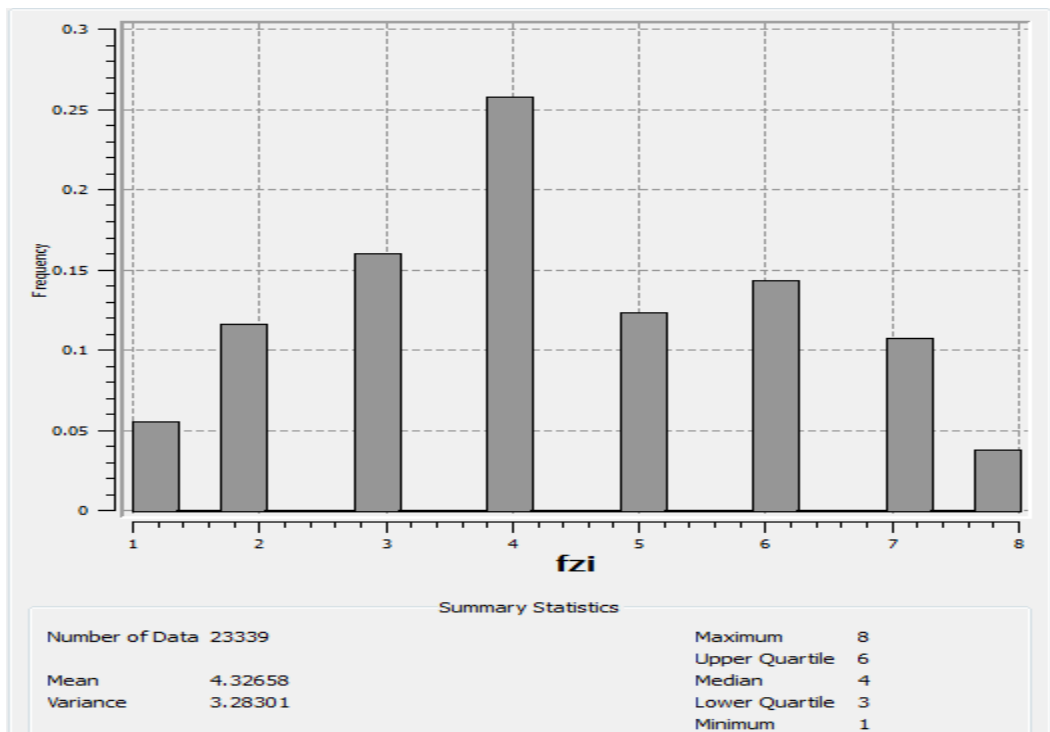


Figure (5.17): Rock types histogram after ANN on all the wells using 23,339 data points, showing a mean of 4.33 and a variance of 3.28

The SIS just like the SGS needs a variogram - a separate variogram for each rock type - because it deals with each rock type as an individual property. Three variograms as mentioned in section 3.4 are computed again for each rock type; all the variograms had a lag number of 100, a lag distance of 10 meters and a lag tolerance of 5 meters. The three variogram directions made are:

- I. Horizontal semi-variogram with an azimuth angle of 45 degrees, dip angle of 0 degrees, tolerance of 25 degrees, and bandwidth of 100 meters.
- II. Omni directional horizontal semi-variogram with an azimuth angle of 0 degrees, dip angle of 0 degrees, tolerance of 180 degrees, and a bandwidth of 1000 meters to capture all the data.
- III. Vertical semi-variogram with an azimuth angle of 0 degrees, dip angle of 90 degrees, tolerance of 1 degree, and a bandwidth of 1 meter.

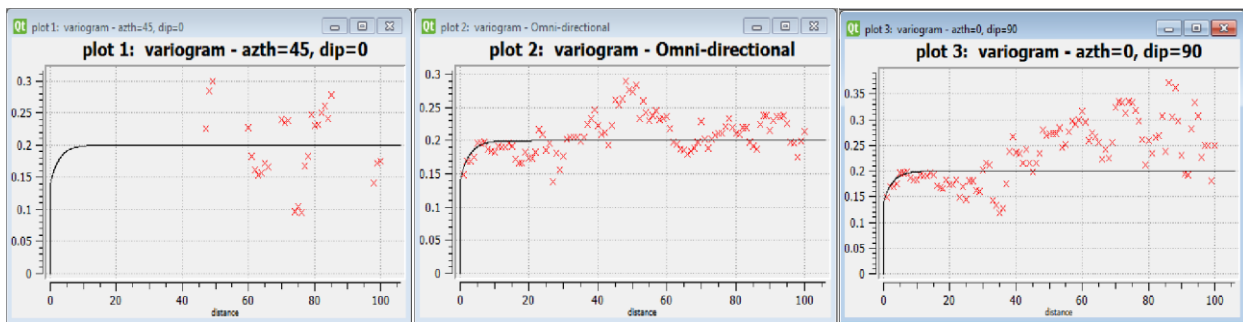


Figure (5.18): Rock type variogram sample

Figure (5.18) shows the three variograms in the three different directions for the first rock type as a sample, the rest of the 7 variograms for the rest of the rock types showed a similar behavior but with different values, so we will explain the first rock type only.

As mentioned earlier in the porosity variograms in section 5.3.2, the three variograms should give all the same values of range, nugget and sill. As can be seen in Figure (5.18) plot 2 of the omni directional variogram and plot 3 of the vertical variogram show the same trends, but plot 1 with an azimuth of 45 degrees does not show reliable results. This is expected as in the porosity variograms, because the wells in the field are not all aligned in one direction so the variogram was not able to find that much data points to use. In this case the values will be taken from plot 2 and 3 only. The sill as can be seen from plot 2 and 3 is around 0.2, unlike the porosity it was exactly 1

because the values were transformed. The variograms also showed a range of around 10 meters, a nugget effect of around 0.15, and all the variograms showed a spherical behavior.

Before starting the SIS, the exact percentage of each rock type should be calculated; unfortunately we can not accurately estimate this from the rock type histogram in Figure (5.17) – hence, EXCEL calculations were carried out. Table (5-4) shows the percentages of each rock type after being computed from EXCEL.

Table (5-4): Rock type percentages

Rock Type	1	2	3	4	5	6	7	8	Total
Sample no.	1289	2703	3726	6012	2875	3340	2510	884	23339
Percentage fraction	0.0552	0.1158	0.1596	0.2575	0.1231	0.1431	0.1075	0.0378	1

The output from the variograms and the percentages are used to start the SIS algorithm in S-Gems. After the algorithm is implemented all the 24,000 grid cells fall within a particular rock type.

Figure (5.19) like Figure (5.8) and Figure (5.13) due to the fact that the field’s horizontal dimensions are much greater than the vertical length/dimension two figures were produced, to be able to see clearly the variation of the porosities in the domain. Figure (5.19), (a) shows an unscaled version where the model can be seen as a very thin sheet, (b) shows the Z scale was enlarged to view the distribution better. The legend shows values of the rock types from 0 to 7, and not from 1 to 8. This is because the SIS does not take the indicator number into consideration, meaning that if for instance the rock type numbers start form 10 till 15, the algorithm will start from 0 till 4. Hence, in our case the 0 refers to 1 and the 1 refers to 2 and so on.

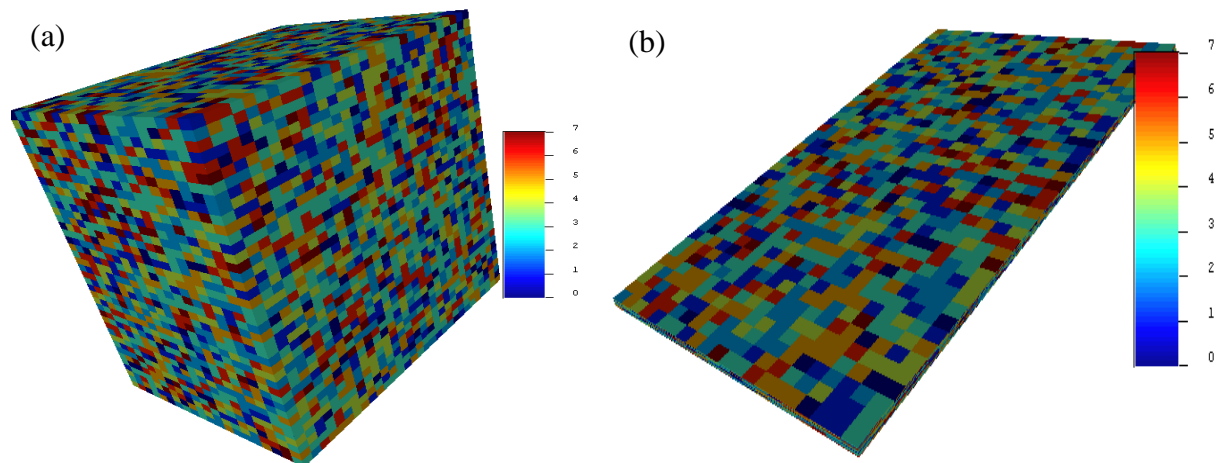


Figure (5.19): Rock type population a) scaled (factor of 100) b) unscaled

Figure (5.20) shows the histogram of the rock type values after being populated, the values have a median value of 3.325 and in Figure (5.17) the median value was 4.326, taking into account what was mentioned earlier, rock type 4 is rock type 3 after the simulation. To make sure that the population process took place correctly, the rock type statistical values after population shown in Figure (5.20) should be compared to the rock type statistical values before population shown in Figure (5.17). Comparing the mean, variance, median, upper and lower quartile we see that the values are very similar, which means that the distribution from the well is the same as the distribution after the population.

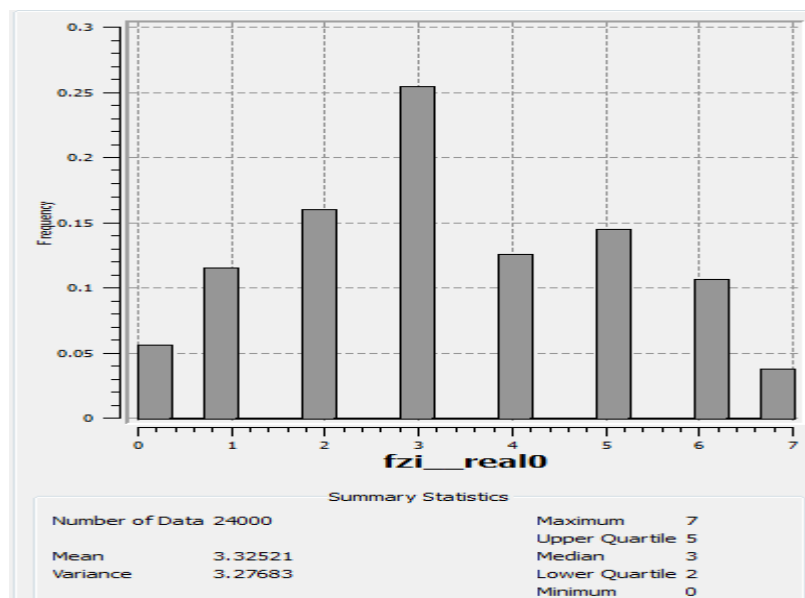


Figure (5.20): Rock type histogram after population on the grid showing 24,000 data points and a mean of 3.33 and a variance of 3.28

5.4 Relative Permeability and Capillary Pressure

Relative permeability and capillary pressure are essential inputs for solving multiphase flow equations/simulation. Normally the relative permeability and capillary pressure curves are obtained from SCAL. Unfortunately, the data obtained from the field site did not contain SCAL data. As mentioned in section 3.5.2 in the absence of SCAL, two phase relative permeabilities can be calculated from resistivity data from logs using the model reported by (Li, 2008).

The steps are as follows:

- (1) Obtain all the deep resistivity and the water saturation logs data for each rock type, and subsequently determine the residual water saturation, and the minimum water saturation from the logs for each corresponding rock type.
- (2) Determine the fully water saturated formation resistivity (R_o) for each rock type; this is the deep resistivity at 100% water saturation.
- (3) Consider a random sample from each rock type and obtain the water saturation and the deep formation resistivity (R_i) for each one of them.
- (4) Calculate the resistivity index (I_r) and the S_w^* for each rock type from equations (3-23) and (3-22) respectively.
- (5) Calculate the relative permeability of the wetting phase (water) at the corresponding water saturation (K_{rw}), using equation (3-21) – as I_r and the S_w^* are now known.
- (6) Implement equation (3-24) to determine the pore size distribution index (λ). Table (5-5) shows all the readings for each rock type used to calculate the pore size distribution index.

Table (5-5): Lamda calculation

Rock type	Swr	Ro	Sw	Rt	Sw*	Ir	Krw	Lamda (λ)
1	0.234	9.3216	0.8053	12.4816	0.745822	1.338998	0.557001	2.1
2	0.187	8.9026	0.654	19.5088	0.574416	2.19136	0.262128	1.41
3	0.201	7.7291	0.516	25.1198	0.394243	3.250029	0.121304	1.58
4	0.19	8.5053	0.6522	21.6262	0.570617	2.542673	0.224416	1.2
5	0.18	6.4739	0.7637	11.472	0.711829	1.772038	0.401701	1.19
6	0.231	9.2926	0.661	15.3068	0.559168	1.647203	0.339465	2.33
7	0.243	7.7469	0.6104	23.3152	0.485337	3.009617	0.161262	1.31
8	0.249	10.6303	0.5445	21.7835	0.393475	2.04919	0.192015	2.6

After getting the λ for each rock type, to get the relative permeability curve for the wetting phase (K_{rw}), equation (3-22) is repeated for equal intervals of S_w starting from the S_{wr} to 1, then equation (3-21) is repeated again for all the new S_w^* to get the K_{rw} .

To get the relative permeability of the non-wetting phase (Oil) equation (3-25) is used with the same S_w^* intervals used for the wetting phase. Now we can plot the two-phase relative permeability curve. Figure (5.21) shows the relative permeability for rock type one as an example of the plots created for all the rock types.

Unfortunately, as mentioned earlier SCAL data was not given for the field, so capillary pressure data cannot be computed for each rock type. To overcome this issue, capillary pressure

data was taken from an analogous field. To calculate capillary pressure for each rock type equation (3-14) was used using the same entry pressure for all of them as the entry pressure from the analogous field and different S_{wr} and Lamda (λ) were obtained from Table (5-5). Figure (5.22) shows the capillary pressure curve from the analogous field used.

5.5 Fluid Properties

PVT analysis was done on oil from only two wells from the field, the PVT analysis was done under reservoir temperature of 120°C. All the tests were done on pressure ranges starting from the reservoir initial pressure (~6000 psi), passing by the bubble point pressure (~2000 psi), till the

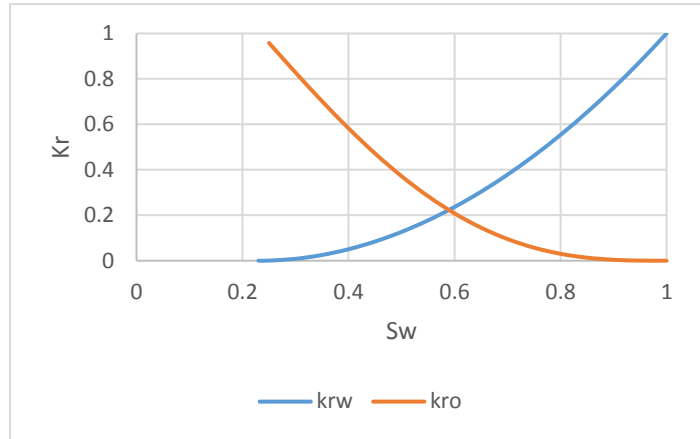


Figure (5.21): Rock type 1 2-phase relative permeability

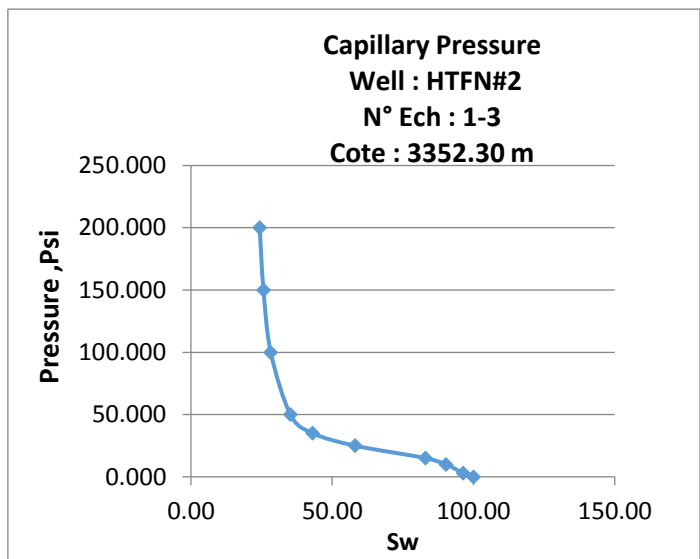


Figure (5.22): Capillary Pressure from analogous field (Confidential)

atmospheric pressure (0 psi). Figure (5.23) shows the oil density, oil formation volume factor, dissolved gas oil ratio and the oil viscosity respectively.

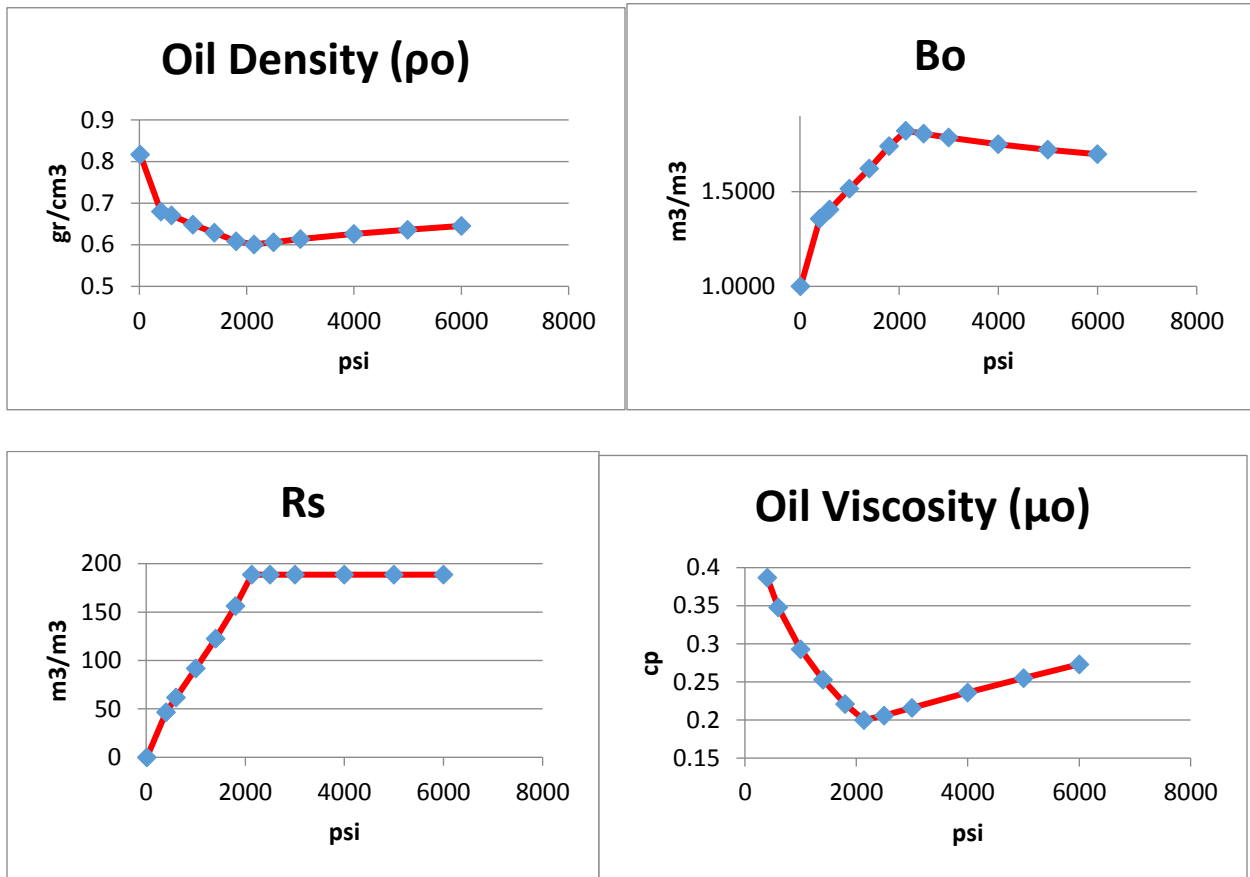


Figure (5.23): Field's fluid properties (Confidential)

As shown in Figure (5.23), all plots are only vs pressure because the temperature was constant during the tests. The oil density decreases slightly as the pressure decreases from the initial reservoir pressure to the bubble point pressure, below the bubble point pressure and up to the atmospheric pressure the density increases sharply. The oil formation volume factor (B_o) is defined as the ratio of the volume of oil (plus the gas in solution) at the prevailing reservoir temperature and pressure to the volume of oil at standard conditions (Ahmed, 2001b). The B_o increases slightly as the pressure decreases from the initial reservoir pressure until the bubble point; below the bubble point and towards atmospheric pressure the B_o decreases sharply.

The dissolved gas oil ratio (R_s) is constant as the pressure decreases from the initial reservoir pressure until the bubble point, below the bubble point and towards atmospheric pressure the R_s

decreases intensely. The oil viscosity decreases slightly as the pressure decreases from the initial reservoir pressure until the bubble point, below the bubble point and towards atmospheric pressure the viscosity increases intensely.

Chapter 6 Computational Setup of the Real Field Case using IC-FERST and ECLIPSE simulators

This chapter presents the process of constructing the real field simulation model using both the Open Source IC-FERST simulator, and the commercial software ECLIPSE. The reservoir data analyzed in Chapter 5, yielding the porosity, rock types, permeability, relative permeability and capillary pressures values in the real field reservoir are used as input to the simulations. The simulations consist of three steps : (I) the pre-processing stage, where the mesh was created with the input geometry of the reservoir; (II) the processing stage – with the various model parameters inserted such as: the boundary conditions; fluid properties (density, viscosity); reservoir properties (porosity, permeability and capillary pressure) and solver parameters; and (III) the post processing stage, where the output was displayed in various forms. The full comparison of the results between the IC-FERST and ECLIPSE simulations is presented in Chapter 7.

6.1 IC-FERST

6.1.1 Pre-Processing Using Trelis (IC-FERST Pre-Processor) – Geometry Setup

As mentioned earlier in section 3.3.1, Trelis is used as a pre-processor for IC-FERST to construct the model mesh. The first step requires defining the vertices or the points that bound the reservoir; these points are taken from the pre-constructed geometry, in the Cartesian coordinate system (X,Y,Z) for the field on PETREL. Figure (5.1) shows the (X, Y) coordinates of the vertices. Figure (6.1) shows the vertices after inserting them into Trelis, Figure (6.1) (a) shows the top view of the vertices, which looks exactly as in Figure (5.1). Two side-views are also shown in Figure (6.1) (b) and (c) which are unscaled and scaled respectively.

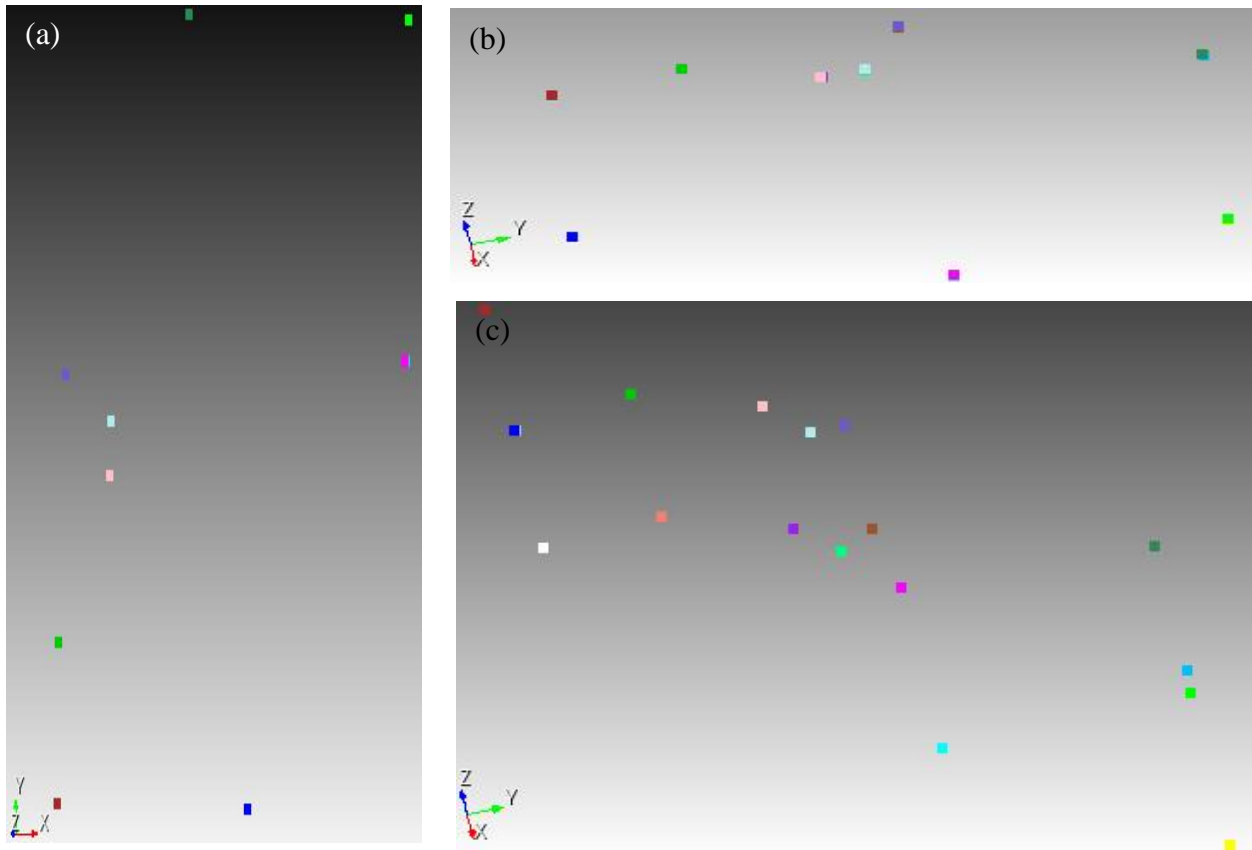


Figure (6.1): Model Vertices a) top view b) side view unscaled c) side view scaled in the Z-direction (factor of 100)

After defining the vertices for the model, these vertices have to be connected with lines, then the set of lines that create a surface are chosen to create the surface, finally a set of surfaces that are required to define a volume are selected as well. Figure (6.2) shows the surfaces after defining them, Figure (6.1) (a) shows the top view of the model, which again looks like Figure (5.1) Figure (6.1) (b1) shows an unscaled side view version where the model can be seen as one thin sheet only, and Figure (6.1) (c) shows a scaled side view where the Z scale was enlarged with a factor of 100 to view the model better.

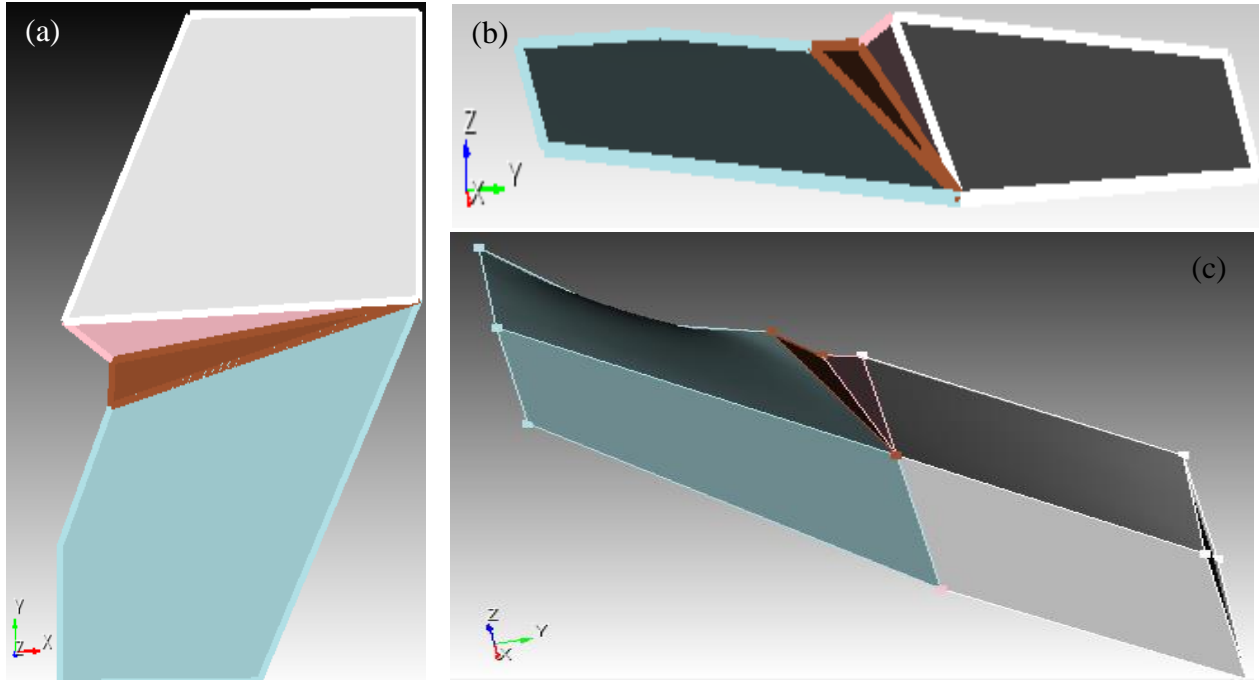


Figure (6.2): Model surfaces a) top view (x-y plane) b) side view unscaled (y-z plane) (c) side view (y-z plane) scaled (factor of 100)

After defining the surfaces 4 volumes were defined as shown in Figure (6.2) because Trelis was not able to create a full surface that takes all the top vertices together, after that all the 4 volumes were united into one volume. All the external surfaces are given the same surface ID. The next step is to define the wells, the wells are defined as bricks with dimensions of 0.5m X 0.5m and a length of the whole reservoir. The wells are all defined as one volume, but the top of the wells are defined as different surface IDs to allow for different boundary conditions to be applied for injection and producing wells separately and to be able to view the results for each well separately. The well's locations are defined as seen in Figure (5.1) and Table (5-1).

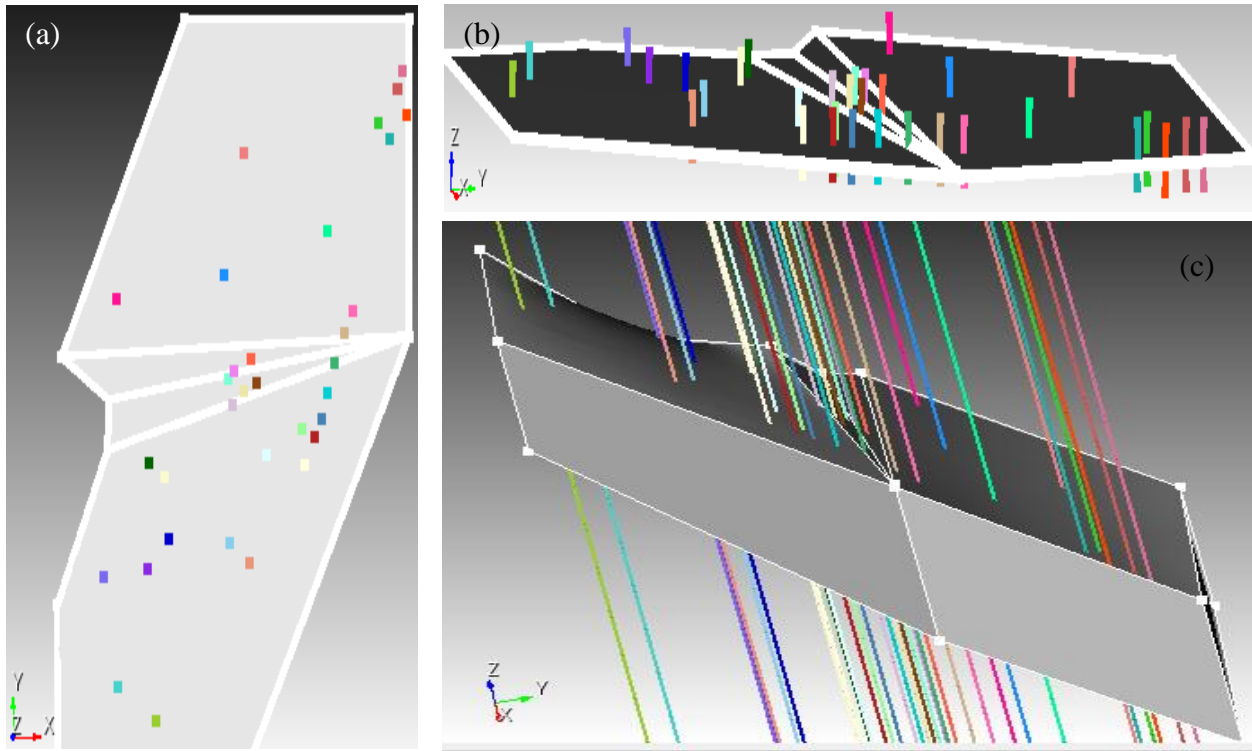


Figure (6.3): Model with wells a) top view (x-y plane) (b) side view (y-z plane) unscaled (c) side view (y-z plane) scaled in the Z-direction (factor of 100)

Figure (6.3) shows the computational domain with the wells; Figure (6.3) (a) shows the top view of the model; Figure (6.3) (b) shows the unscaled side view (y-z plane) where the wells can be seen as very small lines; Figure (6.3) (c) shows the scaled in the Z-direction with a factor of 100 side view (y-z plane) where also the wells can be seen as long lines.

The whole model is divided into two volumes, (V1) the reservoir and (V2) the wells. The model was divided into 34 surfaces, (S1) all the boundaries excluding the well tops; (S2-34) all the well tops. The well tops were given the same surface ID number as their name in trellis shown in Table (5-1).

After defining the wells as shown in Figure (6.3), the wells are subtracted from the reservoir to be cut exactly on the surface of the reservoir and the bottom of the reservoir as shown in Figure (6.4).

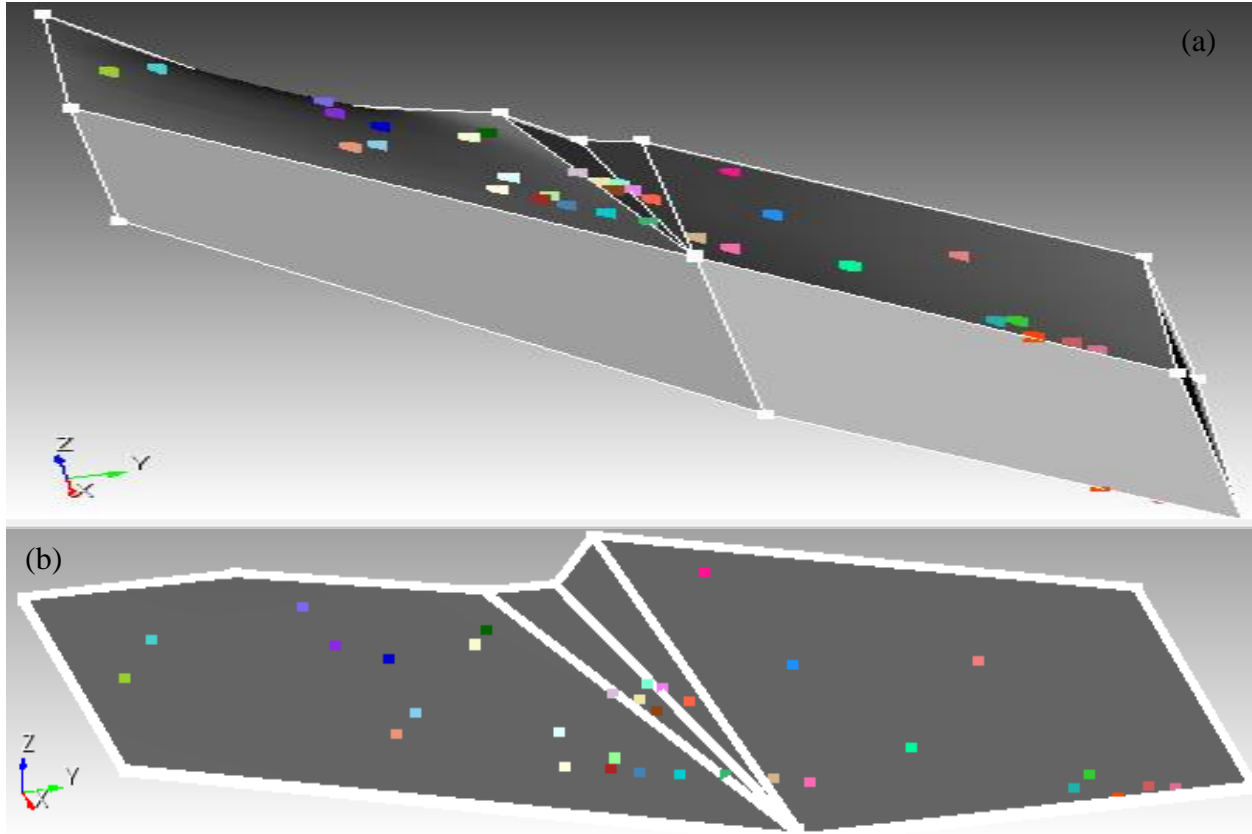


Figure (6.4): Model after subtracting wells a) scaled (factor of 100) b) unscaled

6.1.1.1 Computational Mesh

After all the volumes and surfaces are defined and the wells are placed, the computational domain is ready to be meshed. As mentioned earlier in section 3.3.1 the Trelis smart meshing tool was used to generate the meshes for this model. A tetrahedral mesh was chosen with the finer mesh possible to ensure minimum numerical dispersion error and mesh-independency. The total number of tetrahedral elements created by Trelis was 223,782 elements. Figure (6.5) shows the computational mesh created by Trelis. The mesh file is saved in an Exodus format and as mentioned earlier in section 3.3.2 it is transferred to a GMSH format (file.msh) using a python script developed by the ICFESRT developers' team. This is the input format as required by the IC-FERST simulator.

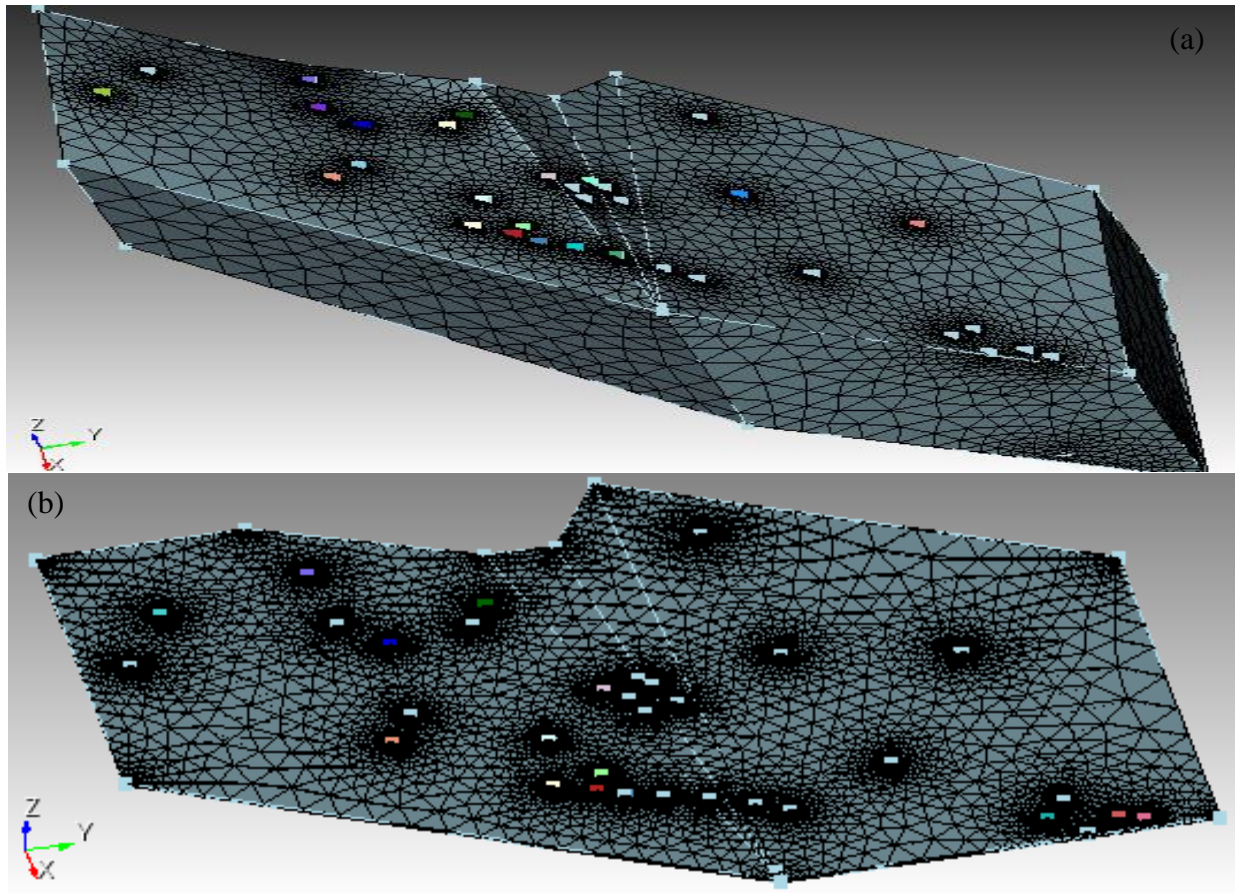


Figure (6.5): Final model after meshing a) scaled (factor of 100) b) unscaled

6.1.2 Setting up the Computational Parameters Using the GUI Diamond IC-FERST simulator

After extracting the geometry mesh with the corresponding volume and surface ID of the model in an Exodus format and converting it to a GMSH format, the model parameters required for carrying out a simulation need to be set-up. These consist of: (I) the initial conditions (II) the boundary conditions; (III) the rock and fluid properties and (IV) the solver parameters including simulation run time. All these are set-up using the user friendly GUI called Diamond. As mentioned in section 3.3.2 Diamond creates an input MPML file that is used for running the simulation using IC-FERST.

6.1.2.1 Initial Conditions

Pressures: The initial reservoir pressure is not known, so a pressure that is above the bubble point pressure was taken to avoid gas in the model. The pressure was set to be at the middle depth of the model as $3.524\text{E}+6$ Pas.

Water Saturation: The initial water saturation is also not known, and thus an assumed value of 0.25 was taken. This value is above all the S_{wr} of all the rock types. Knowing that the initial pressure is above the bubble point pressure, we will inject water to maintain it this way.

Volume fractions (oil and water): We know that there will be no gas and this model will only be two phase, so the oil initial saturation will be set to 0.75.

Velocities/Flow rates: Lastly all the initial velocities were set to zero.

6.1.2.2 Boundary Conditions

Wall Boundaries: Surface identifier number 1 represents all the wall/boundaries of the model – essentially all the outer surfaces of the computational domain, and top of the domain – excluding the top surfaces of the wells. The wall boundary condition is a no flow boundary i.e. no flow will go in or out of the model except from the wells.

Inlet boundaries: Surface identifiers of the 8 injection well tops was set to be a pressure boundary with a boundary pressure of $4\text{E}+7$ Pas.

Outlet Boundaries: surface identifiers of the 25 producing well tops was set also to be a pressure boundary with a boundary pressure of $5\text{E}+6$ Pas.

Figure (7.1) shows all the injection and production wells and Table (5-1) shows their X and Y coordinates.

The phase volume fractions around all the surfaces including the well tops was set to be 100% water, hence, the injection wells will inject water, and the producing wells will not let water in because the pressure gradient difference between the reservoir and the top of the well will not allow for water to flow in.

6.1.2.3 Fluid Properties

The oil fluid properties were taken from the PVT analysis done on the field as discussed in section 5.5 and Figure (5.23) and the water fluid properties were taken to be standard values of water. The water density in the model was set to be 1025 kg/m^3 .

Unfortunately IC-FERST does not have a built-in function to take a graph or a set of points for the oil density as it is shown in Figure (5.23) i.e. with the variation of pressure. Given that our initial pressure was above the bubble point pressure the initial pressure is maintained always above the bubble point pressure, the average oil density of 700 kg/m^3 is considered i.e the average value between the maximum pressure to the bubble point pressure. The water viscosity was also set in the model to be $8.9\text{E-}4 \text{ Pa.s}$.

As for density, the oil viscosity was also taken to be the average value between the maximum initial pressure and the bubble point pressure – yielding an average value of $3.5\text{E-}3 \text{ Pa.s}$. IC-FERST does not currently allow for an oil formation volume factor (B_o) and an dissolved gas oil ratio (R_s) factor to be calculated or used as input parameters - as ECLIPSE does, thus these parameters were not considered the IC-FERST model.

6.1.2.4 Rock Properties

The relative permeability of each rock type was assigned into Diamond using the data from Table (5-5) and as shown in Figure (5.21). This data was entered into the population MATLAB code as mentioned in section 5.2.9; the MATLAB population code distributes every rock type property over the grid according to the location. The same thing was done for the capillary pressure as mentioned in section 5.4 and as shown in Figure (5.22).

The porosity was obtained from the application of S-Gems and subsequently, the permeability was determined using the permeability porosity equations for each rock type shown in Table (5-2); these equations were then applied to the population MATLAB code to populate every cell of the computational domain with porosity and permeability according to the procedure described in section 3.5.4. As mentioned in section 3.5.4, the CSV files exported from the MATLAB population code for every rock property is entered into Diamond using a Python script that was written to read the CSV file in Diamond.

Figure (6.6) shows the rock types after being populated onto the model whilst Figure (6.7) shows the porosity after being populated onto the model as displayed using Paraview postprocessor.

6.1.2.5 Simulation Run times

The simulations were run for 40 years and outputs of flow rates, pressure and volume fractions were produced for every month. The output locations considered are the top of all production wells. The results from the IC-FERST simulations will be described and discussed in conjunction with the ECLIPSE simulation results in Chapter 7. The next section described the model set-up within the ECLIPSE software.

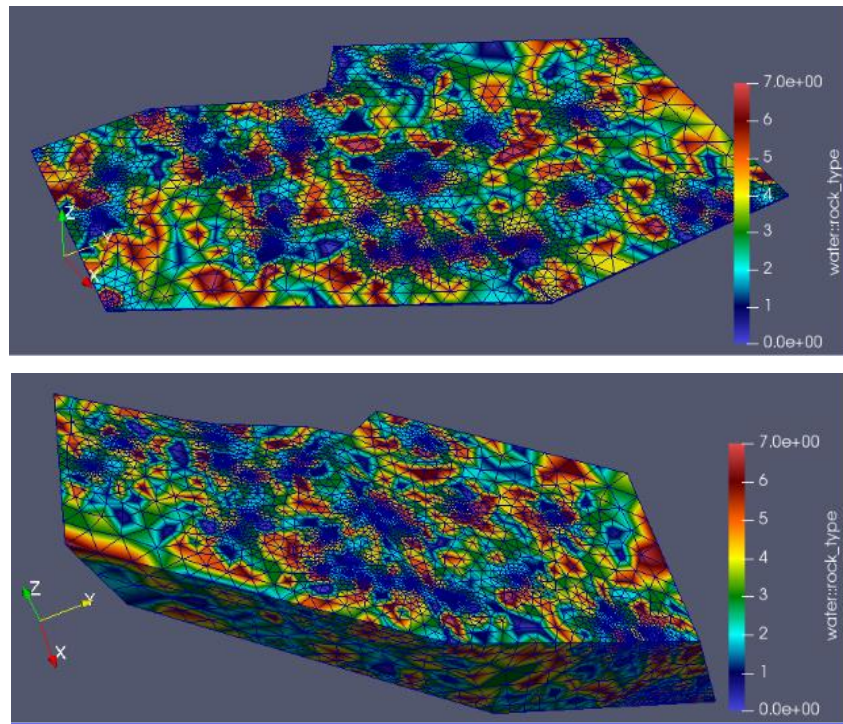


Figure (6.6): Distribution of Rock types as seen using Paraview

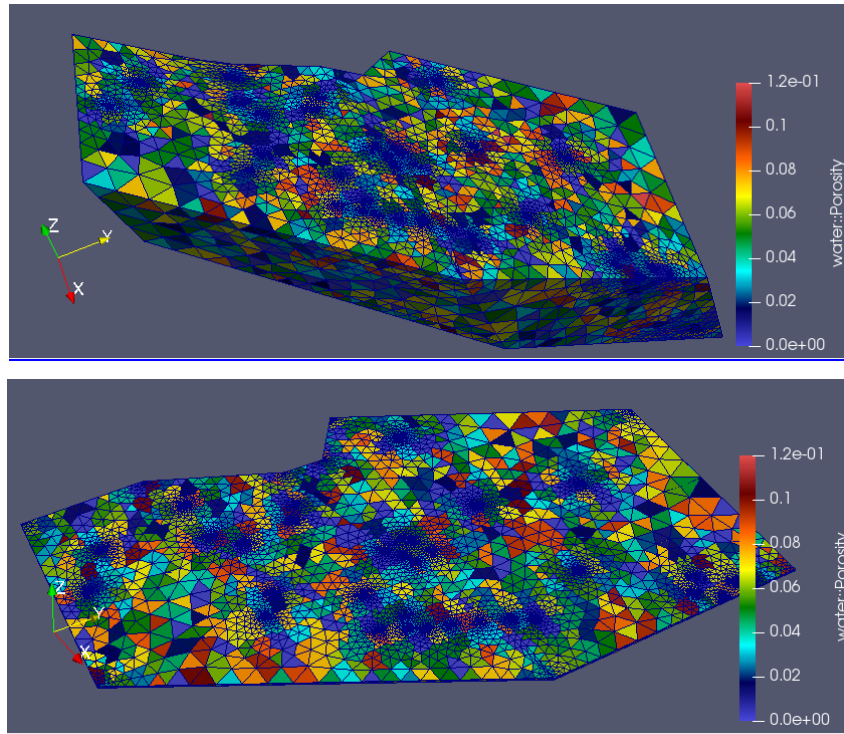


Figure (6.7): Porosity distribution within the computational domain as displayed by Paraview

6.2 ECLIPSE

6.2.1 Static Model Construction Using PETREL (ECLIPSE Pre-Processor)

As ECLIPSE is the industry standard reservoir simulator, it is important to implement it for the real field case, with the aim of comparing the IC-FERST and ECLIPSE simulation results and quantifying any differences. The ECLIPSE simulator is therefore also implemented using initially the PETREL software, as a preprocessor. As mentioned in section 3.2.1, PETREL has all the necessary subroutines integrated into it, so there will be no need to use any other external package as done within IC-FERST.

Building the real case static model of the real field, using PETREL is a very challenging process, and it requires a geologist or even a team of petroleum geologists, starting from interpreting the seismic data up-to building the model structure. The static geological model was already created and provided for the purpose of this research. Figure (6.8) shows the geological model provided. This static model was originally meshed using a cartesian grid with a total number of 944,962 grid cells.

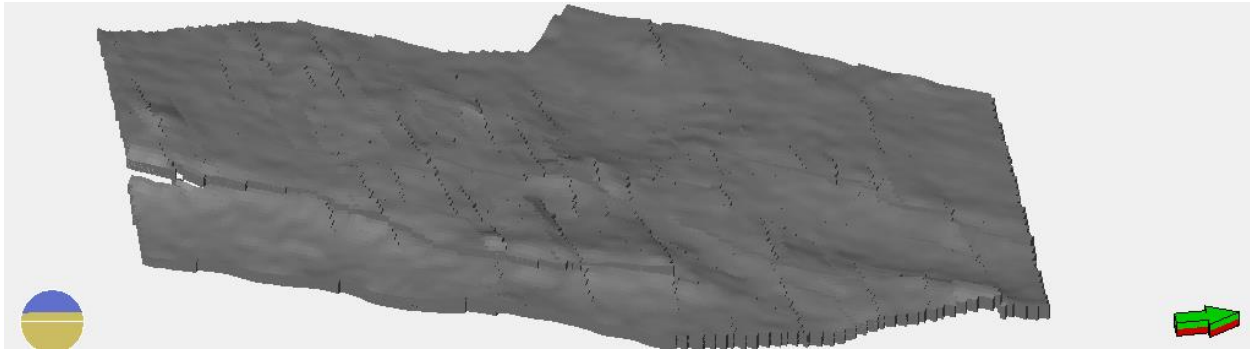


Figure (6.8): Geological model construction within PETREL

The first step is to populate the 944,946 cells with the rock properties and define the well locations and depths. The 33 wells were entered into PETREL with their locations, their depths, and the KB height as discussed in section 5.1.

Recall: the depths were converted from MD into SSTVD. The well type was also entered i.e. as to whether the well is an injector or a producer. The perforation/completion interval was also entered. All the wells were completed along the full depth of the reservoir, just as in IC-FERST implementation. Figure (6.9) shows the wells within the computational domain.

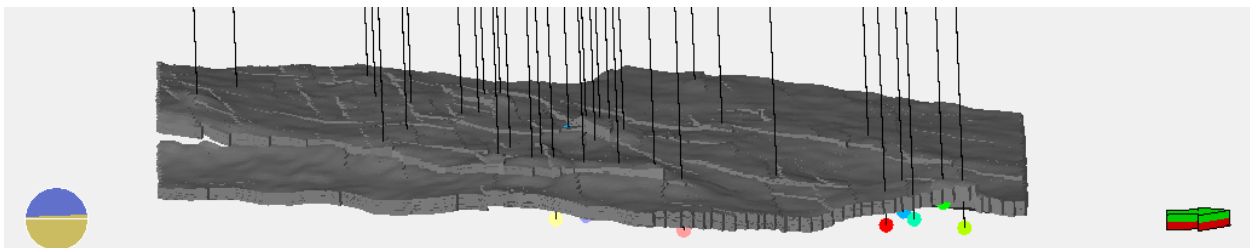


Figure (6.9): Model after adding the well locations and data

The well log data and the core analysis data were already given in LAS file format for each well, and this data was imported into PETREL. Well log data sample along with the completion data and core data sample can be seen in Figure (3.14). As mentioned in section 3.2.1 PETREL has a built-in neural network function that can determine the rock types of the reservoir automatically. However, to ensure compatibility between the IC-FERST and ECLIPSE simulations, the rock types generated earlier in section 5.2.2 by the BRCC was used and imported into PETREL.

As in section 5.3.3, all 30,000 log data points from all the wells is used - instead of only the 1150 core data; thus, the neural network function is first used to populate all the 33 wells with the 8 rock types. The next step involves populating the porosity and the rock types over all the grid data points. To achieve this, the log data should first be upscaled into the grid around the wells as shown in section 3.2.1 Figure (3.15), using PETREL's upscaling feature. Figure (6.10) shows the upscaled log porosity values for the 33 wells.

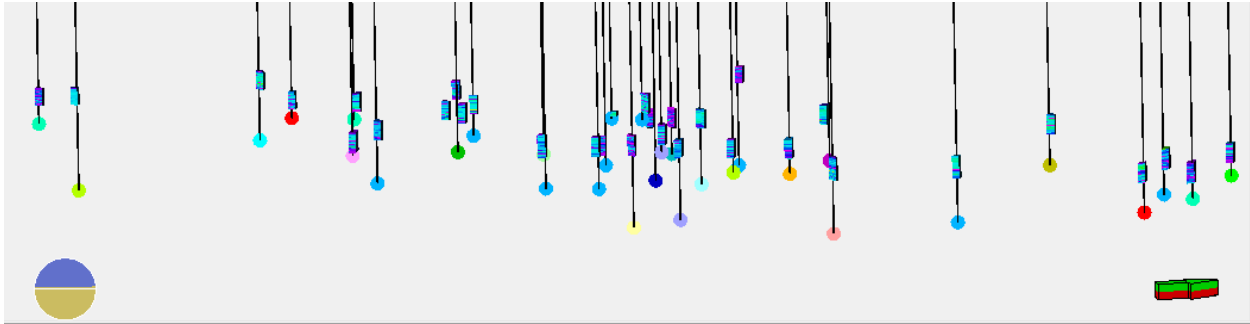


Figure (6.10): Upscaled porosity on all wells as shown in PETREL

The geostatistics functions withing PETREL are subsequently used to populate every cell within the computational domain with the two important properties i.e. of the porosity and rock typing to start with – which will subsequently lead to the permeability. The SGS is used for the porosity population and the SIS is used for the rock typing population. The mean, standard deviation, seed and the variogram options are selected as shown in Figure (6.11). The variogram is calculated automatically and the population process is carried out for all 944,962 grid cells.

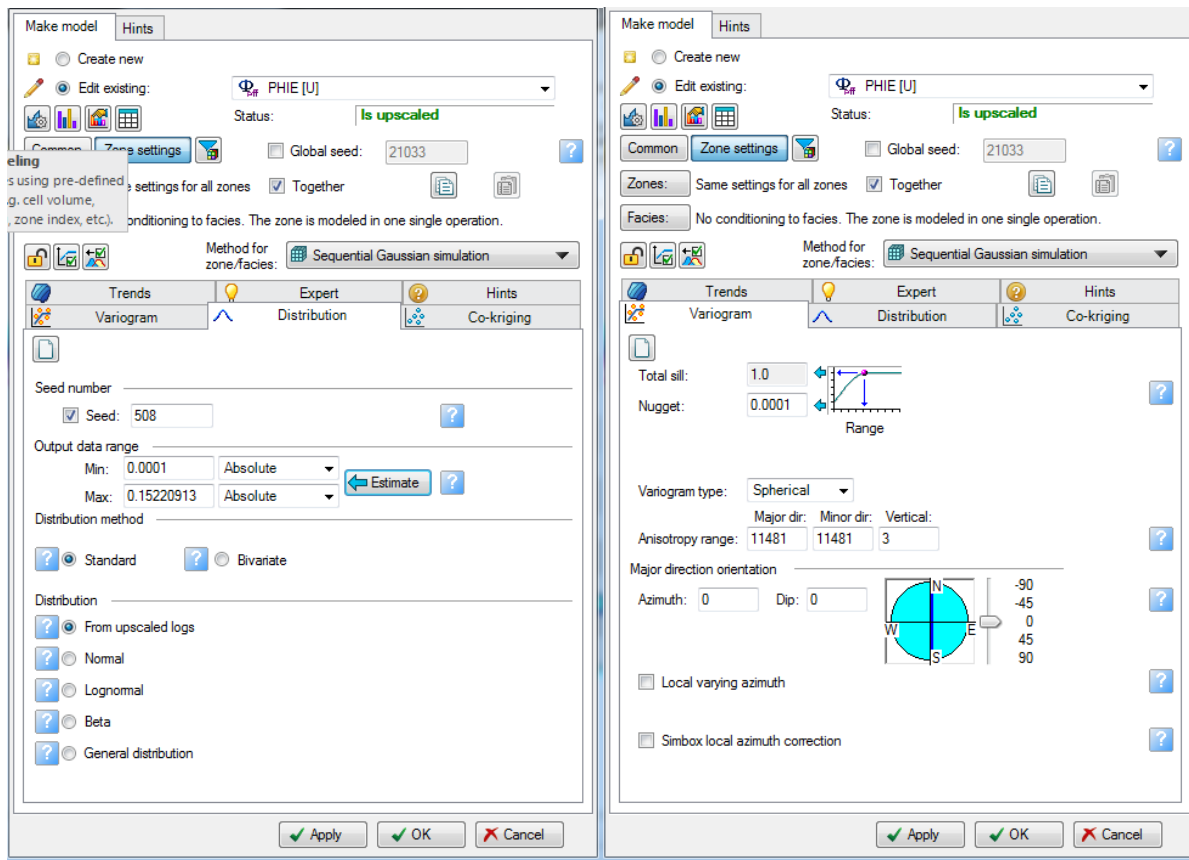


Figure (6.11): Geostatistics population options

As the porosity and the rock types are now established within each grid cell, the 8 equations generated earlier for each rock type are subsequently implemented to obtain the permeabilities in each grid cell. The PETREL calculator function is used; an IF condition is written to assign the porosity using the specific rock type permeability equation corresponding to the rock type of each grid block. Figure (6.12) shows the calculator option with the equation of the first rock type written in an IF condition to assign the porosity of this cell if the cell contains the first rock type.

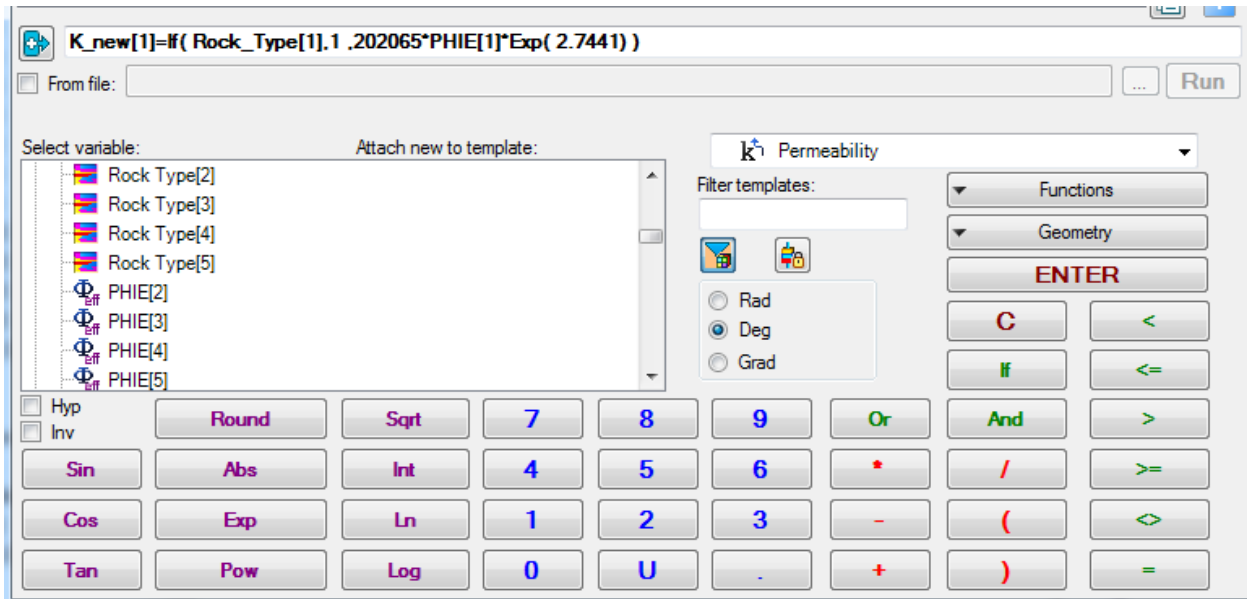


Figure (6.12): PETREL Calculator option, showing the IF statement written for the first rock type equation

The calculator option is used on all the rock types to populate the permeability in all the model grid blocks. Figure (6.13) shows the computational domain after populating all the rock types on all the grid blocks, Figure (6.14) shows the computational domain after populating the porosity on all the grid blocks.

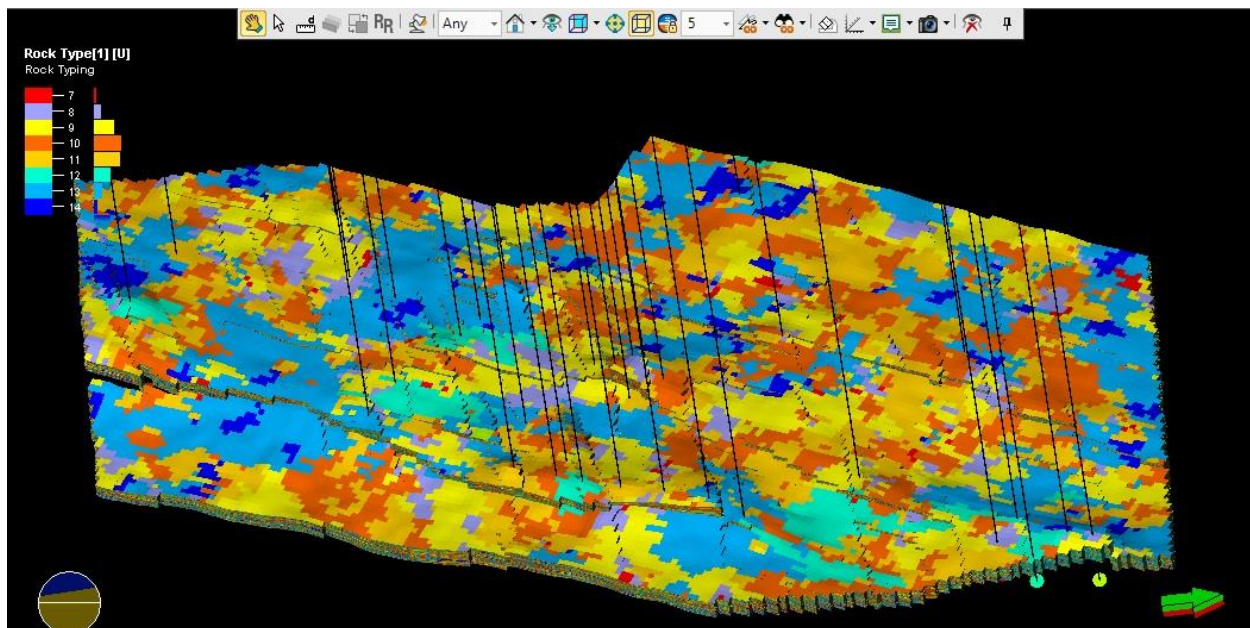


Figure (6.13): Populated rock types in PETREL

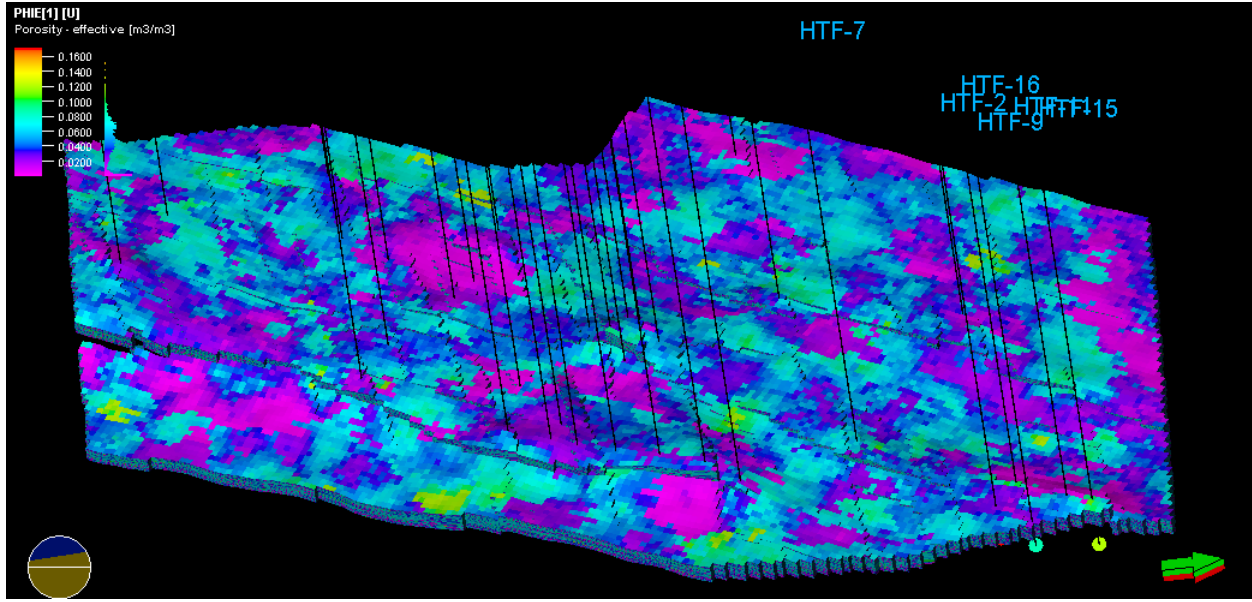


Figure (6.14): Populated porosity in PETREL

Figure (6.15) shows the histogram of the populated porosity. Comparing this histogram with the histogram of the populated porosity using S-GEMS in Figure (5.14), it is clear they follow the same trend and show close values. Figure (6.16) shows the histogram of the populated rock types. Comparing this histogram with the histogram of the populated rock type from S-GEMS in Figure (5.20) we can also see that they follow the same trend and show close values.

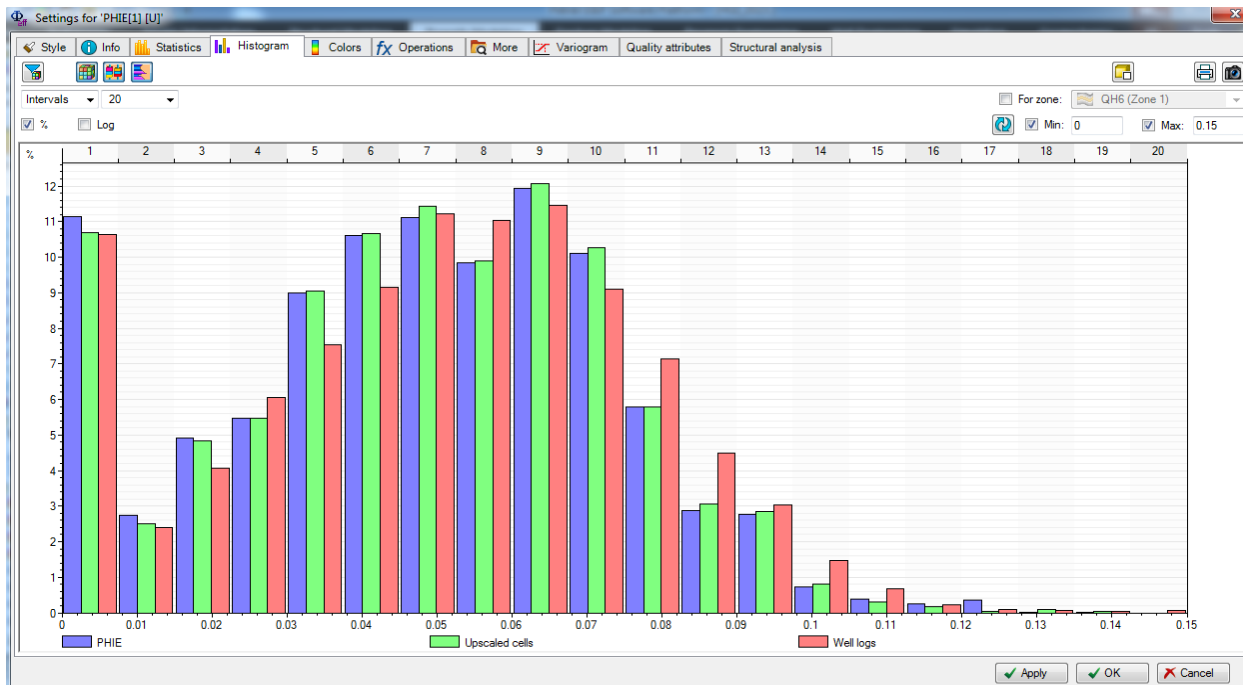


Figure (6.15): Populated porosity histogram within PETREL

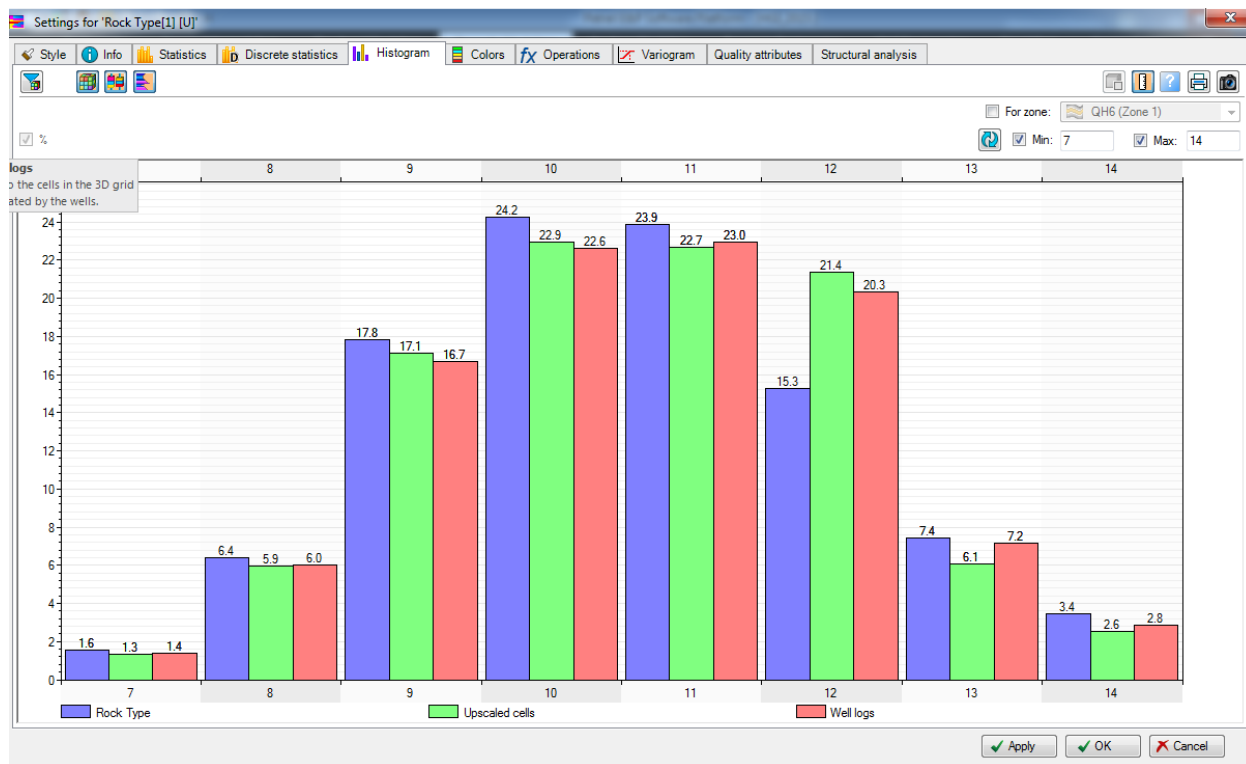


Figure (6.16): populated rock type histogram within PETREL

After populating each computational cell with the appropriate porosity, rock type and permeability, the relative permeability curves of each rock type need to be specified in each grid cell, based on the rock type. The computational domain is subdivided into regions, with each region being characterized by the rock type. Subsequently, the relative permeability curves generated in section 5.4 are entered for each region. To complete our static model the capillary pressure curve shown in Figure (5.22) is entered for all the regions in the model.

6.2.2 Dynamic Model Construction Using PETREL (ECLIPSE Pre-Processor)

Initial and boundary conditions: The model was setup from the beginning to run using Metric units and not Field units, knowing that the initial pressure is above the bubble point pressure and water was injected to maintain it this way, it is known that there will be no gas and this model will only be two phase. The first step will be adjusting the control modes of the producing and injecting wells. All the producing wells were set to produce at a constant bottom hole pressure of 50 barsa and all the injection wells were set to inject water at a constant bottom hole pressure of 400 barsa. The initial reservoir pressure was set to be 352.4 barsa at the middle of the reservoir.

Fluid Properties: The Oil fluid properties consisting of the density, formation volume factor B_o , dissolved gas oil ratio R_s and the viscosity were taken from the PVT analysis done on the field as shown in section 5.5 and Figure (5.23). The water density was set to be 1025 Kg/m^3 and the water viscosity was set to be 0.89 CP.

Simulation run time: Lastly the model was setup to output results every 30.5 days and for 480 months, which means that the model will run for 40 year.

Chapter 7 Results and Analysis

The final aim was to compare the output produced by IC-FERST, with the results from the commercial software ECLIPSE – to be presented in this chapter.

7.1 Both Models Construction Summary

7.1.1 Boundary Conditions

The real case was set to run in both ECLIPSE and IC-FERST using all the input data and model construction steps shown previously in section Chapter 5. IC-FERST uses by default SI units and ECLIPSE was set to use METRIC units. The two models were set to run for 40 years with a time step of 1 month, with an initial reservoir pressure of $3.524\text{E}+6$ Pas. (352.4 bars). The two models had 8 injection wells with an injection control pressure of $4\text{E}+7$ Pas. (400 bars) and 25 producing wells with a production control pressure of $5\text{E}+6$ Pas. (50 bars). The initial water and oil saturations were set to be 0.25 and 0.75 respectively. Figure (7.1) shows the location of all the 8 injection wells along with the 25 production wells.

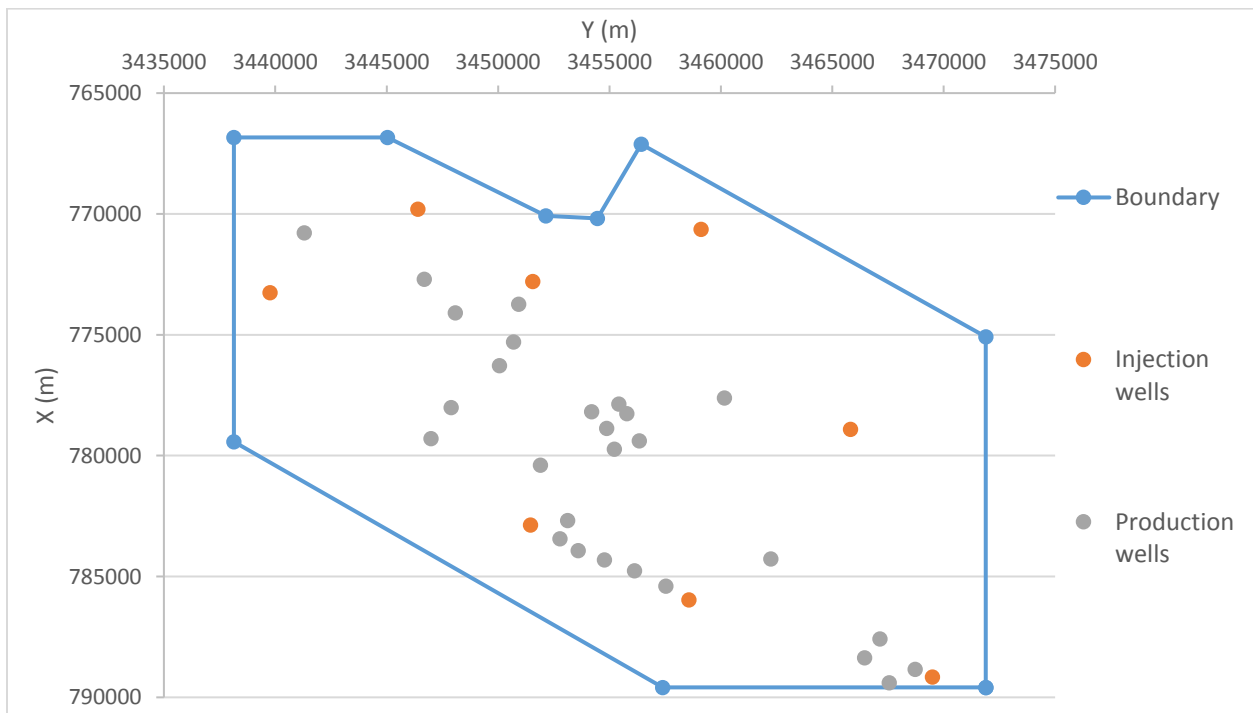


Figure (7.1): Field boundary with Injection and Production well locations

7.1.2 Fluid Properties

The oil fluid properties (oil density, oil formation volume factor, dissolved gas oil ration, and the oil viscosity) for ECLIPSE were taken from the PVT analysis done on the field as shown in section 5.5 and Figure (5.23) and were entered in a table form against pressure. Unfortunately IC-FERST still does not have a built-in function to take a graph or a set of points for the oil density and the oil viscosity. Given that our initial pressure was above the bubble point pressure and the pressure had to be always maintained above the bubble point pressure, so an average value for the oil density and viscosity were taken as 849 kg/m^3 and $8.9\text{E-}3 \text{ Pa.s}$ (8.9 cp) respectively. IC-FERST still does not allow for an oil formation volume factor (Bo) and a dissolved gas oil ratio (Rs) factor, so they were not used in the IC-FERST model. The water fluid properties were taken to be standard values of water in both models that is the density and viscosity were set to be 1025 kg/m^3 and $8.9\text{E-}4 \text{ Pa.s}$ (0.89 cp) respectively.

7.1.3 Rock Properties

The porosity in IC-FERST was assigned using the S-Gems SGS algorithm from the log data after making the 3 semi-variograms. The rock type in IC-FERST was populated using the S-Gems SIS algorithm again after making the 3 semi-variograms and after using the ANN to get the rock type in all the wells from the log data after applying Amaeful technique to get the rock type from the core data. On the other hand, the porosity was assigned in ECLIPSE using the PETREL SGS built-in algorithm which makes the semi-variogram automatically from the log data. The same 8 rock types from Amaeful technique were populated in all the wells using PETREL built-in neural network, then the rock types were assigned using the PETREL built-in SIS algorithm which again makes the semi-variogram automatically.

The same permeability equation was used for each rock type after the population to get the permeability using the porosity in both ECLIPSE and IC-FERST. The relative permeability of each rock type was assigned to each rock type in IC-FERST using the data from Table (5-5), and the capillary pressure was also assigned using the entry pressure of the analogous field and the data in table Table (5-5). In ECLIPSE the relative permeability and the capillary pressure were entered as a table, these tables were generated from also the data in Table (5-5).

7.1.4 Grid and Computational Properties

The grid was pre-built for ECLIPSE using PETREL using contour maps and seismic data of the field. As mentioned in section 4.4 Eclipse showed higher accuracy when using very fine grids, so the model was built to have 944,962 grid cells. The grid was built for IC-FERST using Trelis as show in section 6.1.1. As mentioned in section 4.4 IC-FERST showed high accuracy using fine meshes for complex models, so the model was built to have the maximum number of elements allowed for our model by Trelis smart meshing tool, i.e. 223,782 elements.

The IC-FERST model was run on a core-i7 processor using parallel processing using 12 processors without the adaptivity option and a 16 GB ram memory. The ECLIPSE model was run on a core-i7 processor with 2.00 Ghz computing speed using single processor and an 8 GB ram memory.

7.2 Comparison Between the two Models

7.2.1 Total Field Results Comparison

After the two models were run for 40 years' time period and using the description and settings mentioned in section 7.1, the results were extracted from the CSV file from IC-FERST and from the ECLIPSE office from ECLIPSE. The ECLIPSE units were converted to m³/s to match the IC-FERST units. Figure (7.2) shows a comparison between the total field's oil and water production and water injection rates between IC-FERST and ECLIPSE along the 40 years. Table (7-1) shows the percentage difference between IC-FERST and ECLIPSE for the graphs presented in Figure (7.2).

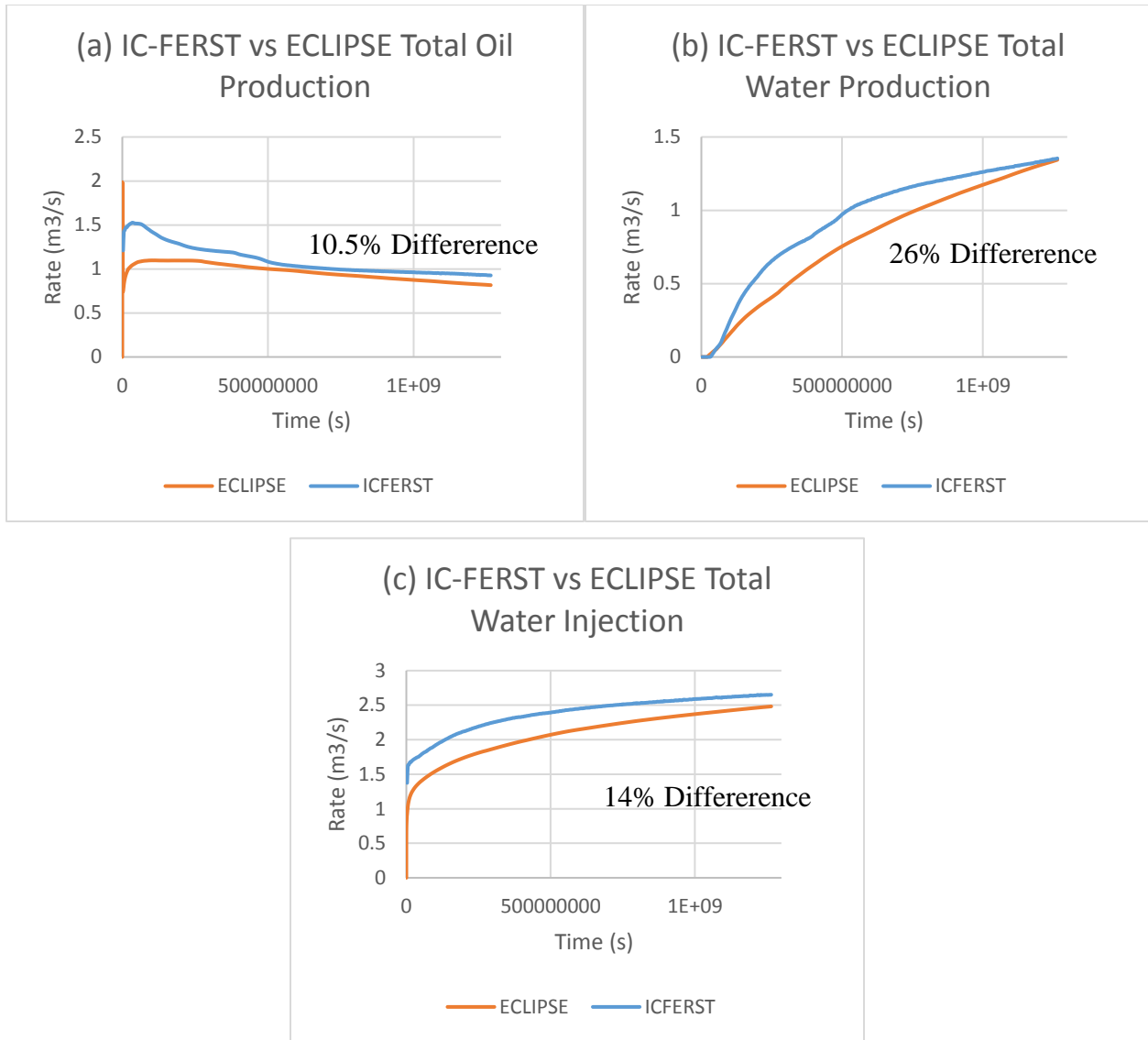


Figure (7.2): Comparison between IC-FERST and ECLIPSE results a) Oil production b) Water production c) Water injection

Table (7-1): Percentage difference between IC-FERST and ECLIPSE for the Oil and Water production and the Water injection

% Difference Oil	% Difference Water	% Difference Injection
10.5	26	14

Looking at Figure (7.2) and Table (7-1), we can tell that IC-FERST gives an acceptable good match with ECLIPSE in all the graphs and that both the packages follow the same trend. Both the models show a high difference between them in the beginning of the run and as the run goes on the results

tend to get closer to each other. This is due to the fact that at the beginning of the run the PDEs are solved with very high conversion error and as the run goes on the PDEs start showing less conversion error as the run stabilizes.

It is noticed that IC-FERST over estimates the oil production, water production and water injection; this mismatch is due to a couple of reasons. The first reason for this over estimation is that IC-FERST lacks the formation volume factor option, the formation volume factor option allows ECLIPSE to compute the injection and production rates at surface condition, whilst IC-FERST computes the injection and production rates at reservoir conditions. The fluid water/oil tend to take up more volume at the surface than at the reservoir conditions, for this reason ECLIPSE shows lower injection and production rates.

The second main reason for this mismatch is that the ECLIPSE model was constructed using contour maps and with high accuracy and details, whilst the IC-FERST model was constructed from the ECLIPSE model to make it as close as possible to the ECLIPSE model. This means that the ECLIPSE model shows more unconformity as can be seen in Figure (7.3) (a), hence, less pore volume and less original oil in place, resulting in less oil production than IC-FERST. Due to this same reason some wells also may have been drilled in a tight section of the reservoir or beside a fault; if this is the case these wells will show lower production and injection rates while maintaining their pressure conditions. This phenomenon will only be detected by ECLIPSE and not by IC-FERST, hence again, less injection and production rates.

The last reason for the mismatch is that IC-FERST still does not take the fluid density and viscosity as a table or as a function in pressure as ECLIPSE does, so as mentioned earlier the density and viscosity were entered in IC-FERST as a constant value whilst in ECLIPSE the values were entered in a table format a function of pressure as shown in Figure (5.23). Looking at Figure (5.23) we see that both the density and viscosity of the fluid tend to decrease with decreasing pressure values, this decrease in the density and viscosity is taken into calculations in ECLIPSE only and not in IC-FERST.

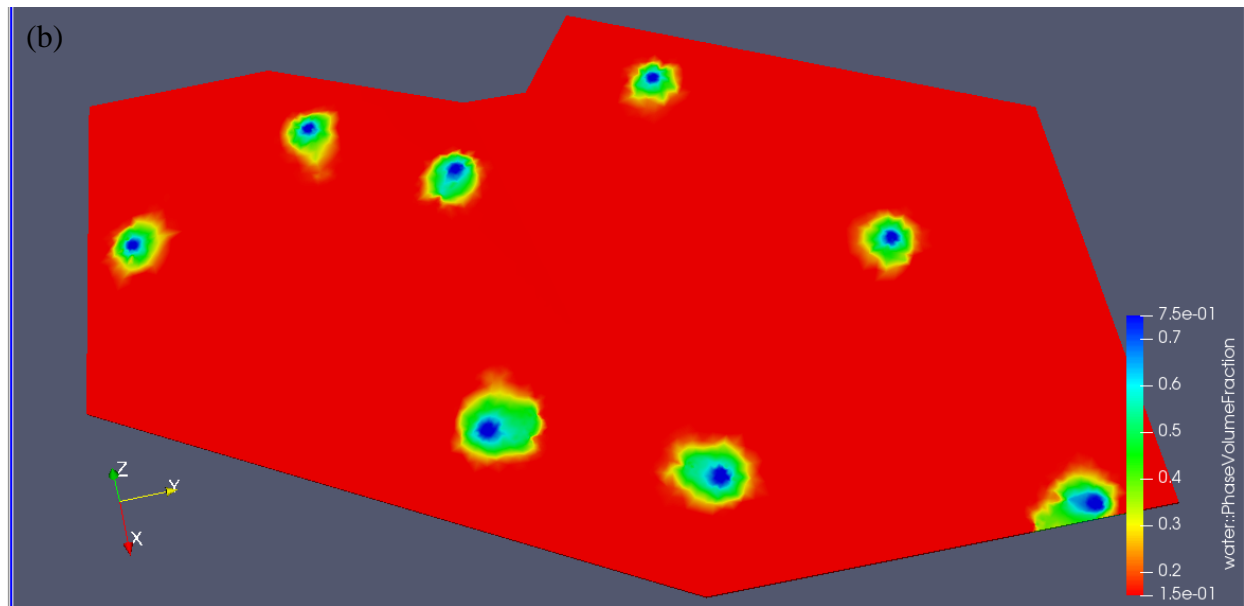
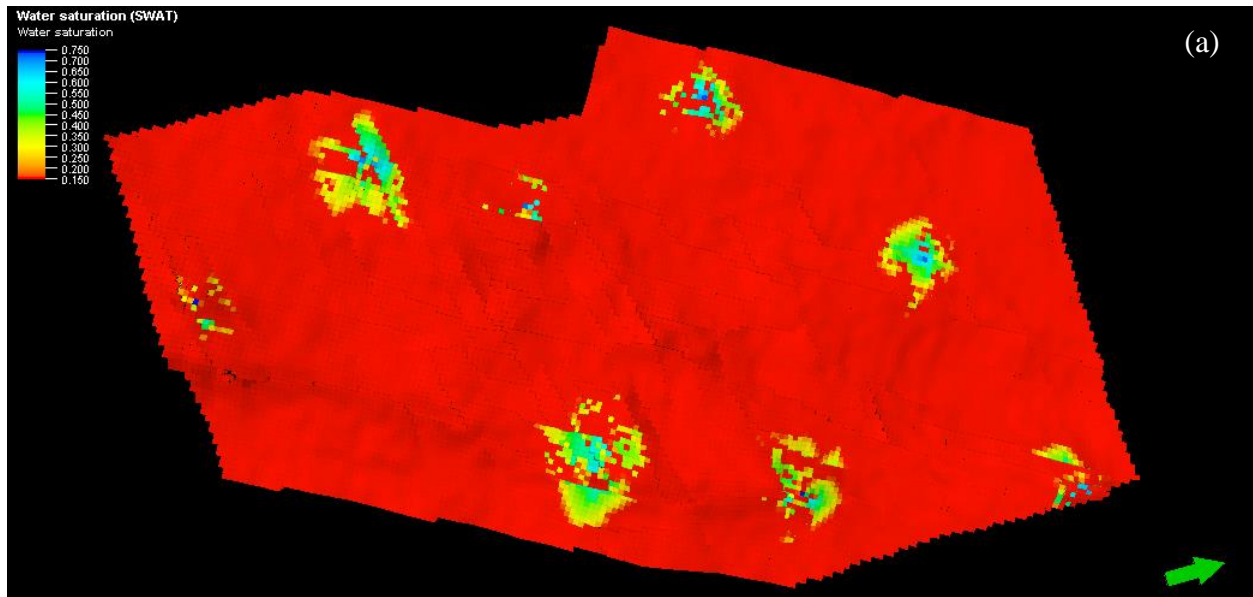


Figure (7.3): Real field case water saturation after 40 years in a) ECLIPSE b) IC-FERST

7.2.2 Well by Well Comparison

To make a more detailed comparison between IC-FERST and ECLIPSE, 10 production wells were chosen to make a detailed comparison between their IC-FERST and ECLIPSE oil and water production rates. Figure (7.4) shows the 10 selected production wells location along with the 8 injection wells locations. Figure (7.5) shows the location of the 10 selected production wells in both IC-FERST and ECLIPSE.

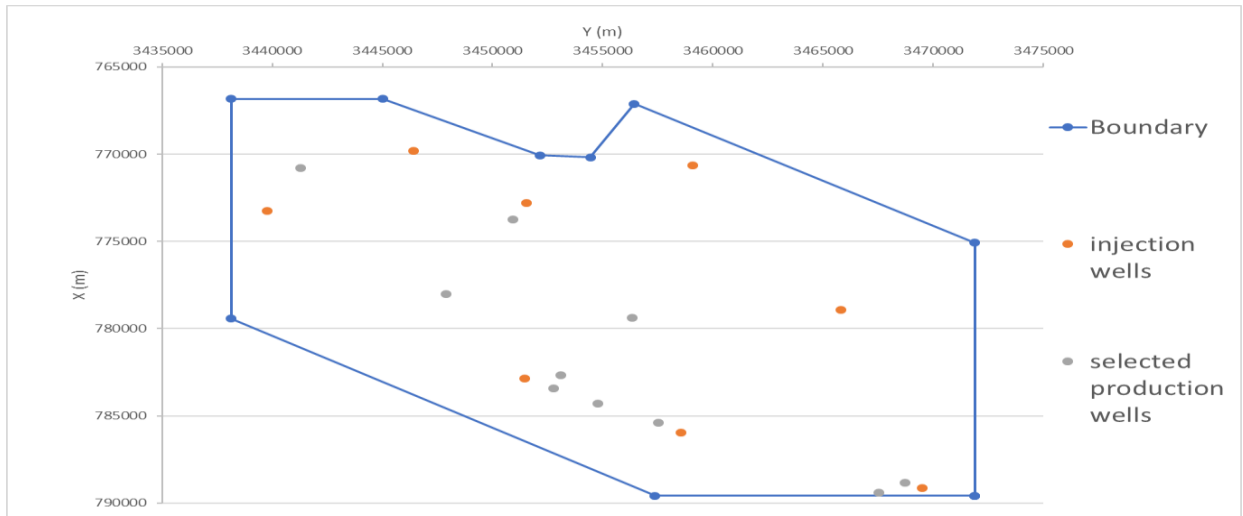


Figure (7.4): 10 selected production wells with the 8 injection wells location

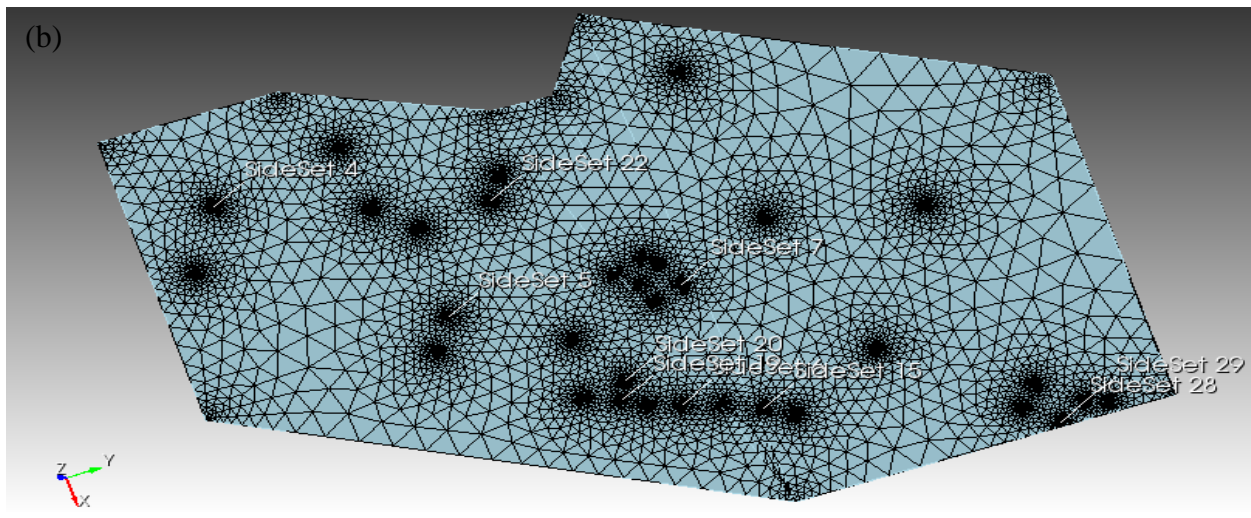
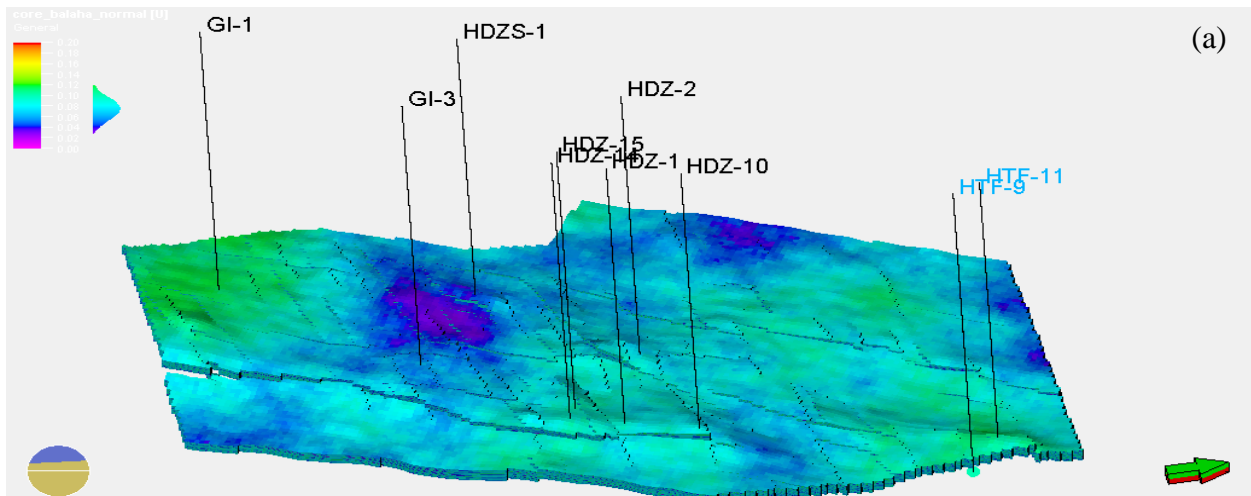


Figure (7.5): 10 selected production well locations in a) ECLIPSE b) IC-FERST

Table (7-2) shows the oil and water production rates over the 40 years run time for both IC-FERST and ECLIPSE for the 10 selected wells; IC-FERST results are shown in blue color and ECLIPSE results are shown in orange color. Table (7-3) shows the percentage difference between IC-FERST and ECLIPSE for both oil and water production rates for each well for the graphs presented in Table (7-2).

Looking at the graphs in Table (7-2), we can tell that IC-FERST gives an acceptable good match with ECLIPSE in almost all the graphs. The graphs show that both the packages follow the same trend, both the models show a high difference between them in the beginning of the run for approximately the first 10, years specially in the oil flow rates; as the run goes on the results tend to get closer to each other. This is due to the same fact mentioned earlier, that at the beginning of the run the PDEs are solved with very high conversion error and as the run goes on the PDEs start showing less conversion error as the run stabilizes.

In both the wells GI-3 and HDZ-2, the water production was zero, meaning that the injected water from the nearest injection well did not reach the production well. Although when looking at the graph of the water production of HDZ-2 we can see a great difference, but when looking at the production rate we can see that it is very small that it could be neglected. On the other hand in wells GI-3 and HDZ-1 water production rates; it can be seen that towards the very end of the run time ECLIPSE starts producing very little water, whilst IC-FERST does not produce water. This states that in ECLIPSE water started reaching the producing well earlier than IC-FERST. All these wells did not show water production in the 40 years' time period because they are geologically located far away from any injection well.

Wells HDZ-14, HDZ-15, HDZS-1, HTF-9 and HTF-11 showed a very good match in the water production rates between the two packages, the two packages followed the same trend and showed very close production rates. Well HDZ-10 did not show a very good match, but had the same start and end point between the two packages. Well GI-1 showed early water production in ECLIPSE and lower water production rates as well.

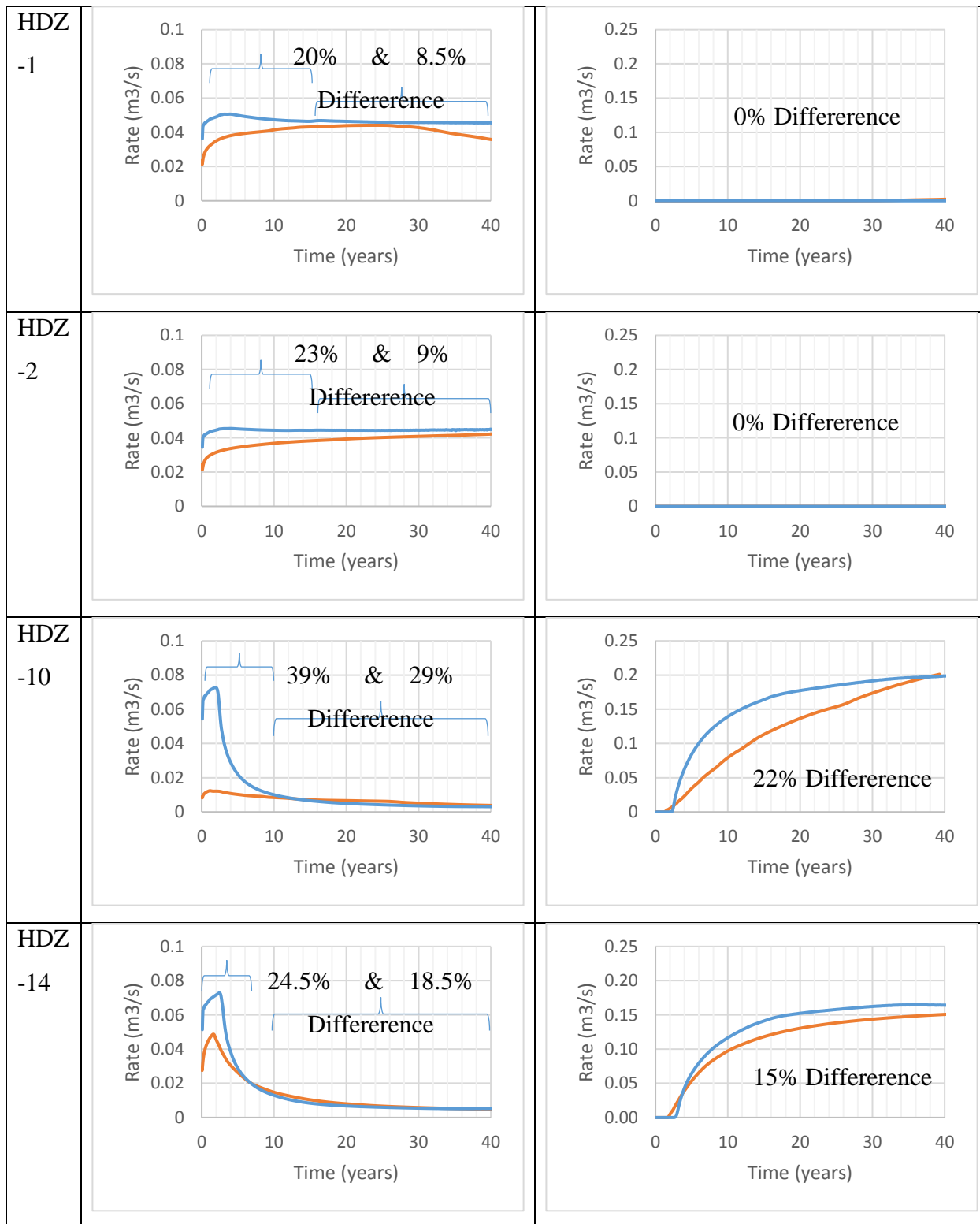
In general all the wells in ECLIPSE experience an earlier water production than IC-FERST, but after IC-FERST starts producing water, the water production rates of IC-FERST is higher than ECLIPSE. This was also noticed in the total field water production graphs shown in Figure (7.2)

(b). This mismatch between the two packages can be explained by the same 3 reasons stated earlier in the total field graph's analysis.

Looking at all the oil production graphs, we can see that all the wells at the starting point showed a great difference between the two packages, towards the mid-time of the run the results get closer to each other and towards the end of the run the results are almost identical. The wells that showed a bigger difference in the starting time are the wells that have water production in them, this shows that when the flow is a multiphase flow IC-FERST tends to overestimate the oil production.

Table (7-2): Oil and Water production rates for the 10 selected well showing ECLIPSE (Orange line) vs IC-FERST (Blue line) water and oil production rates.

Well	Oil Production Rate	Water Production Rate
GI-1		
GI-3		



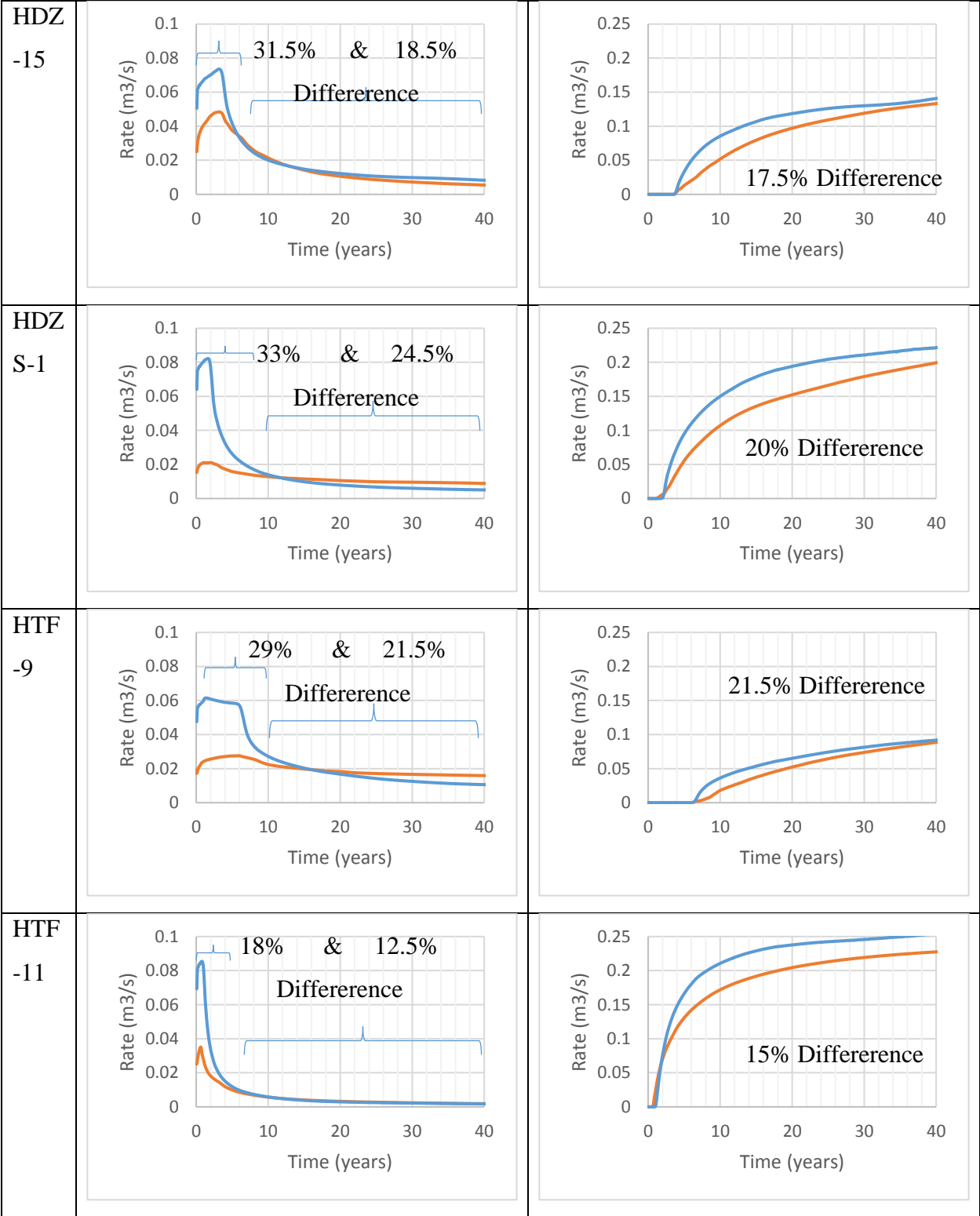


Table (7-3): Percentage difference between IC-FERST and ECLIPSE for the Oil and Water production

Well Name	% Difference Oil Early Time	% Difference Oil Late Time	% Difference Oil All Time	% Difference Water All Time
GI-1	25 (0-15 years)	3 (15-40 years)	12	16.5
GI-3	23 (0-15 years)	10 (15-40 years)	15	N/A
HDZ-1	20 (0-15 years)	8.5 (15-14 years)	13	N/A
HDZ-2	23 (0-15 years)	9 (15-40 years)	15	N/A
HDZ-10	39 (0-10 years)	29 (10-40 years)	31.5	22
HDZ-14	24.5 (0-5 years)	18.5 (5-40 years)	19	15
HDZ-15	31.5 (0-5 years)	18.5 (5-40 years)	20.5	17.5
HDZS-1	33 (0-10 years)	24.5 (10-40 years)	26.5	20
HTF-9	29 (0-15 years)	21.5 (15-40 years)	24.5	21.5
HTF-11	18 (0-5 years)	12.5 (5-40 years)	13	15
Average %	26.5	15.5	19	18

To expand more on the comparison results, the percentage difference in Table (7-3) for the oil production was divided into 3 sections (I) the early time period, (II) the late time period and (III) the full 0 to 40 years. The early time period varies in each well depending on when the two models start to give close results. Looking at the oil total production percentage difference results in Table (7-3), we can see that the 3 highest wells are HTF-9 with a percentage of 24.5%, HDZS-1 with a percentage of 26.5% and HDZ-10 with a percentage of 31.5%. Well HDZ-10 showed this high percentage difference because it is located exactly beside a fault as shown in Figure (7.5), this fault is only present in ECLIPSE as mentioned earlier, hence, the higher IC-FERST production rates. Well HTF-9 is located exactly at the boundary of the model as shown in Figure (7.5) whilst well HDZS-1 is not near a visible fault from the top view nor beside the boundary, its mismatch can be explained as well HDZ-10, but the fault is not visible.

All the other 8 wells showed a maximum difference of 20%. All the 10 wells showed an average of 26.5% difference in the early time oil production period; whilst showing an average of 15.5%

difference in the late oil production time period. The wells showed a total of 19% difference over the 40 year oil production. Looking at the water production percentage differences, the same 2 wells HTF-9 and HDZ-10 showed the largest percentage differences of 21.5% and 22% respectively. All the other 8 wells showed again a maximum difference of 20% and all the 10 wells showed an average of 18.5% difference in the water production.

These percentage difference values are considered very good values and are acceptable given that IC-FERST is still not a commercial package and is still an under development open source package.

7.2.3 Time Step Comparison

In all the previous work in the real field case and in the validation cases, a constant time step was used, hence the effect of increasing or decreasing the time step was not tested. So, as a final test, we will rerun both ECLIPSE and IC-FERST for the real field case but with a week time step instead of a month. This is to make sure that using a large time step, does not result in a numerical dispersion error or results in a less accurate convergence.

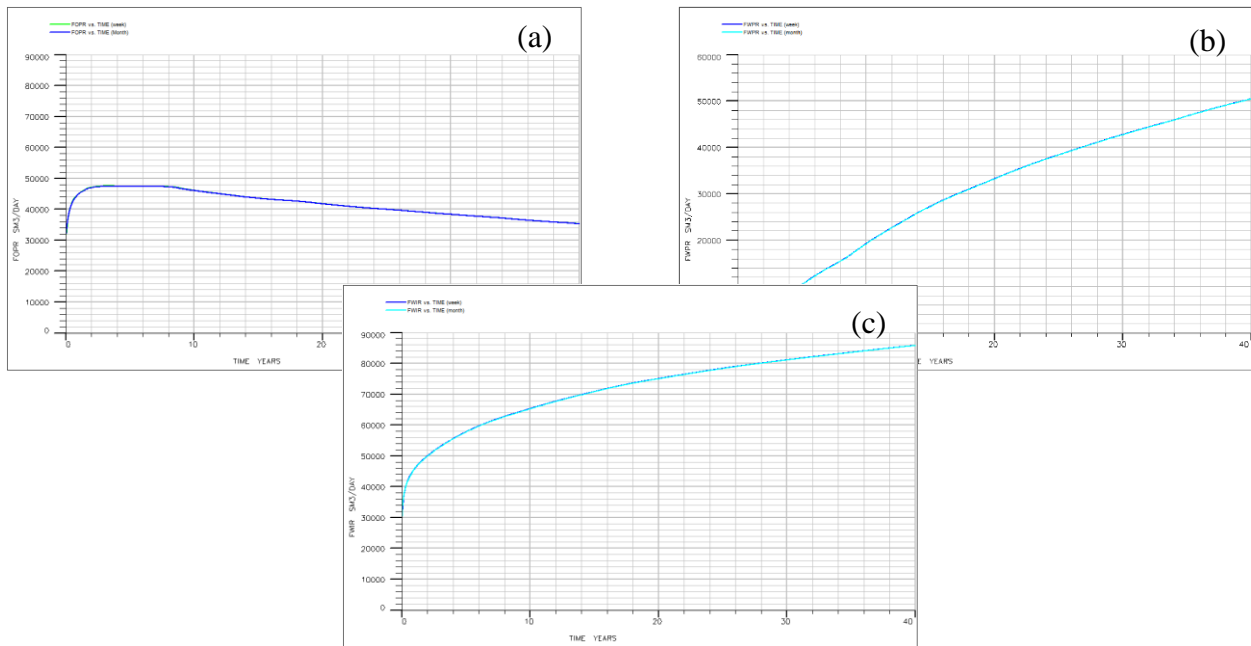


Figure (7.6): ECLIPSE total week vs month timestep a) Oil production b) Water production c) Water injection

Figure (7.6) shows the results for both the one week and one month ECLIPSE runs, showing (a) the total oil production, (b) the total water production and (c) the total water injection whilst Figure (7.7) shows the results for both the one week and one month IC-FERST runs, showing (a) the total oil production, (b) the total water production and (c) the total water injection

Looking at the ECLIPSE results in Figure (7.6), it is clear that both the graphs are identical that they are overlapping each other. Hence, the one month time step did not result in any numerical dispersion. Now, looking at the IC-FERST results in Figure (7.7), it is clear that the graphs are not perfectly overlapping each other; there is a very small difference; this means, that the one month time step only resulted in a very small numerical dispersion.

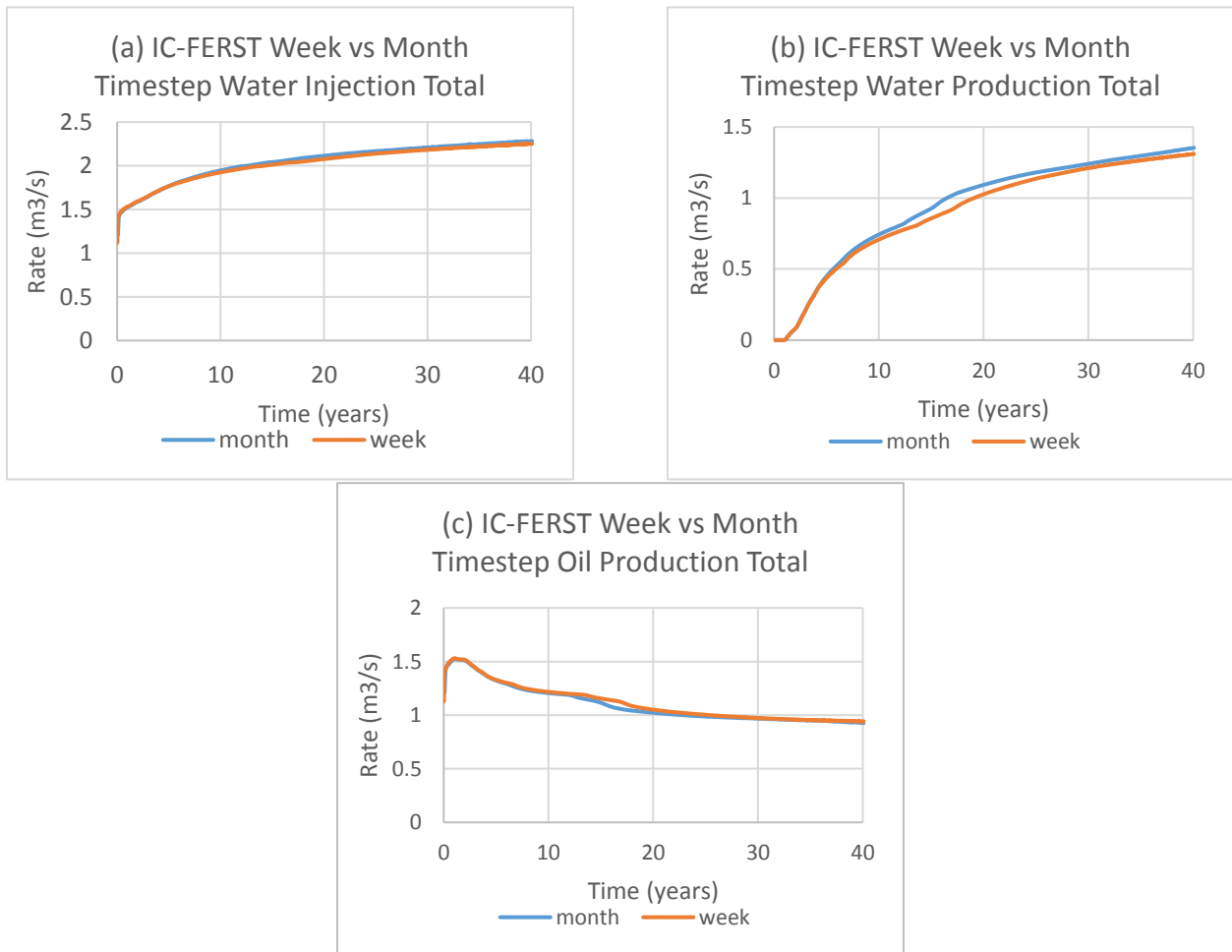


Figure (7.7): IC-FERST total week vs month timestep a) Oil production b) Water production c) Water injection

7.3 Conclusion

After running both IC-FERST and ECLIPSE for the real field case, and after analyzing the results for all the wells all together and for 10 specific wells alone, quantitatively and qualitatively; what can be concluded from the results is that:

- IC-FERST tends to overestimate both the production and injection rates for both water and oil.
- IC-FERST oil production results in the early time period of the run time tends to be higher than ECLIPSE, but after this initial period, the results begin to be much closer to each other. This is reflected in the percentage difference in Table (7-3).
- IC-FERST showed a percentage oil production difference of 10.59%, a water production difference of 26% and a water injection difference of 14% when combining all the 33 wells over the full time period. (Table (7-1)).
- When studying each well alone and taking 10 wells as a sample to study IC-FERST showed an average percentage of 26.5% ranging from 18% to 39% in the early time period for oil production. In the late time period it showed an average percentage difference of 15.5% ranging from 3 to 29% for the oil production. When looking at the full time period it showed an average of 19% ranging from 12% to 31.5% for the oil production. The water production rates showed a total average difference of 18.5% ranging from 15% to 22%. The total, and late time period results show a considerable improvement from the early time period. (Table (7-3))

Possible reasons for the differences are:

- The ECLIPSE model was built using seismic data and hence contains all the unconformity details in the reservoir e.g. faults/fractures, whilst the IC-FERST model did not include such data.
- The ECLIPSE model was setup using the formation volume factor (B_o) and the dissolved gas oil ratio (R_s) whilst IC-FERST does not have these capabilities yet.
- ECLIPSE takes the density and the viscosity values as a graph function in pressure whilst IC-FERST takes them as a constant average value.

Chapter 8 Summary, Conclusion and Recommendations

In this section, a summary of the chapters, as well as the conclusions for this work, is presented. Subsequently, the recommendations for future research are given.

8.1 Summary and Conclusion

The following presents the summary and conclusion for this research:

- To investigate more heterogenous and complex geometries, we presented a recently developed state of the art open source IC-FERST package with an unstructured mesh technique that included both a CVFEM and mesh adaptivity, along with an IMPES formulation to decouple both pressure and saturation equations and parallel processing.
- We implemented and compared the IC-FERST results against the petroleum industry bench mark reservoir simulator ECLIPSE developed by Schlumberger using a structured grid and a FDM using three hypothetical geometries: (I) a quarter five spot with one geological layer; (II) the same model as in (I) but with 5 different geological layers and (III) a full 5 spot with 5 different geological layers. Three different mesh resolutions were applied in both the packages and the adaptivity option was tested in IC-FERST.
- The validation results showed that in all the scenarios good agreements were observed between IC-FERST and ECLIPSE results. The percentage differences observed ranged between: (I) 4.5% and 12% for the oil and water injection, and 23% and 30.5% for the water production; (II) 1% and 5% for the oil and water injection, and 12% and 14.5% for the water production; (III) 2% and 4% for the oil and water injection, and 23% for the water production. IC-FERST showed more accurate results using a fine mesh compared to ECLIPSE, but due to the big run time difference between the IC-FERST fine and coarse mesh, and the very small percentage difference between the two meshes compared to ECLIPSE fine mesh; it is concluded that it is best to run IC-FERST in a coarse mesh for simple geometries to get the best results with the lowest computational time. ECLIPSE takes less computational time in simpler geometries while IC-FERST takes less computational time in more complex geometries. It was not possible to fully exploit the mesh-adaptivity of the IC-FERST software at this stage as it

demonstrated oscillations in the results. Further development need to be conducted regarding this aspect of the software.

- One of the novelties of this work was the analysis of real field data and rock characterization application – and the subsequent transfer of this information into the IC-FERST software. The implementation of a novel rock characterization approach allowed for the discretization of the different rock types in the reservoir to be allocated the correct permeability, capillary pressure and relative permeability. This data was subsequently imbedded into IC-FERST. A specifically written rock characterization code was written, which computes and discretizes the rock types of any reservoir and outputs the permeability equations that are function of porosity for each rock type.
- Implementation of geostatistical techniques was subsequently necessary to populate the IC-FERST model with the rock properties extracted from the rock characterization MATLAB code. The geostatistical calculations were carried out using the open source geostatistical package S-GEMS.
- IC-FERST was modified to allow input of the rock characterization and geostatistics created data from the real field into every cell of the domain. To achieve this, a specific PYTHON script was written to allow for the output from the rock characterization MATLAB code and from S-GEMS to be imbedded into IC-FERST.
- The IC-FERST results from the real field were compared with ECLIPSE simulations, and the percentage difference were estimated for (I) ten individual wells and (II) the total of all production wells. The results showed that a good agreement exists between the IC-FERST and ECLIPSE simulations, with an average percentage difference for the total oil production of 10.5%, the total water production of 26% and the total water injection of 14%. The results for the ten individual wells showed an average percentage difference of 15.5% ranging from 3 to 29% for the oil production in the late time period. Slightly higher differences were observed when the overall period was considered due to the large difference at the early time period of the simulation.
- Possible reasons for the differences are that the ECLIPSE model was built including unconformity details such as fault and fractures, formation volume factors, dissolved gas oil ratios and density and viscosity values as a function of pressure whilst IC-FERST model did not.

- Overall, the results presented showed that IC-FERST can rival with existing commercial reservoir simulators, especially if certain features are added such as: easy incorporation of fractures/faults for real fields, incorporation of density variations with pressure and easy implementation of adaptivity.

8.2 Recommendations/Future Work

To allow for IC-FERST to be a commercial petroleum reservoir simulation full package these recommendations need to be taken into consideration:

- Allow IC-FERST to read geometry formats from existing pre-processor software such as PETREL, that offer a more user friendly way to build complex geometries or read seismic and contour maps data.
- Allow IC-FERST to define wells in the geometry itself without the use of the pre-processor and allow the wells to be perforated in flexible intervals.
- Make the adaptivity options more user friendly.
- Make a proper user manual.
- Make IC-FERST read the rock properties and the initial conditions at the first time step instead of reading them at every time step. This will save a lot of computational time.
- Allow IC-FERST to use oil field units instead of just SI units.
- Allow IC-FERST to consider variations of fluid density and viscosity with pressure.
- Make IC-FERST take the formation volume factor and the dissolved gas oil ratio into consideration.

To enhance further the comparisons between the IC-FERST and ECLIPSE simulations further work/research can be carried out, namely:

- Ability to import an ECLIPSE computational mesh into IC-FERST so as to ensure the same geometrical structures are considered in both software.
- Utilization of the adaptivity capability of IC-FERST to enhance computational times, and also to capture the variability around the faults and fractures.
- Consideration of longer production periods i.e. run simulations for up to 100 years of production to assess water breakthrough in production wells.

- Implementation of IC-FERST on more real field scenarios and comparison with ECLIPSE simulations.

References

- ABD, A. S. & ABUSHAIKHA, A. S. 2020. On the performance of the node control volume finite element method for modeling multi-phase fluid flow in heterogeneous porous media. *Transport in Porous Media*, 135, 409-429.
- ABDALLAH, S., SID ALI, O. & BENMALEK, S. 2016. Rock type and permeability prediction using flow-zone indicator with an application to Berkine Basin (Algerian Sahara). *SEG Technical Program Expanded Abstracts 2016*. Society of Exploration Geophysicists.
- ABED, A. A. 2014. Hydraulic flow units and permeability prediction in a carbonate reservoir, Southern Iraq from well log data using non-parametric correlation. *International Journal of Enhanced Research in Science Technology & Engineering*, 3, 480-486.
- AFKAN, S. B. & MATTHÄI, S. 2011. A new hybrid simulation method for multiphase flow on unstructured grids with representations of material interfaces. *Mathematical Geosciences at the Crossroads of Theory and Practice, IAMG Salzburg 2011, Salzburg proceedings*.
- AGUILAR, C., HUGO, G. & RINCÓN, G. Hydraulic unit determination and permeability prediction based on flow zone indicator using cluster analysis. 2014. *OnePetro*.
- AHMED, T. 2001a. *Reservoir Engineering Handbook*, Houston, Gulf Professional Publishing.
- AHMED, T. 2001b. *Reservoir Engineering Handbook Second Edition*?. Gulf Professional Publishing, Houston, Texas.
- AKAM, S. A., MAHER, T., SCHELL, C. & ARNOTT, S. Flow Quality Indicator (FQI): An Innovative Approach to Permeability Prediction. 2010. *OnePetro*.
- AL-DHAFFERI, A. M. & NASR-EL-DIN, H. A. 2007. Characteristics of high-permeability zones using core analysis, and production logging data. *Journal of Petroleum Science and Engineering*, 55, 18-36.
- AL KUBAISY, J., SALINAS, P. & JACKSON, M. D. A Hybrid Pressure Approximation in the Control Volume Finite Element Method for Multiphase Flow and Transport in Heterogeneous Porous Media. Available at SSRN 4159546.

- ALAVI, M. F. Determination of Reservoir Permeability Based on Irreducible Water Saturation and Porosity from Log Data and Flow Zone Indicator (FZI) from Core Data. 2014. European Association of Geoscientists & Engineers, cp-395.
- AMAEFULE, J. O., ALTUNBAY, M., TIAB, D., KERSEY, D. G. & KEELAN, D. K. Enhanced reservoir description: using core and log data to identify hydraulic (flow) units and predict permeability in uncored intervals/wells. 1993. OnePetro.
- AZEVEDO, L. & SOARES, A. 2017. Geostatistical methods for reservoir geophysics, Springer.
- AZIZ, K. 1979. Petroleum reservoir simulation. Applied Science Publishers, 476.
- AZIZ, K. 1993. Reservoir simulation grids: opportunities and problems. Journal of Petroleum Technology, 45, 658-663.
- BABUŠKA, I. & SURI, M. 1994. The p and h-p versions of the finite element method, basic principles and properties. SIAM review, 36, 578-632.
- BAGCI, A. S. & AKBAS, C. Y. Permeability estimation using hydraulic flow units in carbonate reservoirs. 2007. OnePetro.
- BASTIAN, P. & HELMIG, R. 1999. Efficient fully-coupled solution techniques for two-phase flow in porous media: Parallel multigrid solution and large scale computations. Advances in Water Resources, 23, 199-216.
- BERGER, M. J. & COLELLA, P. 1989. Local adaptive mesh refinement for shock hydrodynamics. Journal of computational Physics, 82, 64-84.
- BLUNT, M. J. 1997. Effects of heterogeneity and wetting on relative permeability using pore level modeling. SPE journal, 2, 70-87.
- BRENNEN, C. E. 2005. Fundamentals of multiphase flow.
- BROOKS, A. N. & HUGHES, T. J. R. 1982. Streamline upwind/Petrov-Galerkin formulations for convection dominated flows with particular emphasis on the incompressible Navier-Stokes equations. Computer methods in applied mechanics and engineering, 32, 199-259.
- BROOKS, R. H. & COREY, A. T. 1966. Properties of porous media affecting fluid flow. Journal of the irrigation and drainage division, 92, 61-88.

- BUCKLEY, S. E. & LEVERETT, M. 1942. Mechanism of fluid displacement in sands. Transactions of the AIME, 146, 107-116.
- BUDD, C. J., HUANG, W. & RUSSELL, R. D. 2009. Adaptivity with moving grids. Acta Numerica, 18, 111-241.
- CARIAGA, E., CONCHA, F. & SEPÚLVEDA, M. 2005. Flow through porous media with applications to heap leaching of copper ores. Chemical Engineering Journal, 111, 151-165.
- CARMAN, P. C. 1939. Permeability of saturated sands, soils and clays. The Journal of Agricultural Science, 29, 262-273.
- CHANDRA, T. 2008. Permeability estimation using flow zone indicator from Well log data. PHIN, 3, m3.
- CHAVENT, G. & JAFFRÉ, J. 1986. Mathematical models and finite elements for reservoir simulation: single phase, multiphase and multicomponent flows through porous media, Elsevier.
- CHAVENT, G. & ROBERTS, J. E. 1991. A unified physical presentation of mixed, mixed-hybrid finite elements and standard finite difference approximations for the determination of velocities in waterflow problems. Advances in Water Resources, 14, 329-348.
- CHEN, Z.-X. 1988. Some invariant solutions to two-phase fluid displacement problems including capillary effect. SPE reservoir engineering, 3, 691-700.
- CHEN, Z. 2007. Reservoir simulation: mathematical techniques in oil recovery, SIAM.
- CHEN, Z., HUAN, G. & MA, Y. 2006. Computational methods for multiphase flows in porous media, SIAM.
- CHILES, J.-P. & DELFINER, P. 2009. Geostatistics: modeling spatial uncertainty, John Wiley & Sons.
- COATES, G. R. & DUMANOIR, J. L. A new approach to improved log-derived permeability. 1973. OnePetro.
- CONSONNI, P., THIELE, M. R., PALAGI, C. L. & AZIZ, K. Flexible gridding techniques for coning studies in vertical and horizontal wells. 1993. OnePetro.

CSIMSOFT 2017. Trelis 16.3 user Documentation.

CUMMING, B., MORONEY, T. & TURNER, I. 2011. A mass-conservative control volume-finite element method for solving Richards' equation in heterogeneous porous media. BIT Numerical Mathematics, 51, 845-864.

D'WINDT, A. Reservoir zonation and permeability estimation: A Bayesian approach. 2007. OnePetro.

DAHLE, H. K., ESPEDAL, M. S., EWING, R. E. & SÆVEREID, O. 1990. Characteristic adaptive subdomain methods for reservoir flow problems. Numerical Methods for Partial Differential Equations, 6, 279-309.

DAKE, L. P. 1978a. Fundamentals of reservoir engineering, Netherlands, ELSEVIER.

DAKE, L. P. 1978b. Fundamentals of Reservoir Engineering: The Netherlands. Elsevier Science Publishers.

DALEN, V. 1979. Simplified finite-element models for reservoir flow problems. Society of Petroleum Engineers Journal, 19, 333-343.

DARCY, H. 1856a. Les Fontaines Publiques de la Ville de Dijon. Dalmont.

DARCY, H. 1856b. Les fontaines publiques de la ville de Dijon: Exposition et application des principes à suivre et des formules à employer dans les questions de distribution d'eau: Ouvrage terminé par un appendice relatif aux fournitures d'eau de plusieurs villes, au filtrage des eaux et à la fabrication des tuyaux de fonte, de plomb, de tôle et de bitume, V. Dalmont.

DENVER, L. E. & PHILLIPS, D. C. 1990. Stratigraphic geocellular modeling. Geobyte;(USA), 5.

DESOUKY, S. 2005. Predicting permeability in un-cored intervals/wells using hydraulic flow unit approach. Journal of Canadian Petroleum Technology, 44.

DEUTSCH, C. V. 2002. Geostatistical reservoir modeling, Oxford University Press, USA.

DEUTSCH, C. V. & JOURNEL, A. G. 1998. Geostatistical software library (GSLIB)(p. 369). Oxford: Oxford University Press.

DEZABALA, E. F., VISLOCKY, J. M., RUBIN, E. & RADKE, C. J. 1982. A chemical theory for linear alkaline flooding. *Society of Petroleum Engineers Journal*, 22, 245-258.

DOYEN, P. M. 1988. Porosity from seismic data: A geostatistical approach. *Geophysics*, 53, 1263-1275.

DURLOFSKY, L. J. 1993. A triangle based mixed finite element—finite volume technique for modeling two phase flow through porous media. *Journal of Computational Physics*, 105, 252-266.

DURLOFSKY, L. J. 1994. Accuracy of mixed and control volume finite element approximations to Darcy velocity and related quantities. *Water Resources Research*, 30, 965-973.

DYKSTRA, H. & PARSONS, R. L. 1950. The prediction of oil recovery by water flood. *Secondary recovery of oil in the United States*, 2, 160-174.

EDWARDS, M. & CHRISTIE, M. A. Dynamically adaptive Godunov schemes with renormalization in reservoir simulation. 1993. OnePetro.

EIA 2014. *International Energy Outlook*. Energy Information Administration.

EYMARD, R., GALLOUËT, T. & JOLY, P. 1989. Hybrid finite element techniques for oil recovery simulation. *Computer Methods in Applied Mechanics and Engineering*, 74, 83-98.

FORSYTH, P. A. 1991. A control volume finite element approach to NAPL groundwater contamination. *SIAM Journal on Scientific and Statistical Computing*, 12, 1029-1057.

FUNG, L.-K., HIEBERT, A. D. & NGHIEM, L. X. 1992. Reservoir simulation with a control-volume finite-element method. *SPE Reservoir Engineering*, 7, 349-357.

FUNG, L. S. K., BUCHANAN, L. & SHARMA, R. 1994. Hybrid-CVFE method for flexible-grid reservoir simulation. *SPE Reservoir Engineering*, 9, 188-194.

GEIGER, S., ROBERTS, S., MATTHÄI, S. K., ZOPPOU, C. & BURRI, A. 2004. Combining finite element and finite volume methods for efficient multiphase flow simulations in highly heterogeneous and structurally complex geologic media. *Geofluids*, 4, 284-299.

GHOLINEZHAD, J., FIANU, J. S. & HASSAN, M. G. 2017. Challenges in modelling and simulation of shale gas reservoirs.

- GLÄSER, D., SCHNEIDER, M., FLEMISCH, B. & HELMIG, R. 2022. Comparison of cell-and vertex-centered finite-volume schemes for flow in fractured porous media. *Journal of Computational Physics*, 448, 110715.
- GOOVAERTS, P. 1997. *Geostatistics for natural resources evaluation*, Oxford University Press on Demand.
- GUNASEKERA, D., COX, J. & LINDSEY, P. The generation and application of K-orthogonal grid systems. 1997. OnePetro.
- HAMILTON, D. E. & JONES, T. A. 1992. Computer modeling of geologic surfaces and volumes.
- HAMZEHLOO, A., BAHLALI, M. L., SALINAS, P., JACQUEMYN, C., PAIN, C. C., BUTLER, A. P. & JACKSON, M. D. 2022. Modelling saline intrusion using dynamic mesh optimization with parallel processing. *Advances in Water Resources*, 164, 104189.
- HASSANIZADEH, M. & GRAY, W. G. 1979. General conservation equations for multi-phase systems: 1. Averaging procedure. *Advances in water resources*, 2, 131-144.
- HEINEMANN, Z. E., BRAND, C., MUNKA, M. & CHEN, Y. M. Modeling reservoir geometry with irregular grids. 1989. OnePetro.
- HELFFERICH, F. G. 1981. Theory of multicomponent, multiphase displacement in porous media. *Society of Petroleum Engineers Journal*, 21, 51-62.
- HELMIG, R. & HUBER, R. 1998. Comparison of Galerkin-type discretization techniques for two-phase flow in heterogeneous porous media. *Advances in Water Resources*, 21, 697-711.
- HELMIG, R., WEISS, A. & WOHLMUTH, B. I. 2007. Dynamic capillary effects in heterogeneous porous media. *Computational Geosciences*, 11, 261-274.
- HOTEIT, H. & FIROOZABADI, A. 2006. Compositional modeling by the combined discontinuous Galerkin and mixed methods. *SPE Journal*, 11, 19-34.
- HUBER, R. & HELMIG, R. 1999. Multiphase flow in heterogeneous porous media: A classical finite element method versus an implicit pressure–explicit saturation-based mixed finite element–finite volume approach. *International Journal for Numerical Methods in Fluids*, 29, 899-920.

HUYAKORN, P. S. & PINDER, G. F. 1978. A new finite element technique for the solution of two-phase flow through porous media. *Advances in Water Resources*, 1, 285-298.

ISAAKS, E. H. & SRIVASTAVA, R. M. 1989. *An introduction to applied geostatistics*: Oxford University Press, 561. Search in.

IZADI, M. & GHALAMBOR, A. 2013. A new approach in permeability and hydraulic-flow-unit determination. *SPE Reservoir Evaluation & Engineering*, 16, 257-264.

JACKSON, M. D., PERCIVAL, J. R., MOSTAGHIMI, P., TOLLIT, B. S., PAVLIDIS, D., PAIN, C. C., GOMES, J. L., EL-SHEIKH, A. H., SALINAS, P. & MUGGERIDGE, A. H. 2015. Reservoir modeling for flow simulation by use of surfaces, adaptive unstructured meshes, and an overlapping-control-volume finite-element method. *SPE Reservoir Evaluation & Engineering*, 18, 115-132.

JENNY, P., WOLFSTEINER, C., LEE, S. H. & DURLOFSKY, L. J. 2002. Modeling flow in geometrically complex reservoirs using hexahedral multiblock grids. *SPE journal*, 7, 149-157.

JOURNEL, A. B. & ALABERT, F. G. 1989. Focusing on spatial connectivity of extreme-valued attributes: Stochastic indicator models of reservoir heterogeneities. *AAPG Bull.:(United States)*, 73.

JOURNEL, A. G. 1974. Geostatistics for conditional simulation of ore bodies. *Economic Geology*, 69, 673-687.

JOURNEL, A. G. 1983. Nonparametric estimation of spatial distributions. *Journal of the International Association for Mathematical Geology*, 15, 445-468.

JOURNEL, A. G. & DEUTSCH, C. V. 1993. Entropy and spatial disorder. *Mathematical Geology*, 25, 329-355.

JOURNEL, A. G. & HUIJBREGTS, C. J. 1978. *Mining geostatistics*. vol. 600 Academic press. London.

KITWARE 2017. ParaView.

KOZENY, J. 1927. *Über kapillare leitung der wasser in boden*. Royal Academy of Science, Vienna, Proc. Class I, 136, 271-306.

- KRIGE, D. G. 1951. A statistical approach to some basic mine valuation problems on the Witwatersrand. *Journal of the Southern African Institute of Mining and Metallurgy*, 52, 119-139.
- KYRIAKIDIS, P. C. & JOURNEL, A. G. 1999. Geostatistical space–time models: a review. *Mathematical geology*, 31, 651-684.
- LACHASSAGNE, P. & LEDOUX, E. 1990. Evaluation of hydrogeological parameters in heterogeneous porous media. *Groundwater management*, 11, 3.
- LARSON, R. G. 1978. Analysis of the physical mechanisms in surfactant flooding. *Society of Petroleum Engineers Journal*, 18, 42-58.
- LARSON, R. G., DAVIS, H. T. & SCRIVEN, L. E. 1982. Elementary mechanisms of oil recovery by chemical methods. *Journal of Petroleum Technology*, 34, 243-258.
- LI, K. 2008. A new method for calculating two-phase relative permeability from resistivity data in porous media. *Transport in Porous Media*, 74, 21-33.
- MA, Y. Z. & ZHANG, X. 2019. *Quantitative geosciences: Data analytics, geostatistics, reservoir characterization and modeling*, Springer.
- MACDONALD, A. C., FÄLT, L. M. & HEKTOEN, A.-L. 1998. Stochastic modeling of incised valley geometries. *AAPG bulletin*, 82, 1156-1172.
- MACKAY, E. 2013. *Reservoir Simulation*, Heriot Watt.
- MANCHUK, J. G. & DEUTSCH, C. V. 2008. *The Structure of Unstructured Grids*.
- MARCONDES, F. & SEPEHRNOORI, K. 2010. An element-based finite-volume method approach for heterogeneous and anisotropic compositional reservoir simulation. *Journal of Petroleum Science and Engineering*, 73, 99-106.
- MATHERON, G. 1971. The theory of regionalised variables and its applications. *Les Cahiers du Centre de Morphologie Mathématique*, 5, 212.
- MATHERON, G. 1973. The intrinsic random functions and their applications. *Advances in applied probability*, 5, 439-468.

- MATTHÄI, S. K., MEZENTSEV, A. & BELAYNEH, M. Control-volume finite-element two-phase flow experiments with fractured rock represented by unstructured 3D hybrid meshes. 2005. OnePetro.
- MATTHÄI, S. K., MEZENTSEV, A. & BELAYNEH, M. 2007. Finite element–node-centered finite-volume two-phase-flow experiments with fractured rock represented by unstructured hybrid-element meshes. *SPE Reservoir Evaluation & Engineering*, 10, 740-756.
- MCBRIDE, D., GEBHARDT, J. E. & CROSS, M. 2012. A comprehensive gold oxide heap leach model: Development and validation. *Hydrometallurgy*, 113, 98-108.
- MELLADO, M. E., CISTERNAS, L. A. & GÁLVEZ, E. D. 2009. An analytical model approach to heap leaching. *Hydrometallurgy*, 95, 33-38.
- MOHAGHEGH, S., BALAN, B. & AMERI, S. 1997. Permeability determination from well log data. *SPE formation evaluation*, 12, 170-174.
- MOLINA-AIZ, F. D., FATNASSI, H., BOULARD, T., ROY, J.-C. & VALERA, D. L. 2010. Comparison of finite element and finite volume methods for simulation of natural ventilation in greenhouses. *Computers and electronics in agriculture*, 72, 69-86.
- MORGAN, K. & PERAIRE, J. 1998. Unstructured grid finite-element methods for fluid mechanics. *Reports on Progress in Physics*, 61, 569.
- MOSÉ, R., SIEGEL, P., ACKERER, P. & CHAVENT, G. 1994. Application of the mixed hybrid finite element approximation in a groundwater flow model: Luxury or necessity? *Water resources research*, 30, 3001-3012.
- MOSTAGHIMI, P., PAVLIDIS, D. & PAIN, C. C. 2015a. Anisotropic mesh adaptivity and control volume finite element methods for numerical simulation of multiphase flow in porous media. *Mathematical Geosciences*, 47, 417-440.
- MOSTAGHIMI, P., PERCIVAL, J. R., PAVLIDIS, D., FERRIER, R. J., GOMES, J. L. M. A., GORMAN, G. J., JACKSON, M. D., NEETHLING, S. J. & PAIN, C. C. 2015b. Anisotropic mesh adaptivity and control volume finite element methods for numerical simulation of multiphase flow in porous media. *Mathematical Geosciences*, 47, 417-440.

- MOSTAGHIMI, P., TOLLIT, B. S., NEETHLING, S. J., GORMAN, G. J. & PAIN, C. C. 2014. A control volume finite element method for adaptive mesh simulation of flow in heap leaching. *Journal of Engineering Mathematics*, 87, 111-121.
- MUNOZ, J. F., RENGIFO, P. & VAUCLIN, M. 1997. Acid leaching of copper in a saturated porous material: parameter identification and experimental validation of a two-dimensional transport model. *Journal of contaminant hydrology*, 27, 1-24.
- NARASIMHAN, T. N. & WITHERSPOON, P. A. 1976. An integrated finite difference method for analyzing fluid flow in porous media. *Water Resources Research*, 12, 57-64.
- NICK, H. M. & MATTHÄI, S. K. 2011. A Hybrid Finite-Element Finite-Volume Method with Embedded Discontinuities for Solute Transport in Heterogeneous Media. *Vadose Zone Journal*, 10, 299-312.
- NICOLAS REMY, A. B., JIANBING WU 2009. *Applied Geostatistics with SGems A User's Guide*, New York, Cambridge University Press.
- NOORUDDIN, H., HOSSAIN, M. E., SUDIRMAN, S. B. & SULAIMANI, T. Field application of a modified Kozeny-Carmen correlation to characterize hydraulic flow units. 2011. OnePetro.
- NORMS 2015. Fluidity manual. In: COLLEGE, I. (ed.). *Applied Modelling & Computation Group AMCG*.
- OLEA, R. A. 2012. *Geostatistics for engineers and earth scientists*, Springer Science & Business Media.
- OR, D. & TULLER, M. 2000. Flow in unsaturated fractured porous media: Hydraulic conductivity of rough surfaces. *Water Resources Research*, 36, 1165-1177.
- PASZKE, A., GROSS, S., MASSA, F., LERER, A., BRADBURY, J., CHANAN, G., KILLEEN, T., LIN, Z., GIMELSHEIN, N. & ANTIGA, L. 2019. Pytorch: An imperative style, high-performance deep learning library. *Advances in neural information processing systems*, 32.
- PATTON, J. T., COATS, K. H. & COLEGROVE, G. T. 1971. Prediction of polymer flood performance. *Society of Petroleum Engineers Journal*, 11, 72-84.
- PEACEMAN, D. W. 2000. *Fundamentals of numerical reservoir simulation*, Elsevier.

- PEDROSA, O. A. & AZIZ, K. 1986. Use of a hybrid grid in reservoir simulation. *SPE Reservoir Engineering*, 1, 611-621.
- PRAKASH, C. 1987a. Examination of the upwind (donor-cell) formulation in control volume finite-element methods for fluid flow and heat transfer. *Numerical Heat Transfer, Part A Applications*, 11, 401-416.
- PRAKASH, C. 1987b. Examination of the upwind (donor-cell) formulation in control volume finite-element methods for fluid flow and heat transfer. *Numerical Heat Transfer*, 4, 401-416.
- PRUESS, K. 1991. TOUGH2-A general-purpose numerical simulator for multiphase fluid and heat flow.
- PURCELL, W. R. 1949. Capillary pressures-their measurement using mercury and the calculation of permeability therefrom. *Journal of Petroleum Technology*, 1, 39-48.
- QUIRK, J. J. 1991. An adaptive grid algorithm for computational shock hydrodynamics.
- REGNIER, G., SALINAS, P., JACQUEMYN, C. & JACKSON, M. D. 2022. Numerical simulation of aquifer thermal energy storage using surface-based geologic modelling and dynamic mesh optimisation. *Hydrogeology Journal*, 30, 1179-1198.
- REMY, N. 2005. S-GeMS: the stanford geostatistical modeling software: a tool for new algorithms development. *Geostatistics banff 2004*. Springer.
- REMY, N., BOUCHER, A. & WU, J. 2009. *Applied geostatistics with SGeMS: A user's guide*, Cambridge University Press.
- RENARD, P. & DE MARSILY, G. 1997. Calculating equivalent permeability: a review. *Advances in water resources*, 20, 253-278.
- ROKICKI, J. 2014. *Computational Fluid Dynamics*. In: NOTES, L. (ed.).
- SAMMON, P. H. Dynamic grid refinement and amalgamation for compositional simulation. 2003. OnePetro.
- SAMPATH, K., PERERA, M. S. A., ELSWORTH, D., MATTHAI, S. K., RANJITH, P. G. & DONG-YIN, L. 2021. Discrete fracture matrix modelling of fully-coupled CO₂ flow–Deformation

processes in fractured coal. *International Journal of Rock Mechanics and Mining Sciences*, 138, 104644.

SCHEIDEGGER, A. E. 1958. The random-walk model with autocorrelation of flow through porous media. *Canadian Journal of Physics*, 36, 649-658.

SCHLUMBERGER 1972. Schlumberger Log Interpretation.

SCHLUMBERGER 2010. Advanced Reservoir Engineering.

SCHLUMBERGER. 2018. ECLIPSE [Online]. Available: <https://www.software.slb.com/products/eclipse> [Accessed].

SCHLUMBERGER, E. U. M. 2009. Technical description. Schlumberger Ltd, 519-538.

SCHMALZ, J. P. & RAHME, H. D. 1950. The variation of waterflood performance with variation in permeability profile. *Prod. Monthly*, 15, 9-12.

SCHMID, K. S., GEIGER, S. & SORBIE, K. S. 2013. Higher order FE–FV method on unstructured grids for transport and two-phase flow with variable viscosity in heterogeneous porous media. *Journal of Computational Physics*, 241, 416-444.

SCHMIDT, G. H. & JACOBS, F. J. 1988. Adaptive local grid refinement and multi-grid in numerical reservoir simulation. *Journal of Computational Physics*, 77, 140-165.

SECH, R. P., JACKSON, M. D. & HAMPSON, G. J. 2009. Three-dimensional modeling of a shoreface-shelf parasequence reservoir analog: Part 1. Surface-based modeling to capture high-resolution facies architecture. *AAPG bulletin*, 93, 1155-1181.

SHEDID, S. A. & ALMEHAIDEB, R. A. 2003. Enhanced reservoir description of heterogeneous carbonate reservoirs. *Journal of Canadian Petroleum Technology*, 42.

SHEWCHUK, J. R. 2002. Delaunay refinement algorithms for triangular mesh generation. *Computational geometry*, 22, 21-74.

SHOKIR, E. M. E.-M. 2006. A novel model for permeability prediction in uncored wells. *SPE Reservoir Evaluation & Engineering*, 9, 266-273.

SIDDIQUI, S., OKASHA, T. M., FUNK, J. J. & AL-HARBI, A. M. 2006. Improvements in the selection criteria for representative special-core-analysis samples. *SPE Reservoir Evaluation & Engineering*, 9, 647-653.

SLICHTER, C. S. 1899. Theoretical investigation of the motion of ground waters. The 19th Ann. Rep. US Geophys Survey., 304-319.

TEZDUYAR, T. E. & PARK, Y. J. 1986. Discontinuity-capturing finite element formulations for nonlinear convection-diffusion-reaction equations. *Computer methods in applied mechanics and engineering*, 59, 307-325.

TIAB, D. & DONALDSON, E. C. 2015. *Petrophysics: theory and practice of measuring reservoir rock and fluid transport properties*, Gulf professional publishing.

TIMUR, A. An investigation of permeability, porosity, and residual water saturation relationships. 1968. OnePetro.

TOBLER, W. R. 1970. A computer movie simulating urban growth in the Detroit region. *Economic geography*, 46, 234-240.

TODD, A. C. 2013. *Reservoir Engineering Manual*, Heriot Watt Institute of Petroleum Engineering.

TRANGENSTEIN, J. A. 2002. Multi-scale iterative techniques and adaptive mesh refinement for flow in porous media. *Advances in Water Resources*, 25, 1175-1213.

VAN DUIJN, C. J., CAO, X. & POP, I. S. 2016. Two-phase flow in porous media: dynamic capillarity and heterogeneous media. *Transport in Porous Media*, 114, 283-308.

VAN DUIJN, C. J., MOLENAAR, J. & DE NEEF, M. J. 1995. The effect of capillary forces on immiscible two-phase flow in heterogeneous porous media. *Transport in porous media*, 21, 71-93.

VER HOEF, J. M., CRESSIE, N. A. C. & GLENN-LEWIN, D. C. 1993. Spatial models for spatial statistics: some unification. *Journal of Vegetation Science*, 4, 441-452.

VERMA, S. & AZIZ, K. A control volume scheme for flexible grids in reservoir simulation. 1997. OnePetro.

- WANG, J., LU, Z., CAI, F. & FENG, Y. 2022. Fully discrete interpolation coefficients mixed finite element methods for semi-linear parabolic optimal control problem. *IEEE Access*.
- WOLFF, M., FLEMISCH, B. & HELMIG, R. 2013. An adaptive multiscale approach for modeling two-phase flow in porous media including capillary pressure. *Water Resources Research*, 49, 8139-8159.
- WU, Y.-S. 2015. *Multiphase fluid flow in porous and fractured reservoirs*, Gulf professional publishing.
- XIE, B., HUANG, Y. & XIAO, F. 2022. A high-fidelity solver based on hybrid numerical methods on unstructured grids for incompressible multiphase flows. *Journal of Computational Physics*, 111299.
- XIE, Z., PAVLIDIS, D., SALINAS, P., PERCIVAL, J. R., PAIN, C. C. & MATAR, O. K. 2016. A balanced-force control volume finite element method for interfacial flows with surface tension using adaptive anisotropic unstructured meshes. *Computers & Fluids*, 138, 38-50.
- YAGHI, H. M. 1999. *Petroleum reservoir simulation using 3-D finite element method with parallel implementation*, Louisiana State University and Agricultural & Mechanical College.
- ZHAN, L., HU, Y., ZOU, L., XU, W., YE, Z., CHEN, R., ZHUANG, D., LI, J. & CHEN, Y. 2022. Effects of multiscale heterogeneity on transport in three-dimensional fractured porous rock with a rough-walled fracture network. *Computers and Geotechnics*, 148, 104836.
- ZHENG, C. & BENNETT, G. D. 2002. *Applied contaminant transport modeling*, Wiley-Interscience New York.